# Development of a gaseous detonation driven hypervelocity launcher

Patrick L. Batchelor

Masters of Engineering

Department of Mechanical Engineering

McGill University

Montreal,Quebec

May 6, 2010

A thesis submitted to the
Faculty of Graduate Studies and Research
In partial fulfillment of the requirements of the degree
Master of Engineering

## ACKNOWLEDGEMENTS

This project would not have been completed if not for aid provided by others. I would like to thank my supervisor Prof. Andrew J. Higgins for his guidance and support over the course of this work and in particular his help in the development of the diagnostics, his work in the machine shop and his time in the lab. I would also like to thank Jimmy Verreault for his help on this project, in particular all his time in the lab running experiments. I would like to thank Nicolas Ponchaut for the use of his Eulerian solver and Daniel Szirti for his help familiarizing me with this solver. I would like to thank Jason Loiseau for our discussions on this topic and his constructive criticism during the course of this work. I would also like to thank the members of the SWPG at McGill University for their thoughts and ideas throughout the course of this work. My thanks also go to the students, past and present, of room MD256 for their interest and support for the project, in particular Alireza Najafiyazdi, David Mack and Malcolm Cairns. Many thanks to the members of McGill University's technical staff who contributed to this project, in particular Gary Savard, John Boisvert, Ray Lemay, Tony Micozzi, Roy Westgate and Sam Minter for their work on the construction of the facility for this project. Furthermore, this work was supported by a DRDC-Valcartier contract, with Paul Harris serving as technical authority. I also thank NSERC and the CSA for the financial support given to me during the course of this work. Finally, I would like to thank my family and friends for their love, support, patience and understanding over the last three years.

## ABSTRACT

The concept of using gaseous detonation waves to generate high-pressure propellant for a single-stage gas gun is investigated theoretically and experimentally. The advantage of this approach (in contrast to conventional light gas guns) is that the resulting launcher is inexpensive to construct and simple to operate, yet is capable of achieving velocities in excess of 3 km/s. Theoretical internal ballistics methods have been developed for the optimization of gas gun systems. A prototype detonation driven gas gun system has been developed. Performance of the gun system is optimized by formulating the detonable mixture to use as propellant, with fuel rich hydrogen/oxygen or helium-diluted hydrogen/oxygen appearing the most promising. All the parameters of the launcher design are explored using a quasi-one-dimensional Euler code to model the internal ballistics. Experimental implementation of the concept is performed with a 1.27-cm-inner-diameter (ID), 1.83-m barrel driven by the detonable gas mixture contained in a 1-m-long, 3.2-cm-ID driver. Velocities of 2.7 km/s are demonstrated with 2.5-g projectiles.

# ABRÉGÉ

Le concept de l'utilisation d'ondes de détonation gazeuses dans le but de générer un combustible à haute pression pour un pistolet à gaz à stade unique est exploré théoriquement et expérimentalement. L'avantage de cette approche (en comparaison avec les pistolets conventionnels à gaz léger) est que le propulseur qui en résulte est peu coûteux à construire et simple à opérer, tout en étant capable d'obtenir des vitesses en excédent de 3 km/s. Des méthodes basées sur la balistique théorique interne ont été développées pour l'optimisation des systèmes de pistolets à gaz. Un prototype de système de pistolet à gaz actionné par détonation a été développé. La performance du système de pistolet à gaz est optimisée en formulant la mixture explosive à utiliser comme combustible, avec l'hydrogène/oxygène riche en hydrogène, ou l'hydrogène/oxygène dilué avec de l'hélium, apparaissant comme les plus prometteuses. Tous les paramètres dans la conception du propulseur sont explorés en utilisant un code d'Euler quasi-dimensionnel afin de modéliser la balistique interne. L'implémentation expérimentale du concept est exécutée avec un canon de 1,27 cm de diamètre interne et de 1,83 m de longueur, actionné par une mixture gazeuse contenue dans une chambre de 1 m de longueur et de 3,2 cm de diamètre interne. Des vitesses de 2,7 km/s sont démontrées avec des projectiles de 2,5 g.

TABLE OF CONTENTS

ACKNOWLEDGEMENTS . . . . . ii

ABSTRACT . . . . . iii

ABRÉGÉ . . . . . iv

LIST OF TABLES . . . . . vii

LIST OF FIGURES . . . . . x

1 Introduction . . . . . 1

2 Internal Ballistic Theory . . . . . 7

2.1 The Lagrange Gradient . . . . . 7
2.2 Simple Wave Gun . . . . . 12
2.2.1 The Optimization of the SWPPIG Gun System . . . . . 22
2.3 The Effects of Chambrage . . . . . 49

3 Detonation Gun Prototype . . . . . 56

3.1 Gun Design . . . . . 56
3.2 Propellant Modeling . . . . . 59
3.3 Performance Modeling . . . . . 63

4 Experiment and Results . . . . . 66

4.1 Diagnostics . . . . . 66
4.2 Projectiles . . . . . 74
4.3 Experimental Details . . . . . 76
4.3.1 Facility Images . . . . . 79
4.4 Results . . . . . 84
4.4.1 Results: 6 foot (183 cm) Barrel . . . . . 84
4.4.2 Results: 12 foot (366 cm) Barrel . . . . . 86
4.4.3 Results: Ignition Location . . . . . 86

5 Discussion . . . . . 88

5.1 Experimental Results . . . . . 88
5.2 Potential Maximization of the Gun System Performance . . . . . 94

6 Conclusion . . . . . 102

References . . . . . 104

A Lagrange Gradient . . . . . 105
B Simple Wave PPIG . . . . . 110
C Gun Materials . . . . . 117
D Results for $u_{1st}$ as a function of $a_\circ$ for different $M_F$ and $\gamma$ . . . . . 122
E Prototype Design Drawings . . . . . 126
F Performance Predictions . . . . . 135
G Velocity Diagnostics Proof of Concept using Helium . . . . . 141
H Shot Data: Projectile . . . . . 142
I Shot Data: Gun . . . . . 145
J Shot Data: Results . . . . . 148
K Mixture Data: Fixed CJ Detonation Pressure of 2400 bar . . . . . 151
L Mixture Data: Fixed Reflected CJ Detonation Pressure of 5720 bar . . . 154
M Mixture Data: Fixed Pre-Detonation Pressure of 106.44 bar . . . . . 157
N Mixture Data: CV Explosion Pressure of 2400 bar . . . . . 160

LIST OF TABLES


Table page

2–1 Strength to Density Ratio for Various Materials . . . . . 28

3–1 Failure Characteristics of the Gun Parts . . . . . 59

3–2 Mass/Length Ratio of the Gun Parts . . . . . 59

3–3 Constant Volume (CV) explosion states for various initial pressures of the $2H_2+O_2$ reaction . . . . . 60

3–4 Chapman-Jouquet (CJ) detonation states for various initial pressures of the $2H_2+O_2$ reaction . . . . . 60

3–5 Reflected Chapman-Jouquet (RCJ) detonation states for various initial pressures of the $2H_2+O_2$ reaction . . . . . 60

3–6 Pressure ratio $P_r = p_\circ/(p_\circ)_{max}$ for various initial pressures of the $2H_2+O_2$ reaction . . . . . 62

3–7 $\zeta_{1^{st}}$ and $x_{1^{st}}$ for various initial pressures of the $2H_2+O_2$ reaction . . . . 62

3–8 $u_{p(ref)}$ and $u_p$ for various initial pressures of the $2H_2+O_2$ reaction . . . 63

3–9 Comparison between analytical and computational methods for determining $u_p$ for various initial pressures of the $2H_2+O_2$ reaction . . . . 64

5–1 Broken projectile data . . . . . 94

C–1 Tube Strength for steel Alloy 1020 (Hot Rolled) . . . . . 117

C–2 Tube Strength for steel Alloy 1020 (Cold Worked) . . . . . 117

C–3 Tube Strength for steel Alloy 1020 (Annealed) . . . . . 117

C–4 Tube Strength for steel Alloy 1020 (Normalized) . . . . . 118

C–5 Tube Strength for steel Alloy 1040 (Hot Rolled) . . . . . 118

C–6 Tube Strength for steel Alloy 1040 (Cold Worked) . . . . . 118

C–7 Tube Strength for steel Alloy 1040 (Annealed) . . . . . 118

C–8 Tube Strength for steel Alloy 1040 (Normalized) . . . . . 119

C–9 Tube Strength for steel Alloy 4140 (Annealed) . . . . . 119

C–10 Tube Strength for steel Alloy 4140 (Normalized) . . . . . 119

C–11 Tube Strength for steel Alloy 4140 (Oil Quenched and Tempered) . . . 119

C–12 Tube Strength for steel Alloy 4340 (Annealed) . . . 120

C–13 Tube Strength for steel Alloy 4340 (Normalized) . . . 120

C–14 Tube Strength for steel Alloy 4340 (Oil Quenched and Tempered) . . . 120

C–15 Tube Strength for Stainless Alloy A440 (Annealed) . . . 120

C–16 Tube Strength for Stainless Alloy A440 (Tempered) . . . 121

C–17 Mass per unit length for Steel Alloys [kg/m] . . . 121

C–18 Mass per unit length for steel Alloy A440 [kg/m] . . . 121

G–1 Data for the helium shots fired into vacuum . . . 141

H–1 Projectile Data . . . 142

I–1 Gun Data . . . 145

J–1 Velcoity data in m/s . . . 148

K–1 Pre-detonation pressure, in bar, for various mixtures corresponding to a CJ detonation pressure of 2400 bar . . . 151

K–2 CV explosion pressure, in bar, for various mixtures corresponding to a CJ detonation pressure of 2400 bar . . . 151

K–3 Reflected CJ detonation pressure, in bar, for various mixtures corresponding to a CJ detonation pressure of 2400 bar . . . 152

K–4 CV explosion temperature, in Kelvin, for various mixtures corresponding to CJ detonation pressure of 2400 bar . . . 152

K–5 CV explosion sound speed, in m/s, for various mixtures corresponding to CJ detonation pressure of 2400 bar . . . 153

K–6 CV explosion specific heat ratio, $\gamma$, for various mixtures corresponding to CJ detonation pressure of 2400 bar . . . 153

L–1 Pre-detonation pressure, in bar, for various mixtures corresponding to a Reflected CJ detonation pressure of 5720 bar . . . 154

L–2 CV explosion pressure, in bar, for various mixtures corresponding to a Reflected CJ detonation pressure of 5720 bar . . . 154

L–3 CJ detonation pressure, in bar, for various mixtures corresponding to a Reflected CJ detonation pressure of 5720 bar . . . 155

L–4 CV explosion temperature, in Kelvin, for various mixtures corresponding to Reflected CJ detonation pressure of 5720 bar . . . 155

L–5 CV explosion sound speed, in m/s, for various mixtures corresponding to Reflected CJ detonation pressure of 5720 bar . . . . . 156

L–6 CV explosion specific heat ratio, $\gamma$, for various mixtures corresponding to Reflected CJ detonation pressure of 5720 bar . . . . . 156

M–1 CV explosion pressure, in bar, for various mixtures corresponding to a pre-detonation pressure of 106.44 bar . . . . . 157

M–2 CJ detonation pressure, in bar, for various mixtures corresponding to a pre-Detonation pressure of 106.44 bar . . . . . 157

M–3 Reflected CJ detonation pressure, in bar, for various mixtures corresponding to a pre-detonation pressure of 106.44 bar . . . . . 158

M–4 CV explosion temperature, in Kelvin, for various mixtures corresponding to pre-detonation pressure of 106.44 bar . . . . . 158

M–5 CV explosion sound speed, in m/s, for various mixtures corresponding to pre-detonation pressure of 106.44 bar . . . . . 159

M–6 CV explosion specific heat ratio, $\gamma$, for various mixtures corresponding to pre-detonation pressure of 106.44 bar . . . . . 159

N–1 Pre-detonation pressure pressure, in bar, for various mixtures corresponding to a CV explosion pressure of 2400 bar . . . . . 160

N–2 CJ detonation pressure, in bar, for various mixtures corresponding to a CV explosion pressure of 2400 bar . . . . . 160

N–3 Reflected CJ detonation pressure, in bar, for various mixtures corresponding to a CV explosion pressure of 2400 bar . . . . . 161

N–4 CV explosion temperature, in Kelvin, for various mixtures corresponding to CV explosion pressure of 2400 bar . . . . . 161

N–5 CV explosion sound speed, in m/s, for various mixtures corresponding to CV explosion pressure of 2400 bar . . . . . 162

N–6 CV explosion specific heat ratio, $\gamma$, for various mixtures corresponding to CV explosion pressure of 2400 bar . . . . . 162

LIST OF FIGURES


Figure page

1–1 Schematic of a conventional powder gun . . . . . 1

1–2 Projectile base pressure, $p$, as a function of projectile position, $x_p$, for a conventional powder gun . . . . . 3

1–3 Schematic of a single stage light gas gun . . . . . 3

1–4 Projectile base pressure, $p$, as a function of projectile position, $x_p$, for a single stage light gas gun . . . . . 4

1–5 Schematic of a two stage light gas gun . . . . . 5

1–6 Launcher operation schematic . . . . . 6

2–1 $f(M_r)$ vs. $M_r$ . . . . . 10

2–2 $g(\gamma, \varphi)$ vs. $\varphi$ for various $\gamma$ . . . . . 11

2–3 Constant diameter PPIG gun . . . . . 12

2–4 Wave processes in a constant diameter PPIG gun . . . . . 13

2–5 $x - t$ diagram showing the paths of the projectile and the first rarefaction wave . . . . . 14

2–6 Infinite chamber length gun compared to a finite chamber length gun with the same initial conditions . . . . . 14

2–7 SWPPIG solutions for equation 2.12 for various values of $\gamma$ . . . . . 16

2–8 SWPPIG solutions for equation 2.17 for various values of $\gamma$ . . . . . 18

2–9 Non-dimensional maximum pressure versus the thickness to inner diameter ratio . . . . . 25

2–10 Non-dimensional mass per unit length versus the thickness to inner diameter ratio . . . . . 26

2–11 Non-dimensional burst pressure versus the thickness to inner diameter ratio . . . . . 27

2–12 $S_r$ vs. gun maximum design pressure . . . . . 29

2–13 Optimal $S_r$ vs. gun maximum design pressure . . . . . 30

2–14 $u_{1^{st}}$ vs. $a_\circ$ for a series of $\gamma$'s with a fixed $M_f$ and $\zeta_\circ$ . . . . . 34

2–15 $u_{1^{st}}$ vs. $a_\circ$ for a series of $\gamma$ 's with $M_f = 10\ \mathrm{Pa\,m^3/kg}$ with $\zeta_{1^{st}} = \zeta_b = 200$ 35

2–16 $u_{1^{st}}$ vs. $a_\circ$ for a series of $\gamma$ 's with a fixed $M_f = 100\ \mathrm{Pa\,m^3/kg}$ with $\zeta_{1^{st}} = \zeta_b = 200$ . . . . . 36

2–17 $u_{1^{st}}$ vs. $a_\circ$ for a series of $\gamma$ 's with $M_f = 1,000\ \mathrm{Pa\,m^3/kg}$ with $\zeta_{1^{st}} = \zeta_b = 200$ . . . . . 36

2–18 $u_{1^{st}}$ vs. $a_\circ$ for a series of $\gamma$ 's with a fixed $M_f = 10,000\ \mathrm{Pa\,m^3/kg}$ with $\zeta_{1^{st}} = \zeta_b = 200$ . . . . . 37

2–19 $u_{1^{st}}$ vs. $a_\circ$ for a series of $\gamma$ 's with $M_f = 100,000\ \mathrm{Pa\,m^3/kg}$ with $\zeta_{1^{st}} = \zeta_b = 200$ . . . . . 37

2–20 $u_{1^{st}}$ vs. $a_\circ$ for a series of $\gamma$ 's with a fixed $M_f = 1,000,000\ \mathrm{Pa\,m^3/kg}$ with $\zeta_{1^{st}} = \zeta_b = 200$ . . . . . 38

2–21 $\Phi_\circ$ vs. $a_\circ$ for a series of $\gamma$ 's with $M_f = 10\ \mathrm{Pa\,m^3/kg}$ with $\zeta_{1^{st}} = \zeta_b = 200$ 38

2–22 $\Phi_\circ$ vs. $a_\circ$ for a series of $\gamma$ 's with a fixed $M_f = 100\ \mathrm{Pa\,m^3/kg}$ with $\zeta_{1^{st}} = \zeta_b = 200$ . . . . . 39

2–23 $\Phi_\circ$ vs. $a_\circ$ for a series of $\gamma$ 's with $M_f = 1,000\ \mathrm{Pa\,m^3/kg}$ with $\zeta_{1^{st}} = \zeta_b = 200$ . . . . . 39

2–24 $\Phi_\circ$ vs. $a_\circ$ for a series of $\gamma$ 's with a fixed $M_f = 10,000\ \mathrm{Pa\,m^3/kg}$ with $\zeta_{1^{st}} = \zeta_b = 200$ . . . . . 40

2–25 $\Phi_\circ$ vs. $a_\circ$ for a series of $\gamma$ 's with $M_f = 100,000\ \mathrm{Pa\,m^3/kg}$ with $\zeta_{1^{st}} = \zeta_b = 200$ . . . . . 40

2–26 $\Phi_\circ$ vs. $a_\circ$ for a series of $\gamma$ 's with a fixed $M_f = 1,000,000\ \mathrm{Pa\,m^3/kg}$ with $\zeta_{1^{st}} = \zeta_b = 200$ . . . . . 41

2–27 Speed of sound vs. temperature for various gases . . . . . 44

2–28 Specific heat ratio vs. temperature for various gases . . . . . 45

2–29 Compression work done vs. temperature on system for various gases . 46

2–30 Heat added to the system to achieve final temperature vs. temperature for various gases . . . . . 47

2–31 Total energy added to the system vs. temperature for various gases . 47

2–32 Chambered PPIG gun . . . . . 49

2–33 $u_{esc(ref)}/a_\circ$ vs. $\gamma$ . . . . . 51

2–34 The percent increase between $u_{esc(ref)}$ and $u_{esc(\infty)}$ vs. $\gamma$ . . . . . 52

2–35 $\Delta u_{esc}/\Delta u_{esc(\infty)}$ vs. $d_\circ/d_p$ . . . . . 53

2–36 $\Delta u_p/\Delta u_{esc(\infty)}$ vs $\gamma u_{p(ref)}/a_\circ$ for various ratios of $d_\circ/d_p$ . . . . . 55

3–1 Launcher schematic . . . . . 56

3–2 Before and after of a barrel expanded by multiple high pressure gun cycles . . . . . 58

3–3 Muzzle velocity vs. pre-detonation pressure for a 6 foot barrel ($\zeta = 288$) 64

3–4 Muzzle velocity vs. pre-detonation pressure for a 12 foot barrel ($\zeta = 288$) . . . . . 65

4–1 Signal from shock pin array . . . . . 67

4–2 Schematic of coil gauge concept 1 . . . . . 68

4–3 Magnet passing through the coil gauge, coil gauge concept 1 . . . . . 68

4–4 Schematic of coil gauge concept 2 . . . . . 69

4–5 Magnet passing perpendicular to coil gauge, coil gauge concept 1 . . . 69

4–6 Signal from coil gauge concept 1 . . . . . 70

4–7 Signal from coil gauge concept 2 . . . . . 71

4–8 Signal lost in noise, coil gauge concept 2 . . . . . 71

4–9 Signal from broken projectile, coil gauge concept 1 . . . . . 72

4–10 Witness plate indicating an intact projectile . . . . . 72

4–11 Witness plate indicating a fragmented projectile . . . . . 73

4–12 Image of an intact projectile . . . . . 74

4–13 Image of a fragmented projectile . . . . . 74

4–14 Projectile Geometries . . . . . 75

4–15 General representation of the projectile . . . . . 76

4–16 Schematic of the fill procedure . . . . . 78

4–17 Image of the guns system . . . . . 79

4–18 Image of the coil gauge system . . . . . 80

4–19 Image of various projectiles . . . . . 81

4–20 Image of the test section . . . . . 82

4–21 Image of the gaseous detonation driven gun facility . . . . . 83

4–22 Muzzle velocity vs. projectile mass for the 6’ (183 cm) barrel at 62.5 atm pre-detonation pressure . . . . . 84

4–23 Muzzle velocity vs. pre-detonation pressure for 6' (183 cm) barrel and projectile mass of 3.2 g . . . . . 85

4–24 Muzzle velocity vs. projectile mass for the 12' (366 cm) barrel at 62.5 atm pre-detonation pressure . . . . . 85

4–25 Muzzle velocity vs. pre-detonation pressure for 12' (366 cm) barrel and projectile mass of 3.2 g . . . . . 86

4–26 Comparison of different ignition locations, 12' barrel, 3.2 g projectile and 62.5 atm pre-detonation pressure . . . . . 87

5–1 Muzzle velocity vs. pre-detonation pressure comparing the 6' and 12' barrels and projectile mass of 3.2 g . . . . . 88

5–2 Correlation between $u_p/u_{p(ideal)}$ and $\gamma u_{p(ideal)}/a_\circ$, accounting for the frictional and convective losses, valid for $\zeta$ between 100 and 250 . . 90

5–3 Muzzle velocity vs. projectile mass for the 6' barrel at 62.5 atm pre-detonation pressure, accounting for the frictional and convective losses . . . . . 91

5–4 Muzzle velocity vs. pre-detonation pressure for 6' barrel and projectile mass of 3.2 g, accounting for the frictional and convective losses . . 91

5–5 Muzzle velocity vs. projectile mass for the 12' barrel at 62.5 atm pre-detonation pressure, accounting for the frictional and convective losses . . . . . 92

5–6 Muzzle velocity vs. pre-detonation pressure for 12' barrel and projectile mass of 3.2 g, accounting for the frictional and convective losses . . . . . 93

5–7 Muzzle velocity vs. mixture composition for a 2 m barrel, projectile mass of 3.2 g and CJ detonation pressure of 2400 bar . . . . . 96

5–8 Muzzle velocity vs. mixture composition for a 2 m barrel, projectile mass of 3.2 g and reflected detonation pressure of 5720 bar . . . . . 97

5–9 Muzzle velocity vs. mixture composition for a 2 m barrel, projectile mass of 3.2 g and pre-detonation pressure of 106.44 bar . . . . . 98

5–10 Muzzle velocity vs. mixture composition for a 2 m barrel, projectile mass of 3.2 g and the criteria $p_{RCJ} < 5720$ bar and $p_{CJ} < 2400$ bar 99

5–11 Muzzle velocity vs. mixture composition for a 2 m barrel, projectile mass of 3.2 g and the criteria $p_{RCJ} \leq 5720$ bar, $p_{CJ} \leq 2400$ bar and $p_{fill} \leq 106.44$ bar . . . . . 99

5–12 Muzzle velocity vs. mixture composition for 2 m barrel, projectile mass of 3.2 g and a CV explosion pressure of 2400 bar . . . . . 100

B–1 Disturbance propogating through a gas in a tube . . . . . 110

B–2 $x - t$ diagram showing the paths of the projectile and the first rarefaction wave . . . . . 114

D–1 $u_{1st}$ vs. $a_\circ$ for different $\gamma$ and $M_F = 1$ kPa m$^3$/kg . . . . . 122

D–2 $u_{1st}$ vs. $a_\circ$ for different $\gamma$ and $M_F = 10$ kPa m$^3$/kg . . . . . 123

D–3 $u_{1st}$ vs. $a_\circ$ for different $\gamma$ and $M_F = 100$ kPa m$^3$/kg . . . . . 123

D–4 $u_{1st}$ vs. $a_\circ$ for different $\gamma$ and $M_F = 1,000$ kPa m$^3$/kg . . . . . 124

D–5 $u_{1st}$ vs. $a_\circ$ for different $\gamma$ and $M_F = 10,000$ kPa m$^3$/kg . . . . . 124

D–6 $u_{1st}$ vs. $a_\circ$ for different $\gamma$ and $M_F = 100,000$ kPa m$^3$/kg . . . . . 125

E–1 Initial Breech and Driver Concept . . . . . 126

E–2 Original Breech Design Dimensions (inches) . . . . . 127

E–3 Original Breech Expanded Dimensions for Barrel Extention (inches) . 128

E–4 Barrel Extension Dimensions (inches) . . . . . 129

E–5 Barrel Flange Dimensions (inches) . . . . . 130

E–6 Barrel Dimensions: Breech End (inches) . . . . . 131

E–7 Barrel and Coupler Dimensions (inches) . . . . . 132

E–8 Driver: Fill End Dimensions (inches) . . . . . 133

E–9 Driver: Breech End Dimensions (inches) . . . . . 134

F–1 $x - t$ diagram for various masses, predetonation pressure of 10 atm . 135

F–2 $x - t$ diagram for various masses, predetonation pressure of 25 atm . 136

F–3 $x - t$ diagram for various masses, predetonation pressure of 50 atm . 136

F–4 $x - t$ diagram for various masses, predetonation pressure of 75 atm . 137

F–5 $x - t$ diagram for various masses, predetonation pressure of 100 atm . 137

F–6 $x - u_p$ diagram for various masses, predetonation pressure of 10 atm . 138

F–7 $x - u_p$ diagram for various masses, predetonation pressure of 25 atm . 139

F–8 $x - u_p$ diagram for various masses, predetonation pressure of 50 atm . 139

F–9 $x - u_p$ diagram for various masses, predetonation pressure of 75 atm . 140

F–10 $x - u_p$ diagram for various masses, predetonation pressure of 100 atm 140

G–1 Results for the helium gun calibration of the velocity coil gauge . . . 141

# CHAPTER 1
# Introduction

Guns capable of reaching velocities of 3 km/s with multi-gram projectiles are usually limited to two-stage light gas guns or very high performance powder guns. These types of launchers are expensive due to the high tolerances required and large dynamic pressures generated. In this work, an inexpensive gaseous-detonation driven launcher is developed that has the potential of reaching velocities in excess of 3 km/s. Since the device does not have a pump tube, as in a two-stage gas gun, the chamber can be fabricated from readily available, low tolerance pipe (mechanical tube). Readily available gases can be used for propellant (hydrogen/oxygen/ helium), eliminating the need to store and handle powdered propellant. The resulting facility can be fabricated and assembled for less than $1,000 US, although additional precautions are necessary due to the handling of high pressure detonable gas.

Traditionally, guns use a solid propellant charge that is ignited via a smaller primer charge. Figure 1–1 is a schematic of a conventional powder (solid propellant) gun labelling all the components of a gun system. The charge is contained inside the chamber and is loaded via the breech, a mechanical opening that allows access to the chamber. The gun represented here has chambrage, a greater chamber internal diameter $d_\circ$ than barrel internal diameter (or projectile diameter) $d_p$. The primer,

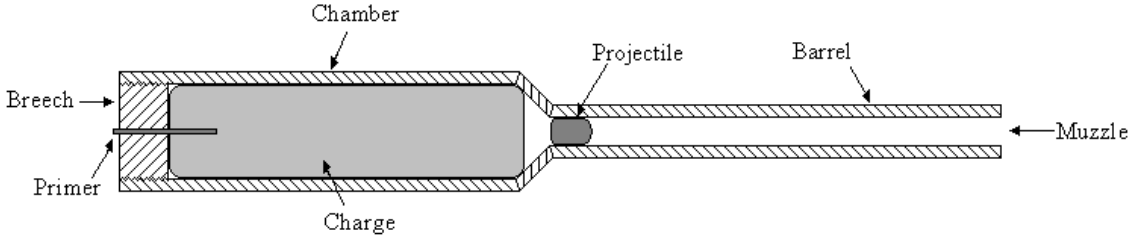


Figure 1–1: Schematic of a conventional powder gun

composed of a more sensitive propellant than the charge, is inserted into the charge, usually from the rear. The primer is ignited either through a heat source, as in a fuse for an ancient gun, or an impact, as in a firing pin for a modern gun. Once ignited, the propellant charge begins to burn producing gas, which raises the pressure in the chamber and accelerates the projectile down the barrel towards the muzzle. The rate at which gas is generated can be controlled by the choice of propellant and/or the geometry of the individual grains of propellant [4]. The pressure profile on the base of the projectile is qualitatively presented in figure 1–2 for a projectile starting at $x_p = 0$ and leaving the barrel at $x_p = x_{muz}$. It can be seen that the peak pressure occurs at some point downstream of the initial location of the projectile. The drawback of the solid propellant gun is that the propellant gas tends to have a much lower sound speed than is attainable by light gas guns. It will be shown in this work that one of the major factors contributing to high gun performance is the initial sound speed of the propellant.

In order to obtain higher initial sound speeds light gases are used as propellants. In the case of an ideal gas sound speed is given by

$$a = \sqrt{\gamma \frac{\overline{R}}{M} T} \tag{1.1}$$

where $a$ is the sound speed, $\gamma$ is the ratio of specific heats $C_p/C_v$, $\overline{R}$ is the universal gas constant, $M$ is the molar mass of the gas and $T$ is the temperature of the gas. Since the propellant gases of a conventional powder gun contains $H_2O$, $CO_2$, and nitrogen oxides, all relatively heavy gases, it can be seen that light gases, such as He and $H_2$, have the potential of out performing these propellants. The simplest gun configuration for utilizing $H_2$ and He as propellants is the single stage light gas gun. Figure 1–3 is a schematic of a single stage light gas gun. Here the conventional breech has been removed and a gas handling system is connected to the chamber. The projectile is isolated from the chamber by a diaphragm. Once the desired chamber pressure is

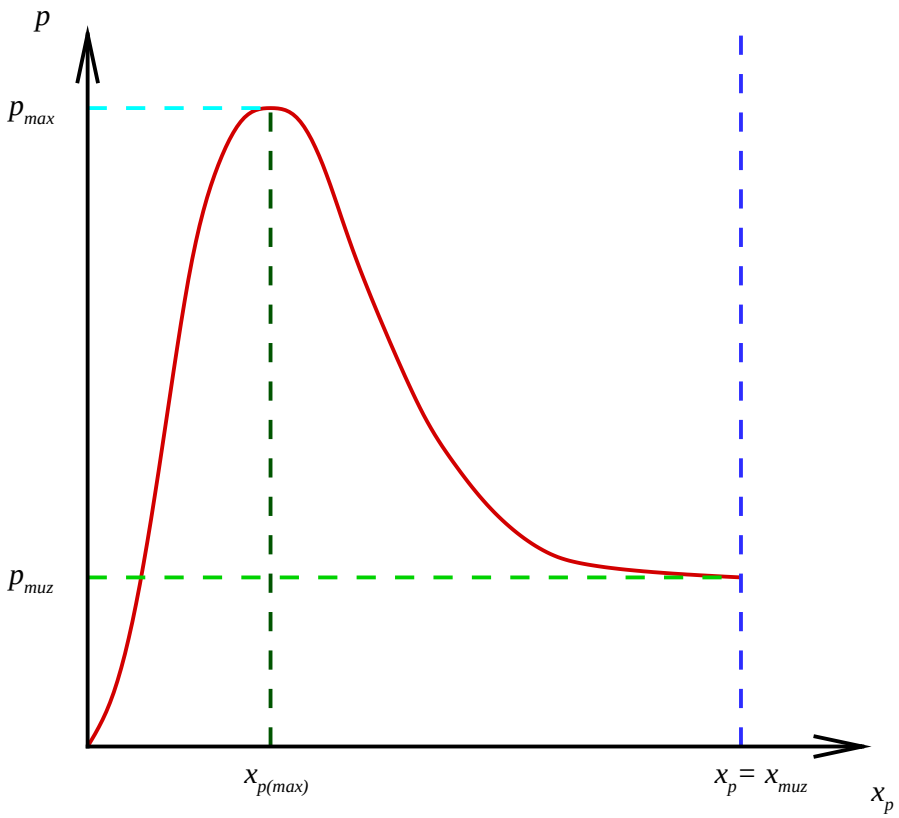


Figure 1–2: Projectile base pressure, $p$, as a function of projectile position, $x_p$, for a conventional powder gun

reached the diaphragm is ruptured and the projectile begins to accelerate. For this type of gun system the peak pressure on the projectile is the initial fill pressure and the relationship between the projectile base pressure and the projectile position is qualitatively represented by figure 1–4. It can be seen that the projectile base pressure drops quite quickly as the projectile accelerates. Whereas, it can be seen from figure 1–2, with proper propellant design, that the base pressure can be more easily

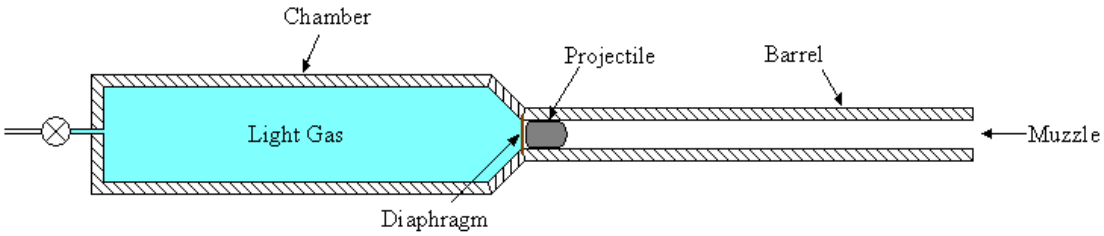


Figure 1–3: Schematic of a single stage light gas gun

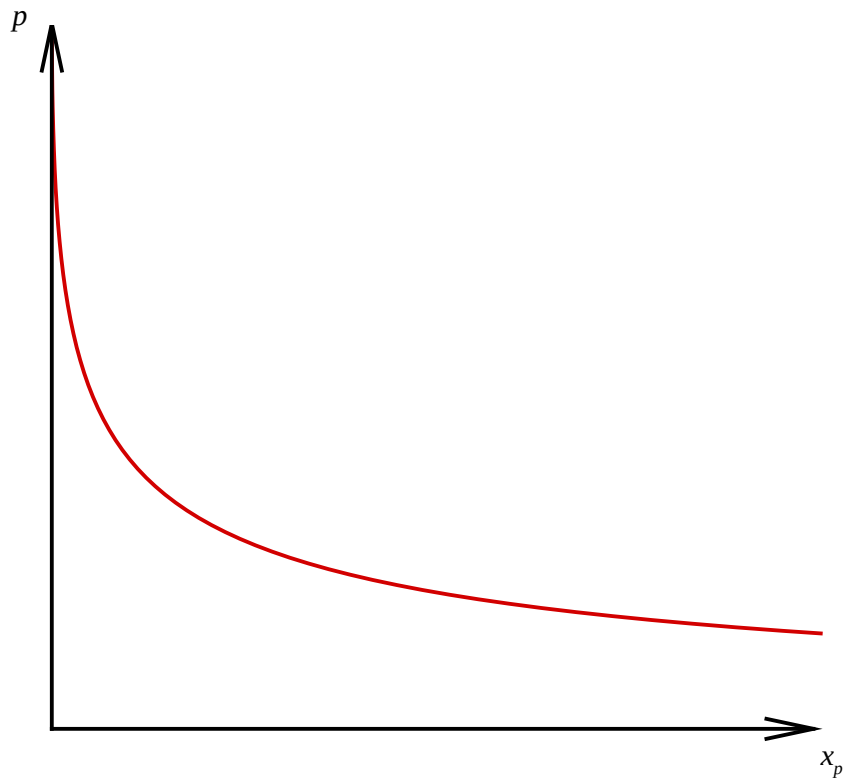


Figure 1–4: Projectile base pressure, $p$, as a function of projectile position, $x_p$, for a single stage light gas gun

controlled. Moreover, higher initial pressures are achievable by using a conventional powder gun. Furthermore, it can be seen from equation 1.1 that the initial sound speed, $a_\circ$, is a function of initial temperature, $T_\circ$. For this type of gun system raising this initial temperature can be achieved by using an external heat source, but this is inefficient and limited in the maximum gas temperature achievable, whereas powder gun propellants burn at much higher temperatures. Thus high performance powder guns can out perform the single stage light gas gun; however, the simplicity of the single stage light gas gun makes it the optimal choice for experimental work requiring projectile velocities within its performance range.

In order to utilize light gas propellants more efficiently, two stage light gas guns have been developed. A schematic of this type of gun system is presented in figure 1–5. This system is essentially a conventional powder gun, the first stage, combined with a light gas gun, the second stage. It works by accelerating a piston, with the

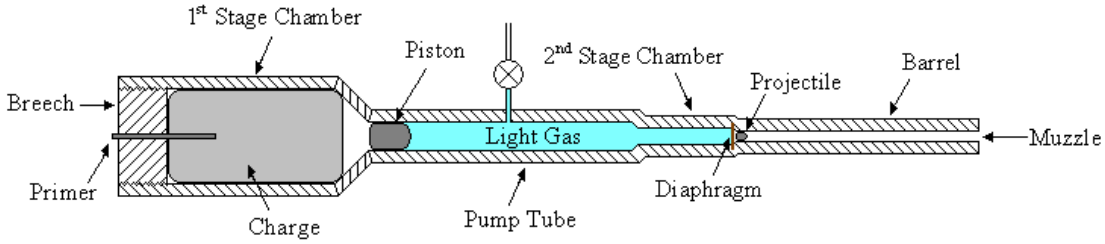


Figure 1–5: Schematic of a two stage light gas gun

products of the powder gun, in a pump tube, which increase both the temperature (and as a result, sound speed) and pressure of the light gas. These systems are very high performing but the projectile masses are quite light when compared to the size of the gun system. Furthermore, these gun systems are expensive to both build and operate. Therefore, it is desirable to design a gun system that can out perform a single stage light gas gun while maintaining its simplicity. To achieve this, the concept of a gaseous detonation driven gas gun is explored.

The concept of using a gaseous detonation as the propellant for a gas gun was suggested by [11], although no experiments were performed and the propellant selected (ethylene/oxygen/nitrogen) was limited in predicted performance to velocities of about 2.5 km/s. A unique facility was developed by [12], in which a 0.5-m-diameter, 110-m-long tube was pressurized at up to 15 atm with hydrogen/oxygen ($4H_2 + O_2$). Detonation in this mixture impacted on a 9.1-kg, gyro-stabilized disk (0.5-m in diameter and 6-mm thick), which was then accelerated down a 50-m-long evacuated section of tube. Velocities of 3.5 km/s were demonstrated, and the facility was used to successfully shock-synthesize diamond upon impact against carbon-rich iron targets. Finally, a Virginia-based company (Utron, Inc. [7]), claims to have developed a combustion light gas gun with muzzle velocities in excess of 4 km/s, although technical details or supporting data have yet to appear.

Figure 1–6 shows a schematic of the detonation driven gun operational process. During a launch the barrel is evacuated while the combustible mixture fills the driver

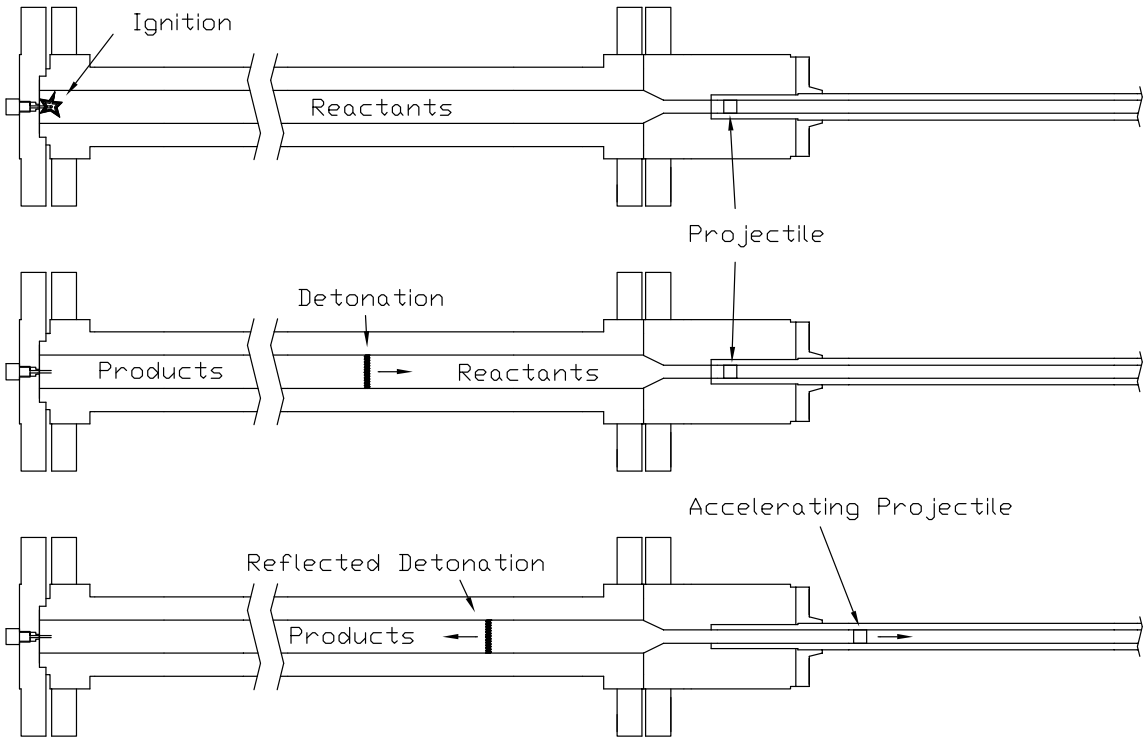


Figure 1–6: Launcher operation schematic

section using a partial pressure mixing method. Once filled and sealed off, the gases are left to mix in the driver for an additional 15 minutes. So far only stoichiometric mixtures of hydrogen and oxygen have been tested. The mixture is then ignited using a weak ignition source (model rocket match igniter) causing a detonation to propagate in the driver. The detonation products propel the projectile towards the muzzle as the reflected detonation travels back towards the breech.

In this work, the concept of the gaseous detonation-driven gas gun is further developed, with particular attention paid to optimizing the detonable mixture composition for increased velocity. Classical internal ballistics methods are explored and reworked with an emphasis on their applications to gun design optimization. A quasi-one-dimensional Eulerian CFD code is used for internal ballistics calculations. A prototype facility is constructed and tested, and the experimental performance is compared to theoretical predictions.

# CHAPTER 2
# Internal Ballistic Theory

In this chapter, different internal ballistic theories are investigated. These theories are developed in such a way to aid in the process of design and performance optimization. The internal ballistic problem to be investigated is that for a preburned propellant ideal gas (PPIG) gun. This assumes that all the propellant is burned and reaches a final state before the projectile begins to move. It will be seen that this problem is multi-dimensional and that the parameters affecting ballistic performance are often interconnected.

## 2.1 The Lagrange Gradient

The Lagrange Gradient is a zeroth order method used to determine the internal ballistics of a gun system. This method gives a analytical solution to the internal ballistics problem while incorporating such complexities as solid propellant geometries and burn times [4]. The drawbacks of this technique is that it only gives a good agreement with experiment for low $m_g/m_p$ (mass of gas/mass of projectile) systems [1]. However, it is worth exploring due to its simplicity and its ability to qualitatively aid in understanding the factors that contribute to the internal ballistics problem.

This derivation for the Lagrange Gradient approximation has been included in appendix A; however, the solution for projectile velocity, $u_p$, for the case of a PPIG is shown here:

$$u_p(x_p) = \sqrt{\frac{1}{\left(1+\frac{1}{3}\frac{m_g}{m_p}\right)}\frac{2A_p x_\circ \overline{p}_\circ}{m_p(\gamma-1)}\left[1-\left(\frac{x_\circ}{x_p+x_\circ}\right)^{(\gamma-1)}\right]} \tag{2.1}$$

where $x_p$ is the position of the projectile in the barrel, $x_\circ$ is the chamber length, $\overline{p}_\circ$ is

the initial average chamber pressure, $A_p$ is the cross-sectional area of the projectile (and chamber since this applies to a constant diameter gun) and $\gamma$ is the specific heat ratio $c_p/c_v$. Recalling the sound speed for an ideal gas, given by equation 2.2, equation 2.1 can be non-dimensionalized to further explore the internal ballistics behaviour of gun systems.

$$a_\circ = \sqrt{\gamma \frac{p_\circ}{\rho_\circ}} \tag{2.2}$$

If the mass of the gas is

$$m_g = \rho_\circ V = \rho_\circ A x_\circ \tag{2.3}$$

then equation 2.1 becomes

$$u_p(x_p) = a_\circ \sqrt{\frac{m_g}{m_p\left(1+\frac{1}{3}\frac{m_g}{m_p}\right)} \frac{2}{\gamma(\gamma-1)}\left[1-\left(\frac{x_\circ}{x_p+x_\circ}\right)^{(\gamma-1)}\right]} \tag{2.4}$$

Introducing the following non-dimensional variables

$$M_r \equiv \frac{m_g}{m_p} \tag{2.5}$$

$$\varphi \equiv \frac{x}{x_\circ} \tag{2.6}$$

Using these non-dimensional variables equation 2.4 can be simplified as

$$u_p(\varphi) = a_\circ \sqrt{2\frac{M_r}{\left(1+\frac{1}{3}M_r\right)} \frac{1}{\gamma(\gamma-1)}\left[1-\left(\frac{1}{\varphi+1}\right)^{(\gamma-1)}\right]} \tag{2.7}$$

This is a useful result because the velocity is purely a function of non-dimensional position $\varphi$, mass ratio $m_g/m_p$, initial sound speed $a_\circ$ and specific heat ratio $\gamma$. Each

of these parameters can then be qualitatively analyzed for their effect on projectile velocity.

Equation 2.7 can be split into

$$u_p(\varphi) = \sqrt{2}a_\circ f(M_r)g(\gamma,\varphi) \tag{2.8}$$

Looking at $f(M_r)$ and taking the limit as $M_r$ goes to infinity it can be shown that:

$$\lim_{M_r\to\infty} f(M_r) = \lim_{M_r\to\infty}\sqrt{\frac{M_r}{\left(1+\frac{1}{3}M_r\right)}} = \sqrt{3} \tag{2.9}$$

For practical reasons, large values of $M_r$ are not physically attainable; therefore, $M_r$ is more a function of design restrictions and has a maximum realistic value within these design restrictions (these design restrictions will be discussed in more details later). Therefore, it is more important to be able to see how quickly $f(M_r)$ approaches $\sqrt{3}$. This is shown in figure 2–1.

In order to determine the effects of $\gamma$, the $g(\gamma,\varphi)$ function can be examined. From equation 2.7, $g(\gamma,\varphi)$ takes the form:

$$g(\gamma,\varphi) = \sqrt{\frac{1}{\gamma(\gamma-1)}\left(1-\left(\frac{1}{\varphi+1}\right)^{(\gamma-1)}\right)} \tag{2.10}$$

Since $g(\gamma,\varphi)$ is a multivariable funtion, the easiest way to explore it is by plotting equation 2.10 for specific $\gamma$'s. These plots are shown in figure 2–2.

It can be seen, when choosing between gases of equal sound speed, that there is a significant benefit to a gas with a lower $\gamma$. However, to obtain a $\gamma < 1.1$ is very difficult to achieve while maintaining a high sound speed [6]. Later in this thesis a more thorough analysis of potential driver gases will be undertaken using NASA's equilibrium code CEA [6].

From this exploration of the Lagrange Gradient model, it has been determined that four factors determine the performance of a constant diameter PPIG gun. These

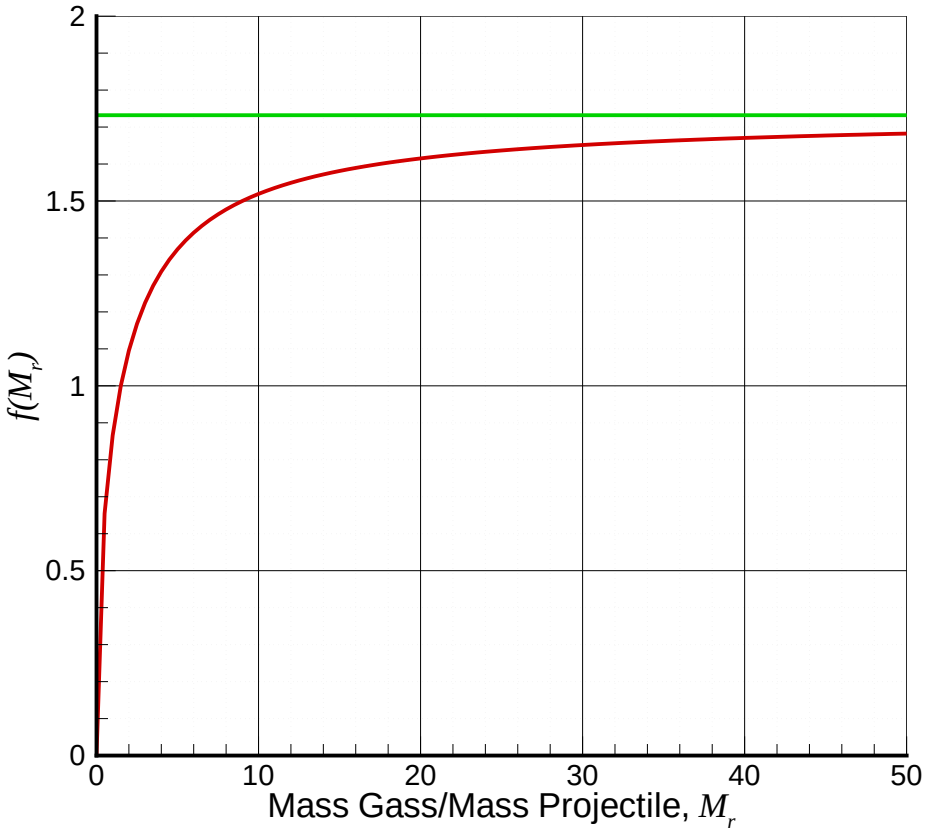


Figure 2–1: $f(M_r)$ vs. $M_r$

factors are the mass ratio, $M_r = m_g/m_p$, initial speed of sound, $a_\circ$, initial specific heat ratio, $\gamma = c_p/c_v$, and non-dimensional position of the projectile in the barrel, $\varphi = x/x_\circ$ (i.e. barrel length). Now that these factors have been identified, a general understanding of what role they take in the internal ballistics process is required.

First it has been shown that a large $M_r$ produces better performance than a low $M_r$. This is because a lighter projectile will accelerate faster than a heavier one for a fixed amount of gas. Conversely, for a fixed projectile mass, a large mass of gas implies a greater overall internal energy in the system. Furthermore, it can be seen from the analysis of $f(M_r)$ that by increasing $M_r$ of the gas by increasing the length of the chamber, $x_\circ$, there are diminishing returns. In other words, gas added further and further from the projectile will have less and less of an effect on the projectile. Thus, when approaching $x_\circ = \infty$, the gas will not have any influence on

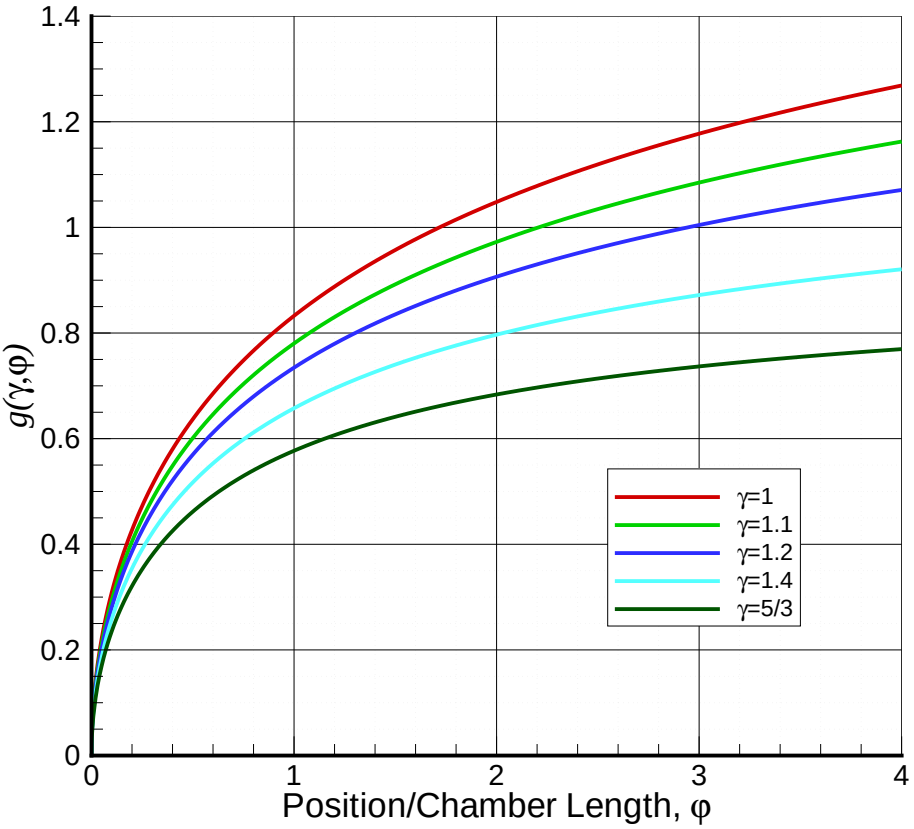


Figure 2–2: $g(\gamma, \varphi)$ vs. $\varphi$ for various $\gamma$

the projectile. It will be shown later that this effective $x_\circ = \infty$ can occur at very short chamber lengths depending on the initial state of the system.

Now looking at $a_\circ$, the sound speed of a gas is what determines how quickly information is transferred through the gas; the derivation of a disturbance travelling in a gas is included in appendix B. Therefore, for a high $a_\circ$, gas that is far from the projectile will have more influence on it earlier in the internal ballistics process resulting in a lower pressure decrease on the projectile as it accelerates down the barrel. It will be shown later that when wave processes are taken into consideration, the effects of the speed of sound become even more pronounced.

The specific heat ratio, $\gamma$ can be a measure of the ability of a gas to store internal energy. The lower the $\gamma$ for a gas the more internal energy this gas is able to store. Therefore, as the projectile travels down the barrel and the gas cools, this internal energy is released slowing this cooling process and maintaining a higher base

pressure on the projectile. From figure 2–2 it was seen that the larger $\varphi$, the more prevalent is this effect. Now, with a better understanding of these variables, more complicated internal ballistics methods can be investigated.

## 2.2 Simple Wave Gun

The definition of a simple wave PPIG is a gun system without chambrage that has an effectively infinite chamber length, as shown in figure 2–3. In a gun system, when the projectile starts to accelerate, rarefaction waves communicate this information upstream towards the breech end of the chamber. This rarefaction wave tells the gas to move towards the projectile to fill the void left by the projectile. In the next increment of time the projectile will be moving even faster so another rarefaction wave starts to travel towards the breech to tell the gas to move even faster to fill this new void. Once the first rarefaction reaches the breech, the volume of gas next to the breech cannot leave contact with the breech wall, thus this first rarefaction wave reflects off the breech and starts to travel back downstream towards the projectile, communicating to the gas that the end wall condition requires it to decelerate. Figure 2–4 shows these wave processes. Eventually this rarefaction wave can catch the projectile, depending on the initial sound speed and barrel length, lowering the base pressure that is pushing it. Furthermore, each subsequent rarefaction wave reduces the base pressure even more at which point the gun can no longer be considered to have an infinitely long chamber. However, the region mapped out on an $x - t$

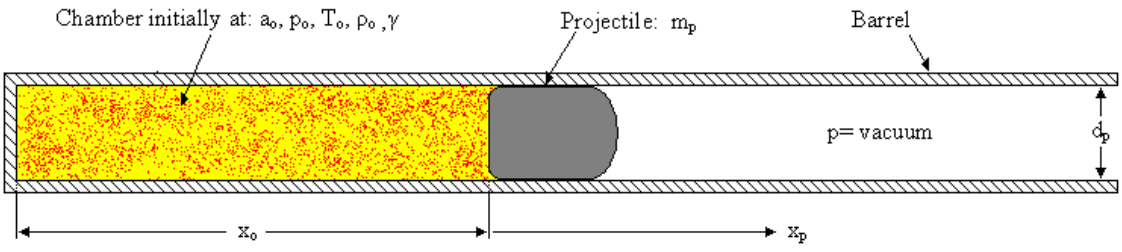


Figure 2–3: Constant diameter PPIG gun

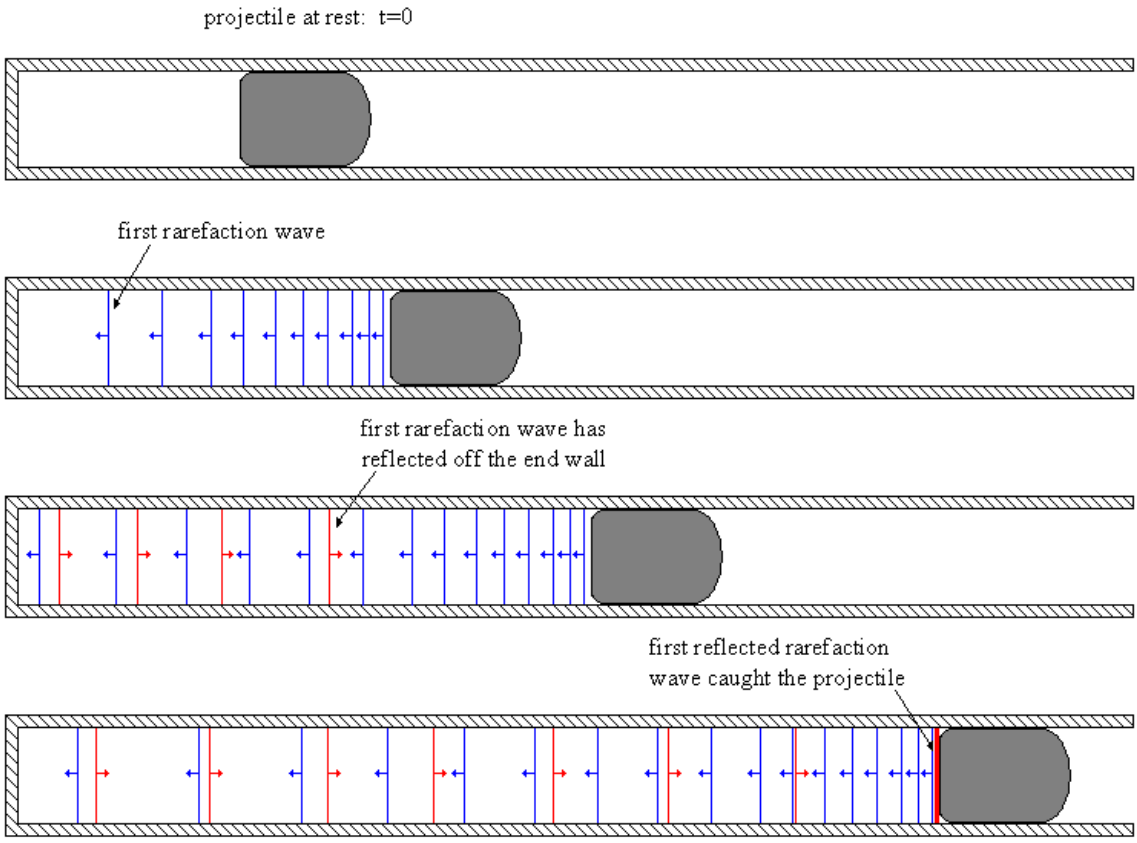


Figure 2–4: Wave processes in a constant diameter PPIG gun

diagram, as shown in figure 2–5, by the projectile path and the path of the first rarefaction is referred to as the Simple Wave Region; therefore, a PPIG gun system with an effectively infinite chamber length is considered, if it has no chambrage, a Simple Wave Gun.

The reason that SWPPIG is of interest is because once the first rarefaction reaches the projectile, increasing the barrel length beyond this point results in a more greatly diminished performance. Figure 2–6 shows this case. The SWG solution is an extremely useful design tool since it is an exact analytical solution from which many design criteria can be derived. Furthermore, these tools can still apply to chambered gun systems which must otherwise be analyzed computationally to get accurate performance predictions. However, it will be shown later that there are methods of approximating a chambered PPIG gun that has an effectively infinitely long chamber by knowing the performance of the corresponding SWPPIG gun.

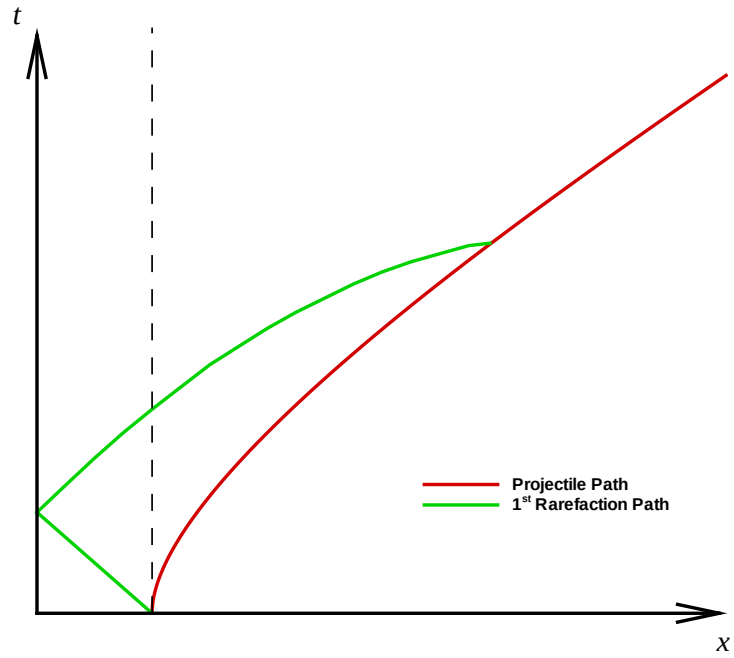


Figure 2–5: $x-t$ diagram showing the paths of the projectile and the first rarefaction wave

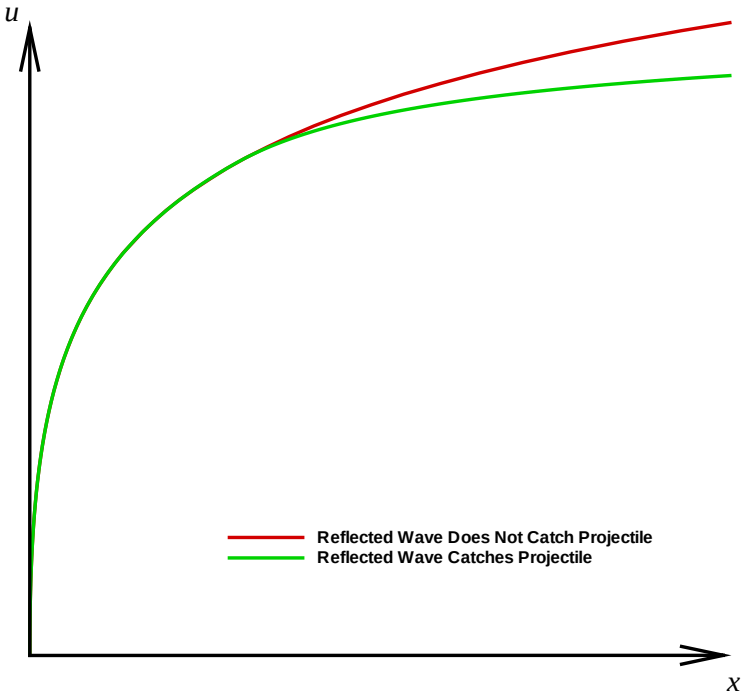


Figure 2–6: Infinite chamber length gun compared to a finite chamber length gun with the same initial conditions

The derivation of the simple wave gun is presented in appendix B; however, to follow will be detailed analysis of the resulting equation and the individual parameters that affect this solution. The solution for the simple wave gun is given in equation 2.11.

$$x_p = \frac{2m_p a_\circ^2}{Ap_\circ(\gamma+1)} \left\{ \frac{\frac{2}{\gamma-1} - \frac{\gamma+1}{\gamma-1}\left[1 - \frac{(\gamma-1)}{2a_\circ}u_p\right]}{\left[1 - \frac{(\gamma-1)}{2a_\circ}u_p\right]^{\frac{\gamma+1}{(\gamma-1)}}} + 1 \right\} \tag{2.11}$$

This can be non-dimensionalized in the form

$$\xi = \frac{2}{(\gamma+1)} \left\{ \frac{\frac{2}{\gamma-1} - \frac{\gamma+1}{\gamma-1}\left[1 - \frac{(\gamma-1)}{2}\psi\right]}{\left[1 - \frac{(\gamma-1)}{2}\psi\right]^{\frac{\gamma+1}{(\gamma-1)}}} + 1 \right\} \tag{2.12}$$

where $\xi$ and $\psi$ are defined as

$$\xi \equiv \frac{Ap_\circ x_p}{m_p a_\circ^2} \tag{2.13}$$

$$\psi \equiv \frac{u_p}{a_\circ} \tag{2.14}$$

Using equations 2.11 and 2.12, $u_p$ and $\psi$ can be solved numerically using a root solving algorithm. However, $u_p$ and $\psi$ can easily be solved implicitly by plotting equation 2.11 or 2.12. This has been done here for equation 2.12, which is valid for all SWPPIGs, using select values of $\gamma$ and shown in figure 2–7. This is a convenient form of the solution since all the possible SWPPIGs can be mapped on a three-dimensional surface. However, by non-dimensionalizing the solution the intricacies of the design problem are lost. Returning to equation 2.11 and rewriting it in the form

$$\frac{Ap_\circ x_p}{m_p a_\circ^2} = \frac{2}{(\gamma+1)} \left\{ \frac{\frac{2}{\gamma-1} - \frac{\gamma+1}{\gamma-1}\left[1 - \frac{(\gamma-1)}{2a_\circ}u_p\right]}{\left[1 - \frac{(\gamma-1)}{2a_\circ}u_p\right]^{\frac{\gamma+1}{(\gamma-1)}}} + 1 \right\} \tag{2.15}$$

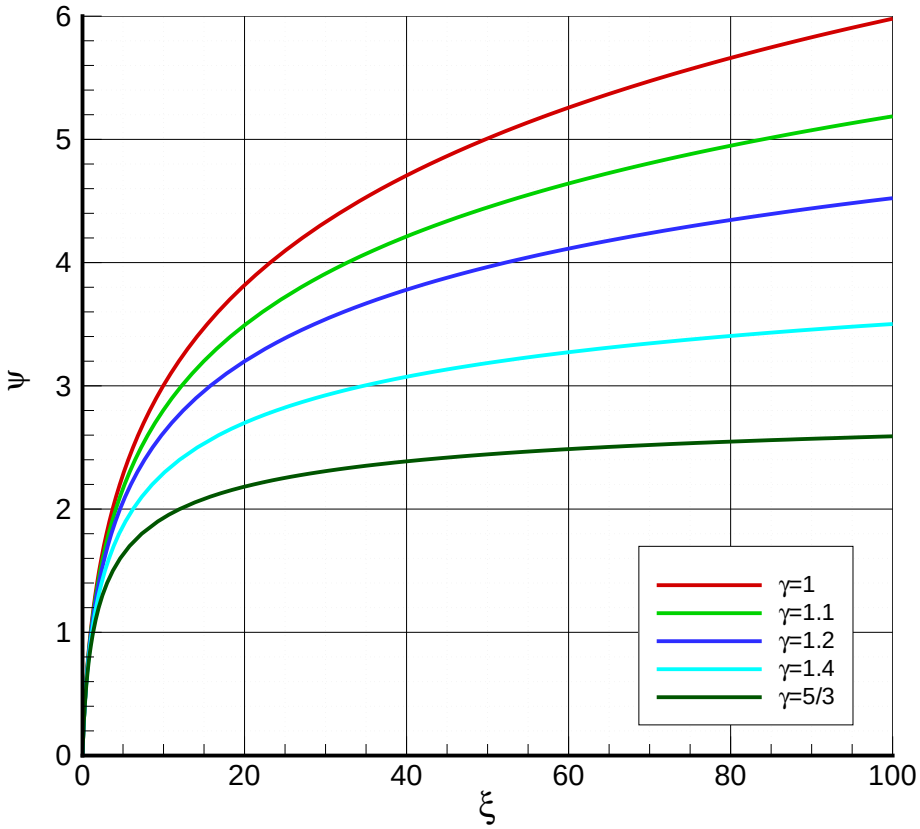


Figure 2–7: SWPPIG solutions for equation 2.12 for various values of $\gamma$

it can be rewritten in a 4 non-dimensional variable form that includes the classical variable $M_r$. Using the knowledge gain from examining the Lagrange gradient this new form of the equation allows a better understanding of what the maximum realistic gun performances are attainable for a SWPPIG.

Now by examining the left hand side of equation 2.15 using the definition of the speed of sound given by equation 2.2 and introducing the diameter of the projectile defined as $d_p$

$$\frac{Ap_\circ x_p}{m_p a_\circ^2} = \frac{d_p}{d_p}\frac{Ap_\circ x_p}{m_p}\frac{\rho_\circ}{\gamma p_\circ} = \frac{1}{\gamma}\frac{m_g}{m_p}\frac{x_p}{d_p} \tag{2.16}$$

Inserting equation 2.16 back into equation 2.15, a non-dimensional form can be obtained

$$\zeta = \frac{2\gamma}{M_r(\gamma+1)} \left\{ \frac{\frac{2}{\gamma-1} - \frac{\gamma+1}{\gamma-1}\left[1 - \frac{(\gamma-1)}{2}\psi\right]}{\left[1 - \frac{(\gamma-1)}{2}\psi\right]^{\frac{\gamma+1}{(\gamma-1)}}} + 1 \right\} \tag{2.17}$$

where the new non-dimensional length is defined as

$$\zeta \equiv \frac{x_p}{d_p} \tag{2.18}$$

From equation 2.17 it can be seen that some of the physicality of the design problem has been re-introduced in the form of $M_r$ and $\zeta$ without losing the generality of a non-dimensional system. However, due to the four dimensions of the equation the solution space can no longer be represented by a single graph. However, by grouping $M_r$ and $\zeta$ together, equation 2.17 can be plotted on a single graph as shown in figure 2–8.

The drawback of equation 2.17 is that, even though it introduces some of the physicality of the problem, there is no way of understanding how each of the design variables affects the performance of a real PPIG gun system. For a conventional gun system which uses a solid propellant powder charge, $M_r$ is a useful tool because it is easy to measure solid propellants in terms of mass; however, for gas phase propellants the mass is obtained by measuring other factors (such as pressure and temperature for an ideal gas). It is much easier to design a PPIG using physical parameters that can be readily measured. Therefore a new system of parameters needs to be developed. By again returning to equation 2.11 and rewriting it in the form

$$\frac{Ap_\circ x_p}{m_p} = \frac{2a_\circ^2}{(\gamma+1)} \left\{ \frac{\frac{2}{\gamma-1} - \frac{\gamma+1}{\gamma-1}\left[1 - \frac{(\gamma-1)}{2a_\circ}u_p\right]}{\left[1 - \frac{(\gamma-1)}{2a_\circ}u_p\right]^{\frac{\gamma+1}{(\gamma-1)}}} + 1 \right\} \tag{2.19}$$

it can be shown that the left side of this equation is only a function of the mechanical characteristics of the gun system. The gas dynamic effects are thus separated from

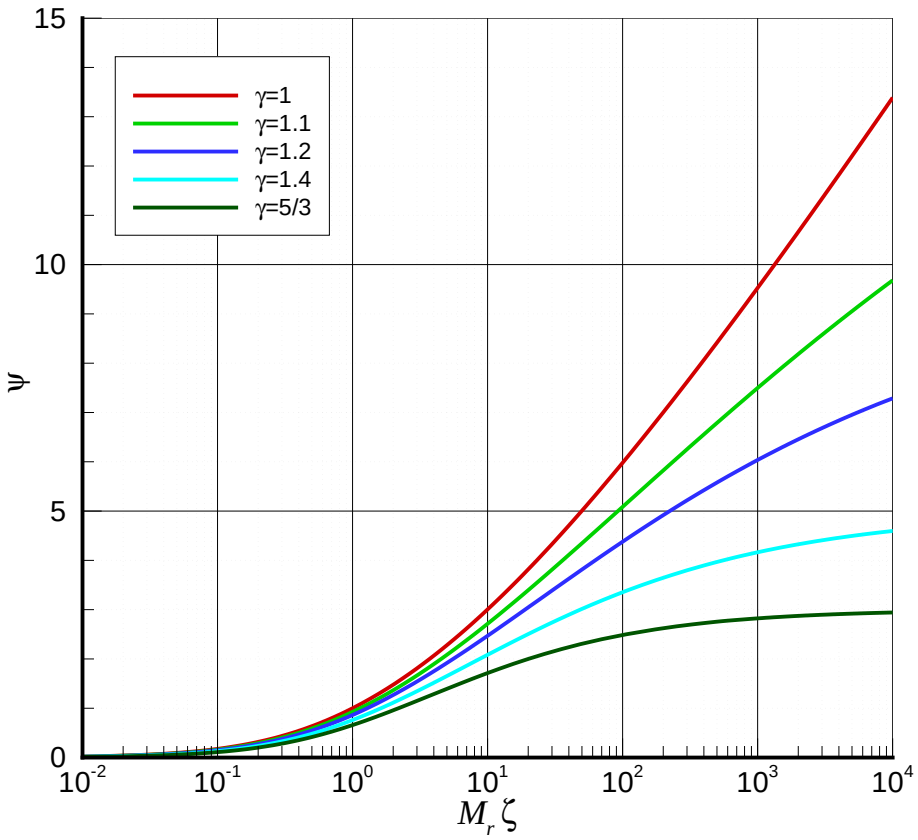


Figure 2–8: SWPPIG solutions for equation 2.17 for various values of $\gamma$

the mechanical effects which was impossible to do with equation 2.12 and not easily done with equation 2.17.

Introducing the new variables

$p_{max}$ the maximum pressure that the gun system can safely operate under

$l_p$ the effective length of the projectile

$\rho_p$ the density of the projectile

and recalling the mass of the projectile is $m_p = \rho_p A l_p$ and examining the left hand side of equation 2.15 the following is obtained

$$\frac{A p_\circ x_p}{m_p} = \frac{p_{max} d_p}{p_{max} d_p} \frac{A p_\circ x_p}{\rho_p A l_p} = \frac{p_\circ}{p_{max}} \frac{p_{max}}{\rho_p} \frac{d_p}{l_p} \frac{x_p}{d_p} \tag{2.20}$$

Introducing the mechanical factor, $M_f$ which is defined as

$$M_f \equiv \frac{p_{max}}{\rho_p}\frac{d_p}{l_p} \tag{2.21}$$

Thus $M_f$ is a function of the following ratios

$$S_r \equiv \frac{p_{max}}{\rho_p} = \frac{\text{maximum pressure}}{\text{projectile density}}$$

which relates the strength of the gun system to the density of the projectile and has units of $pl^3/m$.

$$A_r \equiv \frac{l_p}{d_p} = \frac{\text{projectile length}}{\text{projectile diameter}}$$

which is the aspect ratio between the projectile diameter and projectile length. Furthermore the pressure ratio is defined as

$$P_r \equiv \frac{p_\circ}{p_{max}} = \frac{\text{initial pressure}}{\text{maximum pressure}}$$

which relates the initial pressure to the maximum design pressure. This ratio typically has values between 0 and 1. Values above 1 risk damage to the gun system and/or the projectile.

The non-dimensional position is defined as

$$\zeta \equiv \frac{x_p}{d_p} = \frac{\text{projectile position}}{\text{projectile diameter}}$$

which is the distance traveled in the barrel measured in projectile calibers.

The substitution of $M_f$, $\zeta$ and $P_r$ into equation 2.19 gives

$$P_r M_f \zeta = \frac{p_\circ}{p_{max}} \frac{p_{max}}{\rho_p} \frac{d_p}{l_p} \frac{x_p}{d_p} = \frac{2a_\circ^2}{(\gamma+1)} \left\{ \frac{\frac{2}{\gamma-1} - \frac{\gamma+1}{\gamma-1}\left[1 - \frac{(\gamma-1)}{2a_\circ} u_p\right]}{\left[1 - \frac{(\gamma-1)}{2a_\circ} u_p\right]^{\frac{\gamma+1}{(\gamma-1)}}} + 1 \right\} \tag{2.22}$$

with $u_p$ as a function of six variables (four non-dimensional and two dimensional); however, in the case of maximizing the performance of a gun, equation 2.22 can be reduced to a function of three variables, $a_\circ$, $\gamma$ and $u_p$ , due to the fact that $A_r$, $S_r$, $\zeta$ and $P_r$ all have maximum realistic values. However, there is one more parameter that needs to be addressed before the SWPPIG gun can be thoroughly investigated The question that remains to be asked is for what initial chamber length $x_\circ$ does a given gun system retain an effectively infinitely long chamber?

It was presented by [1] that, for chamber length $x_\circ$, the velocity at the location where the first reflected wave catches the projectile is given as

$$\frac{A p_\circ x_\circ}{m_p a_\circ^2} = \frac{2}{(\gamma+1)} \left\{ \left[1 - \frac{(\gamma-1)}{2a_\circ} u_{1st}\right]^{-\frac{(\gamma+1)}{2(\gamma-1)}} - 1 \right\} \tag{2.23}$$

which in terms of $M_f$, $\zeta$ and $P_r$ becomes

$$\zeta_\circ = \frac{2a_\circ^2}{P_r M_f (\gamma+1)} \left\{ \left[1 - \frac{(\gamma-1)}{2a_\circ} u_{1st}\right]^{-\frac{(\gamma+1)}{2(\gamma-1)}} - 1 \right\} \tag{2.24}$$

This equation gives the chamber length, in terms of projectile diameter, that is required for a gun system to remain a SWPPIG assuming that the projectile leaves the barrel at the instant the first reflected rarefaction catches it. Equation 2.24 is in terms of the muzzle velocity, pressure ratio, mechanical factor, initial sound speed and specific heat ratio.

Alternatively equation 2.24 can be solved for $u_{1st}$ which gives

$$u_{1st} = \frac{2a_\circ}{(\gamma - 1)} \left\{ 1 - \left[ \frac{\gamma + 1}{2a_\circ^2} P_r M_f \zeta_\circ + 1 \right]^{-\frac{2(\gamma-1)}{(\gamma+1)}} \right\} \tag{2.25}$$

This equation gives the velocity of the projectile at the instant that the first reflected rarefaction wave catches it in terms of the chamber length in calibers, the initial speed of sound, the initial specific heat ratio, and the Mechanical factor of the gun system.

Both equation 2.24 and equation 2.25 help a ballistician by approaching the design problem from different angles. Equation 2.24 determines what chamber length required to achieve a desired velocity for a given initial speed of sound, initial specific heat ratio, and mechanical factor of the gun system. This is useful when the size of the gun system is not an issue. However, if the gun system size ($\zeta_\circ$) is a design factor then the initial speed of sound, the initial specific heat ratio, and the mechanical factor of the gun system are now what must be optimized in order to obtain the desired muzzle velocity given by equation 2.25.

The missing element of the above analysis is the consideration of what is the location of the projectile when the first rarefaction wave reaches the projectile. To determine this, equation 2.25 can be substituted for $u_p$ in equation 2.22 to obtain the $\zeta$ position where the first reflection reaches the projectile as a function of $M_f$, $a_\circ$, $\gamma$ and $\zeta_\circ$:

$$\zeta_{1^{st}} = \frac{2a_\circ^2}{M_f(\gamma + 1)} \left\{ \frac{\frac{2}{\gamma-1} - \frac{\gamma+1}{\gamma-1} \left[ \frac{\gamma+1}{2a_\circ^2} P_r M_f \zeta_\circ + 1 \right]^{-\frac{2(\gamma-1)}{(\gamma+1)}}}{\left[ \frac{\gamma+1}{2a_\circ^2} P_r M_f \zeta_\circ + 1 \right]^{-2}} + 1 \right\} \tag{2.26}$$

Thus equation 2.26 can be used in conjunction with equation 2.24 and equation 2.25 as tools in the gun optimization process. To follow will be the optimization of

the simple wave gun using real physical data.

### 2.2.1 The Optimization of the SWPPIG Gun System

In the previous section the equations that describe the operation of the simple wave gun were derived and the problem has been determined to be a function of the gun, the projectile and the propellant, where

gun= $f(\zeta, \zeta_\circ, S_r, P_r)$
projectile= $f(A_r, S_r, P_r)$
propellant= $f(P_r, a_\circ, \gamma)$

In order to optimize the gun system, each of these must be looked at individually as well as globally. First some simplification can be done by making the assumption (or place a design criteria) that the gun system is designed so that if failure occurs then it is the projectile that fails and not the gun itself. Thus $S_r$ and $P_r$ are no longer relevant to the gun. In summary

gun= $f(\zeta, \zeta_\circ)$
projectile= $f(A_r, S_r, P_r)$
propellant= $f(P_r, a_\circ, \gamma)$

Now each of these will be discussed individually.

#### The Gun: Part I

When designing a gun system, the design considerations that usually must be taken into account are how big and how heavy the gun system can be. It is obvious that bigger means heavier and possibly stronger and that smaller means lighter and possibly weaker. It has been shown that a longer barrel means more velocity and

also that a longer chamber means that it takes longer for the first rarefaction to catch the projectile. So it is known that the overall length of a gun system plays a significant role in the gun's performance. Therefore, how a gun's length can be optimized while performing as required must be examined. This however, due to the interconnection between all the parameters that affect the gun, must be explored after the mechanical factor has been determined.

The first step in calculating the mechanical factor is to determine the maximum pressures that a gun system can sustain. This maximum pressure is a function of geometry and material properties. It is stated in [1] that the maximum pressure at which a gun system can typically operate without yielding is approximately 900 MPa in practice. However, a maximum theoretical value can be determined using the relations for a thick walled cylinder with capped ends taken from [14]

$$\sigma = \begin{cases} \sigma_a &= p_i \dfrac{r_i^2}{r_e^2 - r_i^2} \\ \sigma_h &= p_i \dfrac{r_i^2(r_e^2 + r^2)}{r^2(r_e^2 - r_i^2)} \\ \sigma_r &= -p_i \dfrac{r_i^2(r_e^2 - r^2)}{r^2(r_e^2 - r_i^{2}{}^2)} \end{cases} \tag{2.27}$$

where $r$ is the radial position of the stress, $r_i$ is the interior radius of the vessel, $r_e$ is the exterior radius of the vessel, $p_i$ is the internal pressure in the vessel, $\sigma_a$ is the axial stress at $r$, $\sigma_h$ is the hoop stress at $r$, $\sigma_r$ is the radial stress at $r$. The maximum stress given is by

$$(\sigma)_{max} = \begin{cases} (\sigma_a)_{max} &= p_i \dfrac{r_i^2}{r_e^2 - r_i^2} & \\ (\sigma_h)_{max} &= p_i \dfrac{(r_i^2 + r_e^2)}{(r_e^2 - r_i^2)} & \text{at } r = r_i \\ (\sigma_r)_{max} &= -p_i & \text{at } r = r_i \\ \tau_{max} &= p_i \dfrac{(r_e^2)}{(r_e^2 - r_i^2)} & \text{at } r = r_i \end{cases} \tag{2.28}$$

These equations can be solved for the maximum internal pressure $p_i$ in terms of the material yield strength, $\sigma_y$, as

$$(p_i)_{max} = \begin{cases} (p_i)_{max} = \sigma_y \dfrac{r_e^2 - r_i^2}{r_i^2} & \\ (p_i)_{max} = \sigma_y \dfrac{(r_e^2 - r_i^2)}{(r_i^2 + r_e^2)} & \text{at } r = r_i \\ (p_i)_{max} = \sigma_y & \text{at } r = r_i \\ (p_i)_{max} = \sigma_y \dfrac{(r_e^2 - r_i^2)}{(r_e^2)} & \text{at } r = r_i \end{cases} \tag{2.29}$$

It can be seen that

$$\sigma_y \frac{(r_e^2 - r_i^2)}{(r_i^2 + r_e^2)} < \sigma_y \frac{(r_e^2 - r_i^2)}{(r_e^2)} < \sigma_y \frac{r_e^2 - r_i^2}{r_i^2} < \sigma_y$$

Thus a closed end cylinder will yield in the hoop direction before it fails in any other direction; therefore, the equation for maximum pressure before permanent deformation is given by

$$(p_i)_{max} = \sigma_y \frac{(r_e^2 - r_i^2)}{(r_i^2 + r_e^2)} \tag{2.30}$$

This equation can be non-dimensionalized in a form that relates the inner diameter $d_i$ to the wall thickness $t_w$

$$T_r \equiv \frac{t_w}{d_i} \tag{2.31}$$

By using the definition in equation 2.31 and recalling that $t_w = r_e - r_i$, equation 2.30 can be rearranged in the form

$$\frac{(p_i)_{max}}{\sigma_y} = \frac{T_r(T_r + 1)}{(T_r^2 + T_r + \frac{1}{2})} \tag{2.32}$$

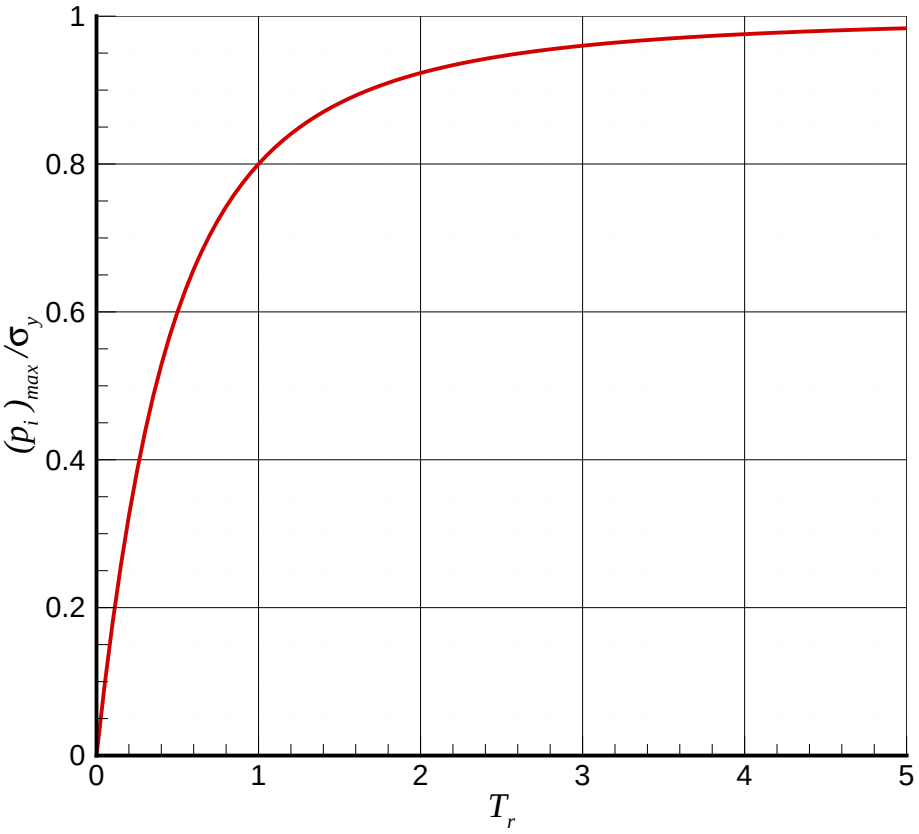


Figure 2–9: Non-dimensional maximum pressure versus the thickness to inner diameter ratio

Equation 2.32 has been plotted in figure 2–9. Furthermore it can be seen from equation 2.32 that when increasing inner diameter the wall thickness must be increased by an equal factor in order to maintain the same structural integrity regardless of the material strength of the vessel. However the mass per unit length of the vessel shell is given as

$$\rho\frac{V}{l} = \rho\pi(r_o^2 - r_i^2) = \rho\pi d_i^2(T_r^2 + T_r) \tag{2.33}$$

which is not a function of $T_r$ alone. Therefore, when scaling up a gun system, a greater proportion of material must be added in order to maintain the strength of the initial gun system. Equation 2.33 is plotted in figure 2–10.

Another parameter that needs to be investigated is the pressure at which a gun system will rupture. There are a number of formulas that are used to estimate the

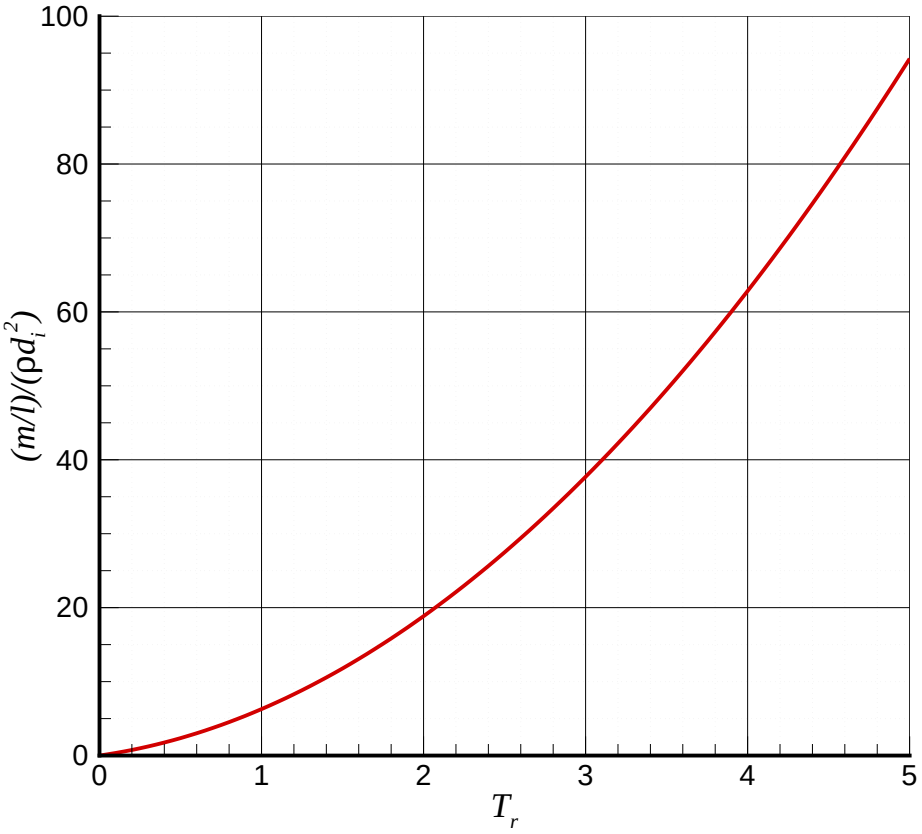


Figure 2–10: Non-dimensional mass per unit length versus the thickness to inner diameter ratio

rupture characteristics of a cylinder. Three of these formulas are presented in [14]. The first is the mean diameter formula which can be used to estimate the rupture pressure for both thick and thin walled vessels. The mean diameter formula is given as

$$(p_{burst})_1 = 2\sigma_u \frac{r_e - r_i}{r_e + r_i} = 2\sigma_u \frac{T_r}{T_r + 1} \tag{2.34}$$

Where $p_{burst}$ is the rupture pressure and $\sigma_u$ is the ultimate strength of the material.

For the very thick walled cylinder the failure pressure can be estimated using

$$(p_{burst})_2 = \sigma_u \ln \frac{r_o}{r_i} = \sigma_u \ln(2T_r + 1) \tag{2.35}$$

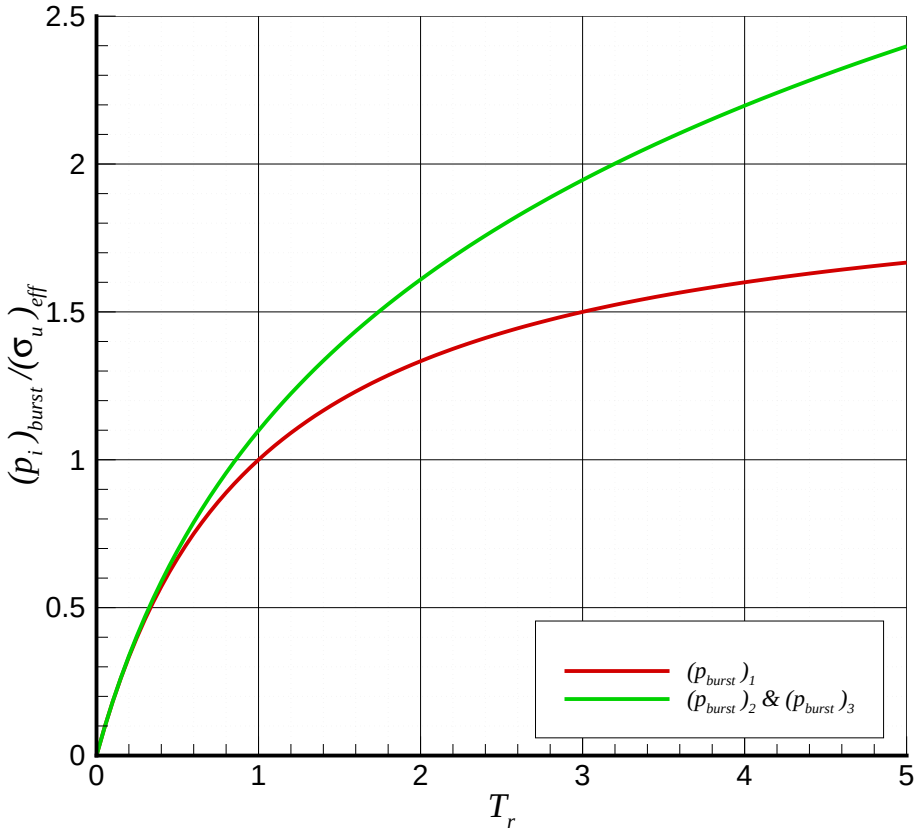


Figure 2–11: Non-dimensional burst pressure versus the thickness to inner diameter ratio

For more accuracy, models have been developed which include the effects of strain hardening in order to better estimate the rupture strength of thick wall vessels

$$(p_{burst})_3 = \frac{2\sigma_y}{\sqrt{3}}\left(2 - \frac{\sigma_y}{\sigma_u}\right)\ln\frac{r_o}{r_i} = \frac{2\sigma_y}{\sqrt{3}}\left(2 - \frac{\sigma_y}{\sigma_u}\right)\ln(2T_r + 1) \tag{2.36}$$

From the equations developed here a maximum theoretical gun pressure can be determined. Using the values for $\sigma_y$ and $\sigma_u$ taken from [3] for the strongest available materials, tables have been assembled in appendix C. From these tables it is reasonable to say that by utilizing high strength steel, a gun system could be made such that it could withstand static chamber pressures in the order of 1200 MPa (given that the chamber diameter is not excessively large, see appendix C). Thus 1200 MPa will be used to determine which projectile materials are the best suited for these applications. The tools developed here will be put to use later in this work during

the development of a prototype system.

**The Projectile**

The projectile has been determined to be a function of the aspect ratio $A_r$, the strength to density ratio $S_r$, and the pressure ratio $P_r$. For sake of argument when optimizing a gun system the assumption is made that it will be designed to operate in a parameter space where the projectile will not break, i.e $P_r \leq 1$. Furthermore it has been assumed that the maximum strength of the projectile is determined by the ultimate strength of the projectile material $\sigma_u$.

The $S_r$ ratio of various materials is shown in table 2–1. Note that if $\sigma_u$ for a particular material is above 1200 MPa (the theoretical maximum gun pressure) then $S_r = 12\,\mathrm{kbar}/\rho$.

From this it can be seen that aluminium and titanium present the best options for projectile materials. However, what is not apparent from this table is that in

Table 2–1: Strength to Density Ratio for Various Materials

| Material | $\rho$ [kg/m$^3$] | $\sigma_u$ [MPa] | $S_r$ [bar m$^3$/kg] |
|---|---|---|---|
| Steel Alloy 4340 (Normalized) | 7850 | 1280 | 1.529 |
| Stainless Alloy 17-7 (Cold Rolled) | 7650 | 1380 | 1.569 |
| Cast Iron Grade 120-90-02 (Tempered) | 7100 | 827 | 1.165 |
| Aluminium Alloy 7075 (T6 Temper) | 2800 | 572 | 2.043 |
| Copper Alloy C17200 (Solution Heat Treated and Aged) | 8250 | 1310 | 1.455 |
| Magnesium Alloy AZ31B (Rolled) | 1770 | 290 | 1.638 |
| Titanium Alloy Ti-6Al-4V (Solution Heat Treated and Aged) | 4430 | 1172 | 2.646 |
| Polycarbonate (PC) | 1200 | 72.4 | 0.603 |
| Polyetheretherketone (PEEK) | 1310 | 103 | 0.786 |

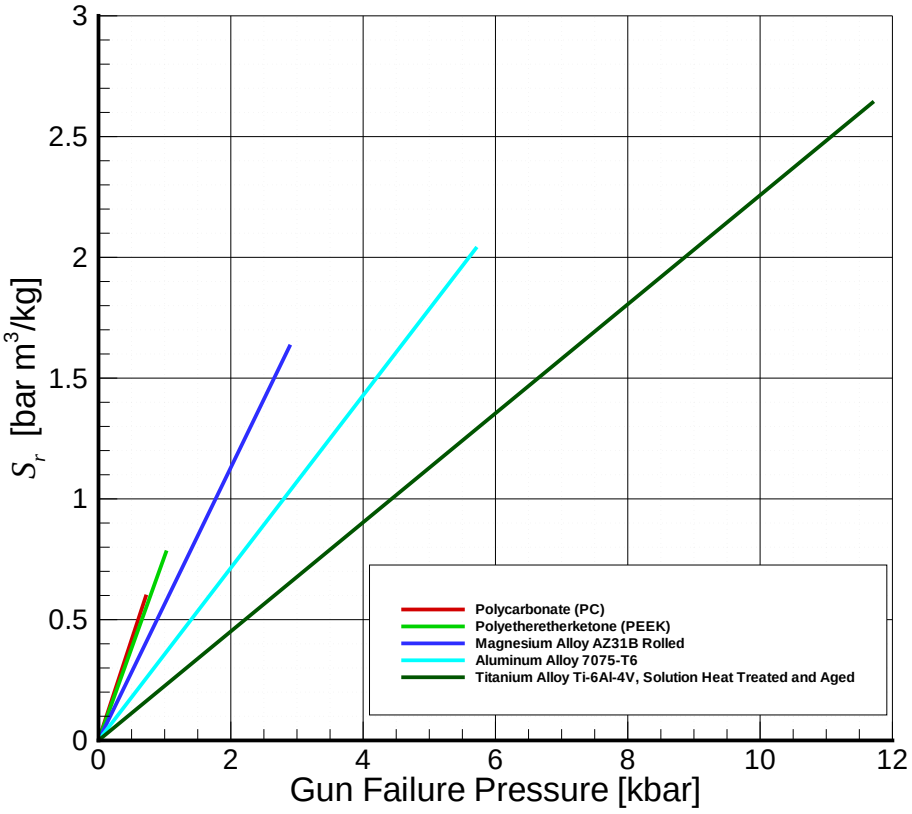


Figure 2–12: $S_r$ vs. gun maximum design pressure

certain cases other materials are optimal. Figure 2–12 shows $S_r$ versus gun maximum design pressure for various materials.

It can be seen from figure 2–12 that, for lower gun design pressures, lighter materials are the better choice. Furthermore, there are ranges of gun pressures that are not optimal for any material, thus the optimal $S_r$ is not a continuous function of gun pressure. Equation 2.37 describes this for the materials presented in figure 2–12, which is then re-plotted in figure 2–13.

$$(S_r)_{opt} = \begin{cases} \dfrac{p_{gun}}{1.2\,kg/m^3} & \text{for} \quad 0 \le p_{gun} \le 0.724\,\text{kbar} \\ \dfrac{p_{gun}}{1.31\,kg/m^3} & \text{for} \quad 0.790 \le p_{gun} \le 1.03\,\text{kbar} \\ \dfrac{p_{gun}}{1.77\,kg/m^3} & \text{for} \quad 1.39 \le p_{gun} \le 2.90\,\text{kbar} \\ \dfrac{p_{gun}}{2.8\,kg/m^3} & \text{for} \quad 4.59 \le p_{gun} \le 5.72\,\text{kbar} \\ \dfrac{p_{gun}}{4.43\,kg/m^3} & \text{for} \quad 9.05 \le p_{gun} \le 11.72\,\text{kbar} \end{cases} \tag{2.37}$$

It can be seen from figure 2–13 that there are large gaps in the gun failure pressure range that are not optimal. There is a low pressure region that includes a high strength magnesium alloy as well as the polymers, polycarbonate (PC) and polyetheretherketone (PEEK), then there is a range of non-optimum gun pressures followed by a small medium pressure region where the high strength aluminium alloy 7075-T6 is the optimum projectile material. Finally, there is an even larger gap in the gun pressure range before the high gun pressure range is reached, in which case a high strength titanium is the optimum projectile material. Thus, when designing a gun system, with figure 2–13 as a guide, once a gun operating pressure is determined the optimal projectile material can be chosen. Furthermore, it is undesirable to develop a gun system with a design pressure within the non-optimal ranges of figure

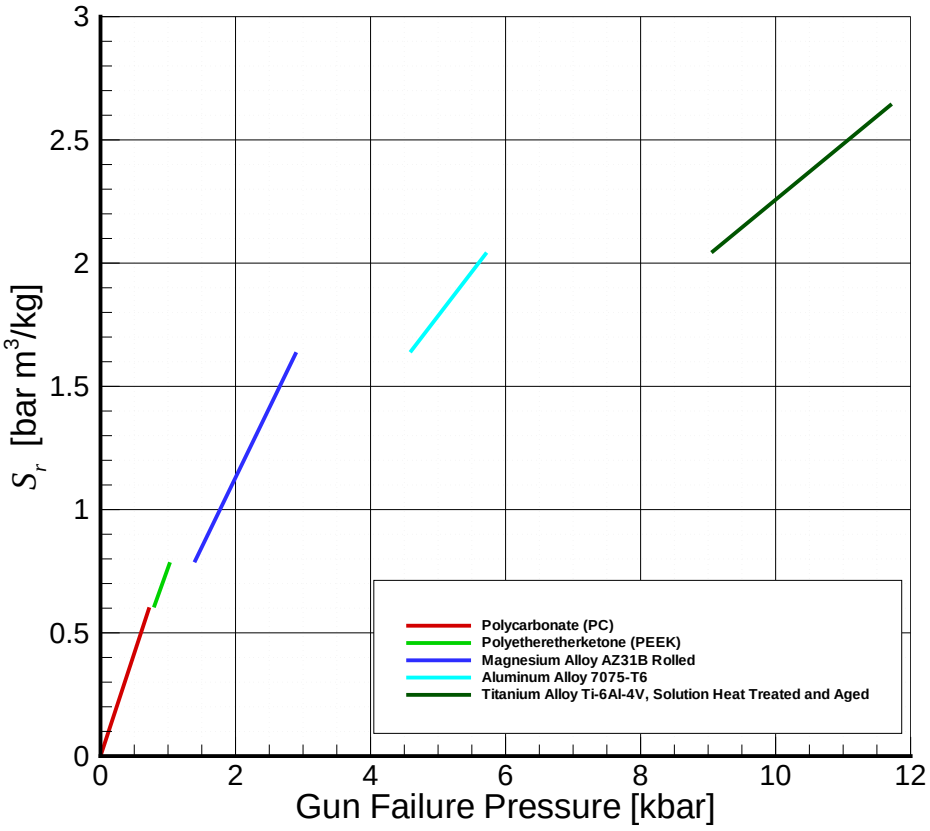


Figure 2–13: Optimal $S_r$ vs. gun maximum design pressure

2–13. For example instead of designing a gun to operate at 4.59 kbar using high strength aluminium as the projectile material, it is better to design a gun to operate at 2.9 kbar using high strength magnesium as the projectile, resulting in a lighter gun system.

The final factor determining the operation of a projectile is its length to diameter ratio. If the projectile is made too thin then it can fail in the bore. However, it is unclear how thin a projectile can be made in practice. From the experience gained in running the projectile trials, a $A_r = 0.3$ was determined to be a safe value. This is consistent with earlier studies done at McGill [5] and [10]. However this is for small caliber projectiles (between 4.3 mm and 12.7 mm). It has been shown by [12] that for a 50 cm diameter bore, discs with an aspect ratio of 0.012 (6 mm) could be launched. However, these projectiles were levitated and spun by using an electromagnetic stator and maximum pressure experience were 300 bar, about 6% the ultimate strength of structural steel. Furthermore at 50 cm the ratio between the machine precision and the characteristic diameter is much smaller than for a small projectile. Thus, for this exercise, the smallest aspect ratio will be taken as 0.3. However, smaller aspect ratios may attainable but, from experience, designing a system for these aspect ratios will increase the systems complexity. It is suggested that these methods be chosen as a last resort after all other avenues of improving performance have been pursued.

The result of this analysis is that maximum realistic values have been obtained for the following

$A_r = 0.3$

$S_r = 2.646$ [bar m$^3$/kg] (titanium projectile $p_{max} = 11.72$ kbar)

$P_r = 1.0$

Thus the maximum realistic value for $M_f = 8.82$ [bar m$^3$/kg]. The last two mechanical parameters to investigate are $\zeta_\circ$ and $\zeta_{1^{st}}$.

**The Gun: Part II**

Now that a range for the mechanical factor has been determined equation 2.25 and equation 2.26 can be explored for a series of $M_f$, $a_\circ$ and $\gamma$ . However, $\zeta_{1^{st}}$ is still an unknown. Determining the losses that are experienced by a gun system during the projectile acceleration/gas expansion process is difficult to do analytically. However it was shown by [1] that the only losses that cannot be neglected (assuming vacuum in front of the projectile) are friction between the projectile and the bore and viscous and convective heat losses between the gas and the boundaries. It has been determined through experiments and operational experience for high temperature gun systems, such as 2-stage light gas guns, that the losses due to aerodynamic friction and convective heat transfer to the barrel wall results in base pressure forces equalling the friction forces at between 200 and 400 calibers down the barrel [1]. Therefore, the barrel length, $\zeta_b$, also has a maximum realistic value. To be conservative the following analysis will use $\zeta_b = 200$ as the base line. Following the postulate that it is desirable to design a gun so that the projectile leaves the barrel at the moment the first reflected rarefaction reaches it then the goal is to optimize $u_{1^{st}}$ for $\zeta_{1^{st}} = 200$.

Returning to equation 2.25 with the assumption that $P_r = 1$

$$u_{1st} = \frac{2a_\circ}{(\gamma - 1)} \left\{ 1 - \left[ \frac{\gamma + 1}{2a_\circ^2} M_f \zeta_\circ + 1 \right]^{-\frac{2(\gamma-1)}{(\gamma+1)}} \right\} \tag{2.38}$$

The non-dimensional chamber length can be rewritten in terms of barrel length

$$\zeta_\circ = \zeta_\circ \frac{\zeta_b}{\zeta_b} = \zeta_b \frac{\zeta_\circ}{\zeta_{1^{st}}} = \zeta_{1^{st}} \Phi_\circ$$

where $\Phi_\circ$ is the new non-dimensional chamber length in terms of the barrel length and $\zeta_b$ is the non-dimensional barrel length in terms of the projectile diameter $d_p$. Therefore equation 2.38 can be rewriten as

$$u_{1st} = \frac{2a_\circ}{(\gamma - 1)} \left\{ 1 - \left[ \frac{\gamma + 1}{2a_\circ^2} M_f \zeta_b \Phi_\circ + 1 \right]^{-\frac{2(\gamma-1)}{(\gamma+1)}} \right\} \tag{2.39}$$

All the mechanical elements are represented in this equation; the mechanical factor $M_f$, the non-dimensional chamber length $\Phi_\circ$ and the non-dimensional barrel length $\zeta_b$. Thus there is an overall mechanical factor that can describe a gun system.

$$M_F = M_f \zeta_b \Phi_\circ = \frac{S_r}{A_r} \zeta_b \Phi_\circ \tag{2.40}$$

Equation 2.40 holds all the non-gas related aspects of the gun system and it is proposed here that it can be used to predict gun performance. Applying 2.40 to equation 2.39 the following is obtained.

$$u_{1st} = \frac{2a_\circ}{(\gamma - 1)} \left\{ 1 - \left[ \frac{\gamma + 1}{2a_\circ^2} M_F + 1 \right]^{-\frac{2(\gamma-1)}{(\gamma+1)}} \right\} \tag{2.41}$$

Previously obtained maximum values $M_f$ and $\zeta_b$ are used to determine a maximum realistic $M_F$ of 100,000 kPa m$^3$/kg. With this, equation 2.41 has been solved for a range of $M_F$ (1 kPa m$^3$/kg to 100,000 kPa m$^3$/kg) in order to determine the effects of $a_\circ$, $\gamma$ and $M_F$ on equation 2.25. These plots are located in appendix D.

Figure 2–14 is a qualitative example of equation 2.41 plotted as $a_\circ$ vs $u_{1^{st}}$ for a series of $\gamma$ s with a fixed $M_F$. It can be seen that there is an optimal speed of sound that provides a maximum value of $u_{1^{st}}$ for a given $\gamma$. By looking at the figures in Appendix D it can be seen that this maximum occurs at a higher speed of sound as

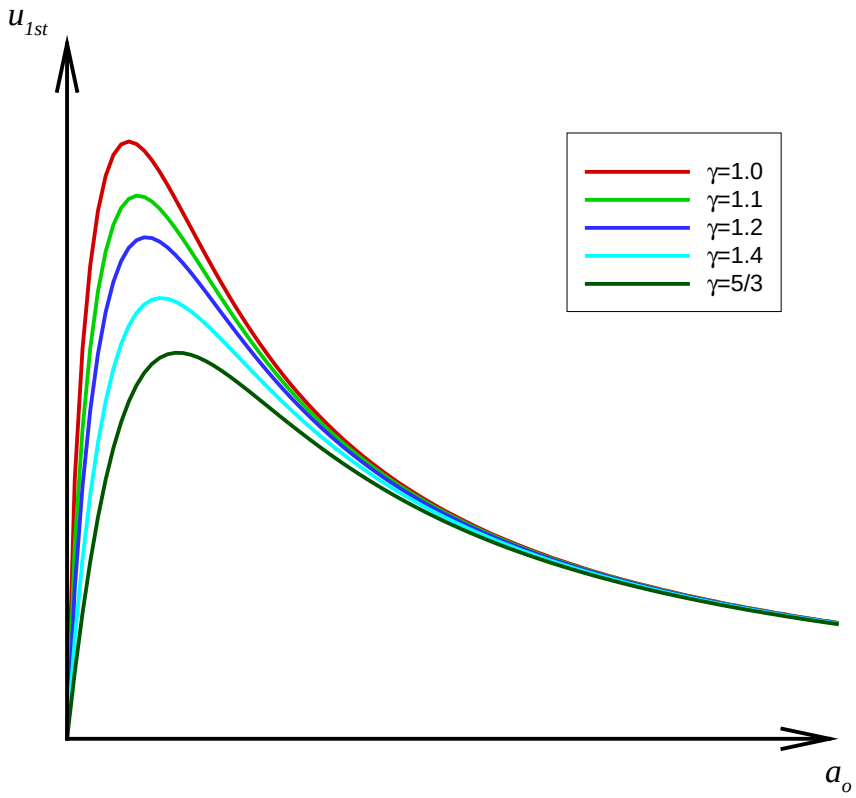


Figure 2–14: $u_{1^{st}}$ vs. $a_\circ$ for a series of $\gamma$'s with a fixed $M_f$ and $\zeta_\circ$

$M_F$ increases. However, the value of $\zeta_{1^{st}}$ is still an unknown. Returning to equation 2.26 and writing it in the form

$$\zeta_{1^{st}} = \frac{2a_\circ^2}{M_f(\gamma+1)} \left\{ \frac{\frac{2}{\gamma-1} - \frac{\gamma+1}{\gamma-1}\left[\frac{\gamma+1}{2a_\circ^2} M_f \zeta_b \Phi_\circ + 1\right]^{-\frac{2(\gamma-1)}{(\gamma+1)}}}{\left[\frac{\gamma+1}{2a_\circ^2} M_f \zeta_b \Phi_\circ + 1\right]^{-2}} + 1 \right\} \tag{2.42}$$

It can be seen that this equation is a function of both $M_f$ and $M_F$ therefore in order to determine the velocity and chamber lengths that are required for the first rarefaction to occur when $\zeta_{1^{st}} = \zeta_b = 200$, equations 2.42 and 2.39 must be solved simultaneously. This must be done implicitly using a root solver. The results are presented here in figures 2–15 through 2–26 which show how chamber length and

muzzle velocity (for $\zeta_{1^{st}} = \zeta_b = 200$) are affected by the Mechanical factor, initial speed of sound and specific heat ratio.

It can be seen in figures 2–15 through 2–20 that there are three regimes. For a low $M_f$, speed of sound is only important for very low sound velocities and the specific heat ratio, $\gamma$, plays a very small role in the magnitude of $u_{1^{st}}$. In the middle range the speed of sound plays a significant role in the magnitude of $u_{1^{st}}$, whereas $\gamma$ plays only a moderate role. However in the range of large $M_f$ it is seen that $\gamma$ has a very significant effect on the magnitude of $u_{1^{st}}$. This is a very important result. It implies that by first calculating $M_f$ then it becomes easier to determine the optimal gas required to achieve the desired gun performance.

From figures 2–21 through figure 2–26 it can be seen that for only very large values of $M_f$ does the $\gamma$ play any role in affecting the magnitude of $\Phi_\circ$ required for the first reflection to occur at $\zeta_{1^{st}} = 200$. Furthermore, these curves are all very close to linear. Thus the designer can evaluate the $M_f$ of their design, then, if a certain

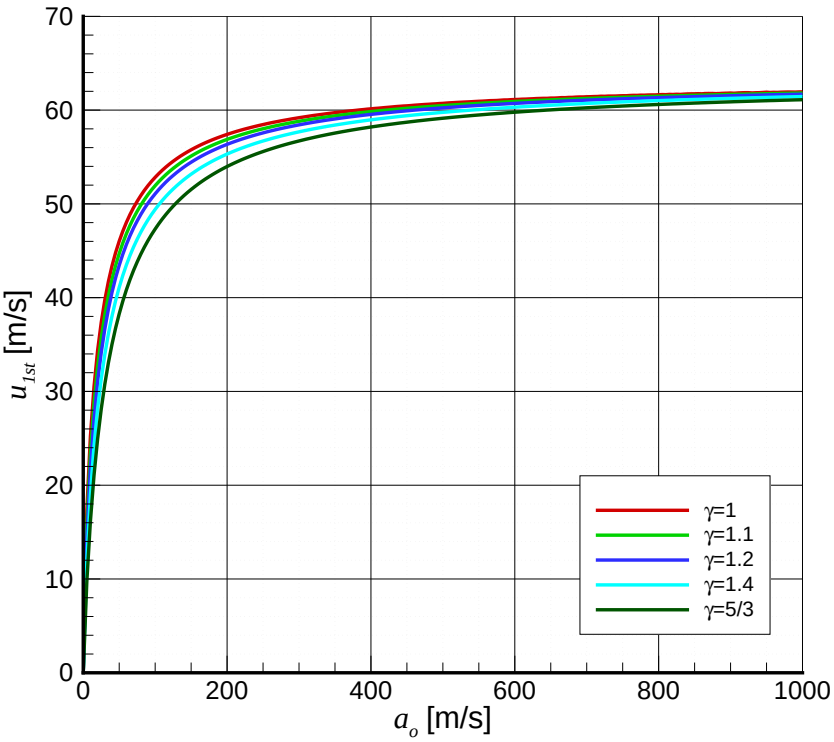


Figure 2–15: $u_{1^{st}}$ vs. $a_\circ$ for a series of $\gamma$'s with $M_f = 10$ Pa m$^3$/kg with $\zeta_{1^{st}} = \zeta_b = 200$

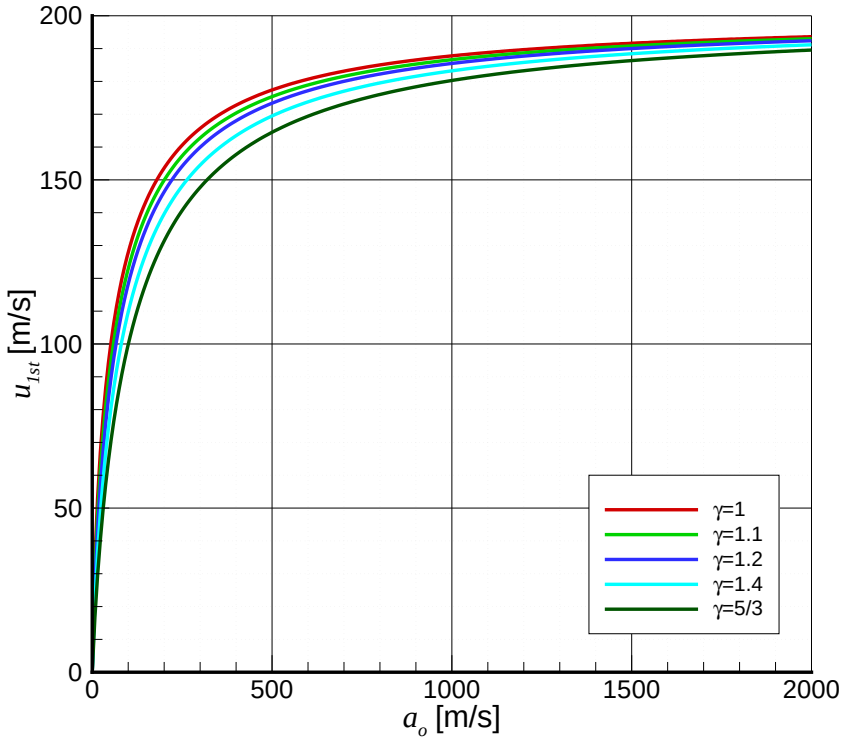


Figure 2–16: $u_{1^{st}}$ vs. $a_\circ$ for a series of $\gamma$'s with a fixed $M_f = 100$ Pa m$^3$/kg with $\zeta_{1^{st}} = \zeta_b = 200$

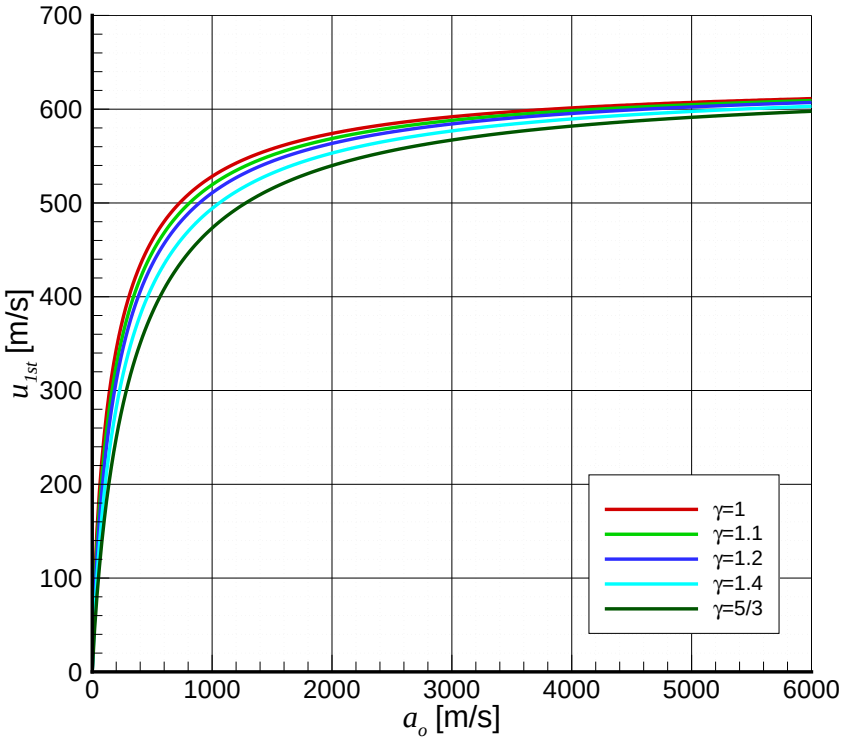


Figure 2–17: $u_{1^{st}}$ vs. $a_\circ$ for a series of $\gamma$'s with $M_f = 1,000$ Pa m$^3$/kg with $\zeta_{1^{st}} = \zeta_b = 200$

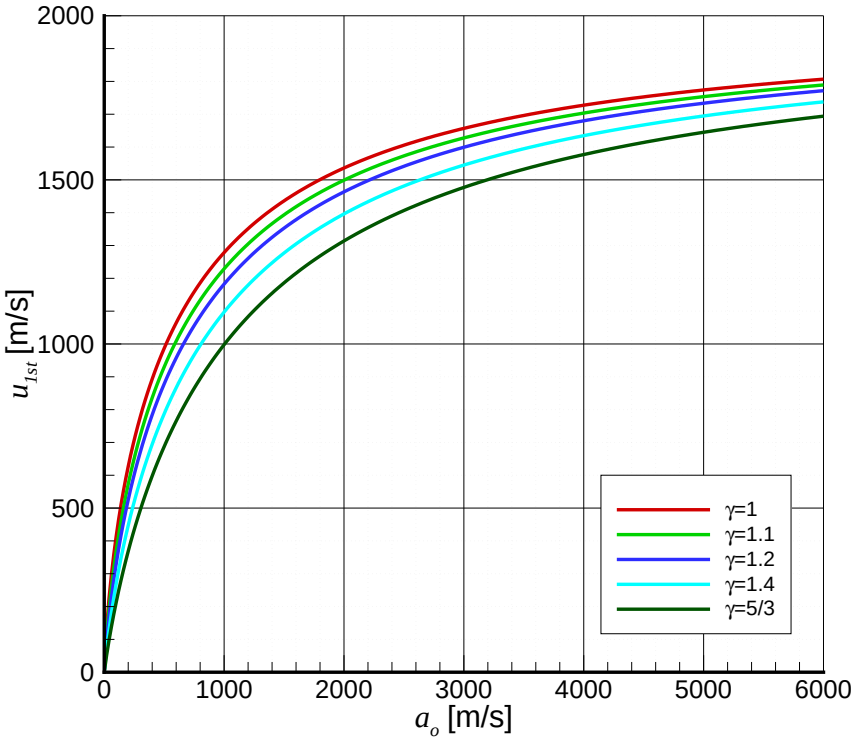


Figure 2–18: $u_{1^{st}}$ vs. $a_\circ$ for a series of $\gamma$'s with a fixed $M_f = 10,000$ Pa m$^3$/kg with $\zeta_{1^{st}} = \zeta_b = 200$

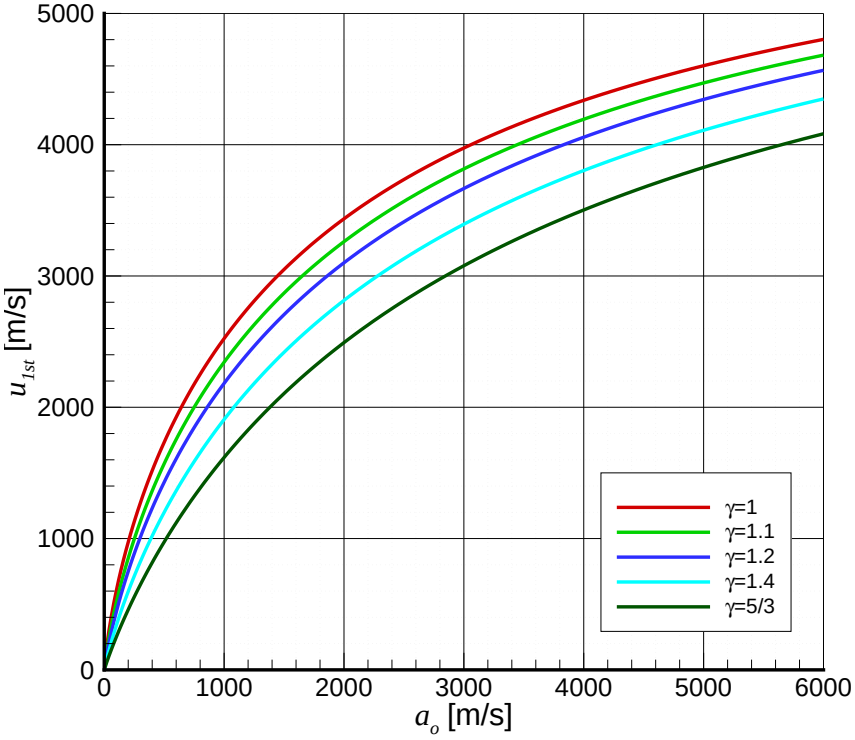


Figure 2–19: $u_{1^{st}}$ vs. $a_\circ$ for a series of $\gamma$'s with $M_f = 100,000$ Pa m$^3$/kg with $\zeta_{1^{st}} = \zeta_b = 200$

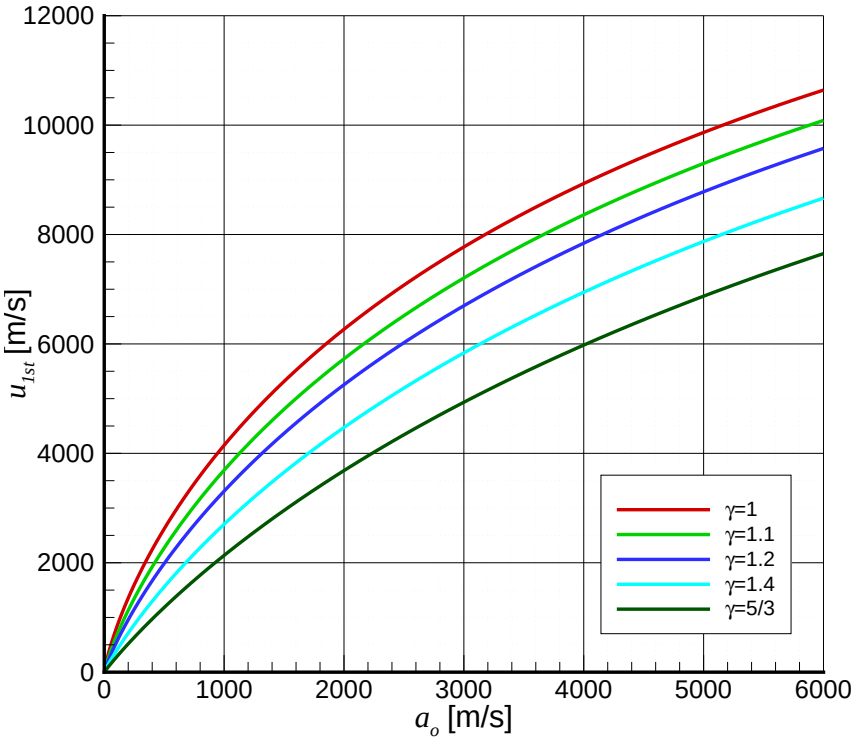


Figure 2–20: $u_{1^{st}}$ vs. $a_\circ$ for a series of $\gamma$'s with a fixed $M_f = 1,000,000$ Pa m$^3$/kg with $\zeta_{1^{st}} = \zeta_b = 200$

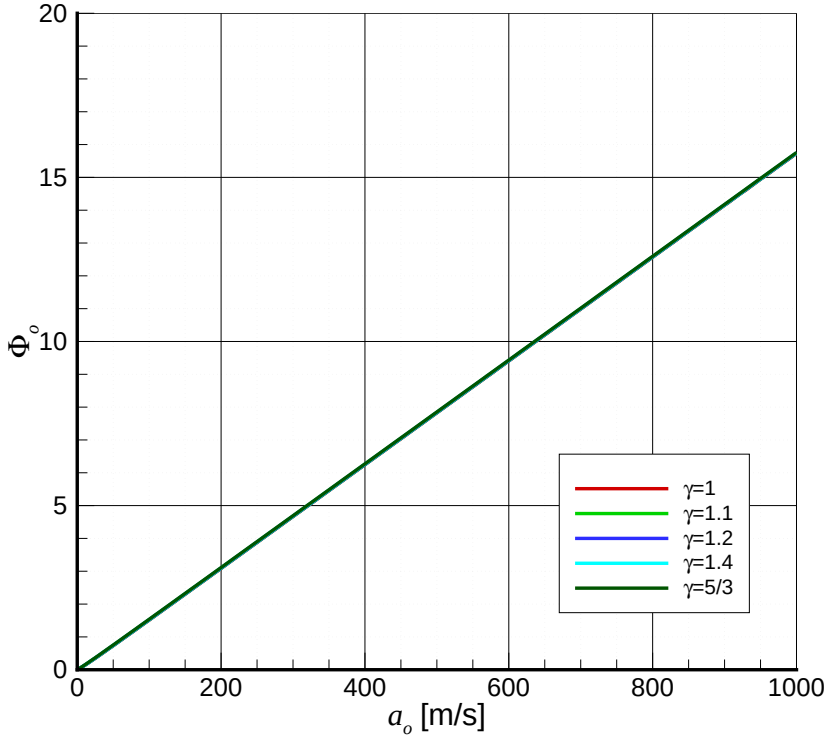


Figure 2–21: $\Phi_\circ$ vs. $a_\circ$ for a series of $\gamma$'s with $M_f = 10$ Pa m$^3$/kg with $\zeta_{1^{st}} = \zeta_b = 200$

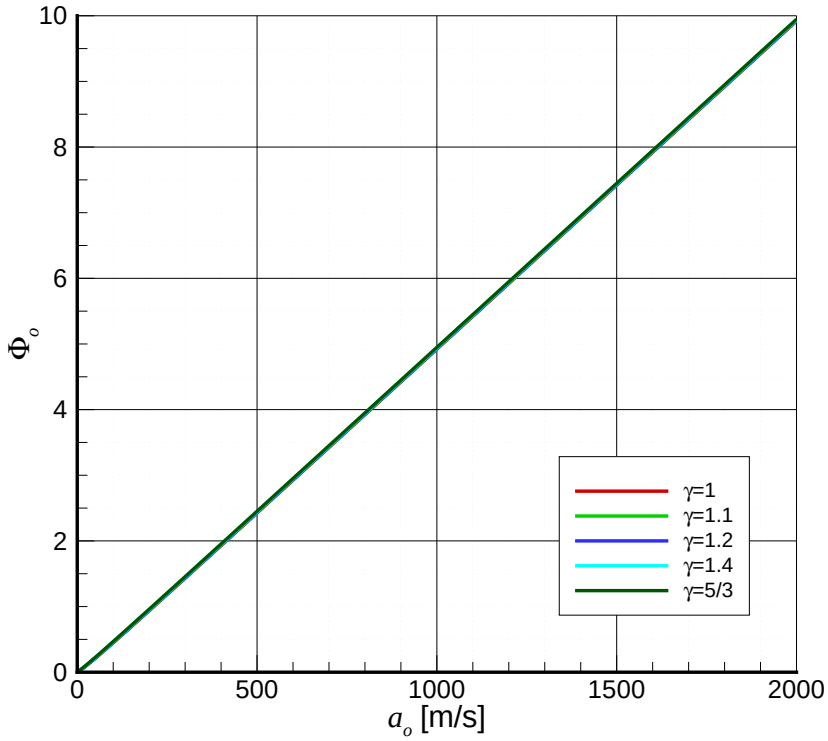


Figure 2–22: $\Phi_\circ$ vs. $a_\circ$ for a series of $\gamma$'s with a fixed $M_f = 100$ Pa m$^3$/kg with $\zeta_{1^{st}} = \zeta_b = 200$

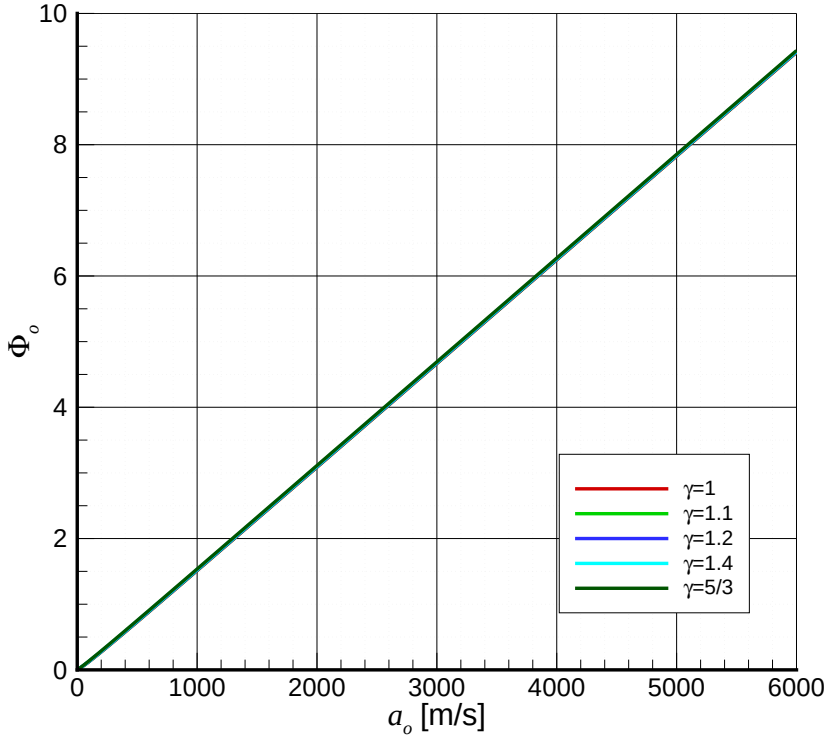


Figure 2–23: $\Phi_\circ$ vs. $a_\circ$ for a series of $\gamma$'s with $M_f = 1,000$ Pa m$^3$/kg with $\zeta_{1^{st}} = \zeta_b = 200$

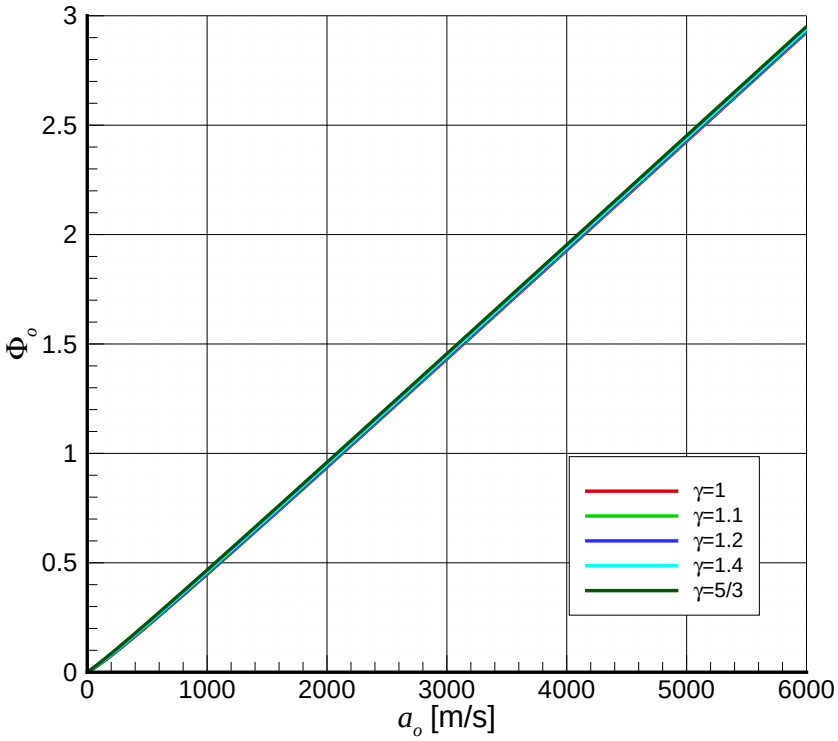


Figure 2–24: $\Phi_\circ$ vs. $a_\circ$ for a series of $\gamma$'s with a fixed $M_f = 10,000$ Pa m$^3$/kg with $\zeta_{1^{st}} = \zeta_b = 200$

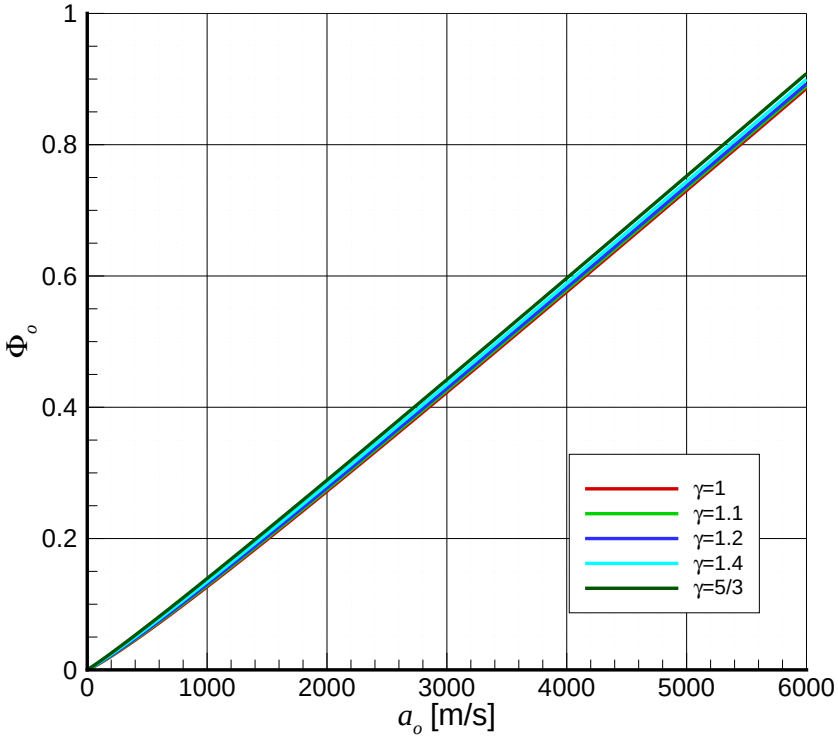


Figure 2–25: $\Phi_\circ$ vs. $a_\circ$ for a series of $\gamma$'s with $M_f = 100,000$ Pa m$^3$/kg with $\zeta_{1^{st}} = \zeta_b = 200$

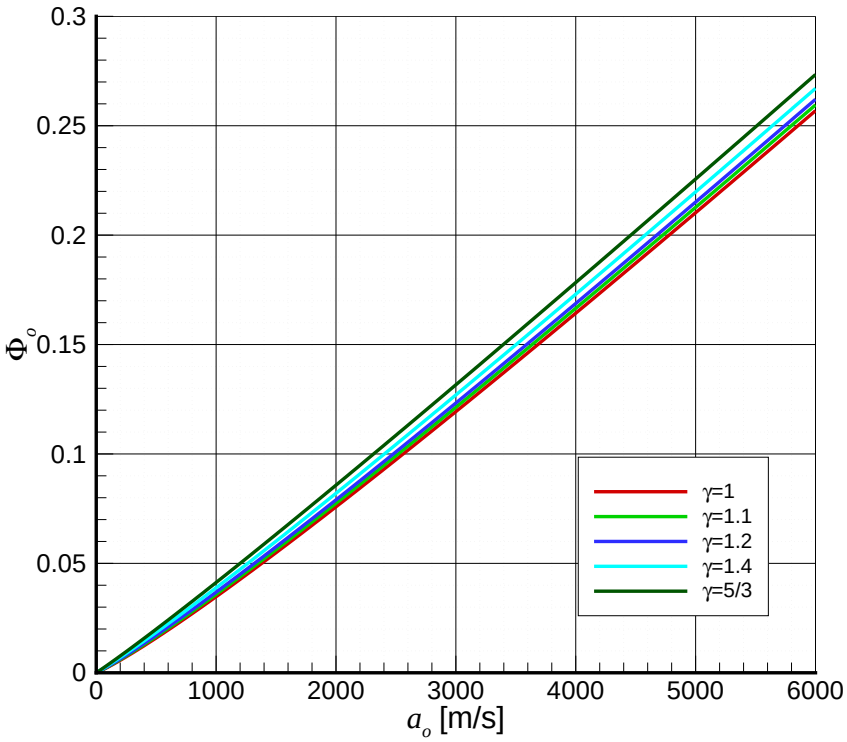


Figure 2–26: $\Phi_\circ$ vs. $a_\circ$ for a series of $\gamma$'s with a fixed $M_f = 1,000,000$ Pa m$^3$/kg with $\zeta_{1^{st}} = \zeta_b = 200$

muzzle velocity is required, they can select the gas properties (of course they must find a real gas that will fulfill this, this subject will be discussed in a later section) that will give them this performance from figures 2–15 through 2–20. Cross referencing these gas properties with the corresponding graph in figures 2–21 through 2–26, a value of $\Phi_\circ$ can be obtained that will provide the desired velocity. Alternatively, if the restriction is the length of the gun system, then figures 2–21 through 2–26 can be used to determine the gas properties that are required and these can then be cross referenced with the corresponding plot in figures 2–15 through 2–20 to determine the muzzle velocity obtained with this gun-gas system. It is most likely that the initial design is either over or under designed but this tool will aid in the iterative process to determine the optimal design (or if the required performance is realistically achievable within the design restrictions placed on the gun system). These tools developed here will be used later in this work in the presentation of the prototype hypersonic gun system that has been built.

It is not always the case that a gun system will operate within its design parameters. For example, a system operating at a sound speed lower than its optimal sound speed, will not perform in the range of figures 2–15 to 2–26. Furthermore it is very possible that a gun system will be operated in the regime where the first reflected shock has reached the projectile before it exits (this will probably be unavoidable in many practical situations, i.e. low $M_f$ systems with restrictions on chamber length). In the first case the simple wave solution will suffice in determining the performance of the gun system, however, in the latter case, the simple wave solution will not suffice in predicting performance and other methods must be used. In [1], Seigel presents an in-depth discussion on the ballistics problem for pre-burned gas guns. He develops the necessary tools to solve the problem numerically using the Method of Characteristics and presents the results in an extensive series of plots. However, for this work, a Quasi-One-Dimensional Euler code has been developed by Nicolas Ponchaut [9], and has been used extensively for evaluating the performance of various gun systems. In the remainder of this work, this code will be the principle tool for making performance predictions.

**The Gas**

So far the gas has only presented itself to the problem in terms of its initial speed of sound $a_\circ$ and the specific heat ratio $\gamma$. However, from an engineering standpoint, these properties cannot be manipulated directly. Thus a more fundamental understanding of these parameters must be obtained. Recall that the speed of sound can be written as

$$a_\circ = \sqrt{\gamma RT} = \sqrt{\gamma \frac{\overline{R}}{M} T} \tag{2.43}$$

where $\overline{R}$ is the universal gas constant and $M$ is the molar mass of the particular propellant gas. So, the speed of sound of the gas can be seen as a function of the

temperature, $T$ and the gas selected. Furthermore the specific heat ratio can be written as:

$$\gamma = \frac{c_p}{c_v} = \frac{c_p}{c_p - R} = \frac{c_p}{c_p - \frac{\overline{R}}{M}} \tag{2.44}$$

$c_p$ is a function of temperature and it is also a function of the gas composition. Moreover, for non-monatomic gases, the molecular weight is also a function of temperature. This is due to either the chemical reactions or dissociation that occur at high temperatures. The effect is that these reactions or dissociations result in requirement of more energy being added to a system in order to raise its temperature. Thus choosing the appropriate gas can be a nontrivial exercise. It was shown in the previous section that a high speed of sound is essential for gun performance. In the meantime, it was also shown that, in the case of very high performing systems, the specific heat ratio is just as important. From equation 2.43 it can be seen that low molecular weight gases are key in obtaining high initial sound speeds. It can also be seen from equation 2.43 that a high gamma also increases the initial sound speed. Conversely, however, it was shown previously that a lower $\gamma$ is beneficial to gun performance. Obtaining a low $\gamma$ requires a gas with many degrees of freedom. Equation 2.45 shows the relation of degrees of freedom to $\gamma$ for an ideal gas [8].

$$\gamma = \frac{f+2}{f} \tag{2.45}$$

So as $f \to \infty$ $\gamma \to 1$, hence a gas with more degrees of freedom will have a lower $\gamma$ than a monatomic gas. However, a gas with many degrees of freedom requires more energy to raise the temperature than a monatomic gas, which has no rotational or vibrational modes to excite. This, however, is why gases with lower $\gamma$ can make desirable propellants. These gases carry this energy with them as they travel down the barrel behind the projectile maintaining the temperature as the gas expands. The result is a less severe pressure drop on the projectile than would occur in a monatomic propellant.

Thus the key to a good propellant is to find the lightest gas with as many possible excitable energy modes. However, the number of excitable energy modes must be weighed against how much energy is required to raise the resulting propellants temperature. To give the reader an understanding of what gases make the ideal propellants figures 2–27 through 2–31 have been constructed presenting the gases $CO_2$, $H_2O$, $N_2$, $O_2$, Air, He, $CH_4$, $NH_3$ and $H_2$, with pressure taken to be 12000 bar (the maximum realistic pressure determined for a gun system) for the aforementioned gases.

Figure 2–27 shows the relationship between sound speed and temperature while figure 2–28 shows the relationship between temperature and the specific heat ratio. These values were obtained using the equilibrium code CEA [6].

It can be seen from figures 2–27 and 2–28 that the different equilibrium states of these gases at the different temperatures result in very interesting trends. It can be seen that for some gases, $\gamma$ will drop with increasing temperatures, then rise only

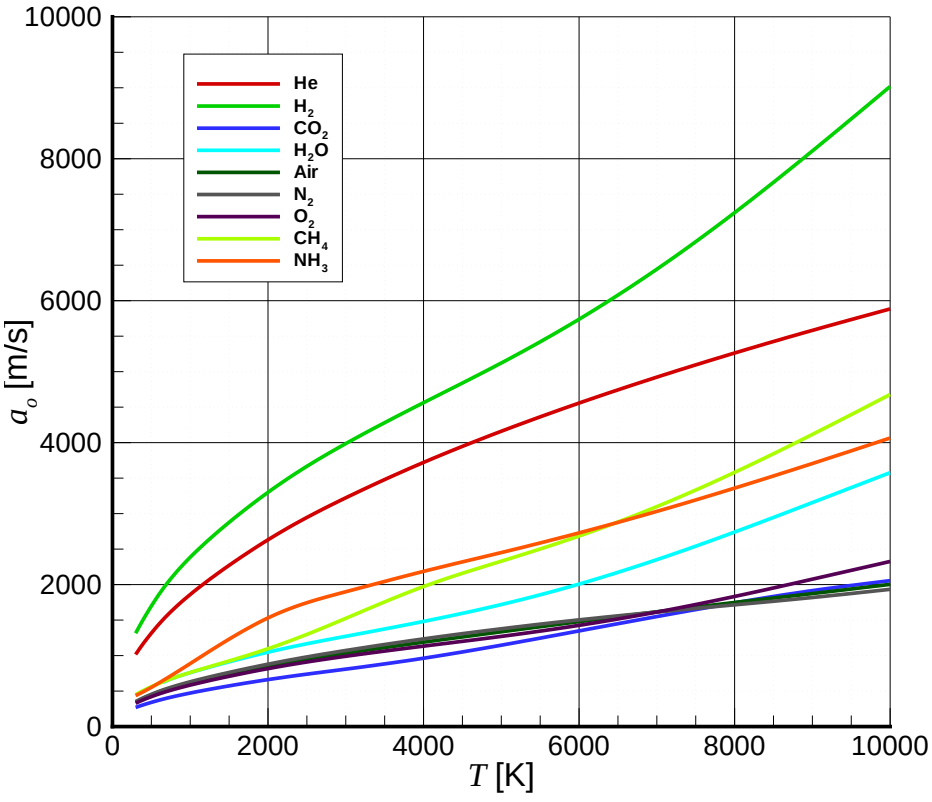


Figure 2–27: Speed of sound vs. temperature for various gases

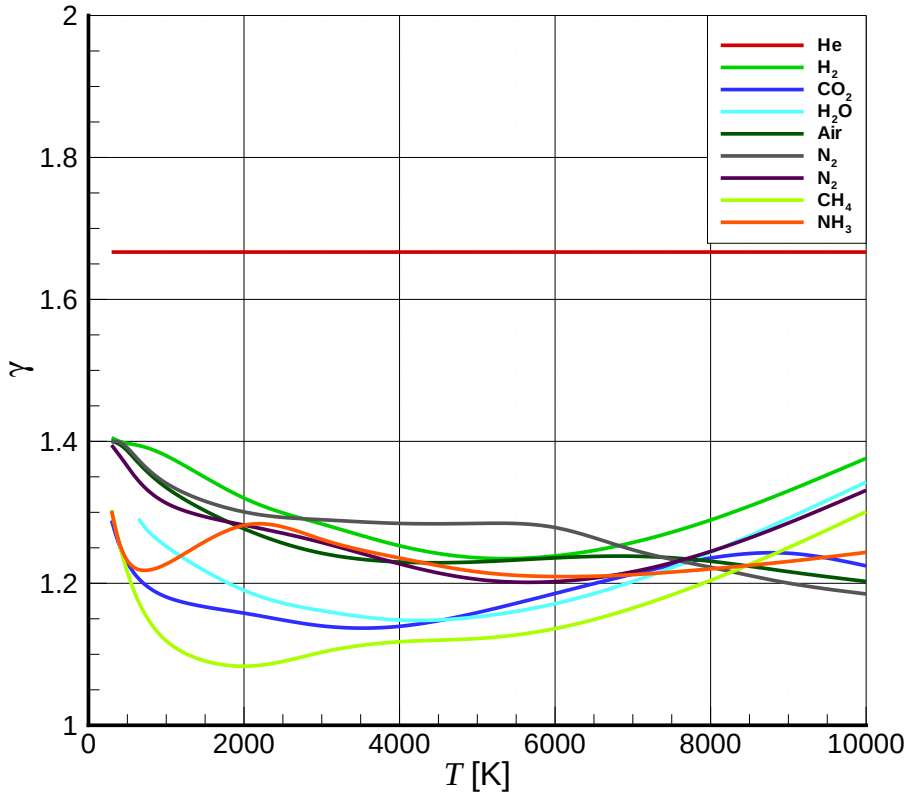


Figure 2–28: Specific heat ratio vs. temperature for various gases

to drop again (for example $NH_3$). For the case of sound speed, it can be seen that the rate of change will decrease only to increase again with temperature for many of the gases. It can be seen that the light gases $H_2$ and He have a much higher sound speed at a given temperature than the other gases. However, there are other gases that start to show improved speeds of sound at higher temperatures, i.e. $CH_4$, $NH_3$ and $H_2O$. The reason these gases are investigated is that they all have low $\gamma$ for a wide range of temperatures which could balance their overall performance with their relatively low sound speed. It is very easy to see that $H_2$ will perform the best at a given temperature, followed by He. However, these other gases are investigated because they are often present in the products of a gun system (with the exception of $CH_4$ and $NH_3$ which are investigated because of their relatively light weight and their low $\gamma$).

However, the amount of energy required to bring these gases to these states must be taken into consideration. For all the gases but $H_2O$, a two step process

was considered. The first is a polytropic compression, from the state $p_\circ = 1.013\,\text{bar}$ and $T_\circ = 298\,\text{K}$, to obtain the required density and then a constant volume heating process to the required temperature and pressure. However, for the $H_2O$, the water starts out as liquid at $p_\circ = 1.013\,\text{bar}$ and $T_\circ = 298\,\text{K}$, it is then raised to the boiling point and evaporated and continues to be heated until it reaches the critical temperature of water, 647.4 K, all through a constant pressure process. Once the water has reached the critical temperature, it is then compressed using the same process that the other gases underwent to reach the required density. Finally it is heated to the final state. Note that these energies are given in terms of a per volume of the gun system basis. It is assumed that the reader has a good understanding of the first law of thermodynamics, therefore the equations will not be introduced here. However the polytropic process used is the following [8]

$$W = p_1 V_1 \ln \frac{V_2}{V_1} \tag{2.46}$$

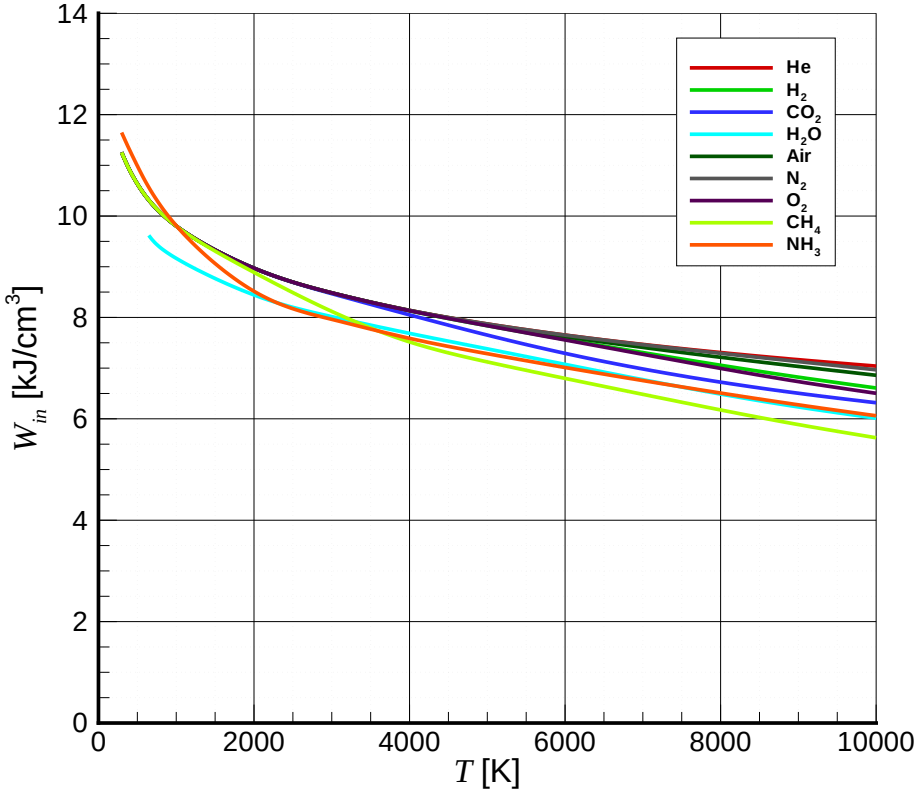


Figure 2–29: Compression work done vs. temperature on system for various gases

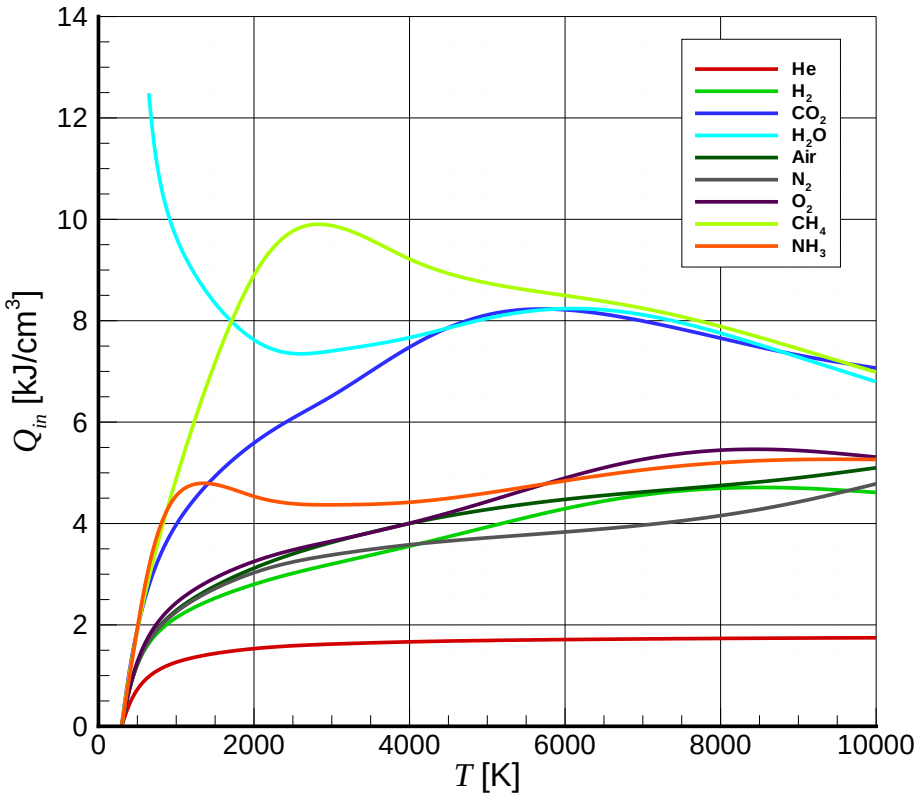


Figure 2–30: Heat added to the system to achieve final temperature vs. temperature for various gases

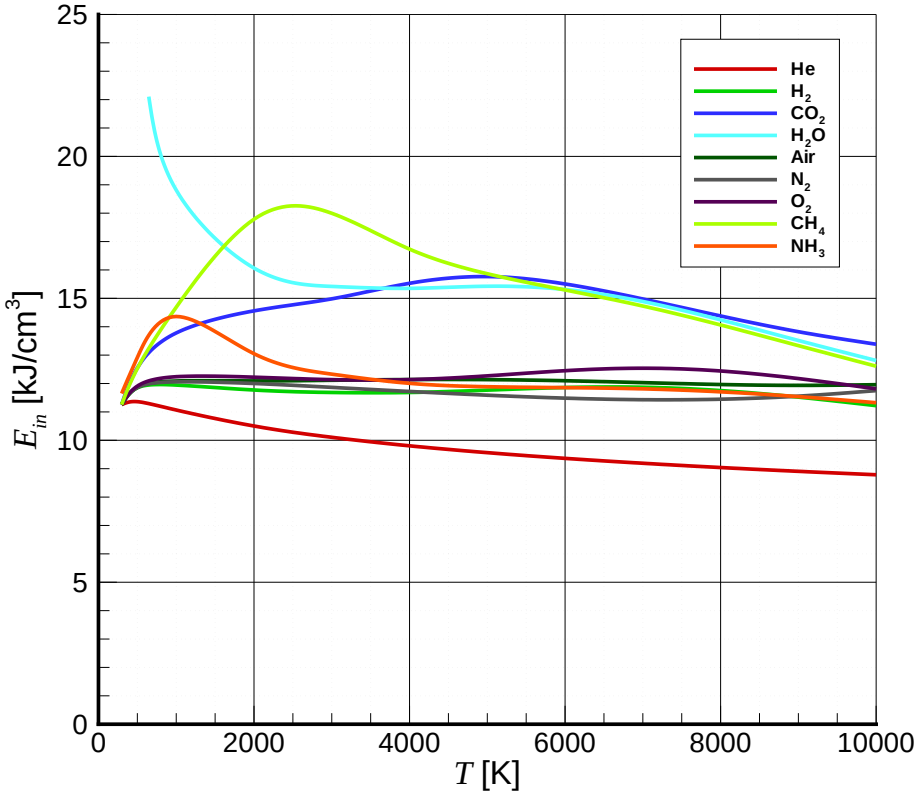


Figure 2–31: Total energy added to the system vs. temperature for various gases

It can be seen that the amount of compression work done in order to obtain the required density for the end state is quite similar for each gas, it drops with the final temperature because following the ideal gas law density drops as pressure increases for a given pressure, thus smaller initial volume of gas gets compressed into the gun chamber when the final temperature is higher. However, the thermal energy input is quite different for each gas. This is due to the different heat capacity these gases have at different temperatures. Furthermore, when a high final temperature is required, the total mass of gas is less than it would be for a lower temperature state with at $p_\circ = 12000\,\text{bar}$. It is presented here on a per volume basis instead of a per mass basis for this reason. The chamber volume and the final pressure are constant in this investigation. Thus for a known chamber volume and an initial state of $p_\circ = 1.013\,\text{bar}$ and $T_\circ = 298\,\text{K}$, the energy required to take this gas to the final state of $p_\circ = 12000\,\text{bar}$ is more useful in a per volume basis than a per mass basis.

From figure 2–31 it can be seen that He requires the least total energy input to reach the desired end state where $CH_4$ along with $CO_2$ require relatively large amounts energy to reach their final states. $H_2O$, due to the need for vaporization before the compression process, requires large amounts of energy to reach the final state especially at low temperatures where the final densities are quite high.

This introduces the question, which is a better propellant, $H_2$ or He? For room temperature applications, the energy input for a He or $H_2$ system is approximately the same. However, at higher temperatures, much more thermal energy is required to get $H_2$ to the same final state as He and it is not until very high, and possibly unrealistic, temperatures that the speed of sound of $H_2$ starts to pull away. This is also a very arbitrary demonstration, due to the fact that any vessel would melt at these temperatures. Thus any process to reach these temperatures must be done in a very short period of time. An example of this is the use of a shock to raise the temperature of a gas. The extreme of this is done using a detonation driven imploding pump tube gun to accelerate projectiles to speeds above 6 km/s [5]. This

system drives an 8 km/s shock in the pump tube. This is provides a good example to compare He to $H_2$. The speed of sound and $\gamma$ of He behind this shock is about 4500 m/s and 1.667, respectively, with a post shock temperature of about 6000 K. The same velocity shock in $H_2$ results in a speed of sound and $\gamma$ of about 3500 m/s and 1.31, respectively, with a post shock temperature of 2650 K. This is the same driver but there is a much higher sound speed for the helium. Though the $H_2$ performed slightly better in experiment, it can be seen that the heating process makes a big difference in what final state is achievable. For this study, detonation is the method of propellant heating that is chosen. The propellant to be investigated is products of stoichiometric hydrogen-oxygen detonation. From figures 2–27 and 2–28 it can be seen that steam has a relatively good speed of sound for a heavier gas as well as having a promising value of $\gamma$ for the temperature achieved by this form of heating (approximately $T = 4350\,\mathrm{K}$ for $T_\circ = 298$ [6]).

## 2.3 The Effects of Chambrage

Now that there is a better understanding of how the other variables effect gun performance, chambrage can be discussed, see figure 2–32. By adding an area change section the performance of a PPIG can be increased. The reason for this is that when the rarefaction waves reach an increase in area section they partially reflect as compression waves [1]. These compression waves will increase the pressure on the base of the projectile when they reach it. This has the effect of the projectile having

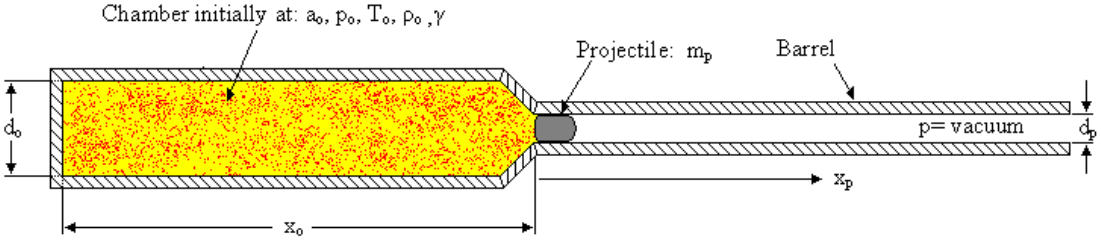


Figure 2–32: Chambered PPIG gun

a greater velocity, at a given position of travel, than the corresponding constant diameter gun. However, these wave interactions make the chambered gun much more difficult to analyze and an accurate solution can only be found computationally. Classically, the effects of area change have been approximated by calculating the $M_r$ for the chambered gun using a method, such as the Lagrange approximation, to estimate the performance by using this modified $M_r$. However, Seigel [1] provides a method that can be used to obtain an even more accurate approximation than the classical methods.

If two PPIG guns of different chambrage have the same $M_r$, then the one with the larger chambrage will obtain a higher velocity in the early stages of acceleration, before many reflected rarefaction interact with it [1]. However, these two PPIG guns with equal $M_r$ will converge to approximately the same projectile velocity in the latter stages of acceleration after numerous interactions with reflected rarefactions. It can be seen however, that if no rarefactions interact with the projectile then the larger chambrage will always have a greater projectile velocity. Thus for an infinitely long chamber the larger the chambrage the larger the attainable velocity for a given $M_r$. Furthermore, this can be extrapolated to postulate that, for a given $a_\circ$, $p_\circ$, $m_p$, a constant diameter gun system that has an effectively infinite chamber length will also have an effectively infinitely long chamber if chambrage is added to the system. This is important because it will allow for the estimation of a chambered gun by knowing the projectile velocity of the corresponding SWPPIG gun.

It has been shown in [1] that the relation between the escape velocity of a chambered gun and the chambrage of that gun is given as:

$$\frac{A_\circ}{A_p} = \frac{d_\circ^2}{d_p^2} = \left[\frac{\upsilon}{1-\sqrt{\left(\frac{\gamma-1}{2}\right)\left(\upsilon^2-1\right)}}\right]^{\frac{2}{\gamma-1}} \left[\frac{\upsilon}{1-\frac{2}{\gamma-1}\sqrt{\left(\frac{\gamma-1}{2}\right)\left(\upsilon^2-1\right)}}\right] \tag{2.47}$$

where

$$\upsilon \equiv \frac{\gamma - 1}{2} \frac{u_{esc}}{a_\circ} \tag{2.48}$$

This approaches the value of $u_{esc}$ for a constant diameter PPIG in the limit of $A_\circ / A_p \rightarrow 1$ that was derived in Appendix B. For this investigation the velocities that pertain to a constant diameter PPIG gun are taken as the reference velocities. Therefore the escape velocity for a constant diameter PPIG is presented here as

$$u_{esc(ref)} = \frac{2a_\circ}{\gamma - 1} \tag{2.49}$$

If equation 2.49 is normalized by $a_\circ$ then the effect that the specific heat ratio $\gamma$ has on the escape velocity can be explored. This has been plotted in figure 2–33. It can be seen that $u_{esc(ref)} \rightarrow \infty$ as $\gamma \rightarrow 1$.

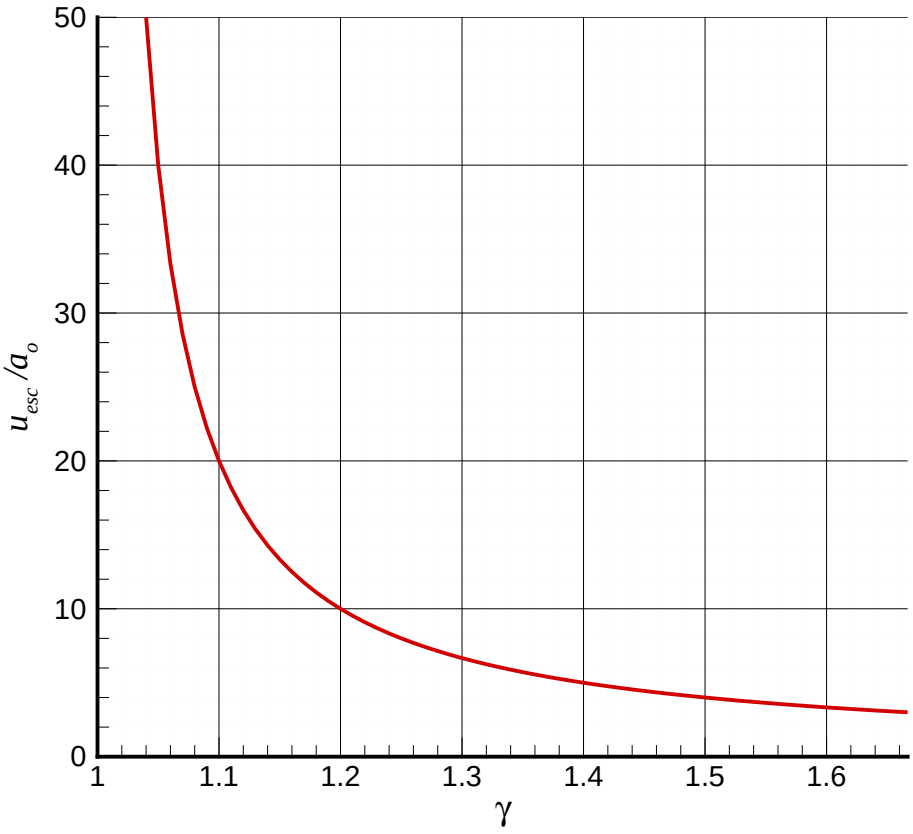


Figure 2–33: $u_{esc(ref)}/a_\circ$ vs. $\gamma$

It has been shown from equation 2.47 that as $d_\circ/d_p \to \infty$, the escape velocity approaches [1]

$$u_{esc(\infty)} = \sqrt{\frac{\gamma+1}{2}}\frac{2a_\circ}{\gamma-1} \tag{2.50}$$

Normalizing this equation with equation 2.49, the percent increase in the escape velocity that is gained from infinite chambrage can be determined as a function of $\gamma$. This takes the form

$$\%\text{ increase} = 100\left(1-\sqrt{\frac{\gamma+1}{2}}\right) \tag{2.51}$$

This has been plotted in figure 2–34. It can be seen that as $\gamma \to 1$ that there is very little gain in the escape velocity for a chambered gun. However, in order to see

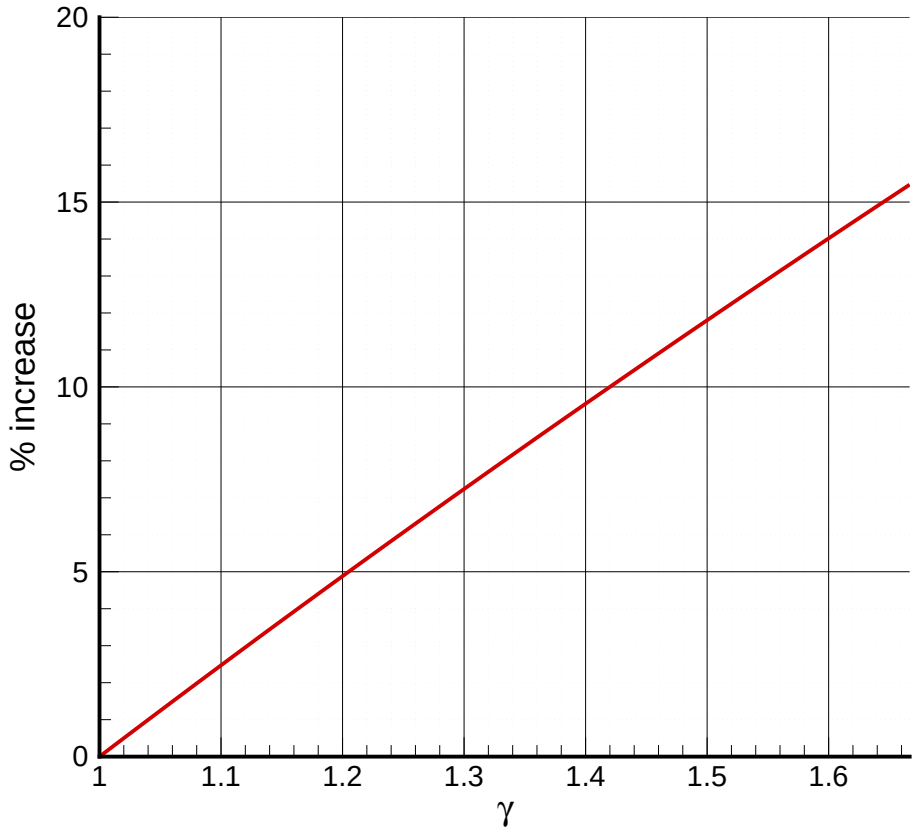


Figure 2–34: The percent increase between $u_{esc(ref)}$ and $u_{esc(\infty)}$ vs. $\gamma$

how chambrage effects chambered guns between $d_\circ/d_p = 1$ and $d_\circ/d_p = \infty$ further analysis must be done. To start, the difference in the escape velocity for infinite chambrage and the escape velocity for no chambrage, taken as the reference escape velocity $u_{esc(ref)}$, becomes

$$\Delta u_{esc(\infty)} = u_{esc(\infty)} - u_{esc(ref)} = \sqrt{\frac{\gamma+1}{2}}\frac{2a_\circ}{\gamma-1} - \frac{2a_\circ}{\gamma-1} = \left(\sqrt{\frac{\gamma+1}{2}} - 1\right)\frac{2a_\circ}{\gamma-1} \tag{2.52}$$

which approaches $\frac{1}{2}a_\circ$ as $\gamma \to 1$

Furthermore, it has been shown by [1] that the escape velocities for a given $d_\circ/d_p$ takes the form

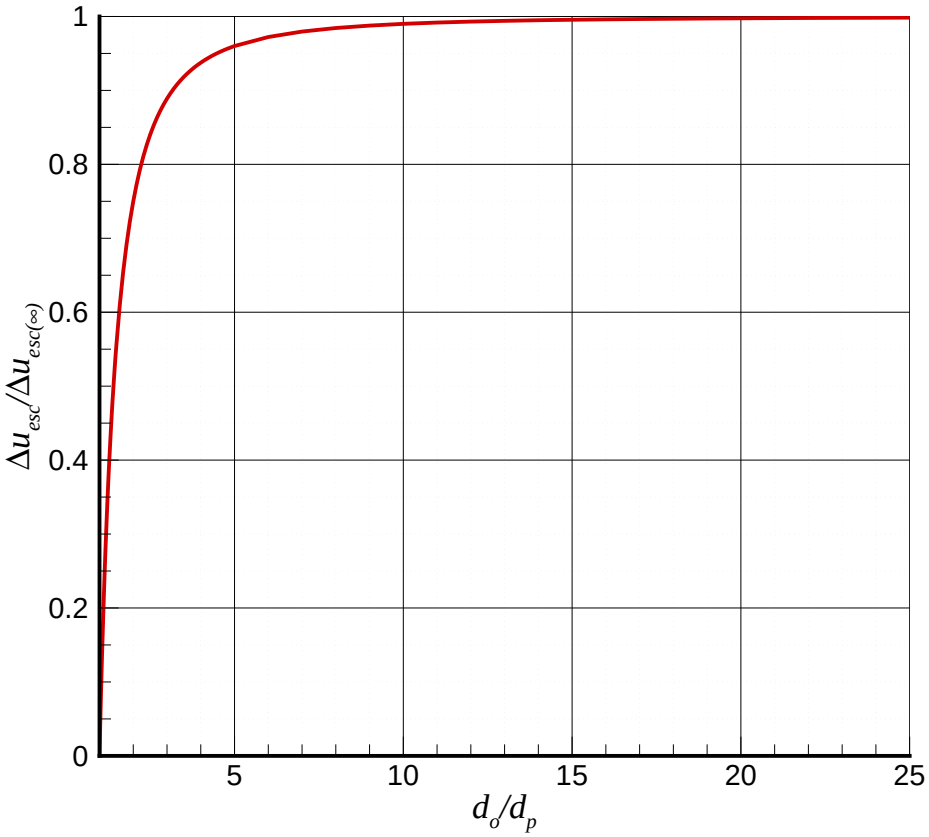


Figure 2–35: $\Delta u_{esc}/\Delta u_{esc(\infty)}$ vs. $d_\circ/d_p$

$$\Delta u_{esc} \cong \Delta u_{esc(\infty)} \left(1 - \frac{d_p^2}{d_\circ^2}\right) \tag{2.53}$$

Equation 2.53 has been plotted in figure 2–35, it can be seen that a $d_\circ/d_p \cong 2.5$ results in $\Delta u_{esc} \cong 0.90 \Delta u_{esc(\infty)}$ and that by $d_\circ/d_p \cong 15$ a gun can be considered essentially to have infinite chambrage.

It has further been observed that the ratio between $\Delta u_p/\Delta u_{esc}$ will follow the trend

$$\Delta u_p/\Delta u_{esc} \cong \begin{cases} \frac{1}{3}\frac{\gamma u_{p(ref)}}{a_\circ} & \text{for} \quad 0 < \frac{\gamma u_{p(ref)}}{a_\circ} < 3 \\ 1 & \text{for} \quad \frac{\gamma u_{p(ref)}}{a_\circ} \geq 3 \end{cases} \tag{2.54}$$

Thus by using the solution for SWPPIG gun to determine $u_{p(ref)}$, equations 2.54, 2.53 and 2.50 can be used to estimate the velocity of a chambered PPIG with an effectively infinitely long breech. Using equation 2.53, equation 2.54 can take the form

$$\Delta u_p/\Delta u_{esc(\infty)} \cong \begin{cases} \frac{1}{3}\left(1 - \frac{d_p^2}{d_\circ^2}\right)\frac{\gamma u_{p(ref)}}{a_\circ} & \text{for} \quad 0 < \frac{\gamma u_{p(ref)}}{a_\circ} < 3 \\ \left(1 - \frac{d_p^2}{d_\circ^2}\right) & \text{for} \quad \frac{\gamma u_{p(ref)}}{a_\circ} \geq 3 \end{cases} \tag{2.55}$$

which can then be plotted for different values of $d_\circ/d_p$. This has been done and presented in figure 2–36. This figure can be used to aid in determining the effects of chambrage added to a SWPPIG.

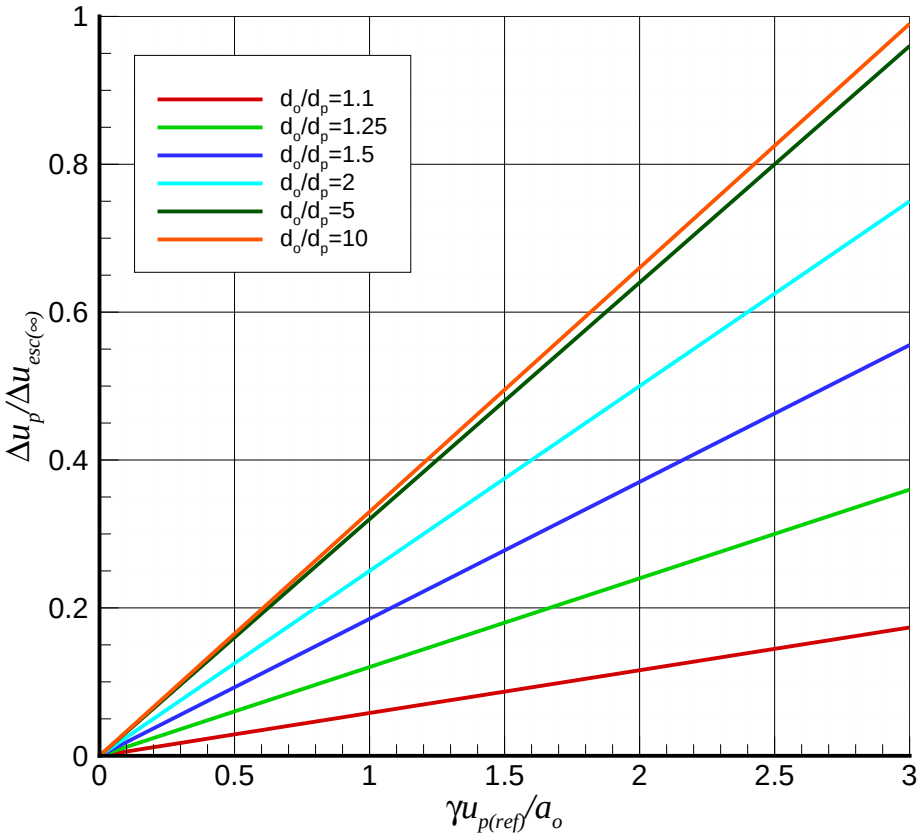


Figure 2–36: $\Delta u_p/\Delta u_{esc(\infty)}$ vs $\gamma u_{p(ref)}/a_\circ$ for various ratios of $d_\circ/d_p$

# CHAPTER 3
# Detonation Gun Prototype

The purpose of this project has been to ultimately build and test the concept of a detonation-driven gas gun. The following analysis utilizes the tools that have been developed in the previous chapter to design a working prototype. Furthermore, simulations have been done in order to predict the gun performance for the products of a stoichiometric hydrogen-oxygen detonation. Data for the products of the hydrogen-oxygen detonations are obtained by using the NASA's CEA equilibrium code [6]. This data is used as the input for the performance simulations which have been done using the code provided by Ponchaut [9]. This chapter presents the step by step design process in detail. Figure 3–1 presents a schematic of the gun system.

## 3.1 Gun Design

In order to keep the cost of the launcher down, readily available mechanical tubing was used in its construction. The reason for this is that the driver section needed to be long, and boring out a piece of rod stock to the diameter required would have added unwanted costs. The launcher was designed with the aid of the theory developed in chapter 2. The design specifications were for a gun with a projectile caliber of 1/2" (12.7 mm). Because the chamber section of the gun is going to experience detonation pressure, the wall must be as thick as possible. Furthermore,

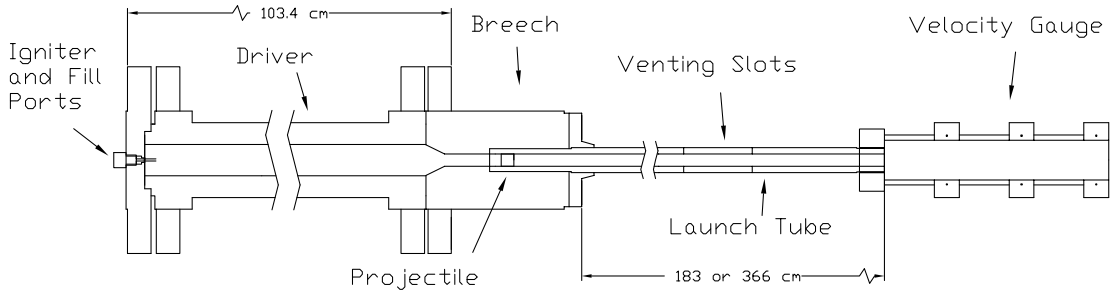


Figure 3–1: Launcher schematic

as seen previously, it is desirable to add chambrage to the gun. From figure 2–35 it can be seen that values of $d_\circ/d_p \geq 2$ provide a $\Delta u_{esc} \geq 0.75\Delta u_{esc(\infty)}$. The best suited mechanical tubing to be found for the driver has a 3" (76.2 mm) exterior diameter, $d_e$, by 1.25" (31.75 mm) inner diameter, $d_i$, and is approximately 40.75" (1.035 m) long. This tube has the wall thickness to inner diameter ratio of $T_r = 0.7$. The yield strength and ultimate strength of this steel are 350 MPa and 420 MPa (cold worked steel alloy 1020), respectively. From equation 2.32 from in chapter 2, the maximum pressure this section, to be referred to as the driver, can sustain without permanent deformation is 2464 bar. Using equation 2.36 from chapter 2 to determine the burst pressure, 4128 bar is obtained. With equation 2.33 from chapter 2, along with the density of the steel (7850 kg/m$^3$), the mass per unit length of the driver section was determined to be 29.6 kg/m. Thus the total mass of the section is approximately 30.6 kg.

The section where the projectile sits will experience the extremely high pressure of a reflected detonation wave; therefore, this section is required to have more strength than the rest of the chamber. Though not true to the definition of breech, this part of the gun will be referred to as the breech through-out this work. The breech has been machined from 4" (101.6 mm) diameter mild steel rod stock to the gun caliber, 1/2" (12.7 mm). This has a thickness to inner diameter ratio of $T_r = 3.5$ which corresponds to a yield pressure of 3392 bar. Furthermore, the burst pressure of this section is determined to be 9805 bar. Due to the thickness of the walls and the relatively small ID, this section has approximately double the mass per unit length, at 62.6 kg/m, than the driver. At 6" (152.4 mm) of length the breech weighs approximately 9.5 kg. It is important that this section does not weigh too much because it must be easy to manually manoeuvre during a gun operation cycle.

Finally, the best choice of barrel material to be found was a 1" (25.4 mm) outer diameter by 1/2" (12.7 mm) inner diameter tube made from a chrome-moly steel (alloy 4130) with yield and ultimate strengths of 435 MPa and 670 MPa, respectively.

This has a thickness to weight ratio of $T_r = 0.5$ which was deemed enough since most of its length will experience pressure far below its failure pressure. The yield and burst pressures were calculated to be 2610 bar and 4703 bar, respectively. The mass per unit length of the barrel was calculated as 2.98 kg/m, implying that it weighs approximately 5.4 kg per 6' (182.88 m) length.

It was found during the operation of the launcher that on high initial pressure experiments, swelling of the barrel occurred where the detonation reflects off the projectile. This was compounded by the ablation of barrel material by the hot detonation products expanding down the barrel behind the projectile. This was predicted but was more severe than expected, see figure 3–2, therefore the breech was expanded to allow for a hardened steel barrel extension of 1.75" OD and 0.5" ID designed to absorb the high pressure of the reflected detonation. The purpose of the hardening was not only to provide strength, but to also add brittleness and allow the piece to crack if it fails, and not ruin the entire breech at the same time. This piece has a thickness to inner diameter ratio of $T_r = 1.25$ and the material used is 4140 alloy steel. Being conservative and not taking into account the added strength from the heat treatment process the yield, and ultimate strength are taken to be 417 MPa and 590 MPa, respectively. This gives the barrel extension an approximate yield pressure

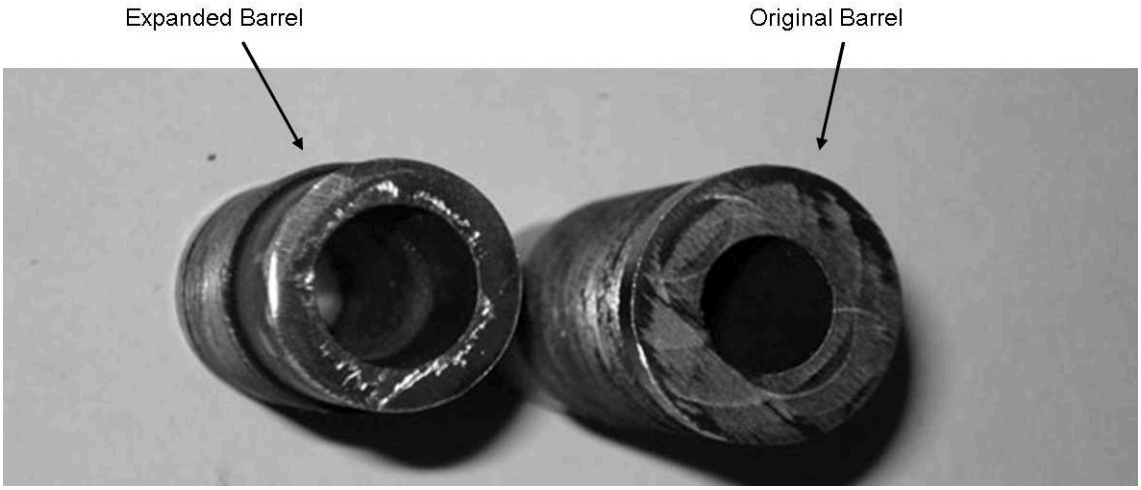


Figure 3–2: Before and after of a barrel expanded by multiple high pressure gun cycles

of 3540 bar and a burst pressure of approximately 7801 bar.

Table 3–1: Failure Characteristics of the Gun Parts

| Gun Part | $\sigma_y$ [MPa] | $\sigma_u$ [MPa] | $T_r$ | $p_{max}$ [bar] | $p_{burst}$ [bar] |
|---|---|---|---|---|---|
| Driver | 350 | 420 | 0.7 | 2464 | 4128 |
| Breech | 350 | 420 | 3.5 | 3392 | 9805 |
| Barrel | 435 | 670 | 0.5 | 2610 | 4703 |
| Barrel Extension | 417 | 590 | 1.25 | 3540 | 7801 |

Table 3–2: Mass/Length Ratio of the Gun Parts

| Gun Section | $\rho$ [kg/m$^3$] | $d_i$ [cm] | $T_r$ | $m/l$ [kg/m] |
|---|---|---|---|---|
| Driver | 7850 | 3.175 | 0.7 | 29.6 |
| Breech | 7850 | 1.27 | 3.5 | 62.6 |
| Barrel | 7850 | 1.27 | 0.5 | 2.98 |
| Barrel Extension | 7850 | 1.27 | 1.25 | 11.2 |

These values have been summarized in tables 3–1 and 3–2. They will be referred to later in this chapter to aid in the estimation of the gun performance. This gun is constructed by having flanges welded to all the tubing in order for all the pieces to be assembled together. Appendix E provides a complete set of part drawings for the gun system.

## 3.2 Propellant Modeling

Before undertaking the design and construction of a detonation driven gas launcher, it is important to identify an optimal propellant. In order to obtain an approximation for the performance of the launcher, the assumption is made that the detonation product reaches equilibrium (i.e constant volume conditions) before allowing the projectile to accelerate (as per Seigel's pre-burned propellant ideal gas gun PPIG gun [1]). In the previous chapter, a detailed analysis of the properties of different gases at different temperatures was done. From this it was seen that steam, as a product of chemical reaction, has good performance characteristics as compared

to another product often associated with combustion, $CO_2$. Therefore hydrogen-oxygen systems are the propellant systems of most interest to be investigated for this prototype. Tables 3–3 through 3–5 show the properties for the detonation products at the CV state, along with the CJ detonation pressures and the pressures of the reflected wave, which are the peak pressures on the system [6].

Table 3–3: Constant Volume (CV) explosion states for various initial pressures of the $2H_2+O_2$ reaction

| $p_\circ$ [atm] | $\rho_{CV}$ [kg/m$^3$] | $p_{CV}$ [bar] | $T_{CV}$ [K] | $a_{CV}$ [m/s] | $\gamma_{CV}$ |
|---|---|---|---|---|---|
| 10 | 4.9115 | 104.88 | 3914.30 | 1557.2 | 1.1355 |
| 25 | 12.279 | 269.61 | 4089.96 | 1582.0 | 1.1398 |
| 50 | 24.557 | 550.00 | 4222.00 | 1599.8 | 1.1427 |
| 75 | 36.836 | 834.18 | 4300.58 | 1609.7 | 1.1442 |
| 100 | 49.110 | 1120.56 | 4355.00 | 1616.5 | 1.1452 |

Table 3–4: Chapman-Jouquet (CJ) detonation states for various initial pressures of the $2H_2+O_2$ reaction

| $p_\circ$ [atm] | $\rho_{CJ}$ [kg/m$^3$] | $p_{CJ}$ [bar] | $T_{CJ}$ [K] | $a_{CJ}$ [m/s] | $\gamma_{CJ}$ |
|---|---|---|---|---|---|
| 10 | 9.0049 | 205.68 | 4138.86 | 1614.1 | 1.1407 |
| 25 | 22.490 | 528.96 | 4334.25 | 1640.9 | 1.1448 |
| 50 | 44.954 | 1079.41 | 4483.77 | 1659.9 | 1.1474 |
| 75 | 67.412 | 1637.29 | 4571.15 | 1670.4 | 1.1488 |
| 100 | 89.868 | 2199.76 | 4632.84 | 1677.5 | 1.1496 |

Table 3–5: Reflected Chapman-Jouquet (RCJ) detonation states for various initial pressures of the $2H_2+O_2$ reaction

| $p_\circ$ [atm] | $\rho_{RCJ}$ [kg/m$^3$] | $p_{RCJ}$ [bar] | $T_{RCJ}$ [K] | $a_{RCJ}$ [m/s] | $\gamma_{RCJ}$ |
|---|---|---|---|---|---|
| 10 | 19.612 | 507.02 | 4684.54 | 1717.27 | 1.1407 |
| 25 | 48.862 | 1304.90 | 4921.42 | 1748.52 | 1.1448 |
| 50 | 97.522 | 2664.29 | 5101.56 | 1770.50 | 1.1474 |
| 75 | 146.14 | 4042.86 | 5206.75 | 1782.71 | 1.1488 |
| 100 | 194.74 | 5432.86 | 5280.34 | 1790.86 | 1.1496 |

Even though it is assumed that the CV conditions drive the projectile, the CJ and RCJ conditions are used to determine the maximum operating pressure of

the gun system. The CJ pressure is used to determine what maximum pressure is sustainable by the gun parts. Even though this pressure acts in very short pulse, as a precaution, it is used to determine the maximum safe operating pressure for the gun. The RCJ pressure is used to determine the best projectile material that should be used for the gun. It can be seen that there are three characteristic pressures for this system. By cross-referencing tables 3–3 to 3–5 with table 3–1 it can be seen that, if the projectile is made from aluminium alloy 7075-T6 ($\sigma_u = 572$ MPa), 100 atm initial fill pressure can be considered the maximum safe pre-detonation pressure. Thus the actual driving pressure is approximately 4.8 times lower than the actual design maximum pressure for the projectile and approximately half the maximum design pressure for the gun system. This is the major drawback of using a detonation to energize the propellant gas because of the lower than optimal driving pressure. However, this must be weighed against the simplicity of the concept.

Now that the system has been defined, an estimation of the gun performance can be made by using the theory developed in the previous section. If the projectile mass is to be approximately 3.2 grams made from aluminum alloy 7075-T6, then the effective projectile length is 0.902 cm and the $A_r = 0.71$. Thus using the reflected detonation pressure at 100 atm pre-detonation pressure to determine the maximum performance of the gun, the $S_r$ is the CV pressure at this fill pressure divided by the density of the 7075-T6. This gives an $S_r = 40.02$ kPa m$^3$/kg. Therefore the mechanical factor for this projectile gun system is $M_f = 56.37$ kPa m$^3$/kg. This will be used to predict the performance of the gun system for the pre-detonation pressures shown in tables 3–3 to 3–5. However, the pressure ratio $P_r$ has yet to be determined for these fill pressures. Using the CV pressure at 100 atm initial pressure as the reference pressure, the $P_r$'s are given in table 3–6.

Using the initial sound speeds and $\gamma$'s in table 3–3 along with the corresponding pressure ratios in table 3–6 and the mechanical factor determined for the gun system,

Table 3–6: Pressure ratio $P_r = p_\circ/(p_\circ)_{max}$ for various initial pressures of the $2H_2+O_2$ reaction

| $p_\circ$ [atm] | $p_{CV}$ [bar] | $P_r$ |
|---|---|---|
| 10 | 104.88 | 0.0936 |
| 25 | 269.61 | 0.2406 |
| 50 | 550.00 | 0.4908 |
| 75 | 834.18 | 0.7444 |
| 100 | 1120.56 | 1.000 |

performance predictions can be made. Recalling that the performance characteristics for the SWPPIG gun must be determined before the effects of chambrage can be estimated. First, the location of the first reflected rarefaction interacting with the projectile must be determined. This can be determined by using equation 2.26 from chapter 2 and realizing that the $\zeta_\circ$ for this system is 40.75"/0.5"=81.5. Table 3–7 gives the location of the first reflected wave interaction for each of the fill pressures of interest.

Table 3–7: $\zeta_{1^{st}}$ and $x_{1^{st}}$ for various initial pressures of the $2H_2+O_2$ reaction

| $p_\circ$ [atm] | $\zeta_{1^{st}}$ | $x_{1^{st}}$ [m] |
|---|---|---|
| 10 | 30.42 | 0.386 |
| 25 | 80.75 | 1.026 |
| 50 | 175.16 | 2.225 |
| 75 | 280.26 | 3.559 |
| 100 | 393.97 | 5.003 |

It can be seen that at pre-detonation pressures above 50 atm the prototype gun, firing a 3.2 g projectile, should operate in the regime where the first reflected wave does not reach the projectile if the barrel is 6' (1.8288 m). Therefore, in this range the methods developed in chapter 2 can be used to give a good approximation of the performance of the gun. However, at the lower pressures this is not the case. The results of the SWPPIG gun calculations for velocity along with the add velocity due to chambrage are presented in table 3–8.

Table 3–8: $u_{p(ref)}$ and $u_p$ for various initial pressures of the $2H_2+O_2$ reaction

| $p_\circ$ [atm] | $u_{p(ref)}$ [m/s] | $u_p$ [m/s] | % diff. |
|---|---|---|---|
| 10 | 964.6 | 1115.4 | 15.64 |
| 25 | 1385.8 | 1603.2 | 15.69 |
| 50 | 1781.0 | 2061.0 | 15.72 |
| 75 | 2042.3 | 2363.8 | 15.74 |
| 100 | 2240.5 | 2593.5 | 15.75 |

It can be seen that the addition of chambrage for this case should give approximately a 15% improvement over a constant diameter PPIG gun at the same initial pressure. Furthermore, the maximum achievable velocity for this gun system firing a 3.2 gram projectile is approximately 2600 m/s for a 6 foot barrel. However, this is an ideal calculation and ignores losses; therefore, it should be expected that actual results will be lower than the values in table 3–8. To follow will be a more accurate approach to calculate muzzle velocity for this gun system.

### 3.3 Performance Modeling

Using the results from CEA, calculations were made with a CFD code provided by [9]. The code is a quasi-one-dimensional Eulerian solver that implements the SLIC scheme (Slope Limiter Centered) and is capable of handling smooth changes in area. The code is initialized by inputting the geometric parameters of the launcher (the cross-sectional area of driver and launch tube, a function modeling the area change, and the mass of projectile) and the properties of the propellant (initial pressure, density and $\gamma$ for a CV explosion). The pressure upstream of the projectile is also an input and is set to vacuum for these calculations. The inputs for the geometry of the driver section are fixed at 3.175 cm ID and 103.45 cm length, while the barrel ID is 1.27 cm. The area change is set to converge linearly over an angle of 42° with respect to the centerline of the driver.

These simulations were done for the range of pre-detonation pressures from 10 atm to 100 atm and the masses 2.5 g, 2.7 g, 2.9 g, 3.1 g, 3.3 g. The results are displayed in the form of $x - t$ and $x - u_p$ diagrams for a specific pre-detonation

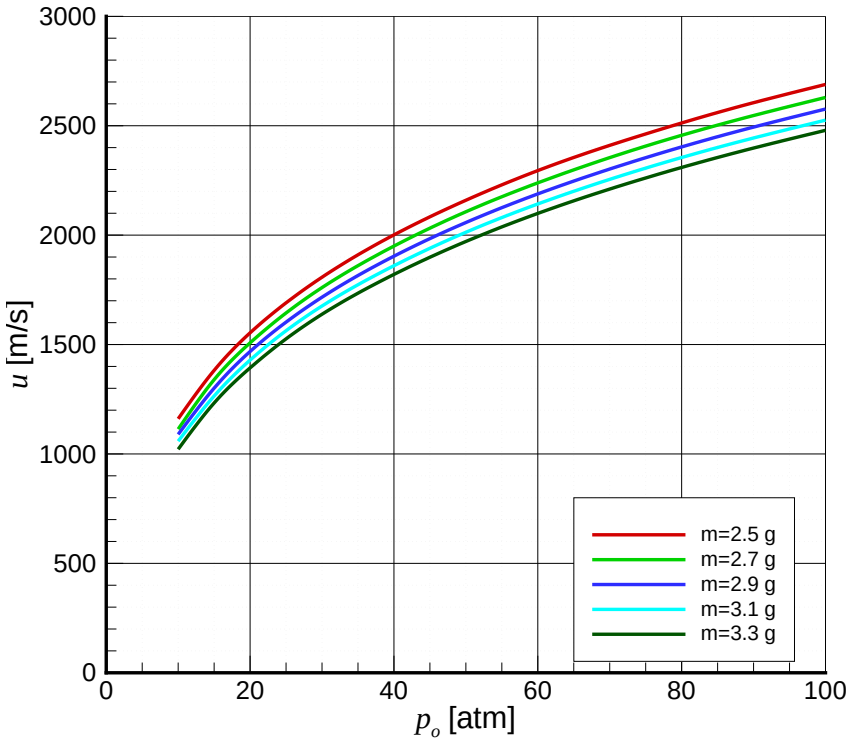


Figure 3–3: Muzzle velocity vs. pre-detonation pressure for a 6 foot barrel ($\zeta = 288$)

pressure in appendix F. Furthermore, each graph displays a curve for each of the masses investigated. Finally figure 3–3 shows the velocity as a function of pressure for a 6 foot barrel ($\zeta = 144$) and figure 3–4 shows the same function for a 12 foot barrel ($\zeta = 288$). It can be seen that there is a large predicted improvement for using the larger barrel length. However, it will be seen from the results that the predictions in [1] hold true and that the improvement at these barrel lengths is negligible due to losses.

Table 3–9: Comparison between analytical and computational methods for determining $u_p$ for various initial pressures of the $2H_2+O_2$ reaction

| $p_\circ$ [atm] | $u_p$ [m/s] Analytical | $u_p$ [m/s] Computational | % diff. |
|---|---|---|---|
| 10 | 1115.4 | 1038.8 | 6.87 |
| 25 | 1603.2 | 1546.9 | 3.51 |
| 50 | 2061.0 | 1994.9 | 3.21 |
| 75 | 2363.8 | 2287.1 | 3.24 |
| 100 | 2593.5 | 2506.0 | 3.37 |

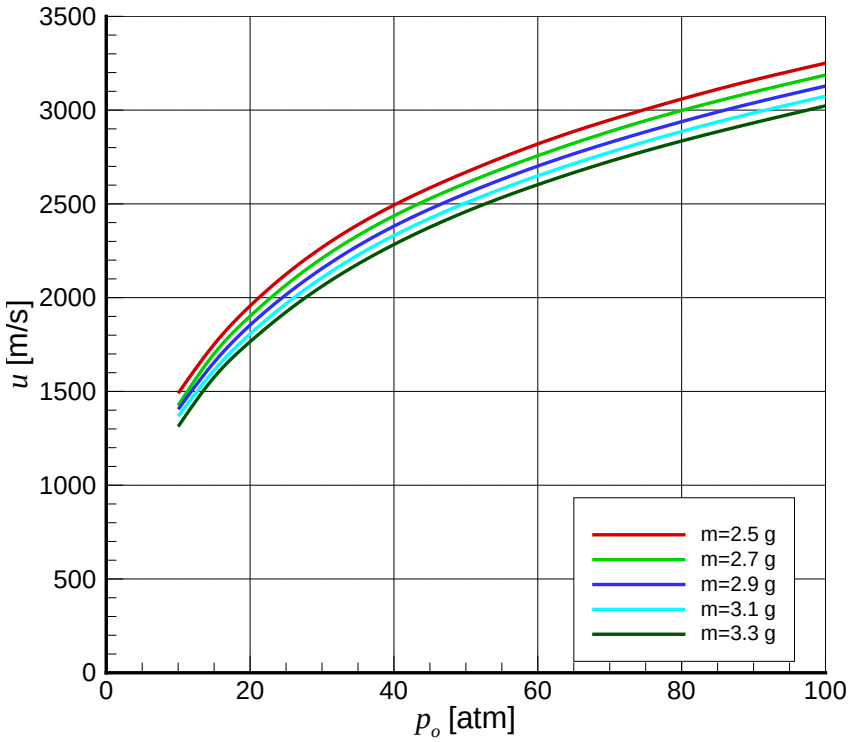


Figure 3–4: Muzzle velocity vs. pre-detonation pressure for a 12 foot barrel ($\zeta = 288$)

A comparison of the results obtained by the Euler code with those in table 3–8 are presented in table 3–9. It can be seen that the results for computational and analytical methods were quite close, and the larger discrepancies at 10 atm pre-detonation pressure were expected because it was determined that at this pressure, the first refection has reached the projectile a fair distance before it exits the barrel. Table 3–9 shows that the analytical method gives a good estimate of velocity for the chambered gun, as long as the corresponding SWPPIG can be considered infinitely long. This is an important result, because the difference in computational time between the methods is quite significant; on the order of a second for the analytical method and on the order of tens of minutes for the computational method. This is a 3 orders of magnitude difference in computational time.

# CHAPTER 4
# Experiment and Results

Experiments were undertaken in order to verify the results obtained from modelling. Initially these experiments used a 6' (183 cm) long barrel; however, it was observed that at overly high initial fill pressures the projectile itself can break. Hence it was postulated that increasing the length of the launch tube could be the most efficient way of increasing projectile velocity as predicted by the performance calculations. However, the barrels of 12' (366 cm) length that were tested proved to be disappointing as a result of losses. Further investigations were done to determine the effects of ignition location. In order to avoid a reflected detonation on the projectile, igniting the mixture from the breech end with the detonation traveling back towards the back flange was tested. A wide range of projectile materials and geometries were also tested in order to determine how to optimize performance. The highest velocity obtained for this gun prototype was 2700 m/s using a 2.5 gram aluminium alloy 7075-T6 projectile with the 12' barrel and an initial fill pressure of 100 atm. The complete set of experimental information is tabulated in appendices H through J.

## 4.1 Diagnostics

Initially, the velocity measurement system used was an array of shock pins designed to pick up the projectiles bow shock. The drawback of this system was that it would not allow for evacuation of the barrel since it requires a gaseous medium to work. Furthermore, even though this system worked well for Szirti in [5], the lower velocities inherent to this gun system cause the projectile to be unresolved in the noise from the expanding propellant gases. Therefore this system was discarded after shot 6. The signal for shot 6 is displayed in figure 4–1.

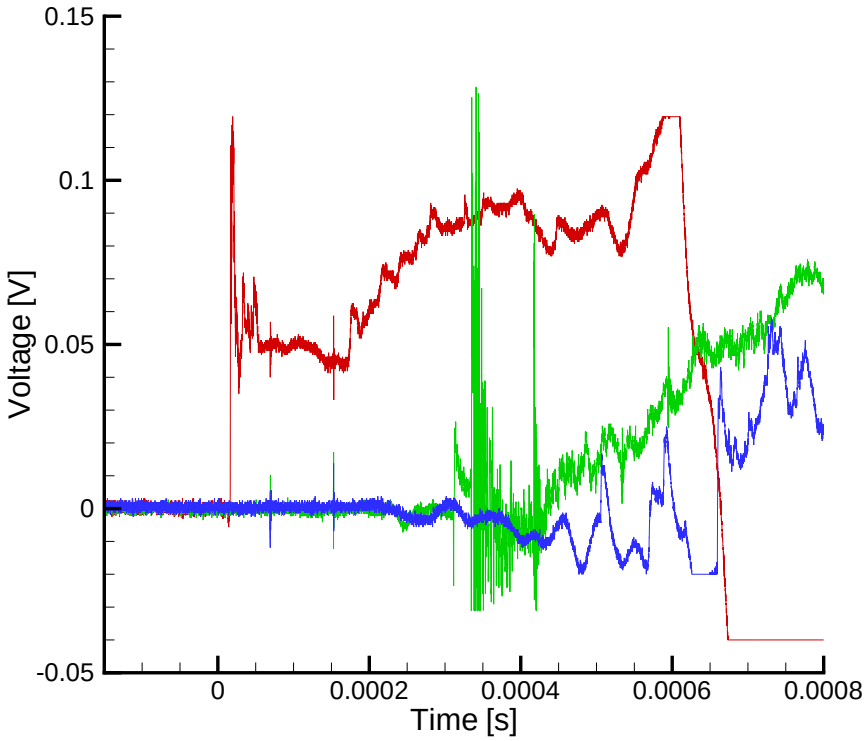


Figure 4–1: Signal from shock pin array

It was decided to use a system based on the concept developed by Bogdanoff et al. in [2]. This concept is based on Faraday's law. By placing a magnet on board the projectile and having this projectile pass through a coil of wire results in a change in the magnetic field, which causes an electromotive force to be induced in the coil [13]. This is a result of conservation of energy. The current is induced in order to maintain the initial magnetic field before the introduction of the external magnetic field to the coil system (this is Lenz's Law [13]).

Faraday's Law is expressed as

$$\varepsilon = -N\frac{\mathrm{d}}{\mathrm{d}t}\left(\int \overrightarrow{B}\cdot \mathrm{d}A\right) = -N\frac{\mathrm{d}}{\mathrm{d}t}(BA\cos\theta) \tag{4.1}$$

Where $\varepsilon$ is the electromotive force (emf) and is measured in Volts (V), N is the number of coils, $B$ is the magnetic field, $A$ is the area encircled by the coils and $\theta$ is the angle between the magnetic field vector and the normal vector to the area. It can be seen that Faraday's law states that the emf is proportional to the rate of

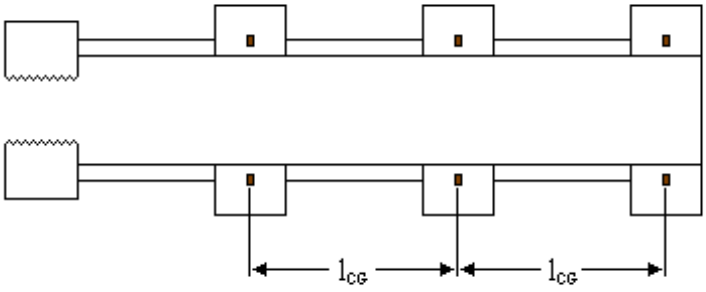


Figure 4–2: Schematic of coil gauge concept 1

change of the magnetic flux $\int \overrightarrow{B} \cdot \mathrm{d}A$ through the coil. From equation 4.1 it can be seen that an emf can be induced through the following processes [13]:

-The magnitude of $\overrightarrow{B}$ changes with time;
-The area enclosed by the coil, $A$, changes with time;
-The angle, $\theta$, between the magnetic field , $\overrightarrow{B}$, and the normal vector of the coil changes with time.

Two coil gauge concepts were built and tested for this project. The first involves a series of coil rings through which the projectile passes after it leaves the barrel.

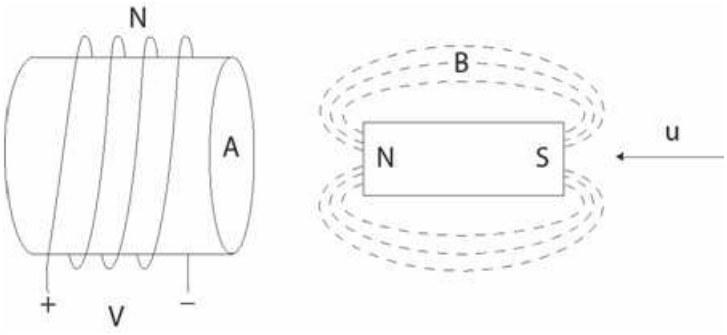


Figure 4–3: Magnet passing through the coil gauge, coil gauge concept 1

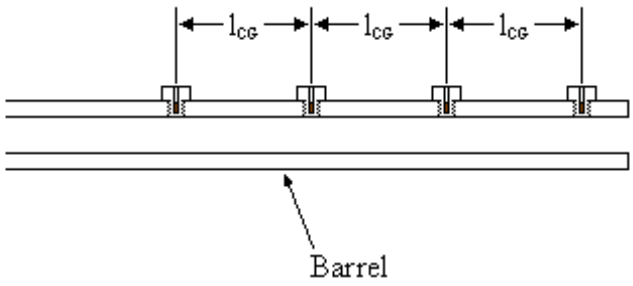


Figure 4–4: Schematic of coil gauge concept 2

This concept is displayed in figure 4–2 and figure 4–3. Furthermore, this concept was tested using helium gas as a propellant and these detail are included in appendix G. The second concept involves a probe being inserted directly into the barrel with the normal vector of the coil perpendicular to the projectiles flight path. This is presented in figures 4–4 and 4–5. As the magnetic field of the projectile interacts with the coil, an emf is induced as implied by equation 4.1. If these coils are set a specified distance apart, then velocity can be inferred by the times measured between these signals. The distance between the coils is represented by $l_{CG}$ in figures 4–2 and 4–4.

The advantage of the first coil gauge concept is that the poles of the magnet are in line with the normal of the coil. Furthermore, the projectile passes through

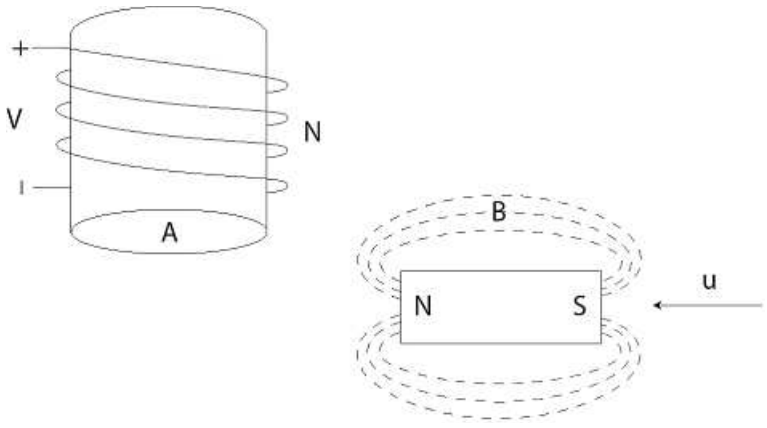


Figure 4–5: Magnet passing perpendicular to coil gauge, coil gauge concept 1

the coil, which allows for the largest possible signal to be produced. For the second coil gauge system, the pole of the magnet is perpendicular to the normal of the coil and therefore, from equation 4.1, a smaller signal is expected. However, the second system has the benefit of taking up less space in the apparatus and it is much easier to exchange one of the probes than it is to disassemble and fix one of the rings in the first concept.

Figure 4–6 is a sample signal from the first concept and figure 4–7 is a sample signal from the second concept. It can be seen that the signal is 2 magnitudes larger for the first concept when compared to the second concept. Furthermore, in the second concept, the signal can become lost in the noise due to the small magnitude as can be seen in figure 4–8. As a result, it was decided that the first concept was a better choice for this application.

This diagnostic also can aid in the verification of a projectile's survival during launch. Figure 4–9 shows a signal that is not as consistent as that in figure 4–6. On further investigation of the figure 4–9, it can be seen that the magnitude of the signal

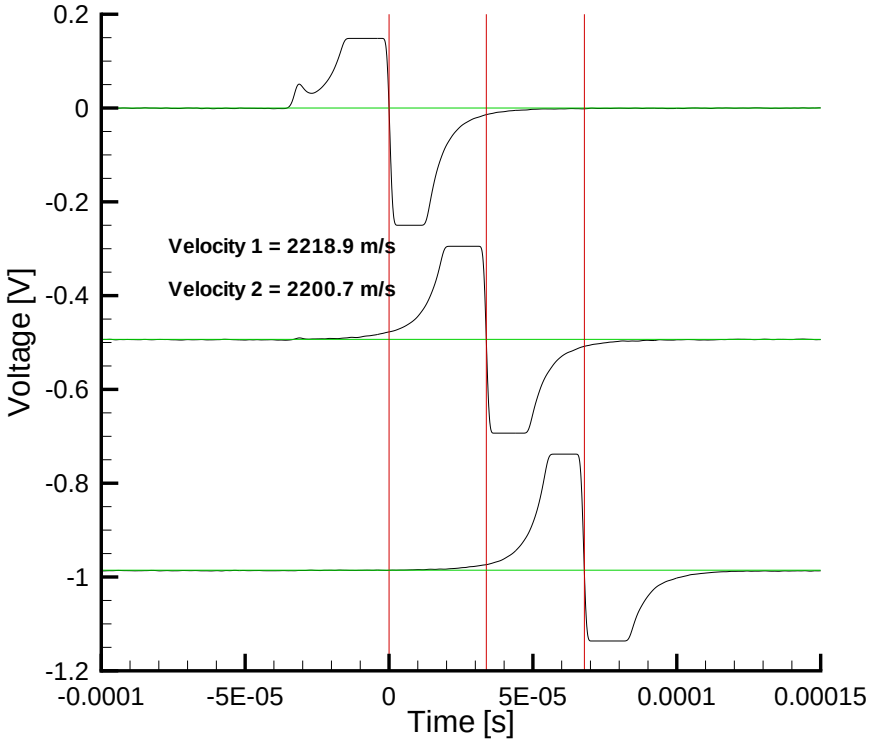


Figure 4–6: Signal from coil gauge concept 1

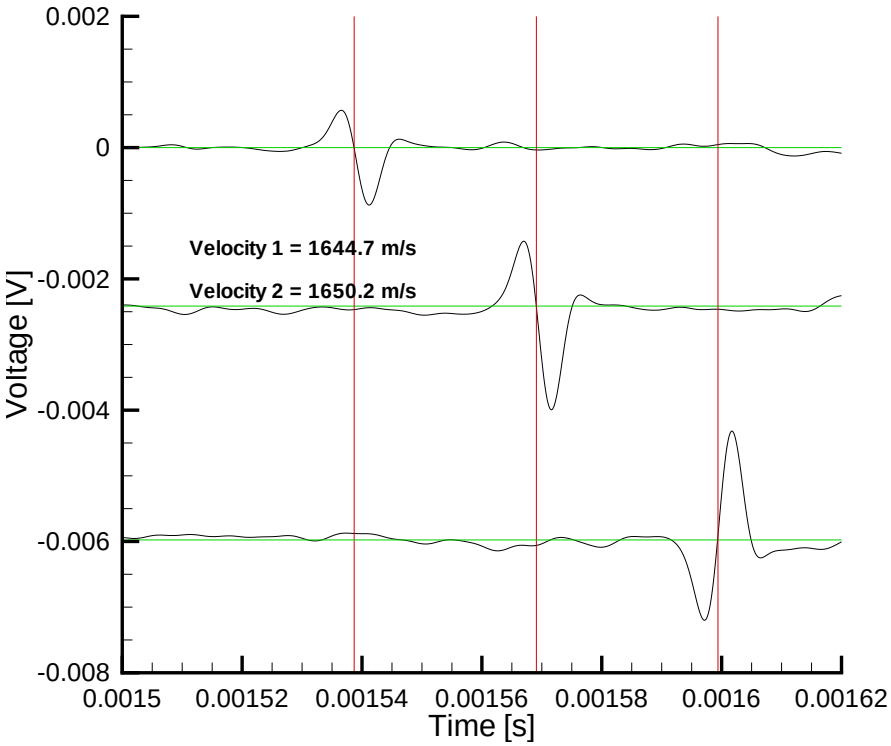


Figure 4–7: Signal from coil gauge concept 2

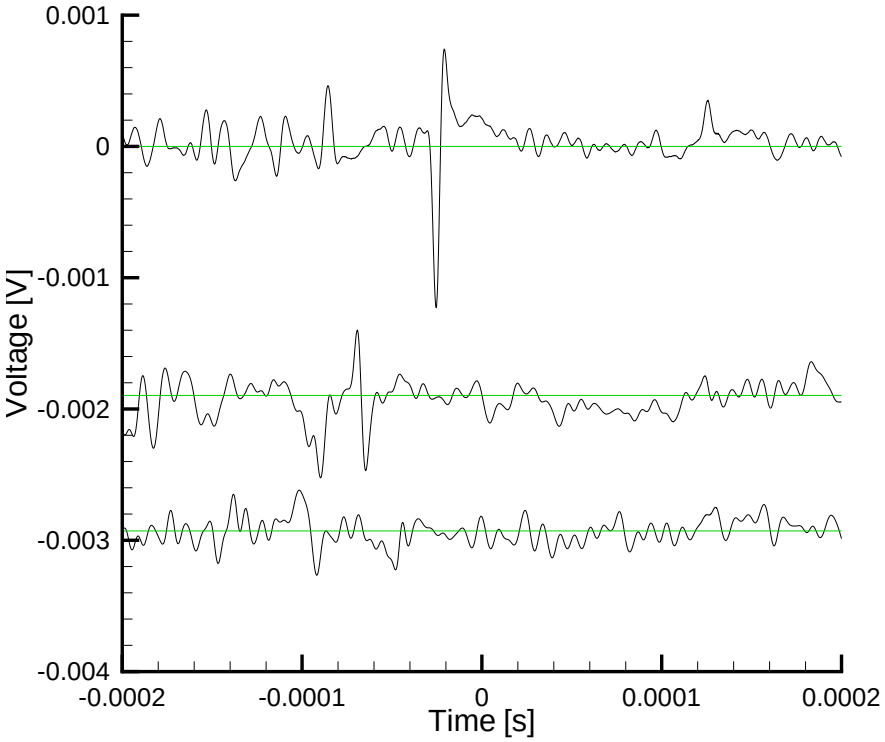


Figure 4–8: Signal lost in noise, coil gauge concept 2

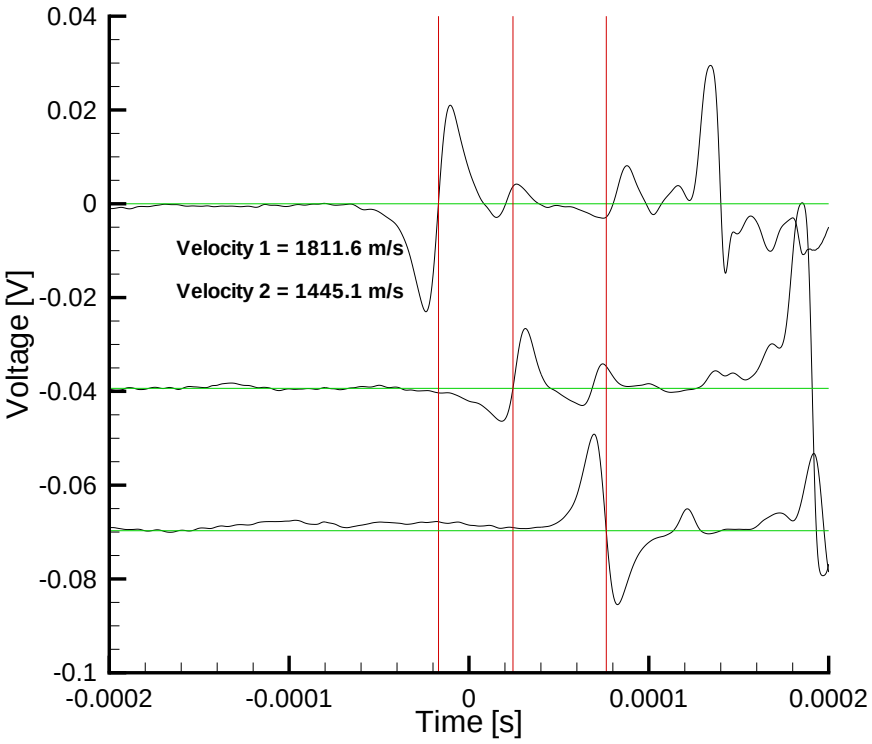


Figure 4–9: Signal from broken projectile, coil gauge concept 1

is changing from coil to coil, which is not evident in figure 4–6. Furthermore it can be seen that the polarity of the signal has changed from coil 2 to coil 3. This would indicate a tumbling magnet as it passes through the coil gauge. This is evidence of

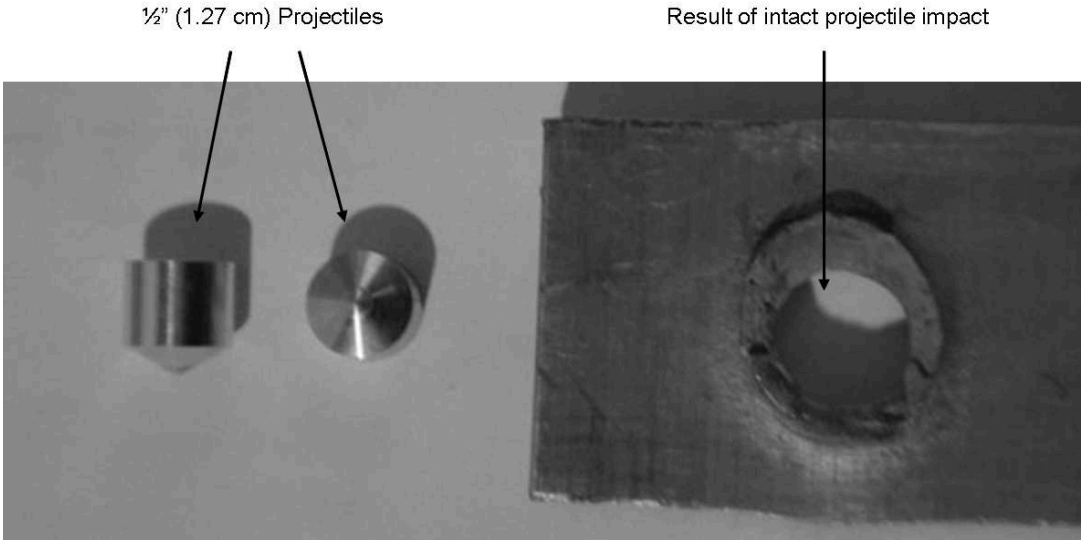


Figure 4–10: Witness plate indicating an intact projectile

a broken projectile, which is further supported by the loss of velocity between coils 2 and 3. If the projectile was just tumbling, the velocity should not drop as much over such a short distance (7.5 cm). Thus this system, along with the witness plate that catches the projectile, can be used to verify projectile integrity without the use of a high speed camera. Figure 4–10 shows the typical impact of an intact $\frac{1}{2}$" (1.27 cm) diameter projectile on a witness plate, whereas figure 4–11 shows the impact pattern of a fragmented projectile. However, to be certain of projectile integrity high speed photography is essential. For that reason, a large portion of the trials for this project were photographed using a HSFC Pro Image-Intensified camera with a COOKEScope strobe for a light source. This system was interconnected with the coil gauge velocity diagnostic in order to synchronise the triggering of the camera with the projectile exiting the muzzle of the barrel. This allows for accurate timing

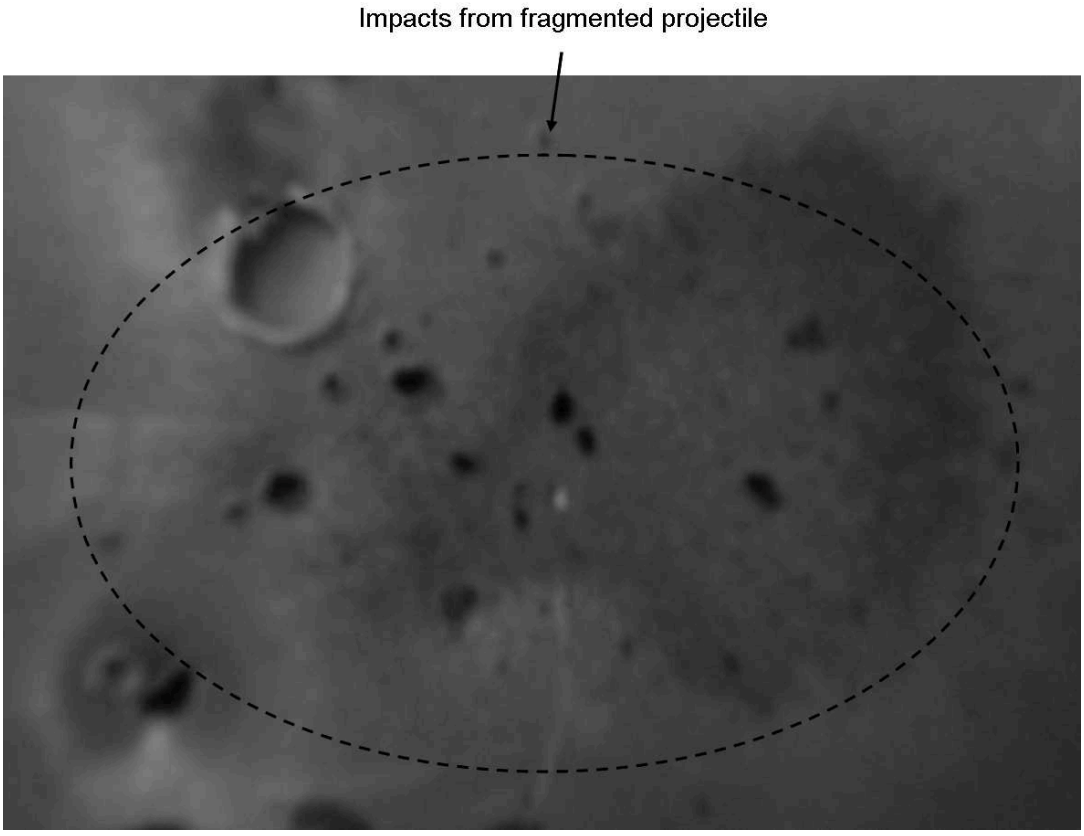


Figure 4–11: Witness plate indicating a fragmented projectile

for the camera, which is essential for still photography of an event that is measured in microseconds. Thus the events were measured and observed using a combination of the coil gauge and high speed photography. Figure 4–12 shows a typical image of an intact projectile in flight, whereas figure 4–13 shows an image of a projectile fragmented by the forces of the launch.

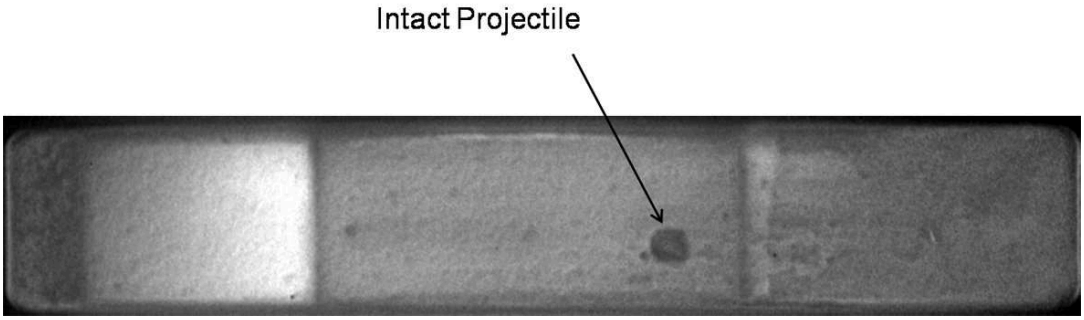


Figure 4–12: Image of an intact projectile

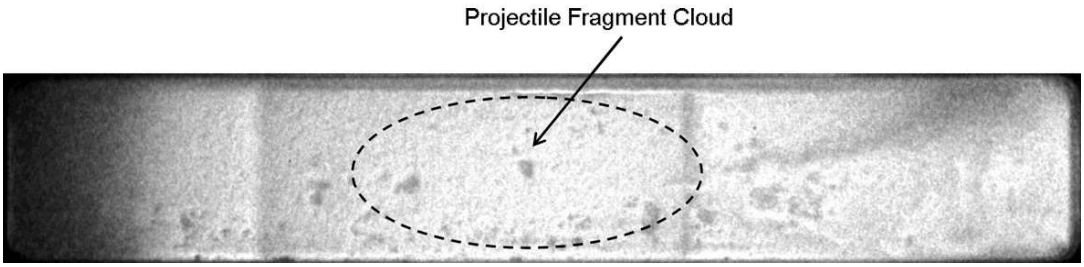


Figure 4–13: Image of a fragmented projectile

## 4.2 Projectiles

Through the course of these experiments, attempts were made to optimize the projectile performance. This was done by varying the geometry of the projectile as well as the material. Materials tested were Lexan (PC), aluminium, aluminium Alloy 7075-T6, and titanium. Due to the increased mass of the aluminium and titanium projectiles extra material was removed. There were 6 basic types of geometries tested. These are displayed in figure 4–14

Projectile Type 1 was used with the shock pin array velocity measuring system. Projectile Type 2 was the prototype projectile for the Coil Gauge concept. It uses a band of flexible magnet (ferrite bonded with synthetic rubber) around its circumference. Projectile Type 3 was a composite projectile with an aluminium disc screwed to a Lexan backing with a rare earth (Neodymium-Iron-Boron) magnet. Projectile Type 4 is a blunted projectile with the rare earth magnet inserted from the front. Projectile Type 5 is a conical projectile with the magnet inserted from the front. Projectile Type 6 is a conical projectile with the magnet inserted from the back.

There are three possible operations applied to these projectiles. The first is the addition of a Bridgman cup, the purpose of which is to prevent blow by of gases by expanding to create a seal between the projectile and the barrel. For the most part this was achieved by plunging a 1/2" ball mill to the required depth ($l_{BC}$), however, some projectiles used a 7/16" ball mill. The second procedure was applied to reduce mass. This involved creating a partial cone, as represented in figure 4–14 by the Type 4 projectile (though type 4 may be totally blunt). The final operation was also applied in order to reduce mass. This involved plunging a 3/8" ball mill in the back

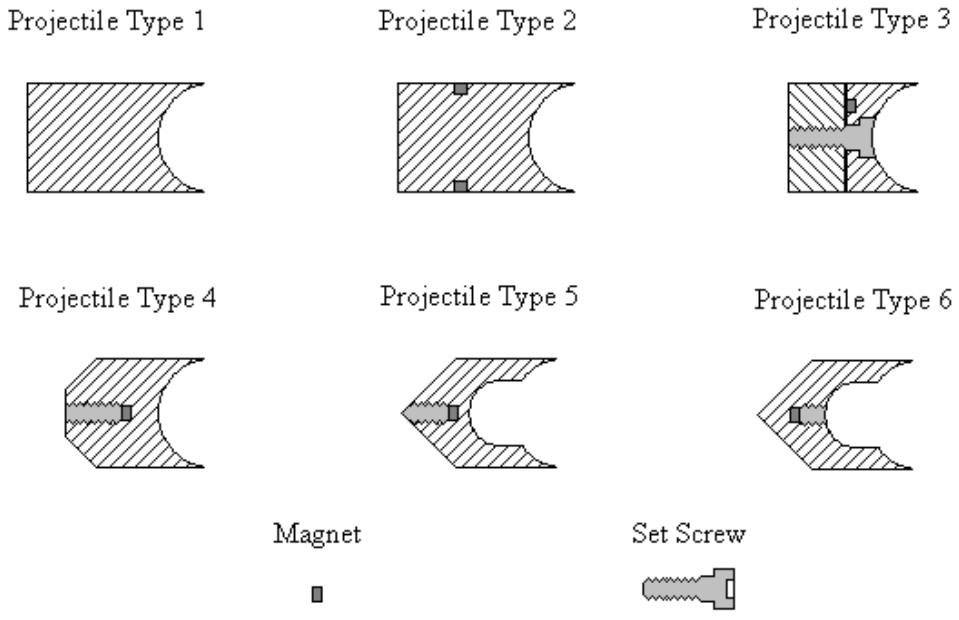


Figure 4–14: Projectile Geometries

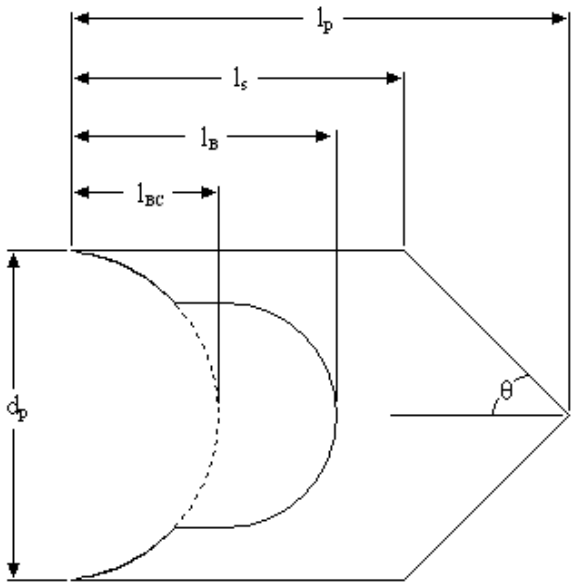


Figure 4–15: General representation of the projectile

of the projectile to the required depth ($l_B$). This is represented in figure 4–14 by both Type 5 and Type 6 projectiles. Figure 4–15 is a general representation of the projectile with $l_p$ as the total projectile length, $l_s$ as the projectile shoulder length, $l_{BC}$ as the depth of the Bridgeman cup, $l_B$ as the material removal bore depth and $\theta$ as the half angle of the cone (or partial cone for Type 4 projectiles). All the projectile data for each trial is tabulated in appendix H.

## 4.3 Experimental Details

The shot procedure involves inserting the diaphragm and pressure checking the gun system with helium. This is done without the projectile and barrel attached so that if the diaphragm was to break, then the projectile would not discharge, which would result in the loss of this projectile. The pressure check allows the system to be tested for leaks that would result in the detonable gas venting from the driver. Even though the gun system is contained within a safety chamber to protect the lab from this situation, it is still an important safety step and it adds certainty to the pre-detonation pressure. Once the check has been done the helium is vented.

Next the projectile is inserted in the barrel and held in place with a drop of cyanoacrylate glue. For most of the trials the projectile has a rare earth magnet inserted inside it as part of the diagnostic system. The exception to this were the first six trials that used a shock pin system to measure velocity and the first 4 experiments using the coil gauge velocity system. These trials used refrigerator magnets rings around the circumference of the projectile.

Once the projectile is inserted, the barrel is attached to the breech and then the entire system is sealed in the safety chamber. Once the safety chamber is sealed the gun filling procedure starts. For most trials the gun was filled with a stoichiometric mixture of hydrogen and oxygen. This was done by a partial pressure filling method where a slug of hydrogen is first injected to pressure $p_1$. Once the pressure is stabilized a slug of oxygen is injected, taking the mixture to $2p_1$. Finally a second slug of hydrogen is injected bringing the pressure to desired pre-detonation pressure, $3p_1 = p_{fill}$. Once filling was completed, the gun was sealed from all but the pressure gauge, here a 4000 psi Omega pressure transducer. The remaining gas in the fill lines is vented to the outside in order to leave no detonable mixture in the filling system. The gas is then left to mix for a period of 15 minutes to allow for uniformity throughout the driver. This procedure is represented by figure 4–16.

In the last minutes of the mixing process the test section is evacuated using a vacuum pump. This is done in order to lessen the effects of the bow shock (note, even though there is no air ahead of the projectile there can still be propellant blow by). Once evacuation is complete and the driver gas mixed, the gun can be fired. For the majority of the trials the mixture is ignited from the fill end using an electric model rocket motor igniter and a 30 Volt DC power source. However, ignition from the breech end was also investigated in order to lessen the initial pressure on the projectile. All the initial gun data is presented in table form in appendix I.

Once the gun has fired, the propellant gases are vented from the safety and test chambers. Furthermore, shop air is injected into the gun from the fill port driving any

residual water out of the gun system in order to prevent rusting and contamination of the next trial. This process can be done comfortably in a period of 2 hours hence, multiple trials can be done in a single day. The velocity data for these trials are presented in appendix J.

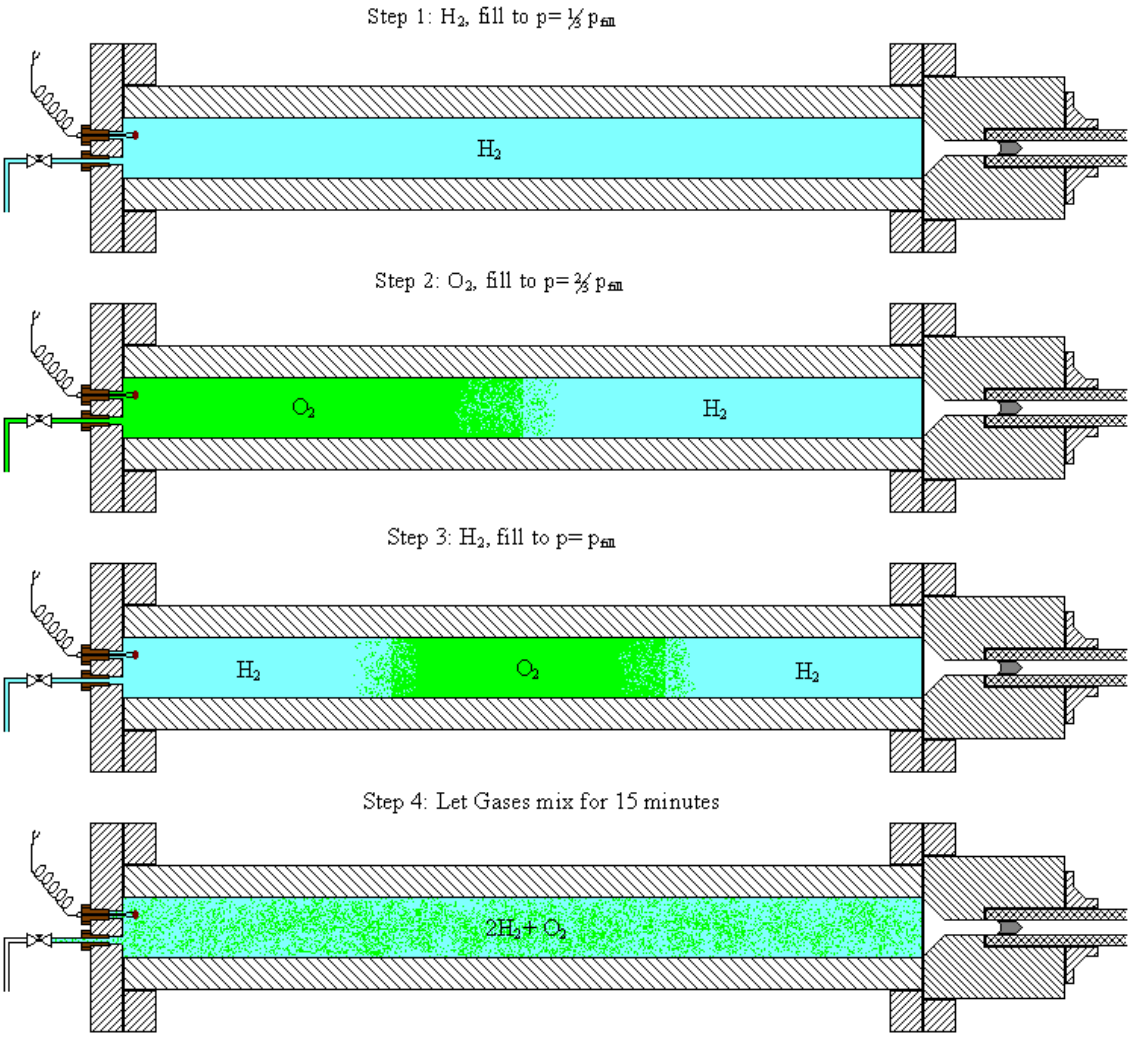


Figure 4–16: Schematic of the fill procedure

### 4.3.1 Facility Images

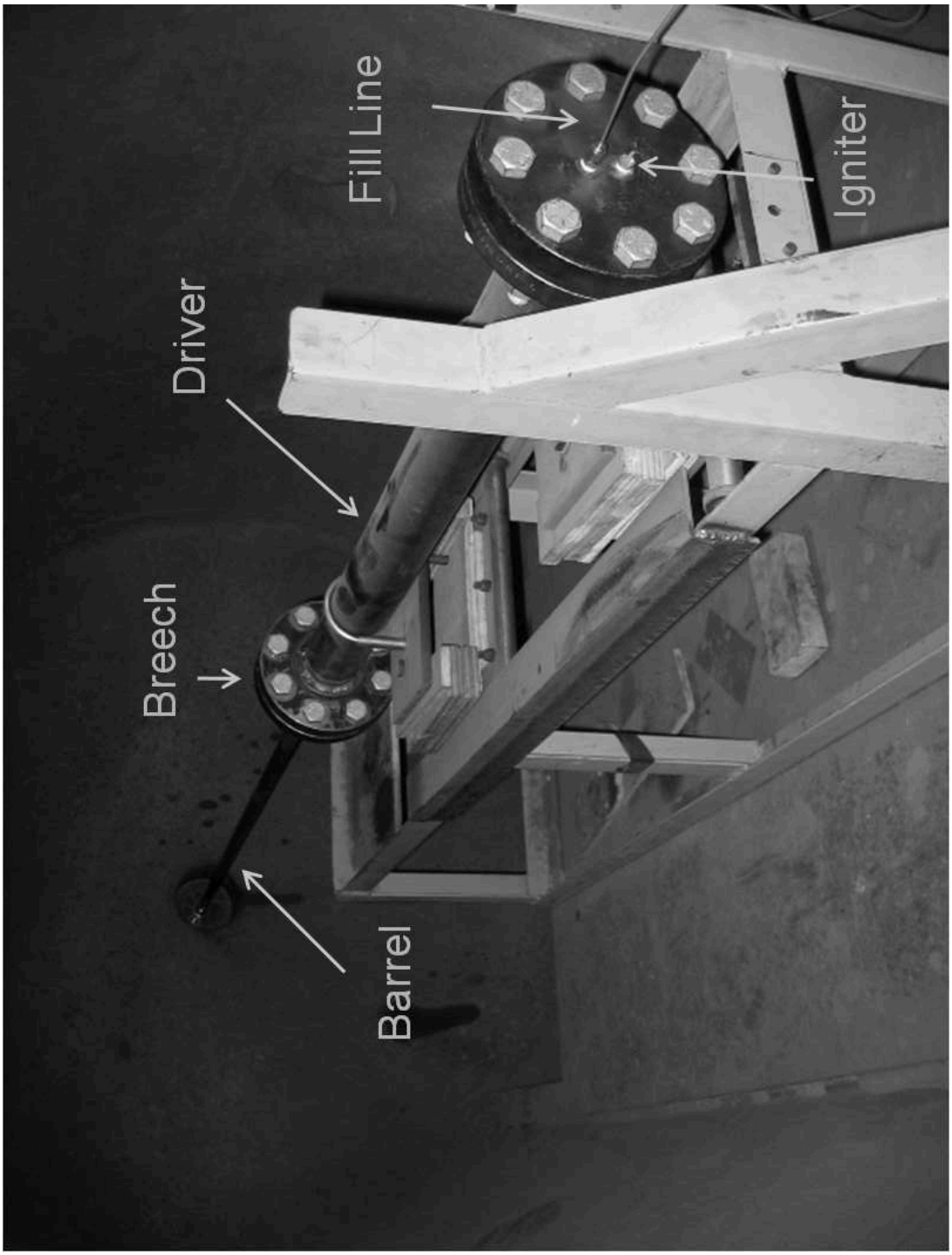


Figure 4–17: Image of the guns system


Figure 4–18: Image of the coil gauge system

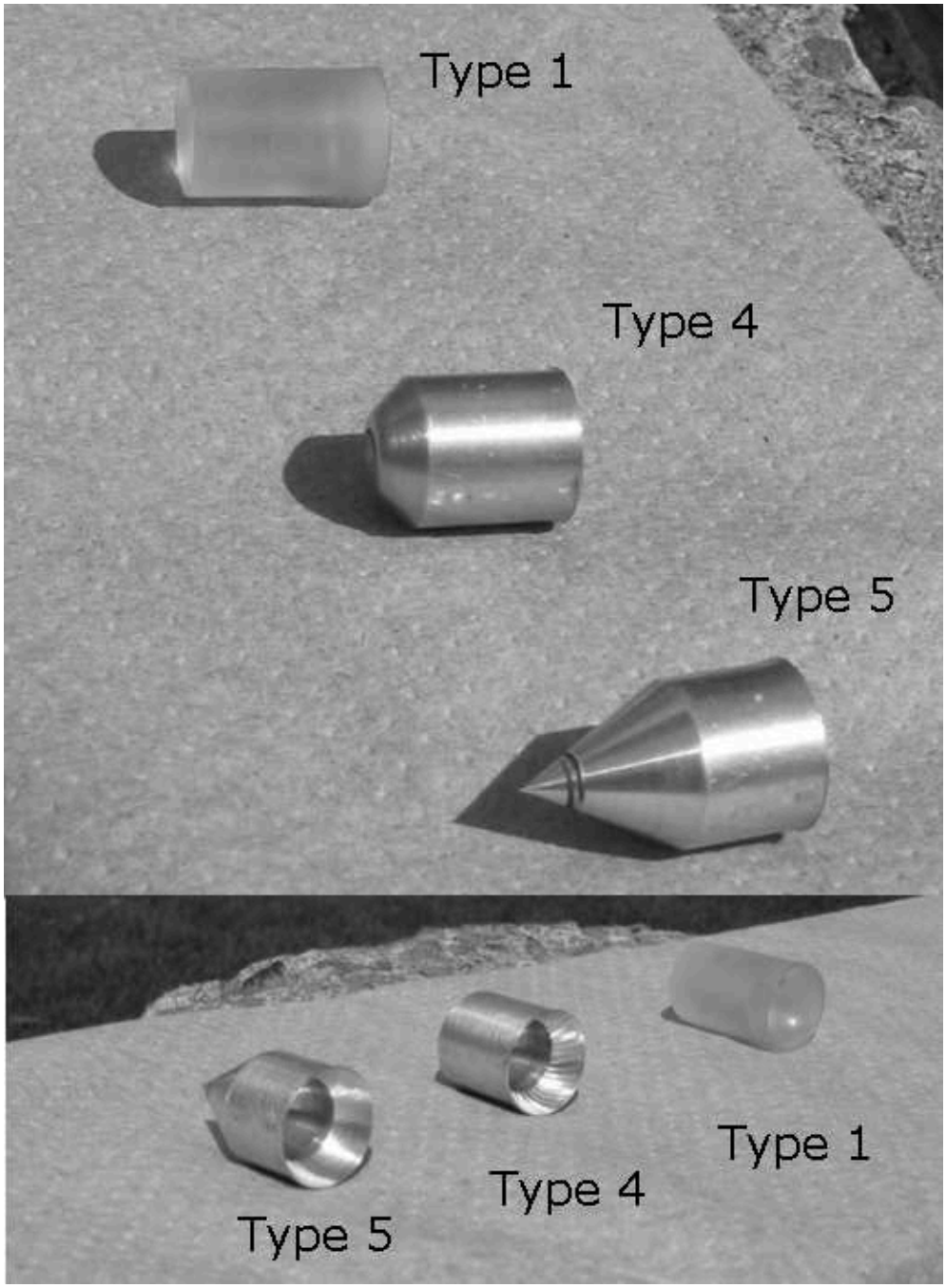


Figure 4–19: Image of various projectiles

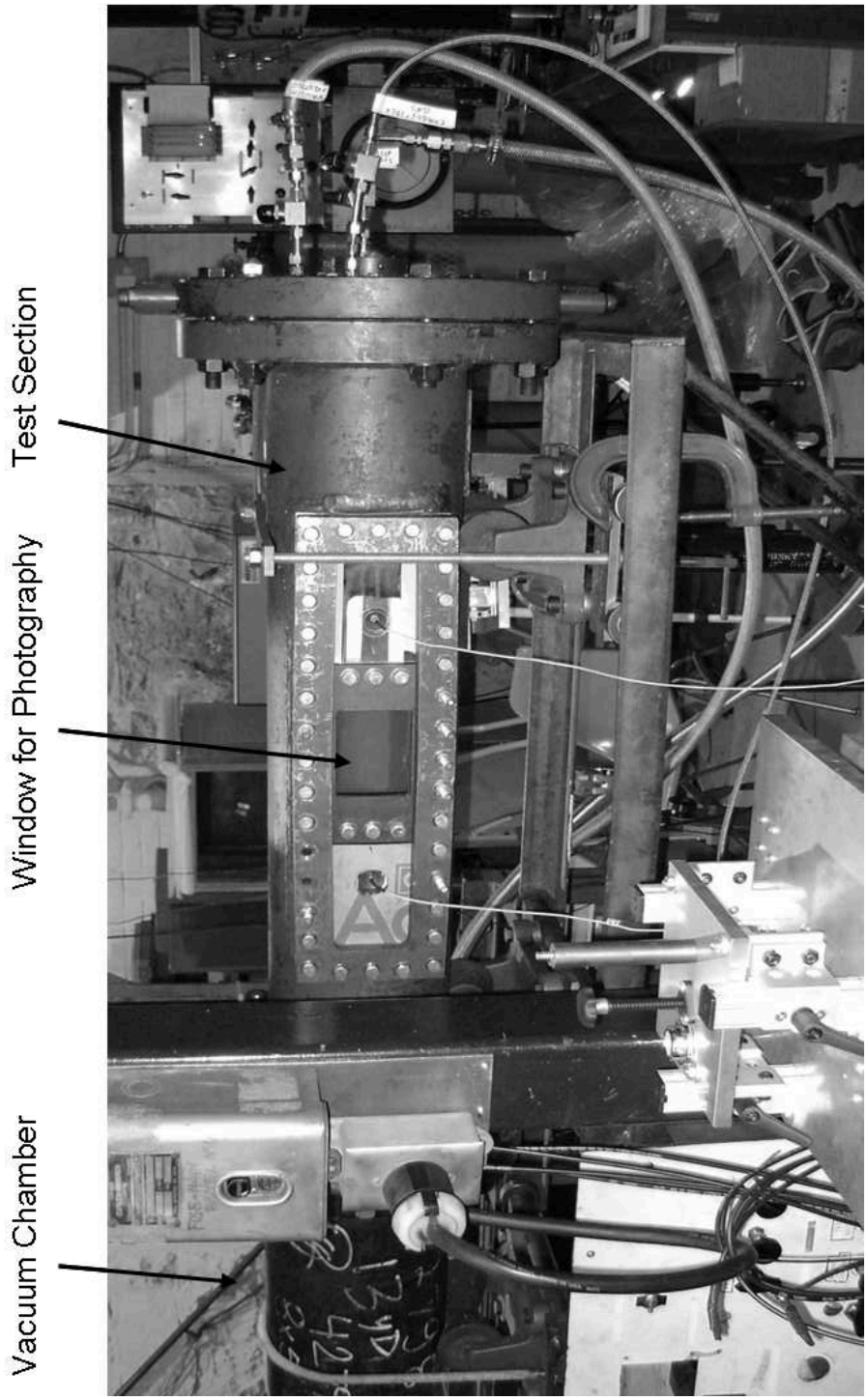


Figure 4–20: Image of the test section

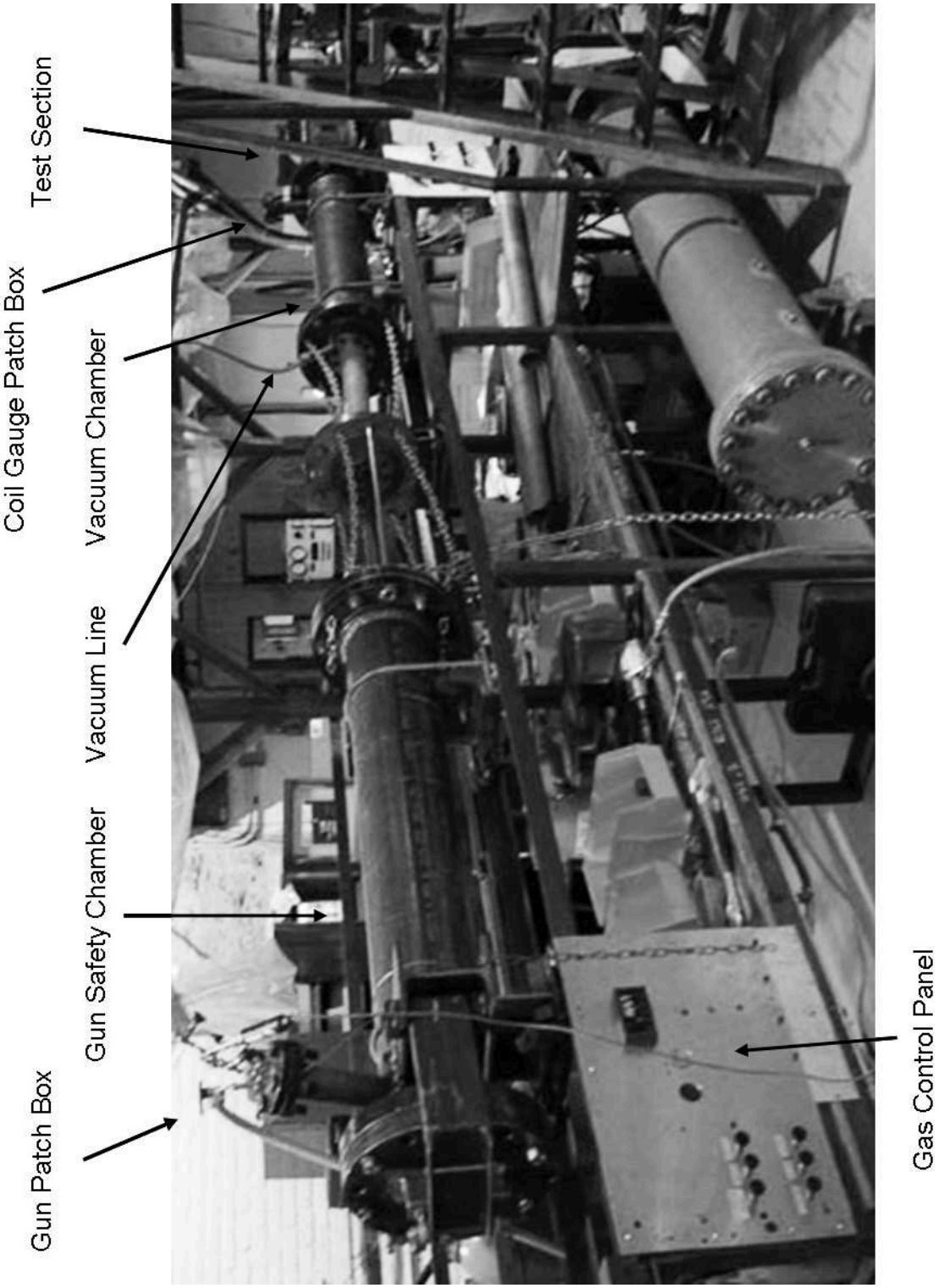


Figure 4–21: Image of the gaseous detonation driven gun facility

## 4.4 Results

### 4.4.1 Results: 6 foot (183 cm) Barrel

The 6 foot (183 cm) barrel gun trials consisted of tests for performance by varying both mass and pre-detonation pressure. The varying mass experiments were done keeping the pre-detonation pressure fixed at 62.5 atm. The results for these experiments compared with the Euler code performance calculations are presented in figure 4–22, while figure 4–23, compares the results of the fixed projectile mass of 3.2 g over a range of pre-detonation pressures.

From figure 4–22 it can be seen that by making the projectile too light (essentially making it too fragile) will cause it to break, whereas figure 4–23 shows that by increasing the pre-detonation pressure above the pre-determined maximum safe pressure can result in projectile failure.

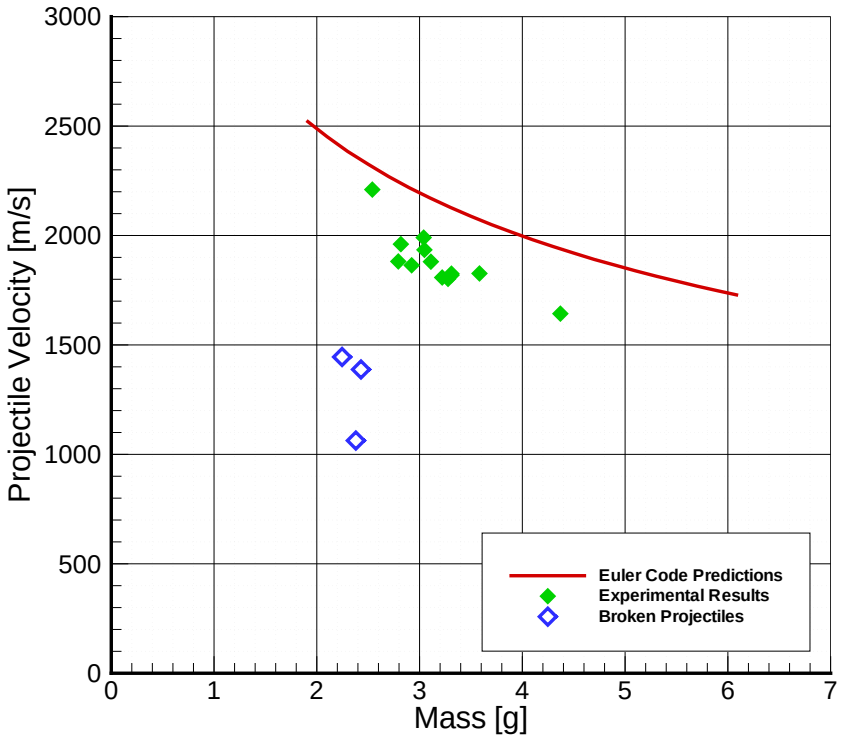


Figure 4–22: Muzzle velocity vs. projectile mass for the 6' (183 cm) barrel at 62.5 atm pre-detonation pressure

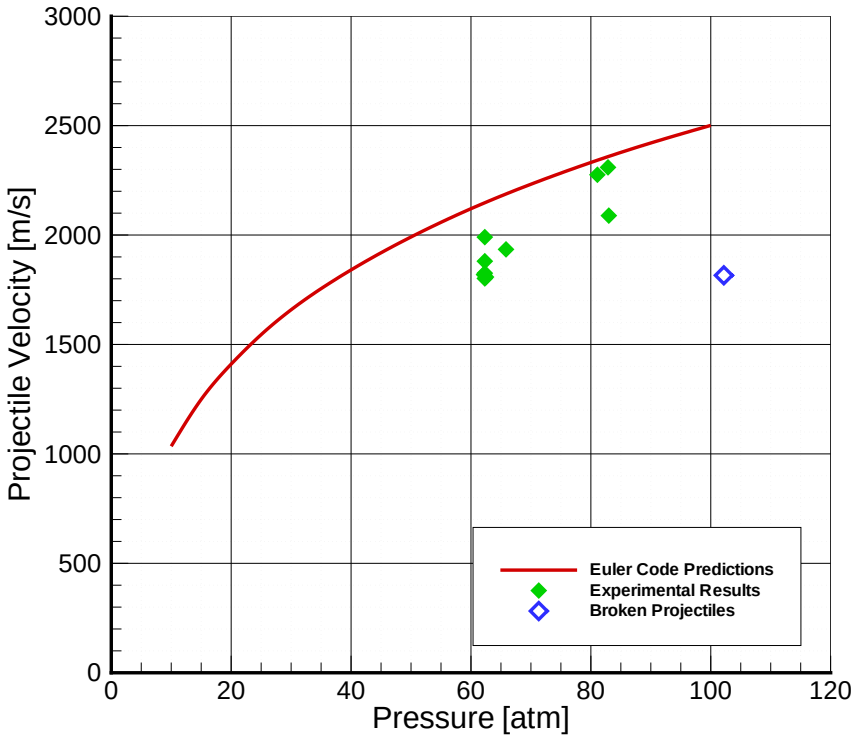


Figure 4–23: Muzzle velocity vs. pre-detonation pressure for 6' (183 cm) barrel and projectile mass of 3.2 g

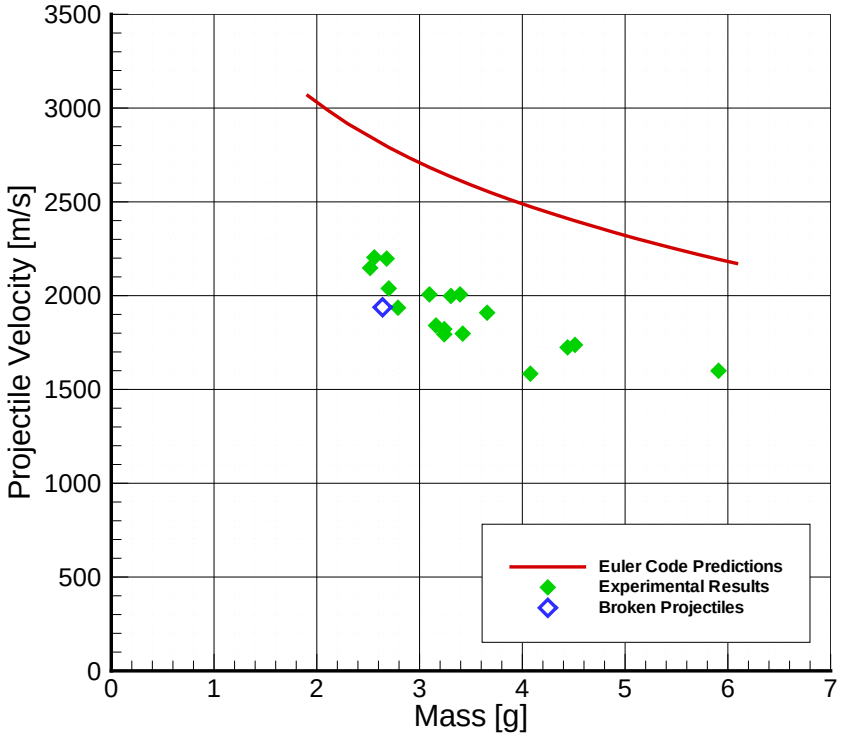


Figure 4–24: Muzzle velocity vs. projectile mass for the 12' (366 cm) barrel at 62.5 atm pre-detonation pressure

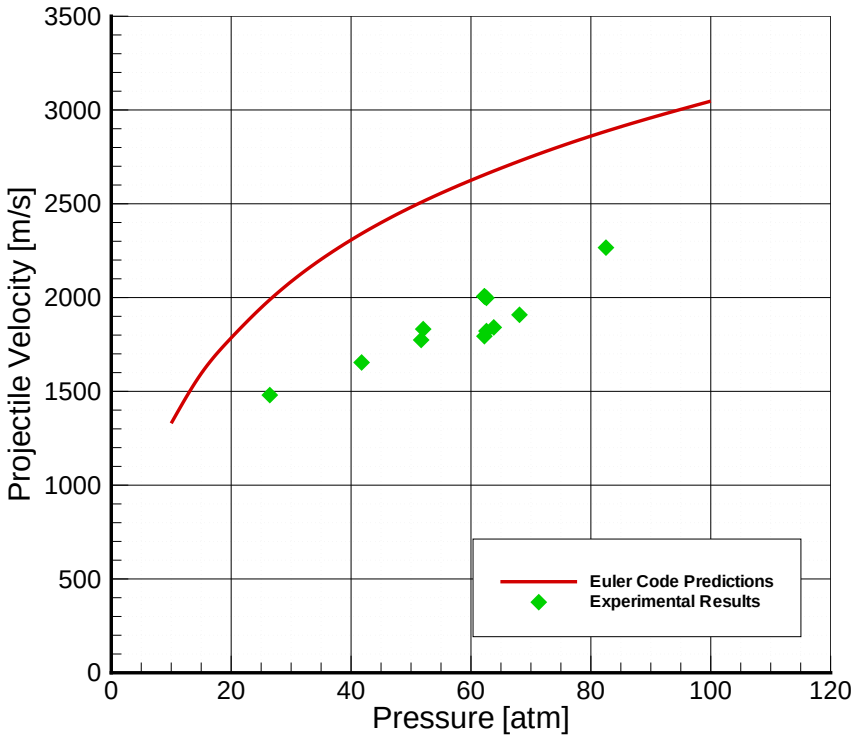


Figure 4–25: Muzzle velocity vs. pre-detonation pressure for 12' (366 cm) barrel and projectile mass of 3.2 g

### 4.4.2 Results: 12 foot (366 cm) Barrel

The 12 foot (366 cm) barrel gun trials consisted of the same tests that were done for the 6 foot barrel. The varying mass results are presented in figure 4–24 and the varying pressure results are presented in figure 4–25.

It can be seen from figures 4–24 and 4–25, when compared to figures 4–22 and 4–23, that there seems to be a larger discrepancy in the predicted results and those actually obtained. However, the trend for the lighter projectiles breaking seems to remain.

### 4.4.3 Results: Ignition Location

The results of the ignition location trials are displayed in figure 4–26. These trials used the 12' barrel and 3.2 g projectiles and were done over a range of pressures. From figure 4–26 it can be seen that there is a definite drop in muzzle velocity when ignition occurs at the breech end of the gun system.

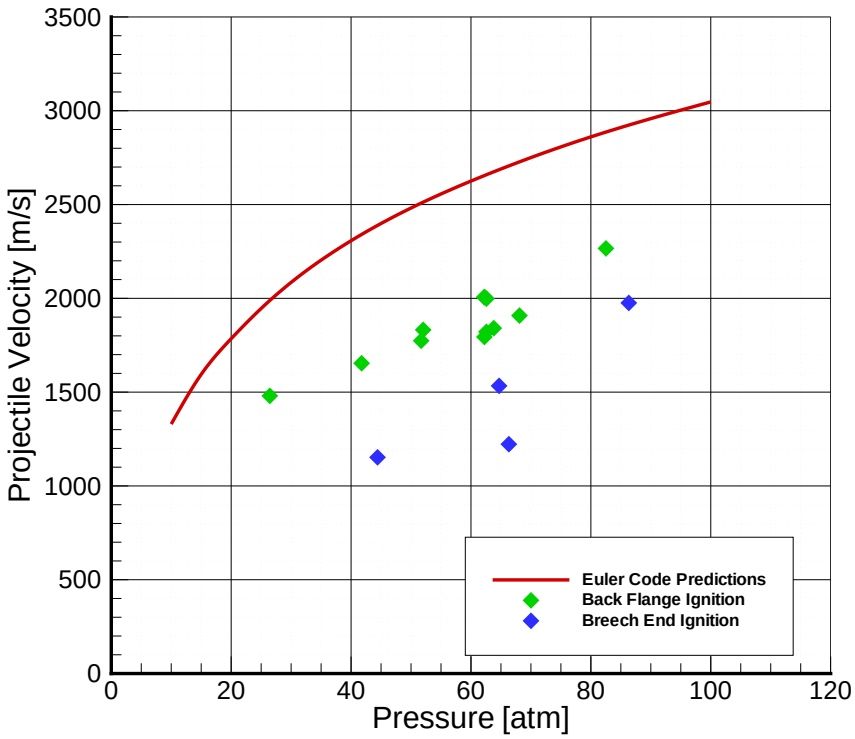


Figure 4–26: Comparison of different ignition locations, 12' barrel, 3.2 g projectile and 62.5 atm pre-detonation pressure

# CHAPTER 5
# Discussion

## 5.1 Experimental Results

From the experimental results it seems that there is almost no benefit from increasing the barrel length. This is further confirmed when plotting figures 4–23 and 4–24 together on the same plot. This has been done and presented in figure 5–1. This result seems to coincide with previous results [1] where the losses result in a maximum effective barrel length. However, for this prototype, this seems to occur at barrel lengths even less than $\zeta = 200$ since the results are approximately the same for the 183 cm ($\zeta = 144$) and the 366 cm ($\zeta = 288$) barrel. This is possibly due to the very high initial temperatures of this mixture, as high as 4350 K, since heat loss is driven by gradients in temperature. Furthermore, this could also be due to the

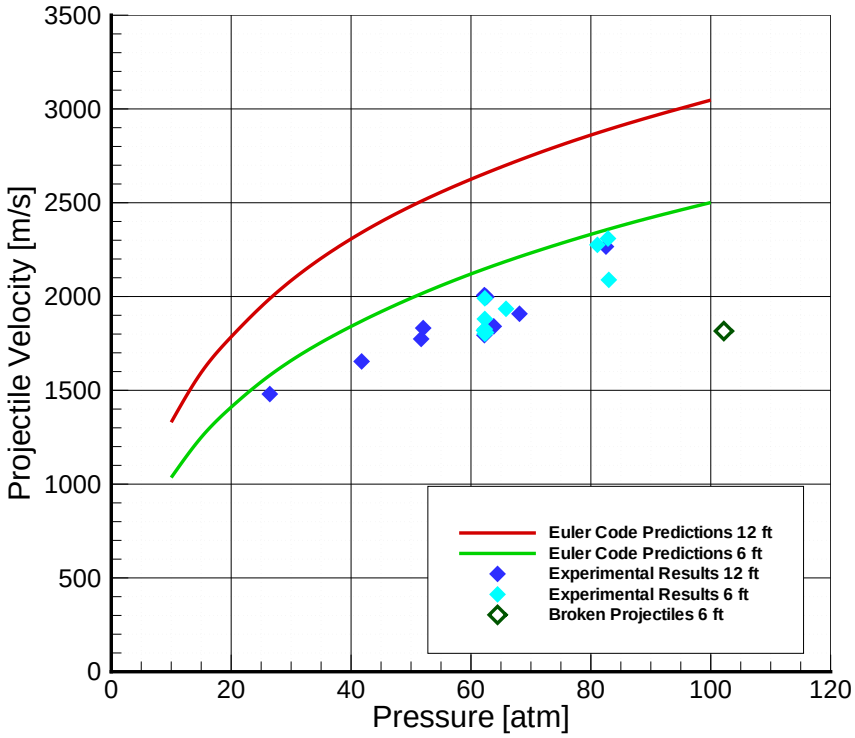


Figure 5–1: Muzzle velocity vs. pre-detonation pressure comparing the 6' and 12' barrels and projectile mass of 3.2 g

transitions along the length of the barrel that the projectile must pass through. If these are not perfectly in alignment, then the projectile could be slowed as it passes through them.

To account for convective and frictional losses, an empirical study was done by Seigel in [1] to estimate these effects. It was postulated that these losses are a function of both $\zeta$ and the quantity $\gamma u_p/a_\circ$. Experiments were done with bore diameters ranging from 0.22" to 4" and the actual velocities obtained were between 10,000 and 23,000 ft/s (3048 to 7010 m/s). This study was done for a range of $\zeta$ from 100 to 250. A polynomial fit for this correlation was determined from the figure presented by Seigel in [1]. This correlation relates the ideal velocity $u_{p(ideal)}$ to the velocity that is affected by losses. It should be noted that the effect of $\zeta$ is assumed constant for this correlation, but in reality under predictions of the velocity should be expected toward $\zeta = 100$ and over predictions of the velocity should be expected toward $\zeta = 250$. The resulting correlation is given by equation 5.1 and has been plotted in figure 5–2.

$$\frac{u_p}{u_{p(ideal)}} = c_1\Theta^6 + c_2\Theta^5 + c_3\Theta^4 + c_4\Theta^3 + c_5\Theta^2 + c_6\Theta + c_7 \tag{5.1}$$

with

$$\Theta \equiv \frac{\gamma u_{p(ideal)}}{a_\circ} \tag{5.2}$$

and

$c_1 = -7.051449 \times 10^{-4}$

$c_2 = 7.879114 \times 10^{-3}$

$c_3 = -3.423272 \times 10^{-2}$

$c_4 = 7.109132 \times 10^{-2}$

$c_5 = -8.037788 \times 10^{-2}$

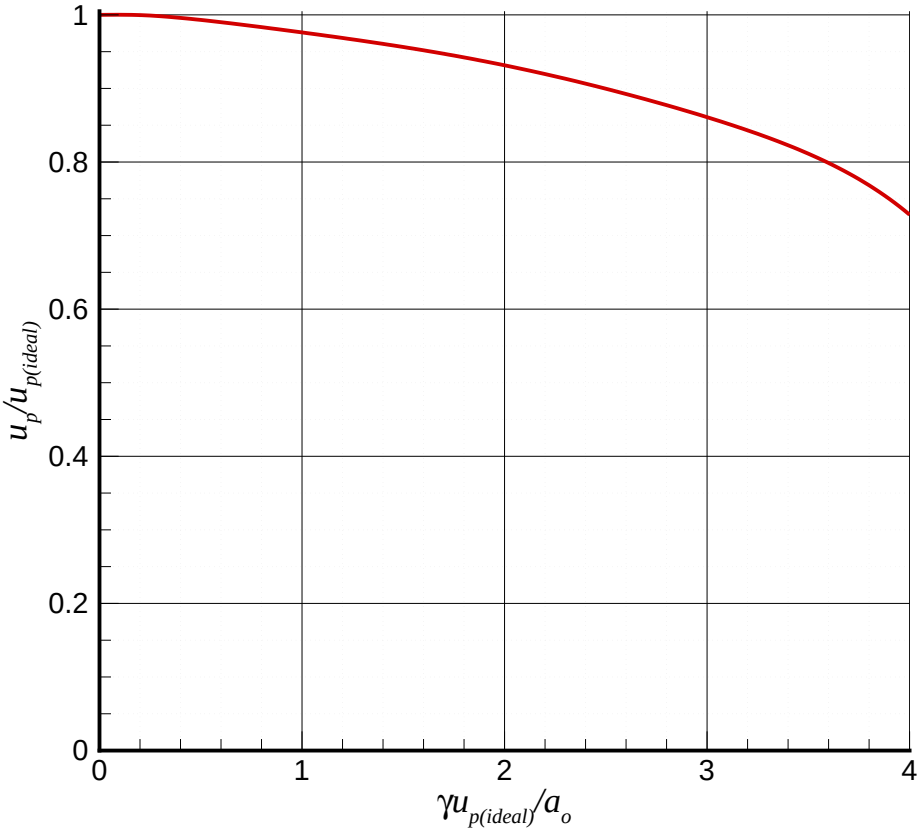


Figure 5–2: Correlation between $u_p/u_{p(ideal)}$ and $\gamma u_{p(ideal)}/a_\circ$, accounting for the frictional and convective losses, valid for $\zeta$ between 100 and 250

$c_6 = 1.248579 \times 10^{-2}$

$c_7 = 1.0$

This correlation can be used to recalculate the predicted velocity by using the ideal calculations done in Chapter 3. This has been done for the results for the 6 foot barrel ($\zeta = 144$) and figures 4–22 and 4–23 are re-plotted in figures 5–3 and 5–4. The same has been done for the 12 foot barrel ($\zeta = 288$) and figures 4–24 and 4–25 are re-plotted in figures 5–5 and 5–6.

It can be seen in figures 5–3 and 5–4 that the correlation given by equation 5.1 accounts for approximately 1/3 to 1/2 of the discrepancy between the predicted ideal velocity and the experimental results. However, the temperature of the mixture ($3H_2$+$O_2$+8He) used by [1] are in the range of 2700 K [6]. In comparison, the temperature of the mixture used for these experiments ranges from 3900 K at 10 atm pre-detonation pressure to 4350 at 100 atm pre-detonation pressure (see table

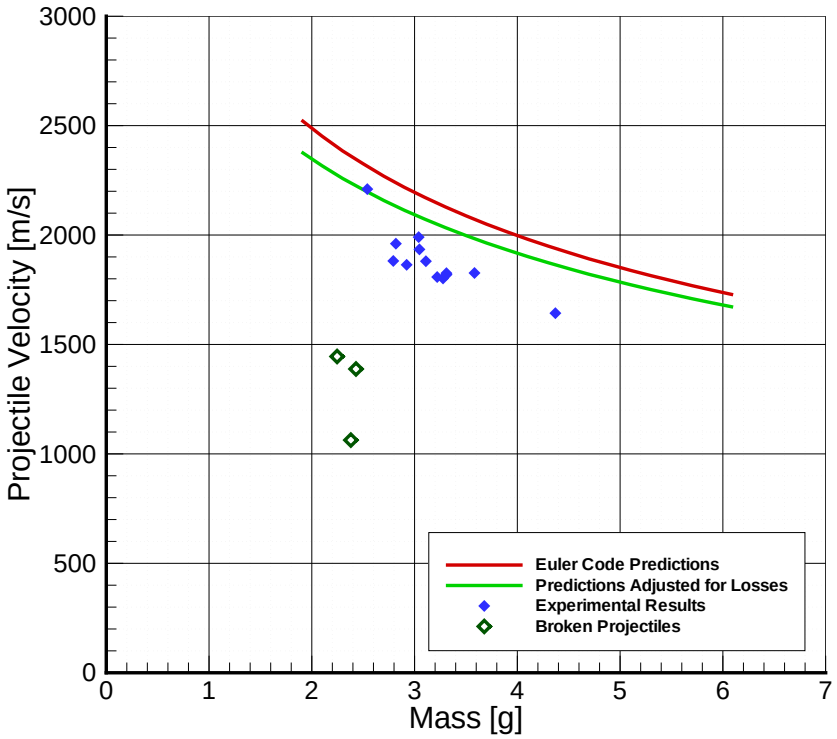


Figure 5–3: Muzzle velocity vs. projectile mass for the 6' barrel at 62.5 atm pre-detonation pressure, accounting for the frictional and convective losses

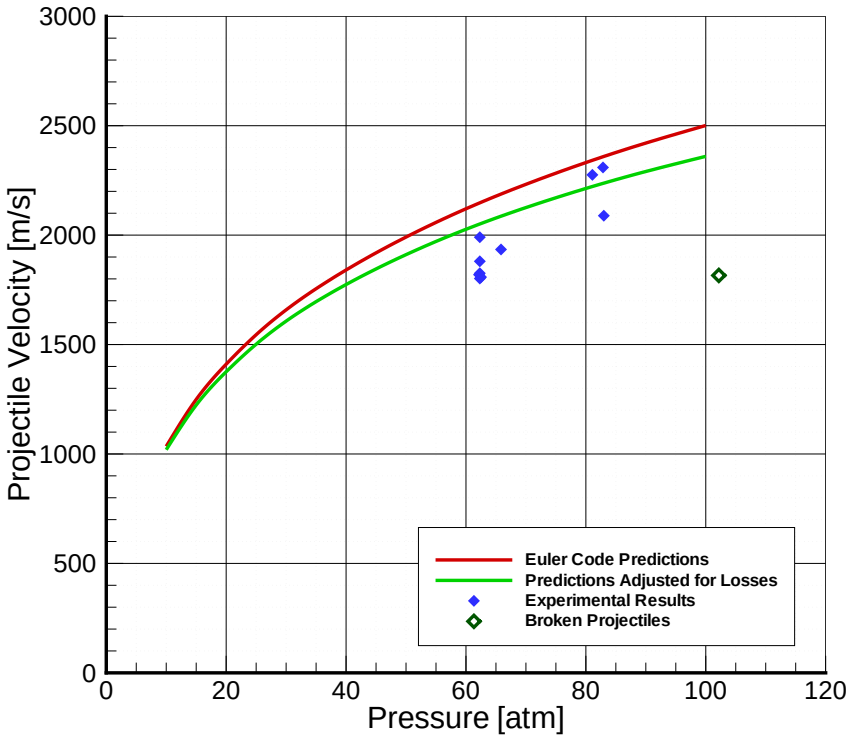


Figure 5–4: Muzzle velocity vs. pre-detonation pressure for 6' barrel and projectile mass of 3.2 g, accounting for the frictional and convective losses

3–3). For the pre-detonation pressure of approximately 62.5 atm in figure 5–3 the CV temperature is approximately 4250 K. This is approximately 60% higher than the initial temperature in the experiment that was used to develop this correlation.

From figures 5–5 and 5–6 it can be seen that the discrepancy in actual velocity and the velocity obtained by the correlation is much larger for the 12 foot barrel than it is for the 6 foot barrel. Furthermore, the correlation represents a much smaller percentage of the discrepancy between the predicted ideal velocity and the experimental results. However, this would be expected since the correlation is not valid for this barrel length as the losses are a function of $\zeta$ which the correlation ignores.

Finally for figures 5–3 and 5–5 the experimental pressures range from 62.2 atm to 63.5 atm. From figures 3–3 and 3–4 this equates to approximately $\pm 0.5\%$ discrepancy in velocity. Furthermore, for figures 5–4 and 5–6 the mass ranges from 3.0 g to 3.4 g, which from figure 3–3 and 3–4 equates to approximately $\pm 1.0\%$ discrepancy.

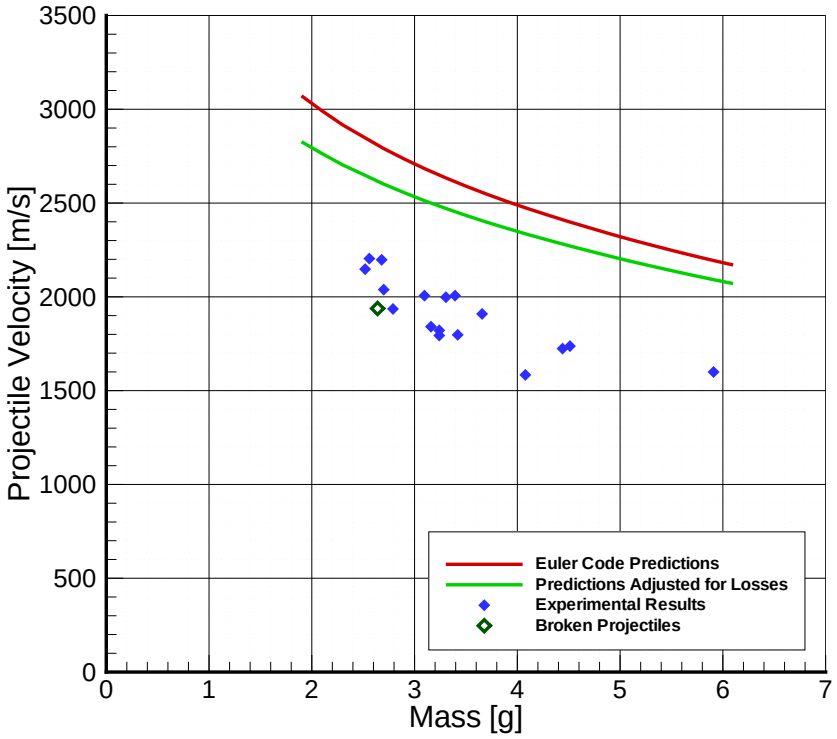


Figure 5–5: Muzzle velocity vs. projectile mass for the 12' barrel at 62.5 atm pre-detonation pressure, accounting for the frictional and convective losses

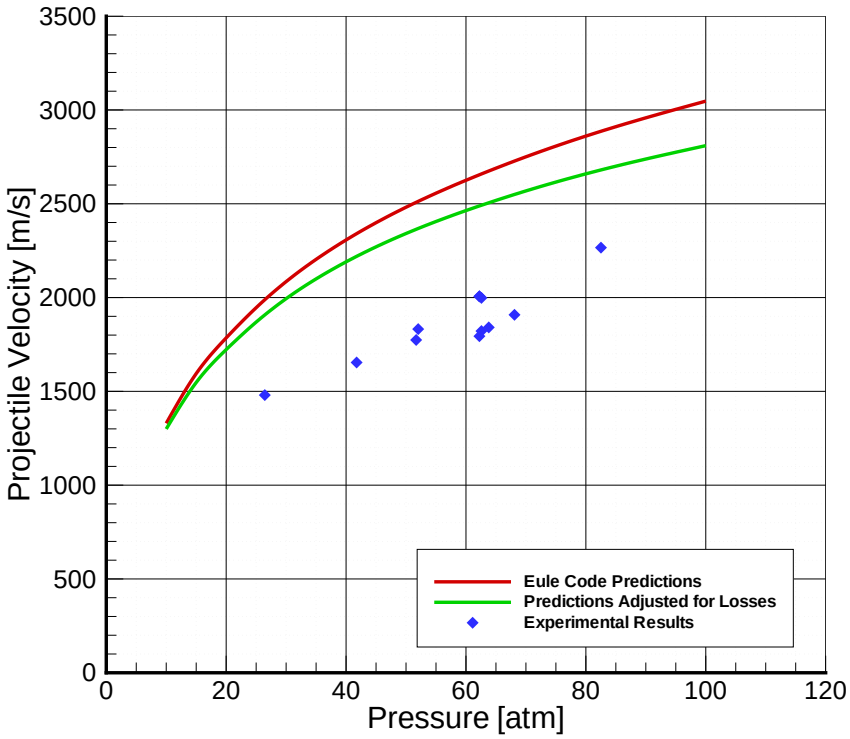


Figure 5–6: Muzzle velocity vs. pre-detonation pressure for 12' barrel and projectile mass of 3.2 g, accounting for the frictional and convective losses

Thus the discrepancy in velocity that is seen in figures 5–3 through 5–6 most likely comes from frictional and convective losses.

### Projectile Survival

One of the issues that had to be overcome over the course of these experimental trials was the survival of the projectile. Table 5–1 shows the projectiles that were confirmed to have broken during the trials. It can be seen that for Lexan (PC) projectiles, pre-detonation pressure above 50 atm risks projectile failure. To overcome this, it was decided to try composite projectiles using an aluminium disc attached to a Bridgman seal made of Lexan (Type 3). These, however, proved not to be strong enough to survive at initial pressures in the order of 60 atm. Thus it was decided to use projectiles made entirely of aluminium. These proved to be able to survive up to 90 atm fill pressures when using a blunted configuration (Type 4); however, when using conical projectiles the mass that had to be removed from the body of the

Table 5–1: Broken projectile data

| Shot # | Material | Mass [g] | Angle $\theta$ | Fill Pressure [bar] | Bored | Seal |
|---|---|---|---|---|---|---|
| 8 | PC | 2.49 | 90° | 72.39 | No | Yes |
| 9 | PC | 2.56 | 90° | 76.88 | No | Yes |
| 10 | PC | 2.54 | 90° | 77.29 | No | Yes |
| 13 | PC | 2.25 | 90° | 61.98 | No | Yes |
| 15 | Al+PC | 2.38 | 90° | 61.98 | No | Yes |
| 16 | Al+PC | 2.43 | 90° | 61.98 | No | Yes |
| 17 | PC | 2.29 | 90° | 52.40 | No | Yes |
| 21 | Al | 2.99 | (90+45)° | 102.53 | Yes | Yes |
| 24 | Al | 2.71 | 30° | 82.81 | Yes | Yes |
| 41 | Al 7075 | 2.75 | 20° | 62.05 | Yes | Yes |
| 43 | Al 7075 | 2.64 | 30° | 62.05 | Yes | Yes |
| 46 | Al 7075 | 2.63 | 20° | 51.71 | Yes | Yes |
| 58 | Ti | 3.36 | 20° | 63.09 | Yes | Yes |
| 62 | Al 7075 | 2.78 | 20° | 41.37 | Yes | Yes |
| 69 | Al 7075 | 4.41 | 20° | 65.91 | Yes | Yes |
| 84 | Al 7075 | 5.67 | 30° | 75.98 | Yes | Yes |

projectile to keep the mass down caused failure to occur at pre-detonation pressures above 64 atm. Therefore it was decided to use the aluminium alloy 7075-T6 as the projectile material. These projectiles proved to be able to survive fill pressures up to 100 atm for 60° projectiles with a Bridgman seal but and no extra material removal (See Shot 064 in appendix I). However, the lower angle projectiles (below 30°) the projectiles proved very fragile when material was removed to reduce their mass.

To try and compensate for the fragility of the projectiles, trials were done testing the effect of ignition location. However, igniting at the breech location results in both lower performance and inconsistent results as seen from figure 4–26.

### 5.2 Potential Maximization of the Gun System Performance

From the experimental results it seems that changing the length of the barrel, which initially seemed the best way to improve gun performance, resulted in no increase in muzzle velocity. Thus all the mechanical routes have been explored that can possibly increase gun performance. Therefore, the only thing left to be done is optimizing the propellant gas. It was seen in Chapter 2 that light gases such as

helium and hydrogen make the best propellants. Therefore, instead of using steam as the propellant, it is possible to use this steam to heat one of these light gases in order to improve performance. To follow is a study of this concept, investigating the use of

$2H_2+O_2+\chi H_2$

$2H_2+O_2+\chi He$

$CH_4+2O_2+1.5\chi He$

$C_2H_4+3O_2+2\chi He$

$2C_2H_6+7O_2+5\chi He$

The coefficient $C\chi$ is chosen so that for a given $\chi$ the ratio between the products of the reaction and the dilatants is equal between each of these mixtures. Furthermore a reference state needs to be chosen to be able to estimate improvements gained by this optimization. This state has been chosen to be $2H_2+O_2$ at 100 atm initial pressure and 298 K initial temperature. Furthermore all the calculations were done using the target mass of 3.2 g using aluminium 7075-T6 ($\sigma_u$ = 572 Mpa) as the projectile material and assume a 2 m barrel.

The first step in the process was to determine the performance of the gun system and calculate all the states corresponding to the CJ detonation pressure of 2400 bar [6]. Here the strength of the projectile is ignored and the performance calculations only take the mass of the projectile into consideration. The pre-detonation, constant volume and reflected CJ detonation pressures are tabulated in appendix K along with the CV temperature, speed of sound and $\gamma$, which are used as inputs for the Euler Code [9]. It can be seen that for the majority of these mixtures the reflected detonation pressure is slightly higher than the ultimate strength of aluminium 7075-T6. Therefore this is the optimal projectile material for the gun system. This follows the criteria in Chapter 2 that states the projectile should be designed to fail before

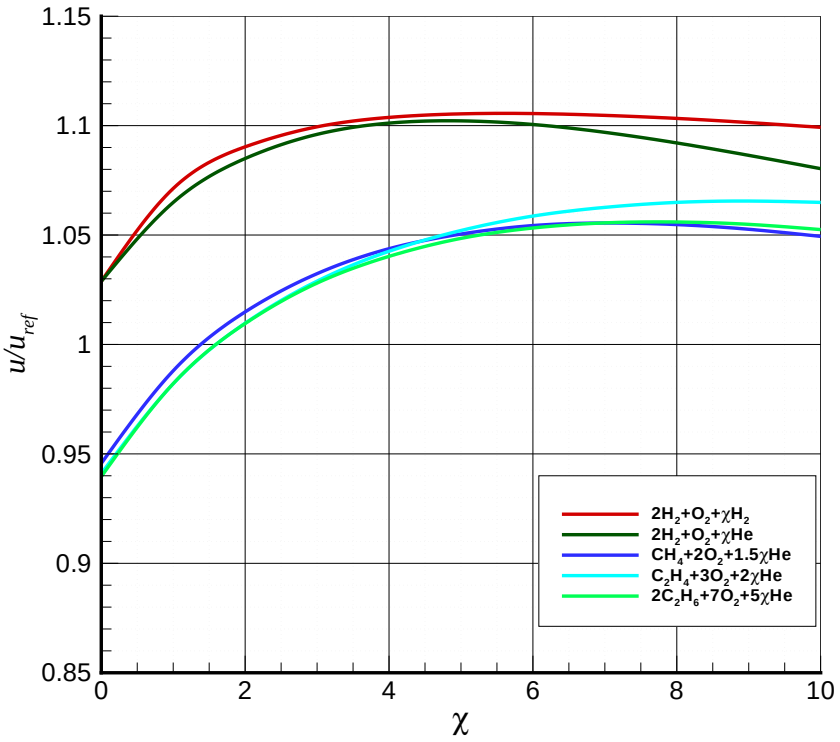


Figure 5–7: Muzzle velocity vs. mixture composition for a 2 m barrel, projectile mass of 3.2 g and CJ detonation pressure of 2400 bar

the gun. The results of these computations are presented in figure 5–7. It can be seen that $2H_2+O_2$ systems diluted with either $H_2$ or He perform quite well when compared to the hydrocarbons diluted with He.

Now the strength of the projectile is taken into account and the states corresponding to the reflected detonation pressure of 5720 bar have been calculated [6]. The pre-detonation, constant volume and CJ detonation pressures are tabulated in appendix L along with the CV temperature, speed of sound and $\gamma$, which are used as inputs for the Euler Code [9]. The results of the computations are presented in figure 5–8. It can be seen that $2H_2+O_2$ systems diluted with either $H_2$ or He still perform quite well when compared to the hydrocarbons diluted with He. However it can be seen when figure 5–8 is compared with figure 5–7 that $2H_2+O_2+\chi H_2$ systems perform even better than $H_2+O_2+\chi$He for a fixed reflected detonation pressure than they do for a fixed CJ pressure.

Due to the reality that these gases are only available at certain pressures and gas handling systems are also limited in their maximum pressure, performance of the system with fixed initial fill pressures must be explored. Since the fill pressure for $2H_2+O_2$ corresponding to a reflected detonation pressure of 5720 bar has a corresponding CJ pressure lower than the 2400 bar determined to be the maximum safe internal pressure for the gun, then this will be taken as the reference fill pressure. Thus the calculations are redone with the fill pressure fixed to 106.44 bar [6]. The constant volume, CJ detonation pressures and reflected detonation pressures are tabulated in appendix M along with the CV temperature, speed of sound and $\gamma$, which are used as inputs for the Euler Code [9]. The results of the computations are presented in figure 5–9. It can be seen that in this case that $2H_2+O_2+\chi H_2$ performs the worst and that it is the hydrocarbon systems that perform the best. This is due to the much higher CV pressures achieved by the hydrocarbon system for than a $2H_2+O_2+\chi H_2$ system of equivalent pre-detonation pressure.

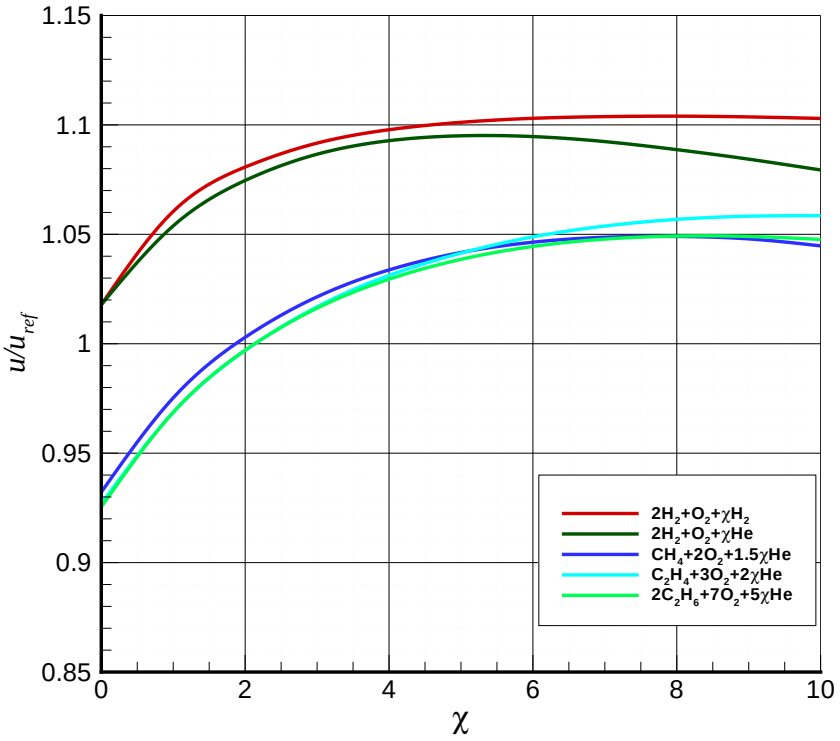


Figure 5–8: Muzzle velocity vs. mixture composition for a 2 m barrel, projectile mass of 3.2 g and reflected detonation pressure of 5720 bar

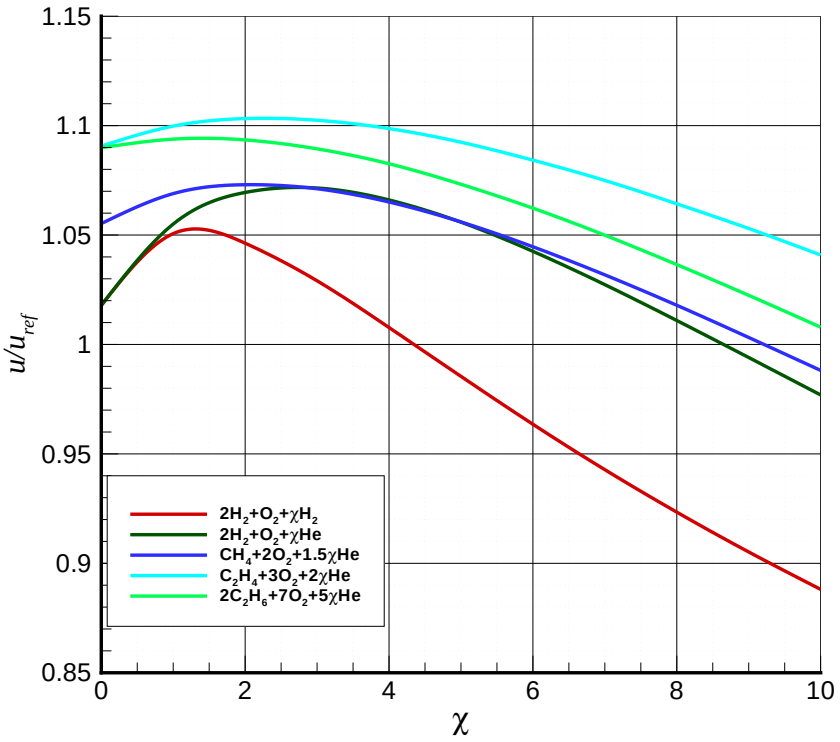


Figure 5–9: Muzzle velocity vs. mixture composition for a 2 m barrel, projectile mass of 3.2 g and pre-detonation pressure of 106.44 bar

Figures 5–7 through 5–9 fix the CJ pressure, reflected CJ pressure, and fill pressure, respectively. Each factor taken individually does not describe the gun system on its own. Figure 5–10 combines figure 5–7 and figure 5–8 so that both the criteria $p_{RCJ} \leq 5720$ bar and $p_{CJ} \leq 2400$ bar are met. However, if the system initial pressure is also a criteria, here defined as $p_{fill} \leq 106.44$ bar, then the system performance as a function of the mixture is represented by figure 5–11. It can be seen that figure 5–10 is almost identical to figure 5–8 but for the curve of $2H_2+O_2+\chi H_2$ above $\chi = 7$ with the best performance given by $2H_2+O_2+9H_2$. However figure 5–11 shows that if the initial fill pressure is an issue, then $2H_2+O_2+2.75He$ is the optimal mixture, followed closely by $C_2H_4+3O_2+16.5He$.

These results show that depending on what aspect of the system is the limiting factor, be it the gun, the projectile or the gas handling system, there are different mixtures that are the optimal for the system. However, this analysis has shown that the fact that there is a detonation in the system is itself a limitation on performance.

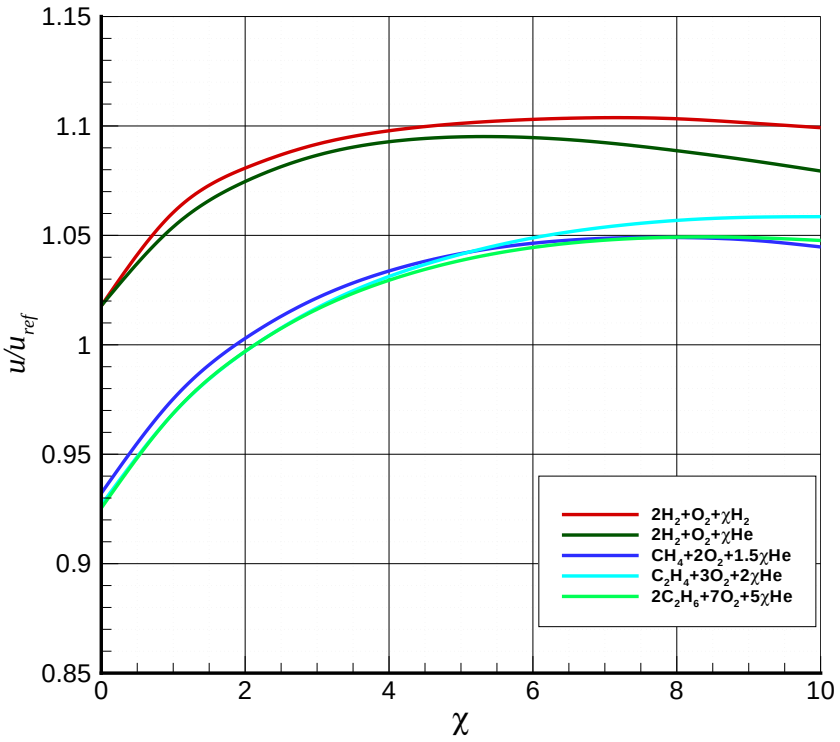


Figure 5–10: Muzzle velocity vs. mixture composition for a 2 m barrel, projectile mass of 3.2 g and the criteria $p_{RCJ} < 5720$ bar and $p_{CJ} < 2400$ bar

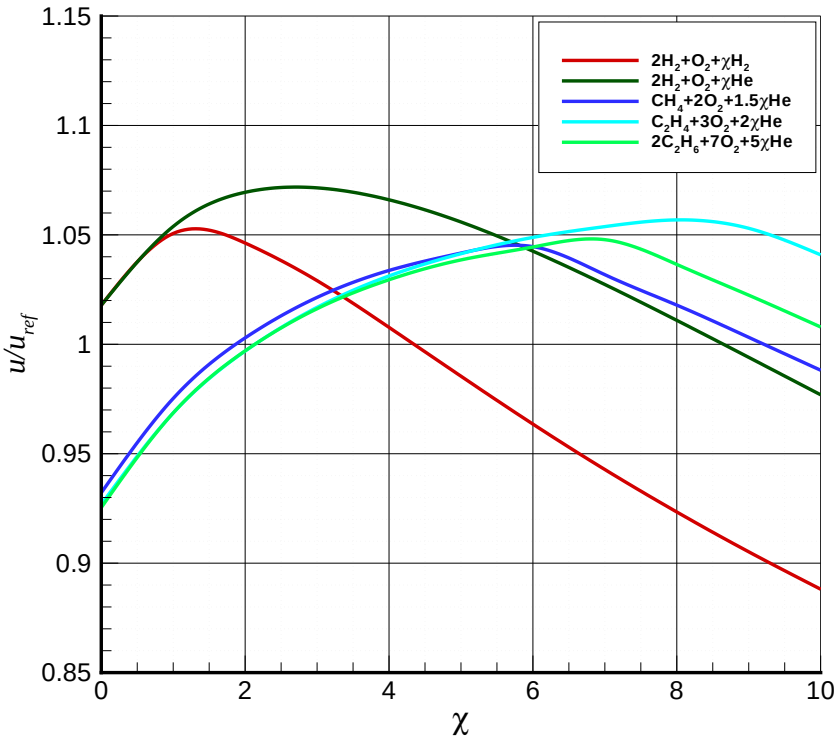


Figure 5–11: Muzzle velocity vs. mixture composition for a 2 m barrel, projectile mass of 3.2 g and the criteria $p_{RCJ} \leq 5720$ bar, $p_{CJ} \leq 2400$ bar and $p_{fill} \leq 106.44$ bar

If these mixtures are combusted in a manner that prevents detonation then a CV pressure of 2400 bar is the limiting factor. The pre-detonation, CJ detonation, and reflected detonation pressure are tabulated in appendix N along with the CV temperature, speed of sound and $\gamma$, [6] which are used as inputs for the Euler Code [9]. It can be seen that if a detonation was to occur then, projectile failure is certain and there is a good possibility that the entire system could fail due to the excessively high CJ and Reflected CJ pressures. However, as an exercise in maximizing the performance of this system, figure 5–12 shows the results of these numerical simulations.

It can be seen that all mixtures perform much better in this mode of combustion, with the best performance being almost identical for $2H_2+O_2+\chi H_2$ and $2H_2+O_2+\chi He$ below $\chi$=6. Furthermore these calculations were done assuming an aluminium alloy 7075-T6 projectile with a strength ratio of $S_r = 0.857$ bar m$^3$/kg for this system. However, since the peak pressure is 2400 bar, then the high strength aluminium alloy AZ31B can be used for the projectile which has a strength ratio of

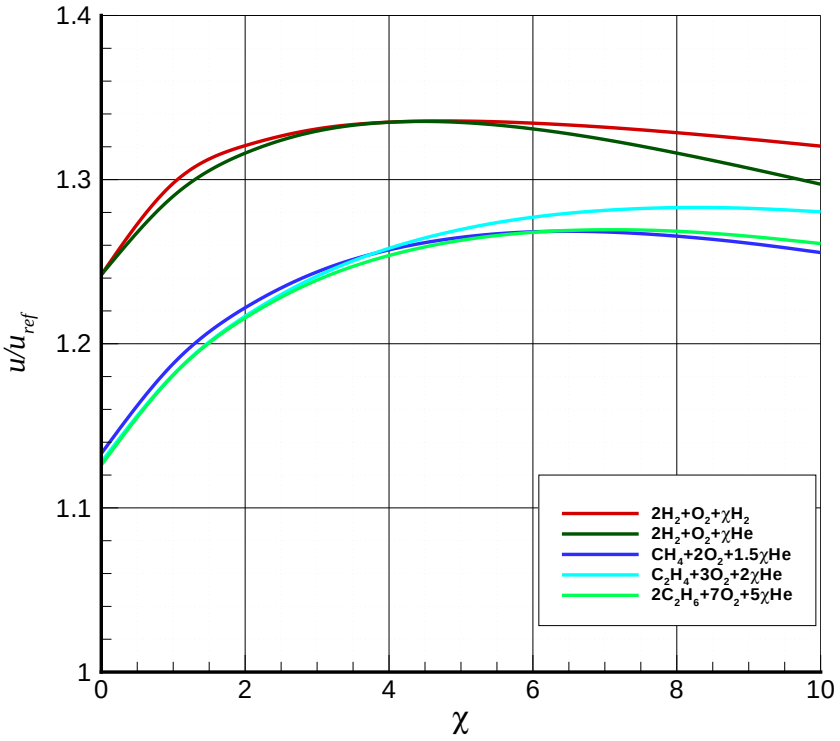


Figure 5–12: Muzzle velocity vs. mixture composition for 2 m barrel, projectile mass of 3.2 g and a CV explosion pressure of 2400 bar

$S_r = 1.356$ bar m$^3$/kg in this case. Thus a magnesium projectile of the same geometry as the aluminium projectile in these simulations will have a mass of 2.023 g. Taking this into account, the gun system can achieve velocities in excess of 150% of the reference state of $2H_2$+$O_2$ at a fill pressure of 100 atm and initial temperature of 298 K. This can be achieve by using either $7H_2$+$O_2$ at $p_{fill}$=298.4 bar and 298 K or $2H_2$+$O_2$+4He at $p_{fill}$=228.9 bar and 298 K [6]. At first glance it would seem that the latter mixture is better choice due to the lower fill pressure, however, when comparing the CV temperatures of these cases, 2740 K for the $7H_2$+$O_2$ mixture and 3590 K for the $2H_2$+$O_2$+4He mixture [6], it should be expected that the convective heat losses from the former mixture would be less that those for the latter mixture.

# CHAPTER 6
# Conclusion

The theoretical methods developed in this work have provided the tools required to develop a detonation-driven gas gun. These methods have proven to generate results that are in good agreement with the numerical modelling. The resulting prototype achieved a maximum velocity of 2700 m/s with a 2.5 g aluminium alloy 7075-T6 projectile. The experimental results were approximately 85% of the predicted values. This was determined to be primarily a result of frictional and convective losses. The analysis shows that there is potential to improve the performance of the system by utilizing stronger materials and by using $2H_2+O_2+9H_2$ as the propellant. If the system is optimized for the high strength titanium alloy Ti-6Al-4V, which was determined to be the optimal projectile material, initial chamber pressures of twice that of the prototype can be achieved. If $2H_2+O_2+9H_2$ is used as the propellant, calculations show that there is the potential to improve the gun performance by 8% over a $2H_2+O_2$ propellant at the same constant volume pressure.

Finally, there is even greater potential in improving performance by using a constant volume explosion rather than a detonation to heat the propellant. It was shown that the reflected detonation on the projectile results in the driving pressure to be approximately 4.5 times less than the peak pressure on the projectile. Thus, by achieving the CV state without detonating the mixture, a gun system optimized for a titanium alloy Ti-6Al-4V projectile has the potential of achieving driver pressures of approximately 10 times those of the prototype.

In closing, the use of detonable gas as the driver for a single stage gas gun appears a viable and economical alternative to two-stage gas guns. The launcher can be fabricated at a cost approximately two orders of magnitude lower than a two-stage gas gun of equivalent velocity and projectile mass capability. Furthermore, the

use of readily available gases permits bypassing issues related with acquiring and storing solid propellants (and associated initiators). However, there is the need for high pressure gas handling systems in order to operate this type of gun system.

# REFERENCES


[1] Seigel A.E., "The theory of high speed guns," *AGARDograph 91,* 1965

[2] Bogdanoff D.W. and Knowlen C., "Magnetic detector for projectiles in tubes," *AIAA Journal*, vol. 28, pp. 1942-1944.

[3] Callister Jr. W.D., *Material Science and Engineering, an Introduction*, John Wiley & Sons, Inc., 6th Edition, 2003.

[4] Carlucci, D.E. and Jacobson, S.S., Ballistics, *Theory and Design of Guns and Ammunition*, CRC Press, 2008.

[5] Szirti D., "Development of a single-stage implosion-driven hypervelocity launcher," Master Thesis, McGill University, 2008.

[6] Gordon, S. and McBride, B.J., "Computer Program for the Calculation of Complex Chemical Equilibrium Composition and Application," NASA Reference Publication 1311, 1994.

[7] Untron Inc., http://utroninc.com/, 2008.

[8] Moran, M.J. and Shapiro, H.N., *Fundamentals of Engineering Thermodynamics*, John Wiley & Sons, Inc., 4th Edition, 2000.

[9] Ponchaut N.F., "Euler solver for rapidly deforming domains," unpublished, contact author at nicola@alumni.caltech.edu, 2006.

[10] Batchelor P. and Higgins A.J., "Ignition of reactive metal particles in supersonic flow," *Combustion Institute/Canadian Section, Spring Technical Meeting*, Kingston, Ontario, Canada, May 9-12, 2004, Session A-Paper #3.

[11] Presles H.N. and Bauer P., "Detonation products gun," *Rev. Sci Instrum.*, American Institute of Physics, 1983, vol. 54, num. 11, pp. 1511-1512.

[12] Kryukov P.V., "Review of investigations under way on the large-scale Tsniimash ballistic facility," *International Journal of Impact Engineering*, Academic Press, 1999, vol. 232, pp. 501-508.

[13] Serway, R.A. and Beichner, R.J., *Physics for Scientists and Engineers with Modern Physics*, Saunders College Publishing, 5th Edition, 2000.

[14] Young, W.C. and *Budynas, R.G., Roark's Formulas for Stress and Strain*, McGraw-Hill, 7th Edition, 2002.

# APPENDIX A
## Lagrange Gradient

This derivation follows the same principles as those shown in [4] but here it is done for a PPIG whereas in [4] it was derived for the case of a burning solid propellant.

The underlying assumption in the Lagrange Gradient derivation is that at any time $t$, the density in the volume is uniform throughout, i.e. there are no spatial gradients. In a gun system there is a chamber (where the propellant gas is stored before launch), the projectile, and the bore (the tube through which the projectile will travel during launch). The Lagrange Gradient also assumes that there is no chambrage (a difference in area between the chamber and the bore). Considering the gas in the chamber under these assumptions then the density can be written as

$$\rho = \rho(x_g, t) \tag{A.1}$$

Where $x_g$ is the position in the gas behind the projectile. It can be seen that after $t = 0$ and the projectile starts to move the gas will also start to move. Thus there is a need to find the relationship between the velocity of the projectile and the velocity of the gas.

Starting from continuity

$$\frac{\partial \rho}{\partial t} + \frac{\partial}{\partial x_g}(\rho u_{x_g}) = 0 \tag{A.2}$$

where $u_{x_g}$ is the velocity of the gas at position $x_g$. Expanding the above and applying

the uniform density assumption results in

$$\frac{\partial \rho}{\partial t} + \rho \frac{\partial u_{x_g}}{\partial x_g} = 0 \tag{A.3}$$

which when isolating the $\rho$ terms (and knowing that $\rho$ is only a function of $t$) gives

$$\frac{1}{\rho}\frac{\partial \rho}{\partial t} = -\frac{\partial u_{x_g}}{\partial x_g} \tag{A.4}$$

Starting with a fixed amount of gas with mass $m_g$ the density can be written as

$$\rho(t) = \frac{m_g}{V(t)} \tag{A.5}$$

where $V(t)$ is the gas volume at any time $t$. If the cross sectional area, $A$, is constant through the chamber and bore then

$$V(t) = A x_p(t) \tag{A.6}$$

where $x_p(t)$ is the position of the base of the projectile. Substituting these expressions for density and volume into equation A.4, the following is obtained

$$\frac{1}{x_p}\frac{\partial x_p}{\partial t} = \frac{\partial u_{x_g}}{\partial x_g} \tag{A.7}$$

Integrating equation A.7 gives

$$\frac{1}{x_p}\frac{\partial x_p}{\partial t}\int_0^{x_g} \mathrm{d}x_g = \int_0^{u_{x_g}} \mathrm{d}u_{x_g} \tag{A.8}$$

and relationship between the gas velocity and the projectile velocity (where $dx/dt = u_p$) is obtained

$$u_{x_g}(x_g) = \frac{u_p}{x_p} x_g \tag{A.9}$$

It can be seen from equation A.9 that the gas particle velocity varies linearly, with the slope $u_p/x$, from the breech face to the projectile base and, as stated in [4],is a primary assumption of the Lagrange approximation.

Using this relation, the kinetic energy of the gas driving the projectile can now investigated. This is given as

$$KE_g = \frac{1}{2} m_g u_{x_g}^2 \tag{A.10}$$

But since $m_g$ can writtrn as a function of volume and density (by rearranging equation A.5) then equation A.10 can be rewritten as

$$KE_g = \frac{1}{2} \rho A \int_0^{x_p} u_{x_g}^2 \, \mathrm{d}x_g \tag{A.11}$$

substituting equation A.9 into the above gives

$$KE_g = \frac{1}{2} \rho A \int_0^{x_p} \frac{u_p^2}{x_p^2} x_g^2 \, \mathrm{d}x_g \tag{A.12}$$

which when evaluated becomes

$$KE_g = \frac{1}{6} \rho A x_p u_p^2 \tag{A.13}$$

and the total kinetic energy (ignoring recoil and recalling that $m_g = \rho A x$) is

$$KE_{tot} = KE_p + KE_g = \frac{1}{2} m_p u_p^2 + \frac{1}{6} m_g u_p^2 \tag{A.14}$$

This is an important result and will be used in the following derivation for $u_p(x)$. Assume that the reservoir of gas in the chamber is initially at $p_\circ$ and $\rho_\circ$. If the process that accelerates the projectile is isentropic the pressure at any time $t$ can be related

to the initial pressure using the isentropic relation.

$$\frac{p}{p_\circ} = \left(\frac{\rho}{\rho_\circ}\right)^{\gamma} = \left(\frac{v}{v_\circ}\right)^{-\gamma} \tag{A.15}$$

where $v$ is the specific volume of the gas and the ratio of the specific heats of the gas is given as $\gamma$. The volume of the gas driving the projectile $V(x_p)$ is given as

$$V(x_p) = (x_p + l)A \tag{A.16}$$

where $l$ is the chamber length. In terms of specific volume this is

$$v(x_p) = (x_p + l)\frac{A}{m_g} \tag{A.17}$$

Substituting this into the isentropic relation an expression for the average chamber pressure is obtained

$$\frac{\overline{p}}{\overline{p}_\circ} = \left(\frac{\rho}{\rho_\circ}\right)^{\gamma} = \left(\frac{v}{v_\circ}\right)^{-\gamma} \tag{A.18}$$

Now, if the work done on the system is given as

$$W = A\int_{x_\circ}^{x_p} \overline{p}\,\mathrm{d}x_p \tag{A.19}$$

then the left hand side of equation A.19 is equal to the change in kinetic energy of the system which is just

$$W = \Delta KE_{tot} = \frac{1}{2}\left(m_p + \frac{1}{3}m_g\right)\left[u_p^2(x_p) - u_p^2(x_\circ)\right] \tag{A.20}$$

Substituting this and equation A.18 into equation A.19 the following is obtained

$$\frac{1}{2}\left(m_p + \frac{1}{3}m_g\right)\left[u_p^2(x_p) - u_p^2(x_\circ)\right] = A\overline{p}_\circ\int_{x_\circ}^{x_p}\left(\frac{x_p + l}{x_\circ + l}\right)^{-\gamma}\mathrm{d}x_p \tag{A.21}$$

Evaluating this integral results in

$$\frac{1}{2}\left(m_p + \frac{1}{3}m_g\right)\left[u_p^2(x_p) - u_p^2(x_\circ)\right] = A\overline{p}_\circ \frac{\left[(x_p+l)^{(1-\gamma)} - (x_\circ+l)^{(1-\gamma)}\right]}{(1-\gamma)(x_\circ+l)^{-\gamma}} \tag{A.22}$$

Taking $u_\circ = 0$ at $x_\circ = 0$ further simplification gives

$$\frac{1}{2}m_p\left(1+\frac{1}{3}\frac{m_g}{m_p}\right)u_p^2(x_p) = \frac{Al\overline{p}_\circ}{(\gamma-1)}\left[1-\left(\frac{l}{x_p+l}\right)^{(\gamma-1)}\right] \tag{A.23}$$

Solving for $u_p^2(x)$

$$u_p^2(x_p) = \frac{1}{\left(1+\frac{1}{3}\frac{m_g}{m_p}\right)}\frac{2Al\overline{p}_\circ}{m_p(\gamma-1)}\left[1-\left(\frac{l}{x_p+l}\right)^{(\gamma-1)}\right] \tag{A.24}$$

Thus the solution for the projectile velocity given by the Lagrange Gradient approximation is

$$u_p(x_p) = \sqrt{\frac{1}{\left(1+\frac{1}{3}\frac{m_g}{m_p}\right)}\frac{2Al\overline{p}_\circ}{m_p(\gamma-1)}\left[1-\left(\frac{l}{x_p+l}\right)^{(\gamma-1)}\right]} \tag{A.25}$$

## APPENDIX B
## Simple Wave PPIG

This is a summary of the derivation presented by Seigel in [1]. Before tackling the derivation of the simple wave gun model, one must first have some understanding of how acoustic disturbances travel in a gas. This is due to the fact that changes in the gas, during the interal ballistics process, are a result of the acoustic disturbances travelling in the propellant. Though these disturbances are infinitesimal when taken individually, the sum of these disturbances cause finite changes in the propellant.

From figure B–1 it can be seen that the thickness of the gas layer changes over the duration d$t$ of the wave passage. Therefore the mass of gas in a layer of gas traversed by a wave is given as

$$A(u_D - u)\rho \mathrm{d}t = A(u_D - u - \mathrm{d}u)\mathrm{d}t(\rho + \mathrm{d}\rho) \tag{B.1}$$

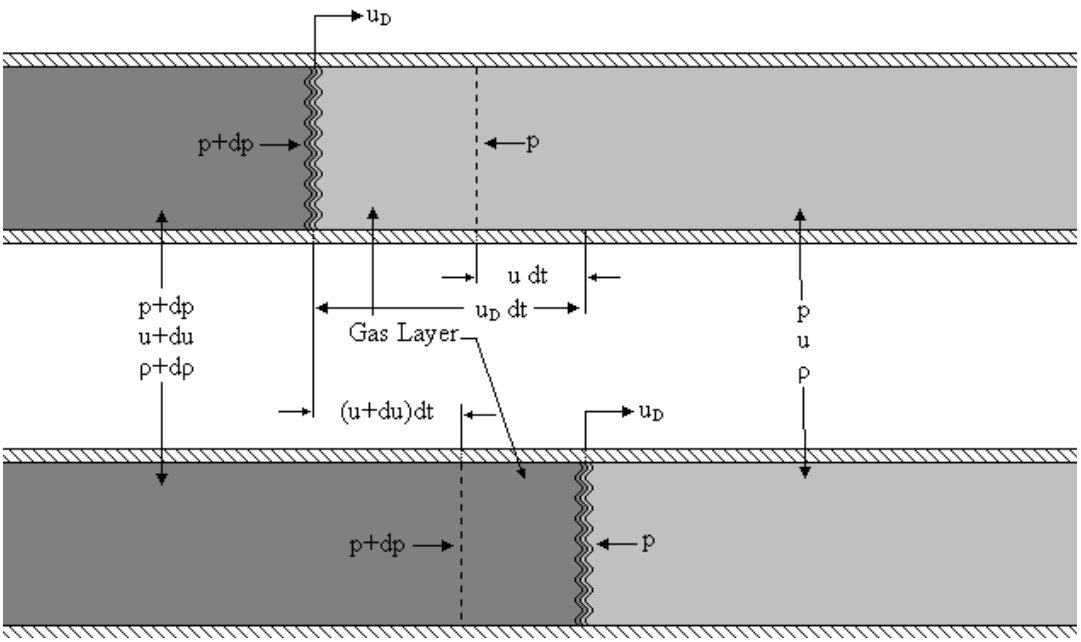


Figure B–1: Disturbance propogating through a gas in a tube

where

$u_D$ =Disturbance velocity

$A$ =Cross-Sectional Area of the Tube

This is the Continuity Equation for a disturbance in a gas.

From figure B–1 it can be seen that during the passage of the disturbance wave, a pressure value of $p + \mathrm{d}p$ acts on the left side of the layer. Whereas, the ambient pressure $p$ acts on the right side of the layer. Therefore the net pressure acting on the gas layer is $\mathrm{d}p$. This pressure variance across the disturbance results in an acceleration of the gas layer which by applying Newton's Law the layer gives

$$A\mathrm{d}p = A(u_D - u)\rho\mathrm{d}t\frac{\mathrm{d}u}{\mathrm{d}t} \tag{B.2}$$

This is the Momentum Equation for a disturbance travelling in a gas

Solving the mass equation for $\mathrm{d}u$ the following is obtained

$$\mathrm{d}u = \frac{\mathrm{d}\rho}{\rho + \mathrm{d}\rho}(u_D - u) \tag{B.3}$$

Substituting this into the momentum equation and solving for $\mathrm{d}p/\mathrm{d}\rho$ the following is obtained, for small $\mathrm{d}\rho$

Solving for $\mathrm{d}u$ our mass equation becomes

$$\frac{\mathrm{d}p}{\mathrm{d}\rho} = (u_D - u)^2 \tag{B.4}$$

Since the wave is assumed to be an acoustic wave then the sound speed is defined as

$$a^2 = \left(\frac{\partial p}{\partial \rho}\right)_s \tag{B.5}$$

Thus from equation B.4

$$a^2 = (u_D - u)^2 \tag{B.6}$$

which implies that

$$(u_D - u) = a \text{ or } (u_D + u) = a \tag{B.7}$$

From this it can be seen that the conservation of momentum equation becomes

$$\mathrm{d}p = a\rho \mathrm{d}u \tag{B.8}$$

across a $u + a$ disturbance wave or

$$\mathrm{d}p = -a\rho \mathrm{d}u \tag{B.9}$$

across a $u - a$ disturbance wave.

The quantity $a\rho$ can be seen as the acoustic inertia. It is the mass per unit time traversed by a disturbance wave. It can be seen from equations B.8 and B.9 that for a small $a\rho$, a small change in pressure results in a given velocity change, However, for large $a\rho$, the pressure change must be large to produce the same velocity change.

Rewriting these equations in terms of changes occurring while traveling along a disturbance rather than across a disturbance gives

$$\mathrm{d}p + a\rho \mathrm{d}u = 0 \tag{B.10}$$

along a $u + a$ disturbance path or

$$\mathrm{d}p - a\rho\mathrm{d}u = 0 \tag{B.11}$$

along a $u - a$ disturbance path.

These are the characteristic equations for a gas travelling in a constant diameter tube. The equations can be rewriten in the form of the "Riemann Function".

$$\mathrm{d}\sigma = \left(\frac{\mathrm{d}p}{a\rho}\right)_s \tag{B.12}$$

Thus the characteristic equations become

$$\mathrm{d}u + \mathrm{d}\sigma = 0 \tag{B.13}$$

along a characteristic line of slope $\mathrm{d}x/\mathrm{d}t = u + a$, and

$$\mathrm{d}u - \mathrm{d}\sigma = 0 \tag{B.14}$$

along a characteristic line of slope $\mathrm{d}x/\mathrm{d}t = u - a$. The $u + a$ and $u - a$ characteristic lines are thus the paths of disturbances.

For an infinitely long chamber equation B.10 represents what is known as the simple wave, This is the region swept out on a $t - x$ diagram by the first rarefaction disturbance produced by an accelerating projectile and when this wave, reflected from the breech wall, catches up with, and interacts with, this projectile.

From the definition of $\sigma$ equation B.13 can be rewritten as

$$\mathrm{d}u + \frac{\mathrm{d}p}{a\rho} = 0 \tag{B.15}$$

which upon integration becomes

$$u + \int \frac{\mathrm{d}p}{a\rho} = 0 \tag{B.16}$$

which in the form of the Riemann function becomes

$$u + \sigma = \sigma_\circ \tag{B.17}$$

Where the velocity, $u$, is taken to be zero when $p = p_\circ$ and $\sigma = \sigma_\circ$

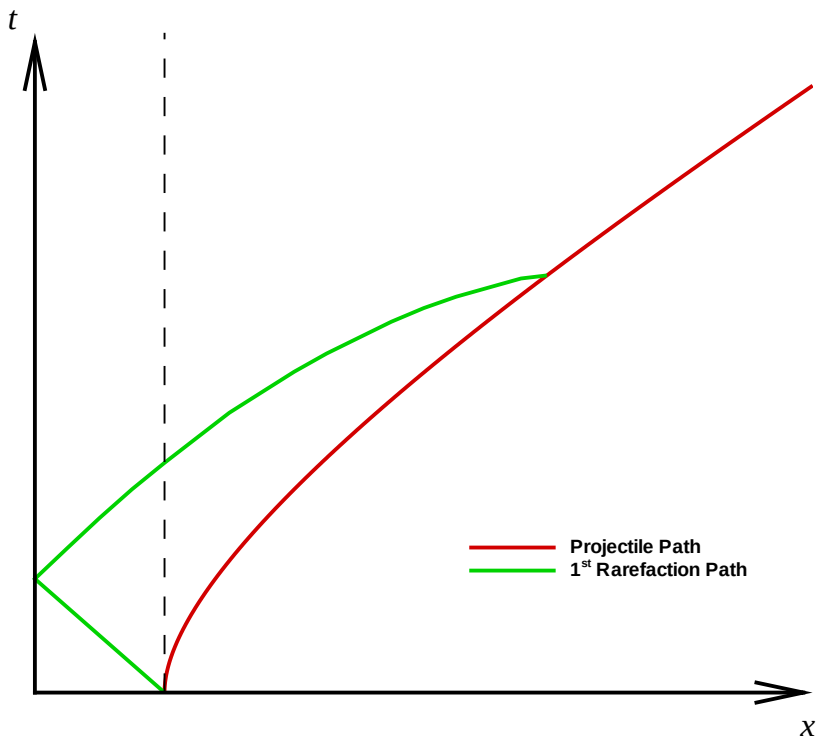


Figure B–2: $x-t$ diagram showing the paths of the projectile and the first rarefaction wave

Returning to the equation for traveling along an $u + a$ characteristic

$$\mathrm{d}p = -a\rho\mathrm{d}u \tag{B.18}$$

which when integrate gives

$$u = \int_{p}^{p_\circ} \frac{\mathrm{d}p}{a\rho} \tag{B.19}$$

It is seen that the velocity of the gas expanding from rest at the initial pressure $p_\circ$ in a constant diameter, infinite chamber gun, depends only on the relationship between the pressure and the acoustic impedance.

For an ideal gas undergoing an isentropic process the following relations apply

$$p = \rho RT \tag{B.20}$$

$$p = \rho^\gamma \frac{p_\circ}{\rho_\circ} \tag{B.21}$$

The acoustic impedence becomes

$$a\rho = \frac{\gamma p_\circ}{a_\circ} \left(\frac{p}{p_\circ}\right)^{\frac{\gamma+1}{2\gamma}} \tag{B.22}$$

For an ideal gas, the sound speed is

$$a^2 = \frac{\gamma p}{\rho} = \gamma RT \tag{B.23}$$

and the Riemann function becomes

$$\sigma = \frac{2a}{\gamma - 1} \tag{B.24}$$

where $\sigma = 0$ at $a = 0$

Substituting equation B.22 into equation B.15 and performing the integration with $p = p_\circ$ at $u = u_\circ = 0$ the following is obtained

$$\frac{p}{p_\circ} = \left(1 - \frac{(\gamma - 1)}{2a_\circ} u\right)^{\frac{2\gamma}{\gamma - 1}} \tag{B.25}$$

Furthermore the maximum (escape) velocity can be determined in the limit of $p/p_\circ \to 0$ This can be shown to be

$$u_{esc} = \frac{2a_\circ}{\gamma - 1} \tag{B.26}$$

From this it can be seen that as $a_\circ \to \infty$ or $\gamma \to 1$ that $u_{esc} \to \infty$.

Recalling Newton's Law

$$m_p \frac{\mathrm{d}u}{\mathrm{d}t} = pA \tag{B.27}$$

From equation B.25 and equation B.27 the following is obtained

$$u\left(1 - \frac{(\gamma - 1)}{2a_\circ} u\right)^{-\left(\frac{2\gamma}{\gamma - 1}\right)} \mathrm{d}u = \frac{p_\circ A}{m_p} \mathrm{d}x \tag{B.28}$$

This can be integrated with $u = 0$ at $x = 0$ to obtain

$$x = \frac{2m_p a_\circ^2}{A p_\circ (\gamma + 1)} \left\{ \frac{\frac{2}{\gamma - 1} - \frac{\gamma + 1}{\gamma - 1}\left[1 - \frac{(\gamma - 1)}{2a_\circ} u\right]}{\left[1 - \frac{(\gamma - 1)}{2a_\circ} u\right]^{\frac{\gamma + 1}{2(\gamma - 1)}}} + 1 \right\} \tag{B.29}$$

This is the Simple Wave Gun solution for an ideal gas.

## APPENDIX C
## Gun Materials

Table C–1: Tube Strength for steel Alloy 1020 (Hot Rolled)

| $\rho = 7850$ kg/m$^3$, $\sigma_y = 210$ MPa, $\sigma_u = 380$ MPa | | | | | |
|---|---|---|---|---|---|
| $T_r$ | $\frac{m}{l}[kg/m]$ | $(p_i)_{max}$ [MPa] | $(p_f)_1$ [MPa] | $(p_f)_2$ [MPa] | $(p_f)_3$ [MPa] |
| 0.05 | $1294.7d_i^2$ | 19.95 | 36.19 | 36.22 | 33.45 |
| 0.25 | $7706.7d_i^2$ | 80.77 | 152.0 | 154.1 | 142.3 |
| 0.5 | $18496.1d_i^2$ | 126.0 | 253.3 | 263.4 | 243.3 |
| 0.75 | $32368.2d_i^2$ | 152.1 | 325.7 | 348.2 | 321.6 |
| 1 | $49323.0d_i^2$ | 168.0 | 380.0 | 417.5 | 385.6 |
| 2 | $147969.0d_i^2$ | 193.8 | 506.7 | 611.6 | 564.9 |

Table C–2: Tube Strength for steel Alloy 1020 (Cold Worked)

| $\rho = 7850$ kg/m$^3$, $\sigma_y = 350$ MPa, $\sigma_u = 420$ MPa | | | | | |
|---|---|---|---|---|---|
| $T_r$ | $\frac{m}{l}[kg/m]$ | $(p_i)_{max}$ [MPa] | $(p_f)_1$ [MPa] | $(p_f)_2$ [MPa] | $(p_f)_3$ [MPa] |
| 0.05 | $1294.7d_i^2$ | 33.26 | 40.00 | 40.03 | 44.94 |
| 0.25 | $7706.7d_i^2$ | 134.6 | 168.0 | 170.3 | 191.2 |
| 0.5 | $18496.1d_i^2$ | 210.0 | 280.0 | 291.1 | 326.8 |
| 0.75 | $32368.2d_i^2$ | 253.4 | 360.0 | 384.8 | 432.0 |
| 1 | $49323.0d_i^2$ | 280.0 | 420.0 | 461.4 | 518.0 |
| 2 | $147969.0d_i^2$ | 323.1 | 560.0 | 676.0 | 758.9 |

Table C–3: Tube Strength for steel Alloy 1020 (Annealed)

| $\rho = 7850$ kg/m$^3$, $\sigma_y = 295$ MPa, $\sigma_u = 395$ MPa | | | | | |
|---|---|---|---|---|---|
| $T_r$ | $\frac{m}{l}[kg/m]$ | $(p_i)_{max}$ [MPa] | $(p_f)_1$ [MPa] | $(p_f)_2$ [MPa] | $(p_f)_3$ [MPa] |
| 0.05 | $1294.7d_i^2$ | 28.03 | 37.62 | 37.65 | 40.69 |
| 0.25 | $7706.7d_i^2$ | 113.5 | 158.0 | 160.2 | 173.1 |
| 0.5 | $18496.1d_i^2$ | 177.0 | 263.3 | 273.8 | 295.9 |
| 0.75 | $32368.2d_i^2$ | 213.6 | 338.6 | 361.9 | 391.1 |
| 1 | $49323.0d_i^2$ | 236.0 | 395.0 | 434.0 | 469.0 |
| 2 | $147969.0d_i^2$ | 272.3 | 526.7 | 635.7 | 687.0 |

Table C–4: Tube Strength for steel Alloy 1020 (Normalized)

| $\rho = 7850$ kg/m$^3$, $\sigma_y = 345$ MPa, $\sigma_u = 440$ MPa | | | | | |
|---|---|---|---|---|---|
| $T_r$ | $\frac{m}{l}[kg/m]$ | $(p_i)_{max}$ [MPa] | $(p_f)_1$ [MPa] | $(p_f)_2$ [MPa] | $(p_f)_3$ [MPa] |
| 0.05 | $1294.7d_i^2$ | 32.78 | 41.90 | 41.94 | 46.17 |
| 0.25 | $7706.7d_i^2$ | 132.7 | 176.0 | 178.4 | 196.4 |
| 0.5 | $18496.1d_i^2$ | 207.0 | 293.3 | 305.0 | 335.7 |
| 0.75 | $32368.2d_i^2$ | 249.8 | 377.1 | 403.2 | 443.8 |
| 1 | $49323.0d_i^2$ | 276.0 | 440.0 | 483.4 | 532.1 |
| 2 | $147969.0d_i^2$ | 318.5 | 586.7 | 708.2 | 779.6 |

Table C–5: Tube Strength for steel Alloy 1040 (Hot Rolled)

| $\rho = 7850$ kg/m$^3$, $\sigma_y = 290$ MPa, $\sigma_u = 520$ MPa | | | | | |
|---|---|---|---|---|---|
| $T_r$ | $\frac{m}{l}[kg/m]$ | $(p_i)_{max}$ [MPa] | $(p_f)_1$ [MPa] | $(p_f)_2$ [MPa] | $(p_f)_3$ [MPa] |
| 0.05 | $1294.7d_i^2$ | 27.56 | 49.56 | 49.56 | 46.03 |
| 0.25 | $7706.7d_i^2$ | 111.5 | 208.0 | 210.8 | 195.8 |
| 0.5 | $18496.1d_i^2$ | 174.0 | 346.7 | 360.4 | 334.8 |
| 0.75 | $32368.2d_i^2$ | 210.0 | 445.7 | 476.5 | 442.5 |
| 1 | $49323.0d_i^2$ | 232.0 | 520.0 | 571.3 | 530.6 |
| 2 | $147969.0d_i^2$ | 267.7 | 693.3 | 836.9 | 777.3 |

Table C–6: Tube Strength for steel Alloy 1040 (Cold Worked)

| $\rho = 7850$ kg/m$^3$, $\sigma_y = 490$ MPa, $\sigma_u = 590$ MPa | | | | | |
|---|---|---|---|---|---|
| $T_r$ | $\frac{m}{l}[kg/m]$ | $(p_i)_{max}$ [MPa] | $(p_f)_1$ [MPa] | $(p_f)_2$ [MPa] | $(p_f)_3$ [MPa] |
| 0.05 | $1294.7d_i^2$ | 46.56 | 56.19 | 56.23 | 63.07 |
| 0.25 | $7706.7d_i^2$ | 188.5 | 236.0 | 239.2 | 268.3 |
| 0.5 | $18496.1d_i^2$ | 294.0 | 393.3 | 409.0 | 458.7 |
| 0.75 | $32368.2d_i^2$ | 354.8 | 505.7 | 540.6 | 606.3 |
| 1 | $49323.0d_i^2$ | 392.0 | 590.0 | 648.2 | 727.0 |
| 2 | $147969.0d_i^2$ | 452.3 | 786.7 | 949.6 | 1065.0 |

Table C–7: Tube Strength for steel Alloy 1040 (Annealed)

| $\rho = 7850$ kg/m$^3$, $\sigma_y = 355$ MPa, $\sigma_u = 520$ MPa | | | | | |
|---|---|---|---|---|---|
| $T_r$ | $\frac{m}{l}[kg/m]$ | $(p_i)_{max}$ [MPa] | $(p_f)_1$ [MPa] | $(p_f)_2$ [MPa] | $(p_f)_3$ [MPa] |
| 0.05 | $1294.7d_i^2$ | 33.73 | 49.56 | 49.56 | 51.47 |
| 0.25 | $7706.7d_i^2$ | 136.5 | 208.0 | 210.8 | 218.9 |
| 0.5 | $18496.1d_i^2$ | 213.0 | 346.7 | 360.4 | 374.3 |
| 0.75 | $32368.2d_i^2$ | 257.1 | 445.7 | 476.5 | 494.8 |
| 1 | $49323.0d_i^2$ | 284.0 | 520.0 | 571.3 | 593.2 |
| 2 | $147969.0d_i^2$ | 327.7 | 693.3 | 836.9 | 869.1 |

Table C–8: Tube Strength for steel Alloy 1040 (Normalized)

| $\rho = 7850$ kg/m$^3$, $\sigma_y = 375$ MPa, $\sigma_u = 590$ MPa | | | | | |
|---|---|---|---|---|---|
| $T_r$ | $\frac{m}{l}[kg/m]$ | $(p_i)_{max}$ [MPa] | $(p_f)_1$ [MPa] | $(p_f)_2$ [MPa] | $(p_f)_3$ [MPa] |
| 0.05 | $1294.7d_i^2$ | 35.63 | 56.19 | 56.23 | 56.31 |
| 0.25 | $7706.7d_i^2$ | 144.2 | 236.0 | 239.2 | 239.6 |
| 0.5 | $18496.1d_i^2$ | 225.0 | 393.3 | 409.0 | 409.5 |
| 0.75 | $32368.2d_i^2$ | 271.6 | 505.7 | 540.6 | 541.3 |
| 1 | $49323.0d_i^2$ | 300.0 | 590.0 | 648.2 | 649.1 |
| 2 | $147969.0d_i^2$ | 346.2 | 786.7 | 949.6 | 950.9 |

Table C–9: Tube Strength for steel Alloy 4140 (Annealed)

| $\rho = 7850$ kg/m$^3$, $\sigma_y = 417$ MPa, $\sigma_u = 655$ MPa | | | | | |
|---|---|---|---|---|---|
| $T_r$ | $\frac{m}{l}[kg/m]$ | $(p_i)_{max}$ [MPa] | $(p_f)_1$ [MPa] | $(p_f)_2$ [MPa] | $(p_f)_3$ [MPa] |
| 0.05 | $1294.7d_i^2$ | 39.62 | 62.38 | 62.43 | 62.57 |
| 0.25 | $7706.7d_i^2$ | 160.4 | 262.0 | 265.6 | 266.2 |
| 0.5 | $18496.1d_i^2$ | 250.2 | 436.7 | 454.0 | 455.0 |
| 0.75 | $32368.2d_i^2$ | 302.0 | 561.4 | 600.2 | 601.5 |
| 1 | $49323.0d_i^2$ | 333.6 | 655.0 | 719.6 | 721.2 |
| 2 | $147969.0d_i^2$ | 384.9 | 873.3 | 1054.2 | 1056.5 |

Table C–10: Tube Strength for steel Alloy 4140 (Normalized)

| $\rho = 7850$ kg/m$^3$, $\sigma_y = 655$ MPa, $\sigma_u = 1020$ MPa | | | | | |
|---|---|---|---|---|---|
| $T_r$ | $\frac{m}{l}[kg/m]$ | $(p_i)_{max}$ [MPa] | $(p_f)_1$ [MPa] | $(p_f)_2$ [MPa] | $(p_f)_3$ [MPa] |
| 0.05 | $1294.7d_i^2$ | 62.24 | 97.14 | 97.22 | 97.88 |
| 0.25 | $7706.7d_i^2$ | 251.9 | 408.0 | 413.6 | 416.4 |
| 0.5 | $18496.1d_i^2$ | 393.0 | 680.0 | 707.0 | 711.8 |
| 0.75 | $32368.2d_i^2$ | 474.3 | 874.3 | 934.6 | 941.0 |
| 1 | $49323.0d_i^2$ | 524.0 | 1020.0 | 1120.6 | 1128.2 |
| 2 | $147969.0d_i^2$ | 604.6 | 1360.0 | 1641.6 | 1652.9 |

Table C–11: Tube Strength for steel Alloy 4140 (Oil Quenched and Tempered)

| $\rho = 7850$ kg/m$^3$, $\sigma_y = 1570$ MPa, $\sigma_u = 1720$ MPa | | | | | |
|---|---|---|---|---|---|
| $T_r$ | $\frac{m}{l}[kg/m]$ | $(p_i)_{max}$ [MPa] | $(p_f)_1$ [MPa] | $(p_f)_2$ [MPa] | $(p_f)_3$ [MPa] |
| 0.05 | $1294.7d_i^2$ | 149.2 | 163.8 | 163.9 | 187.9 |
| 0.25 | $7706.7d_i^2$ | 603.8 | 688.0 | 697.4 | 799.2 |
| 0.5 | $18496.1d_i^2$ | 942.0 | 1146.7 | 1192.2 | 1366.2 |
| 0.75 | $32368.2d_i^2$ | 1137.0 | 1474.3 | 1576.0 | 1806.0 |
| 1 | $49323.0d_i^2$ | 1256.0 | 1720.0 | 1889.6 | 2165.3 |
| 2 | $147969.0d_i^2$ | 1449.2 | 2293.3 | 2768.2 | 3172.1 |

Table C–12: Tube Strength for steel Alloy 4340 (Annealed)

| $\rho = 7850$ kg/m$^3$, $\sigma_y = 472$ MPa, $\sigma_u = 745$ MPa | | | | | |
|---|---|---|---|---|---|
| $T_r$ | $\frac{m}{l}[kg/m]$ | $(p_i)_{max}$ [MPa] | $(p_f)_1$ [MPa] | $(p_f)_2$ [MPa] | $(p_f)_3$ [MPa] |
| 0.05 | $1294.7d_i^2$ | 44.85 | 70.95 | 71.01 | 70.98 |
| 0.25 | $7706.7d_i^2$ | 181.5 | 298.0 | 302.1 | 302.0 |
| 0.5 | $18496.1d_i^2$ | 283.2 | 496.7 | 516.4 | 516.2 |
| 0.75 | $32368.2d_i^2$ | 341.8 | 638.6 | 682.6 | 682.4 |
| 1 | $49323.0d_i^2$ | 377.6 | 745.0 | 818.5 | 818.2 |
| 2 | $147969.0d_i^2$ | 435.7 | 993.3 | 1199.0 | 1198.6 |

Table C–13: Tube Strength for steel Alloy 4340 (Normalized)

| $\rho = 7850$ kg/m$^3$, $\sigma_y = 862$ MPa, $\sigma_u = 1280$ MPa | | | | | |
|---|---|---|---|---|---|
| $T_r$ | $\frac{m}{l}[kg/m]$ | $(p_i)_{max}$ [MPa] | $(p_f)_1$ [MPa] | $(p_f)_2$ [MPa] | $(p_f)_3$ [MPa] |
| 0.05 | $1294.7d_i^2$ | 81.91 | 121.9 | 122.0 | 125.8 |
| 0.25 | $7706.7d_i^2$ | 331.5 | 512.0 | 519.0 | 535.4 |
| 0.5 | $18496.1d_i^2$ | 517.2 | 853.3 | 887.2 | 915.2 |
| 0.75 | $32368.2d_i^2$ | 624.2 | 1097.1 | 1172.9 | 1209.9 |
| 1 | $49323.0d_i^2$ | 689.6 | 1280.0 | 1406.2 | 1450.6 |
| 2 | $147969.0d_i^2$ | 795.7 | 1706.7 | 2060.1 | 2125.1 |

Table C–14: Tube Strength for steel Alloy 4340 (Oil Quenched and Tempered)

| $\rho = 7850$ kg/m$^3$, $\sigma_y = 1620$ MPa, $\sigma_u = 1760$ MPa | | | | | |
|---|---|---|---|---|---|
| $T_r$ | $\frac{m}{l}[kg/m]$ | $(p_i)_{max}$ [MPa] | $(p_f)_1$ [MPa] | $(p_f)_2$ [MPa] | $(p_f)_3$ [MPa] |
| 0.05 | $1294.7d_i^2$ | 153.9 | 167.7 | 167.7 | 193.8 |
| 0.25 | $7706.7d_i^2$ | 623.1 | 704.0 | 713.6 | 824.6 |
| 0.5 | $18496.1d_i^2$ | 972.0 | 1173.3 | 1219.9 | 1409.7 |
| 0.75 | $32368.2d_i^2$ | 1173.1 | 1508.6 | 1612.7 | 1863.5 |
| 1 | $49323.0d_i^2$ | 1296.0 | 1760.0 | 1933.6 | 2234.3 |
| 2 | $147969.0d_i^2$ | 1495.4 | 2346.7 | 2832.6 | 3273.2 |

Table C–15: Tube Strength for Stainless Alloy A440 (Annealed)

| $\rho = 7800$ kg/m$^3$, $\sigma_y = 415$ MPa, $\sigma_u = 725$ MPa | | | | | |
|---|---|---|---|---|---|
| $T_r$ | $\frac{m}{l}[kg/m]$ | $(p_i)_{max}$ [MPa] | $(p_f)_1$ [MPa] | $(p_f)_2$ [MPa] | $(p_f)_3$ [MPa] |
| 0.05 | $1286.5d_i^2$ | 39.43 | 69.05 | 69.10 | 65.20 |
| 0.25 | $7657.6d_i^2$ | 159.6 | 290.0 | 294.0 | 277.4 |
| 0.5 | $18378.3d_i^2$ | 249.0 | 483.3 | 502.5 | 474.2 |
| 0.75 | $32162.1d_i^2$ | 300.5 | 621.4 | 664.3 | 626.8 |
| 1 | $49008.8d_i^2$ | 332.0 | 725.0 | 796.5 | 751.6 |
| 2 | $147026.5d_i^2$ | 383.1 | 966.7 | 1166.8 | 1101.0 |

Table C–16: Tube Strength for Stainless Alloy A440 (Tempered)

| $\rho = 7800$ kg/m$^3$, $\sigma_y = 1650$ MPa, $\sigma_u = 1790$ MPa | | | | | |
|---|---|---|---|---|---|
| $T_r$ | $\frac{m}{l}[kg/m]$ | $(p_i)_{max}$ [MPa] | $(p_f)_1$ [MPa] | $(p_f)_2$ [MPa] | $(p_f)_3$ [MPa] |
| 0.05 | $1286.5d_i^2$ | 156.8 | 170.5 | 170.6 | 195.8 |
| 0.25 | $7657.6d_i^2$ | 634.6 | 716.0 | 725.8 | 832.9 |
| 0.5 | $18378.3d_i^2$ | 990.0 | 1193.3 | 1240.7 | 1423.9 |
| 0.75 | $32162.1d_i^2$ | 1194.8 | 1534.3 | 1640.2 | 1882.3 |
| 1 | $49008.8d_i^2$ | 1320.0 | 1790.0 | 1966.5 | 2256.8 |
| 2 | $147026.5d_i^2$ | 1523.1 | 2386.7 | 2880.9 | 3306.2 |

Table C–17: Mass per unit length for Steel Alloys [kg/m]

| $T_r$ | $d_i = 0.5$” | $d_i = 1$” | $d_i = 2$” | $d_i = 4$” | $d_i = 8$” | $d_i = 16$” |
|---|---|---|---|---|---|---|
| 0.05 | 0.2088 | 0.8353 | 3.3412 | 13.365 | 53.460 | 213.84 |
| 0.25 | 1.2430 | 4.9721 | 19.888 | 79.553 | 318.21 | 1272.9 |
| 0.5 | 2.9832 | 11.933 | 47.732 | 190.93 | 763.71 | 3054.8 |
| 0.75 | 5.2207 | 20.883 | 83.531 | 334.12 | 1336.5 | 5346.0 |
| 1 | 7.9553 | 31.821 | 127.28 | 509.14 | 2036.6 | 8146.2 |
| 2 | 23.866 | 95.464 | 381.85 | 1527.4 | 6109.7 | 24438 |

Table C–18: Mass per unit length for steel Alloy A440 [kg/m]

| $T_r$ | $d_i = 0.5$” | $d_i = 1$” | $d_i = 2$” | $d_i = 4$” | $d_i = 8$” | $d_i = 16$” |
|---|---|---|---|---|---|---|
| 0.05 | 0.2075 | 0.8300 | 3.3199 | 13.280 | 53.119 | 212.48 |
| 0.25 | 1.2351 | 4.9404 | 19.762 | 79.046 | 316.19 | 1264.7 |
| 0.5 | 2.9642 | 11.857 | 47.428 | 189.71 | 758.85 | 3035.4 |
| 0.75 | 5.1874 | 20.750 | 82.997 | 332.00 | 1328.0 | 5311.9 |
| 1 | 7.9046 | 31.619 | 126.47 | 505.90 | 2026.6 | 8094.3 |
| 2 | 23.714 | 95.856 | 379.42 | 1517.7 | 6070.8 | 24283 |

# APPENDIX D
## Results for $u_{1st}$ as a function of $a_\circ$ for different $M_F$ and $\gamma$

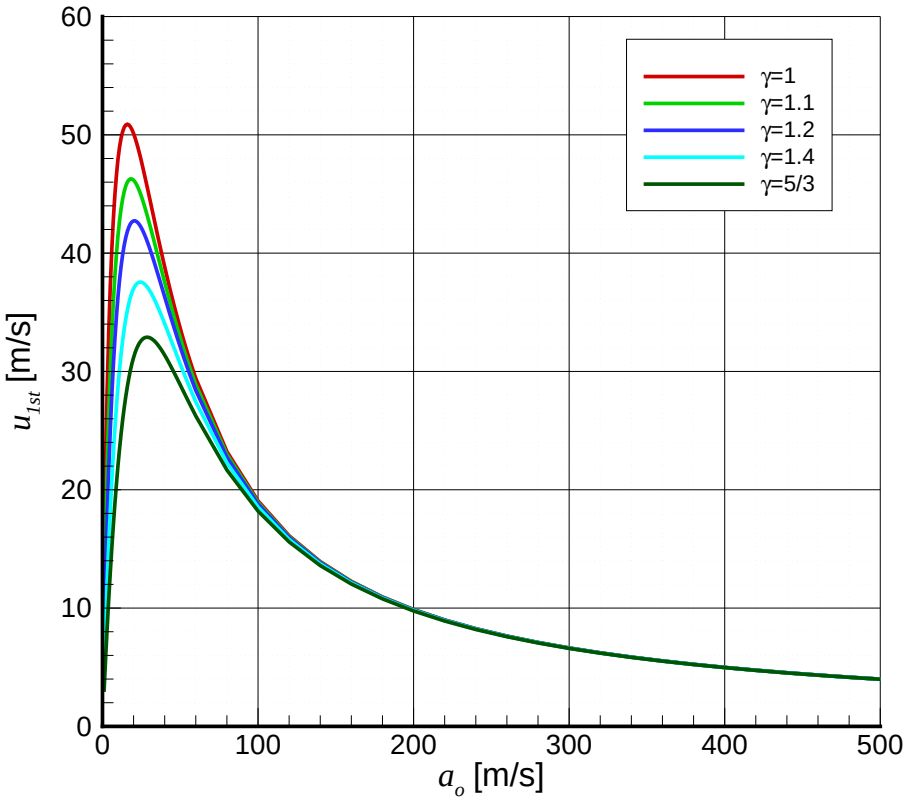


Figure D–1: $u_{1st}$ vs. $a_\circ$ for different $\gamma$ and $M_F = 1$ kPa m$^3$/kg

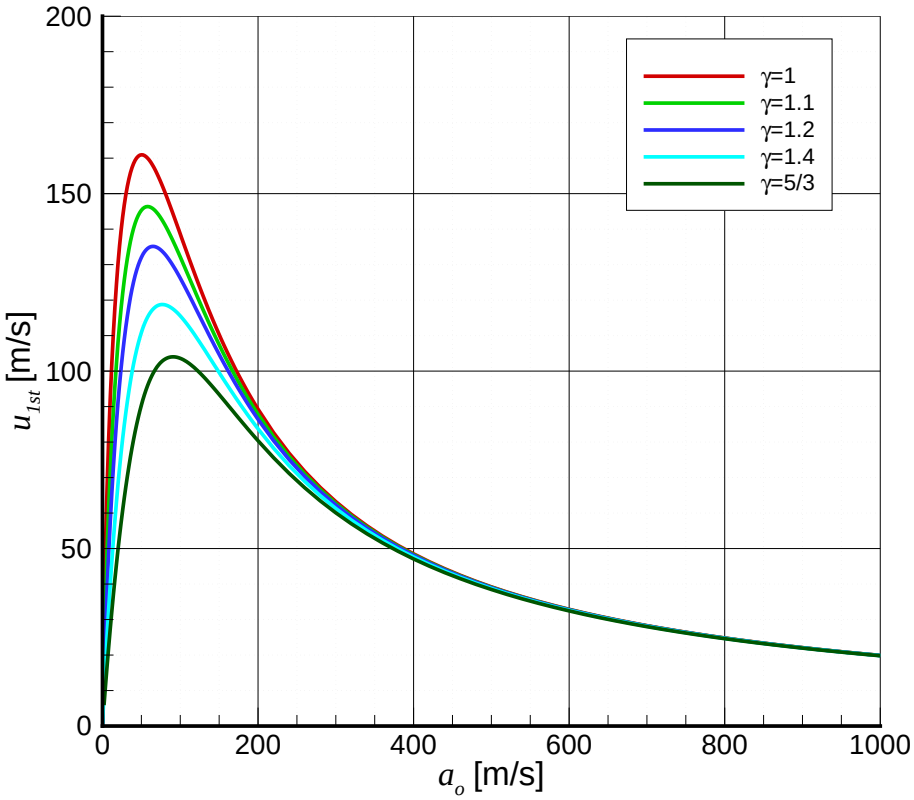


Figure D–2: $u_{1st}$ vs. $a_\circ$ for different $\gamma$ and $M_F = 10$ kPa m$^3$/kg

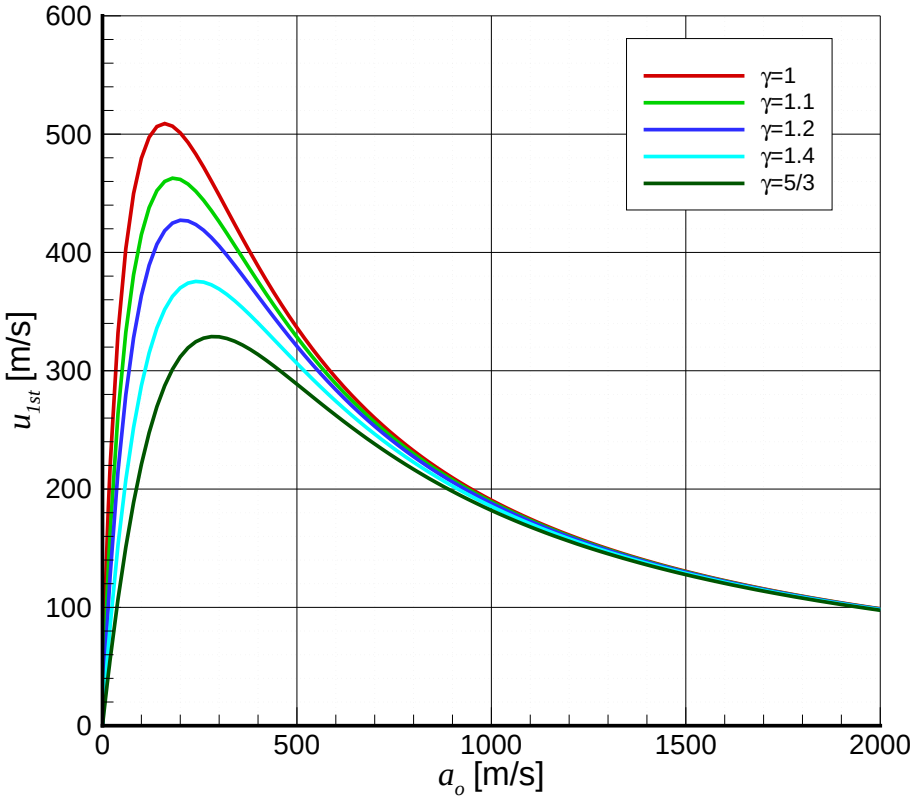


Figure D–3: $u_{1st}$ vs. $a_\circ$ for different $\gamma$ and $M_F = 100$ kPa m$^3$/kg

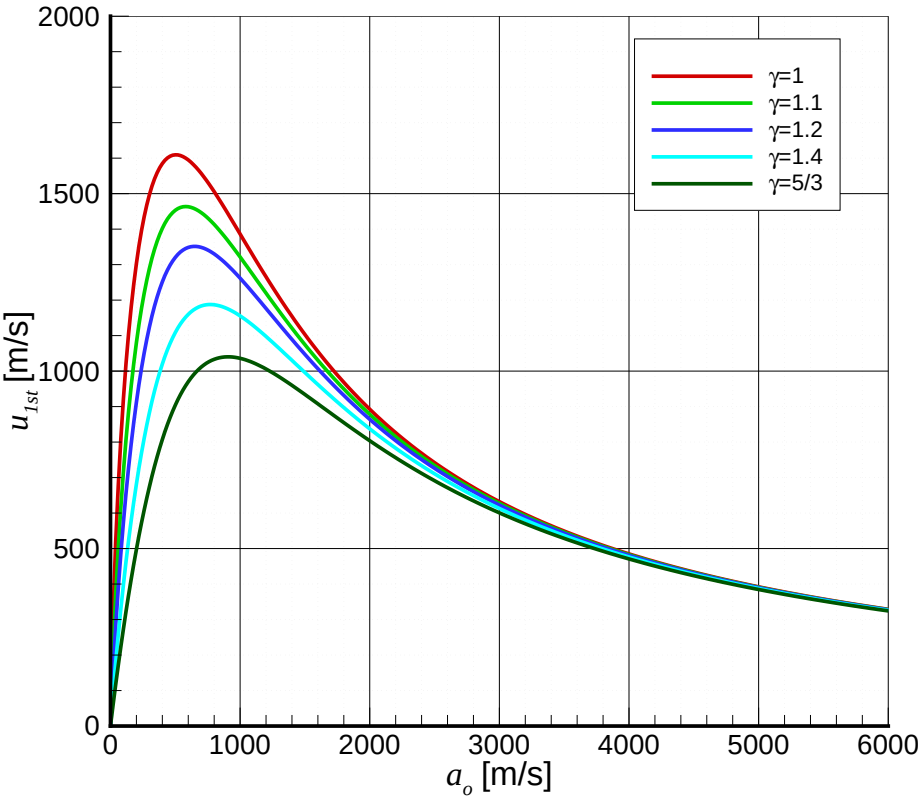


Figure D–4: $u_{1st}$ vs. $a_\circ$ for different $\gamma$ and $M_F = 1,000$ kPa m$^3$/kg

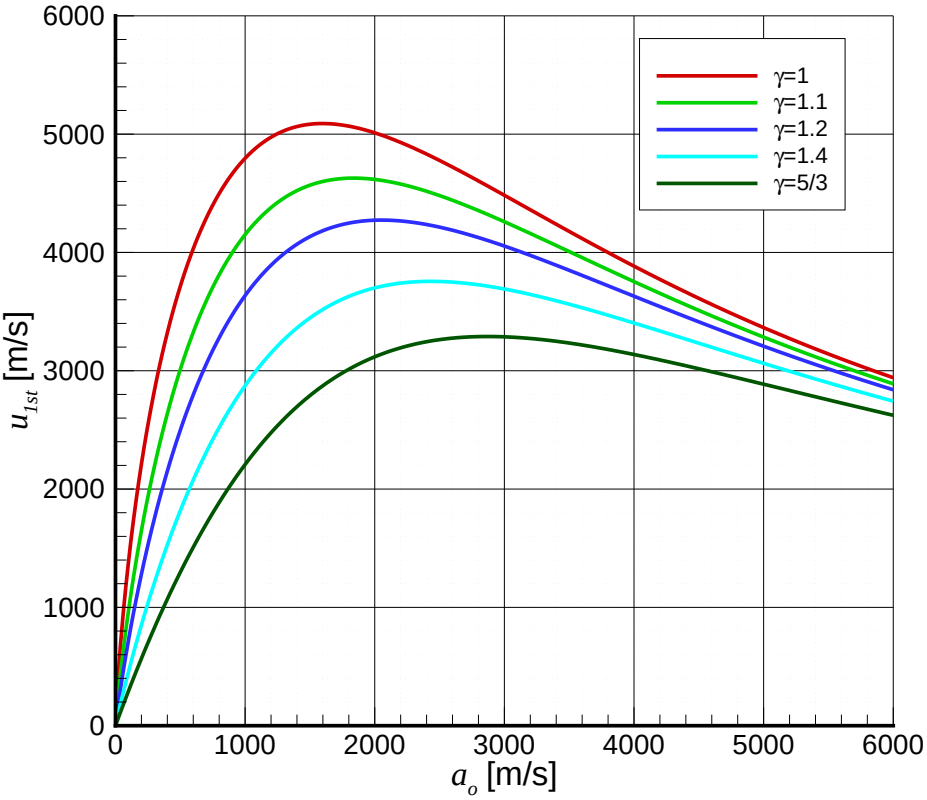


Figure D–5: $u_{1st}$ vs. $a_\circ$ for different $\gamma$ and $M_F = 10,000$ kPa m$^3$/kg

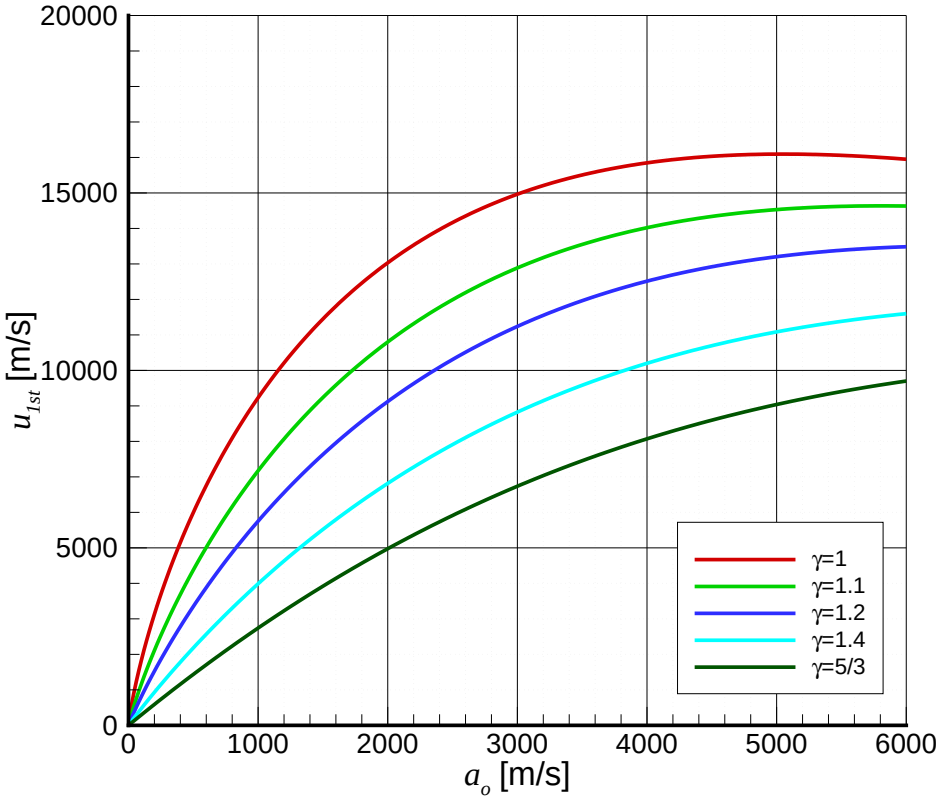


Figure D–6: $u_{1st}$ vs. $a_\circ$ for different $\gamma$ and $M_F = 100,000$ kPa m$^3$/kg

# APPENDIX E
## Prototype Design Drawings

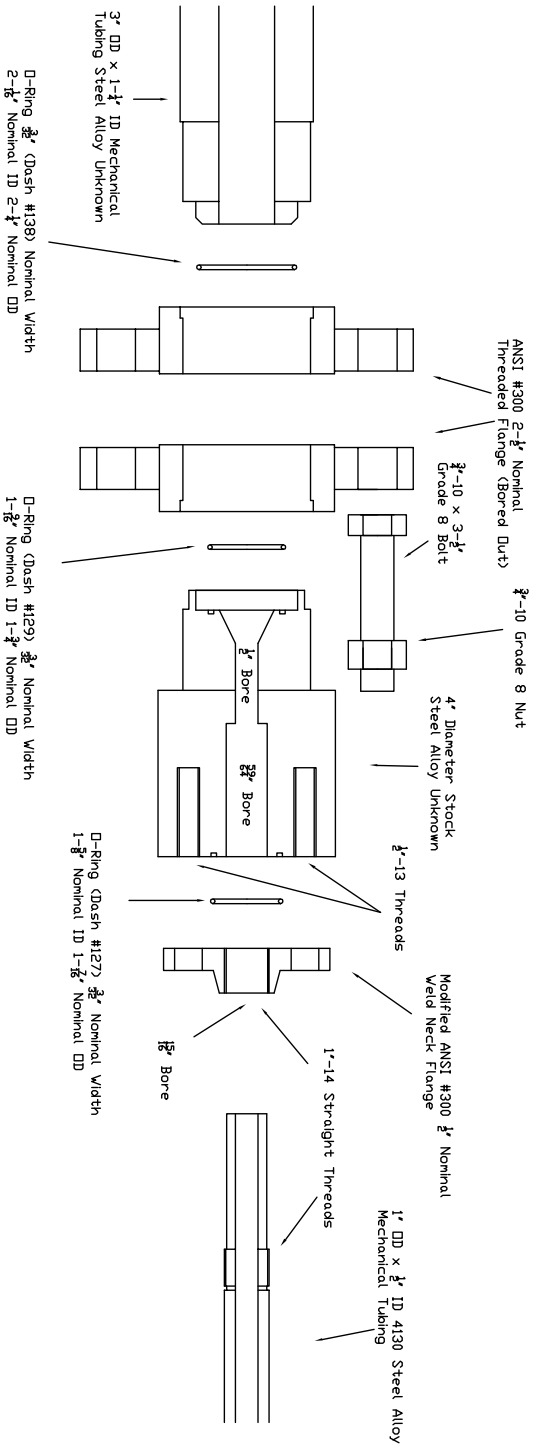


Figure E–1: Initial Breech and Driver Concept

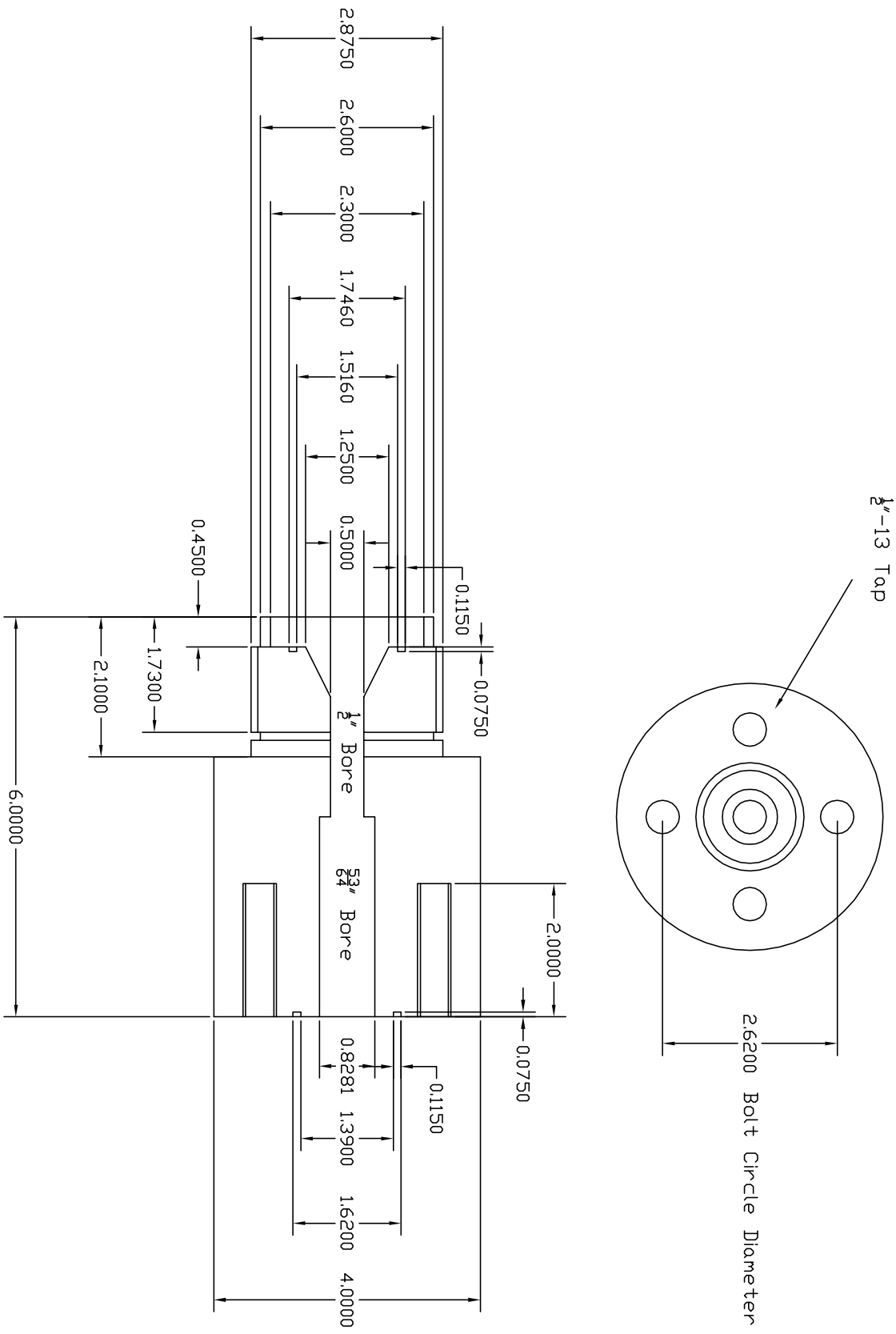


Figure E–2: Original Breech Design Dimensions (inches)

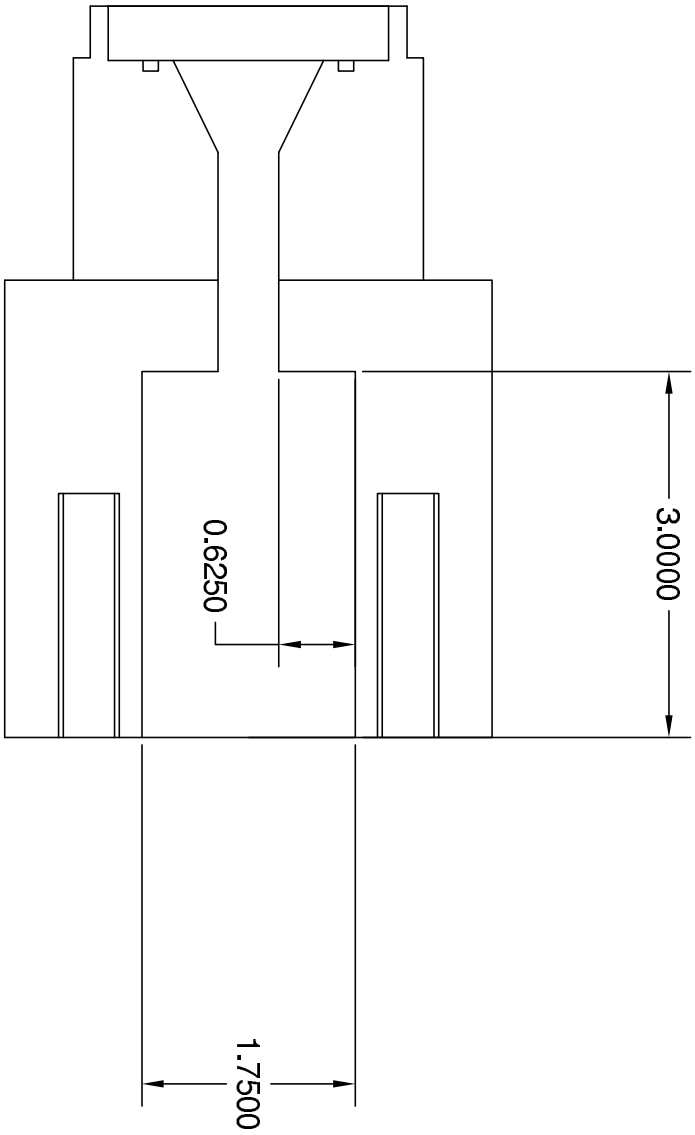


Figure E–3: Original Breech Expanded Dimensions for Barrel Extention (inches)

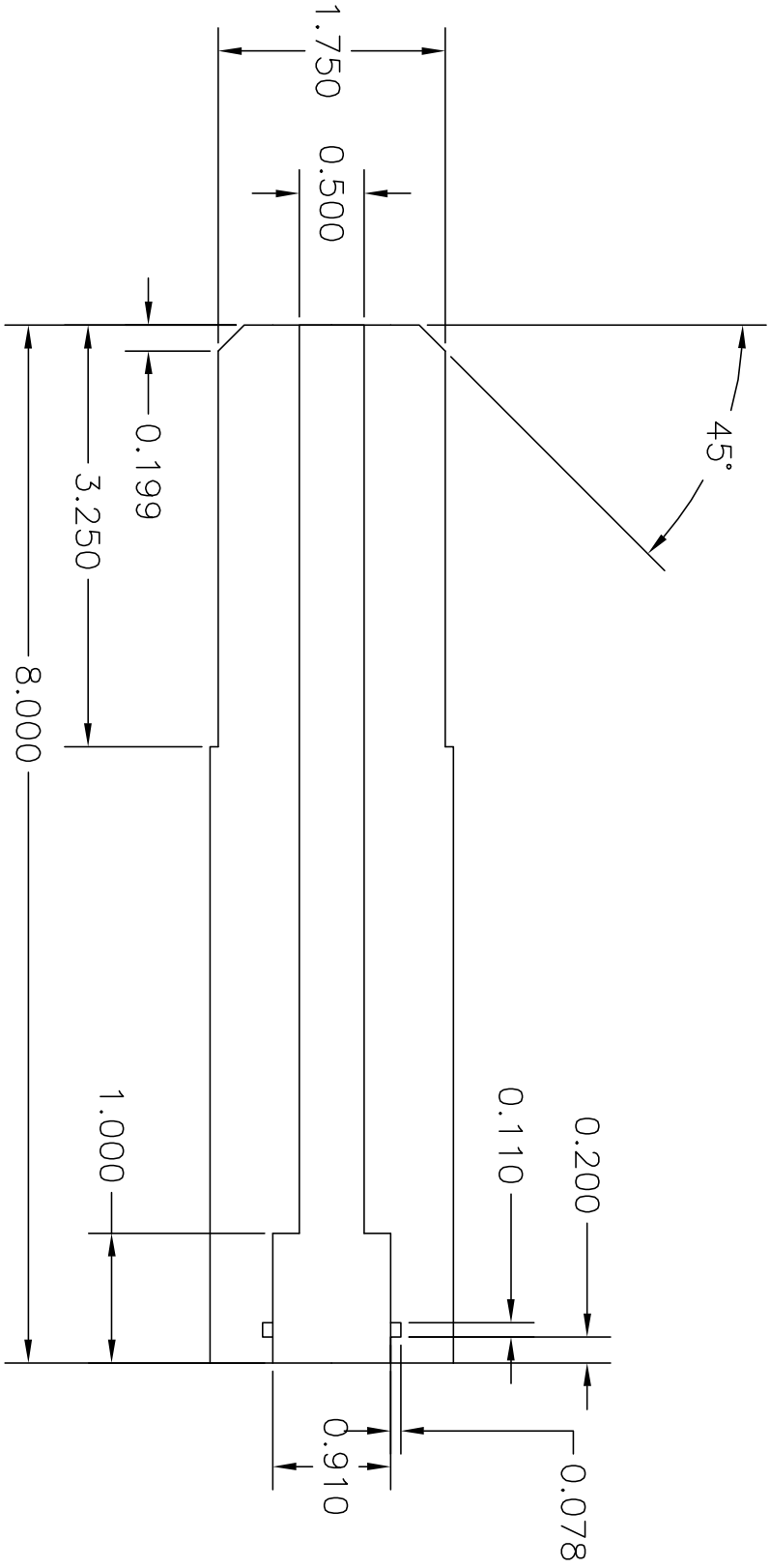


Figure E–4: Barrel Extension Dimensions (inches)

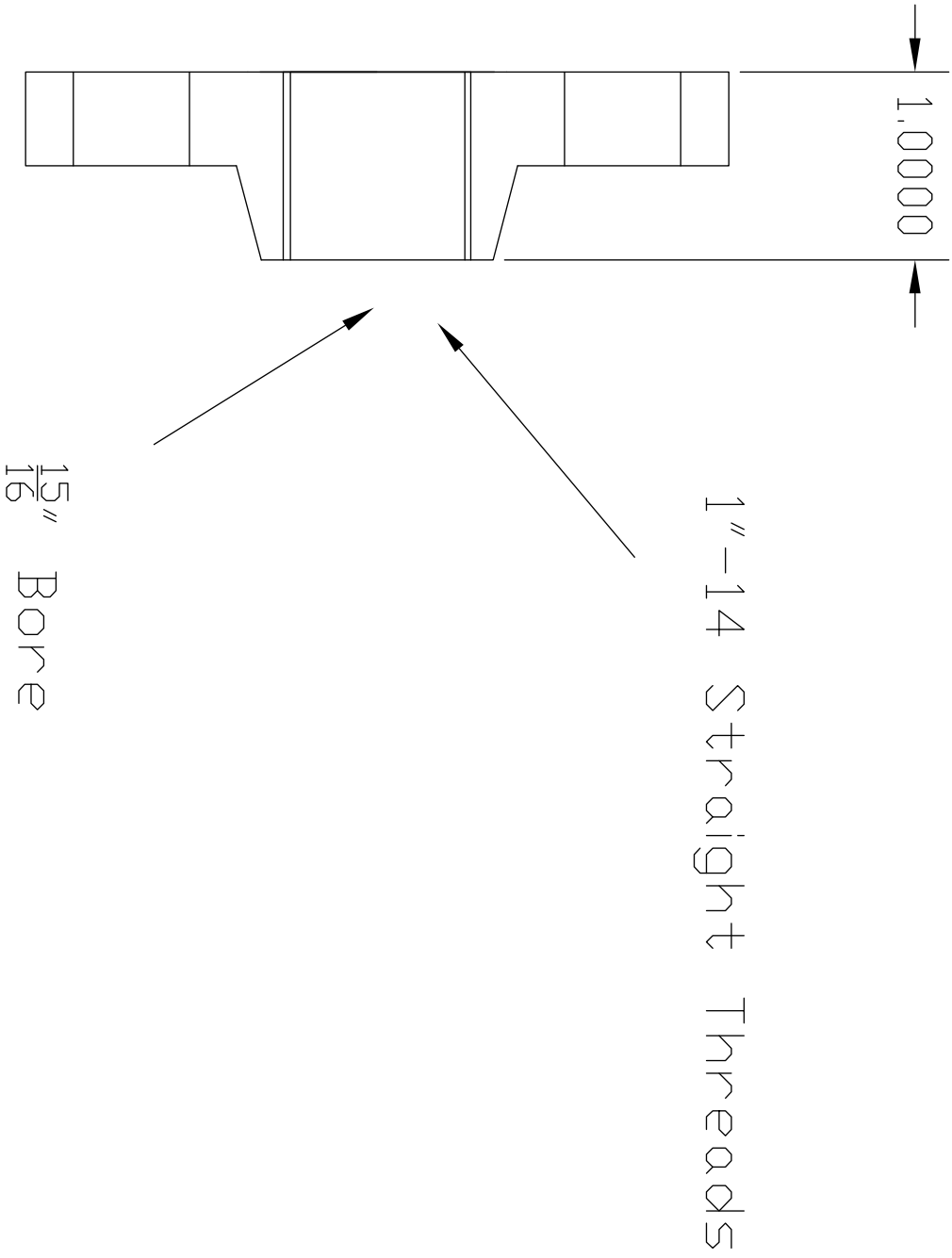


Figure E–5: Barrel Flange Dimensions (inches)

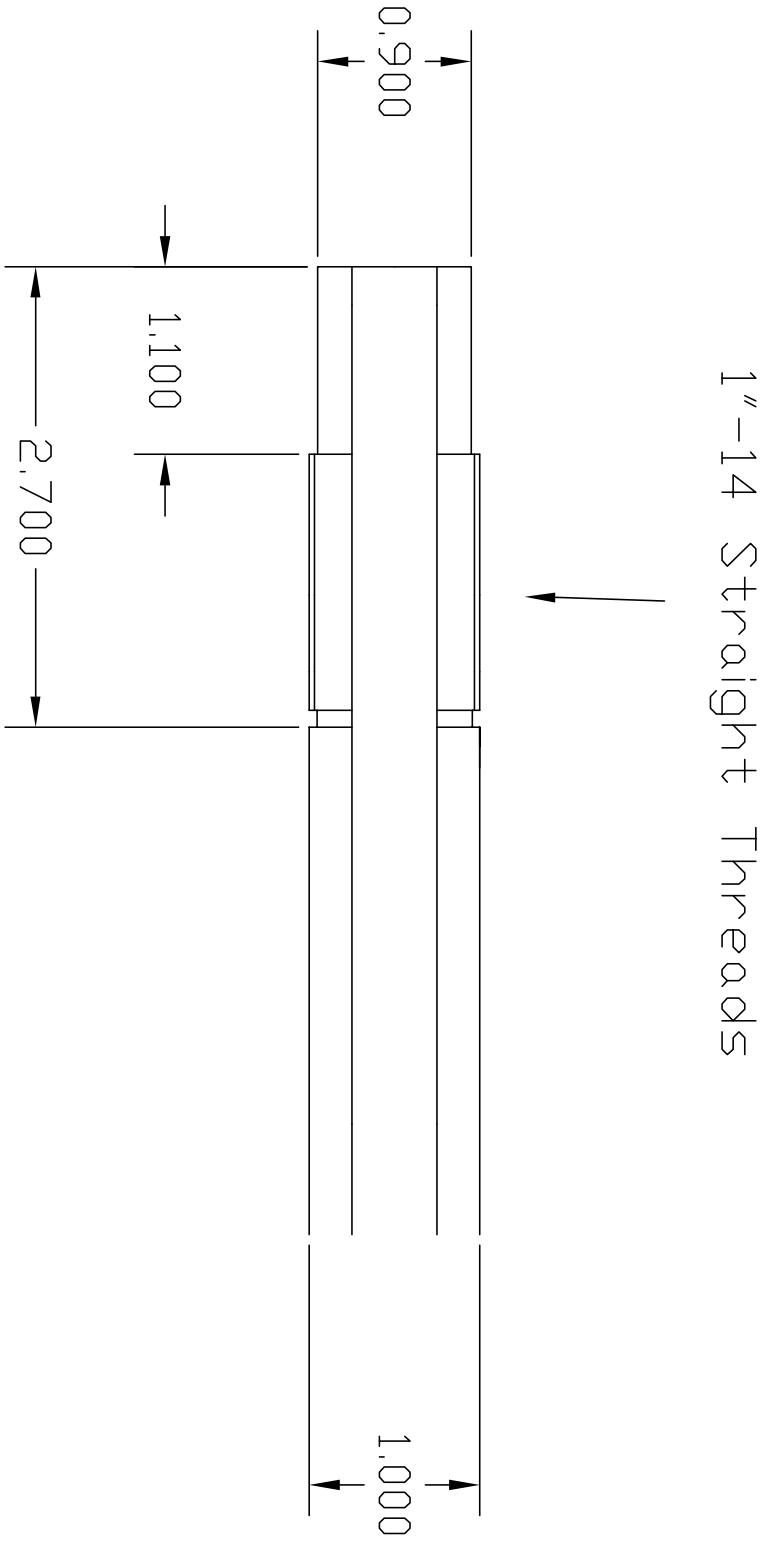


Figure E–6: Barrel Dimensions: Breech End (inches)

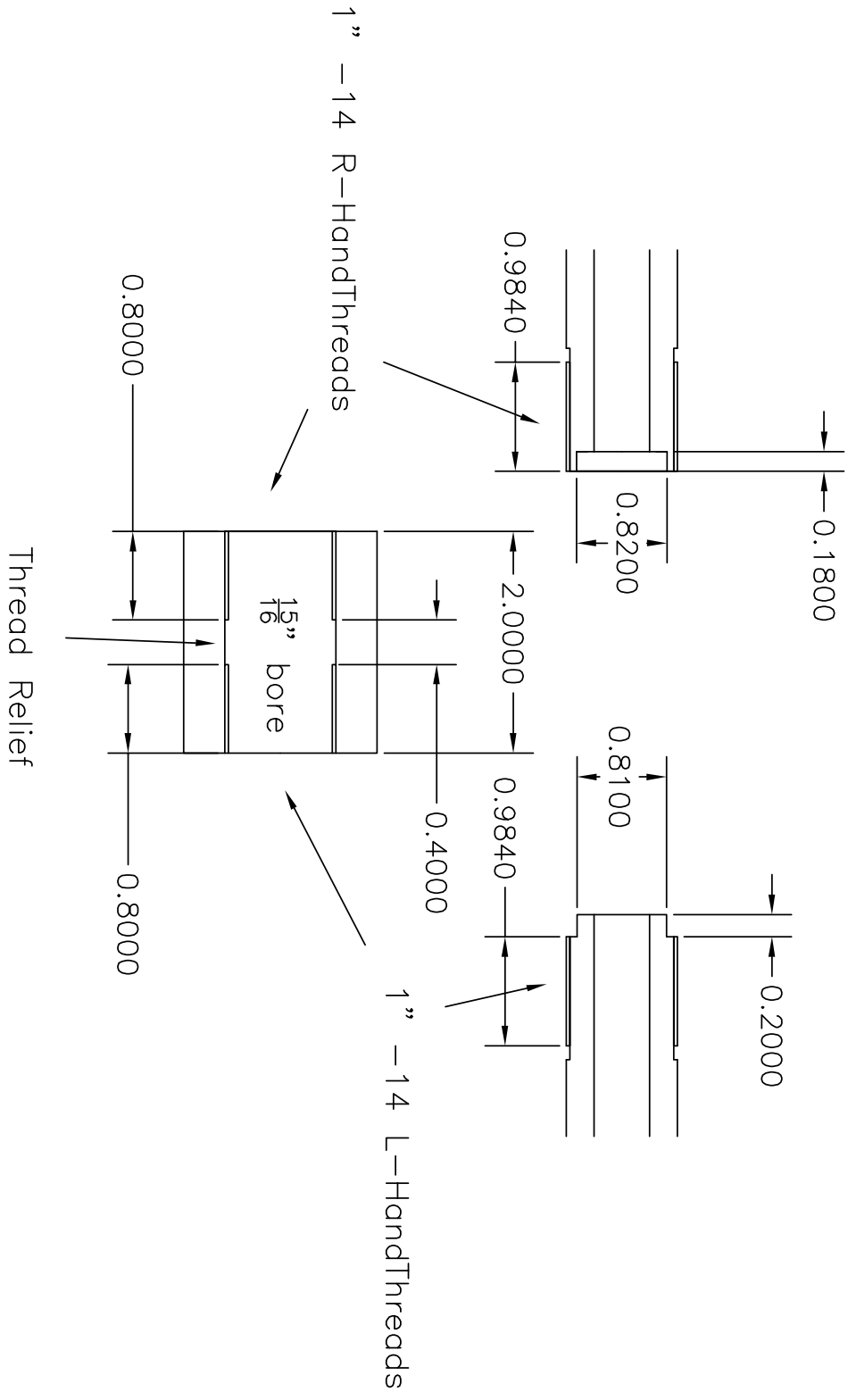


Figure E–7: Barrel and Coupler Dimensions (inches)

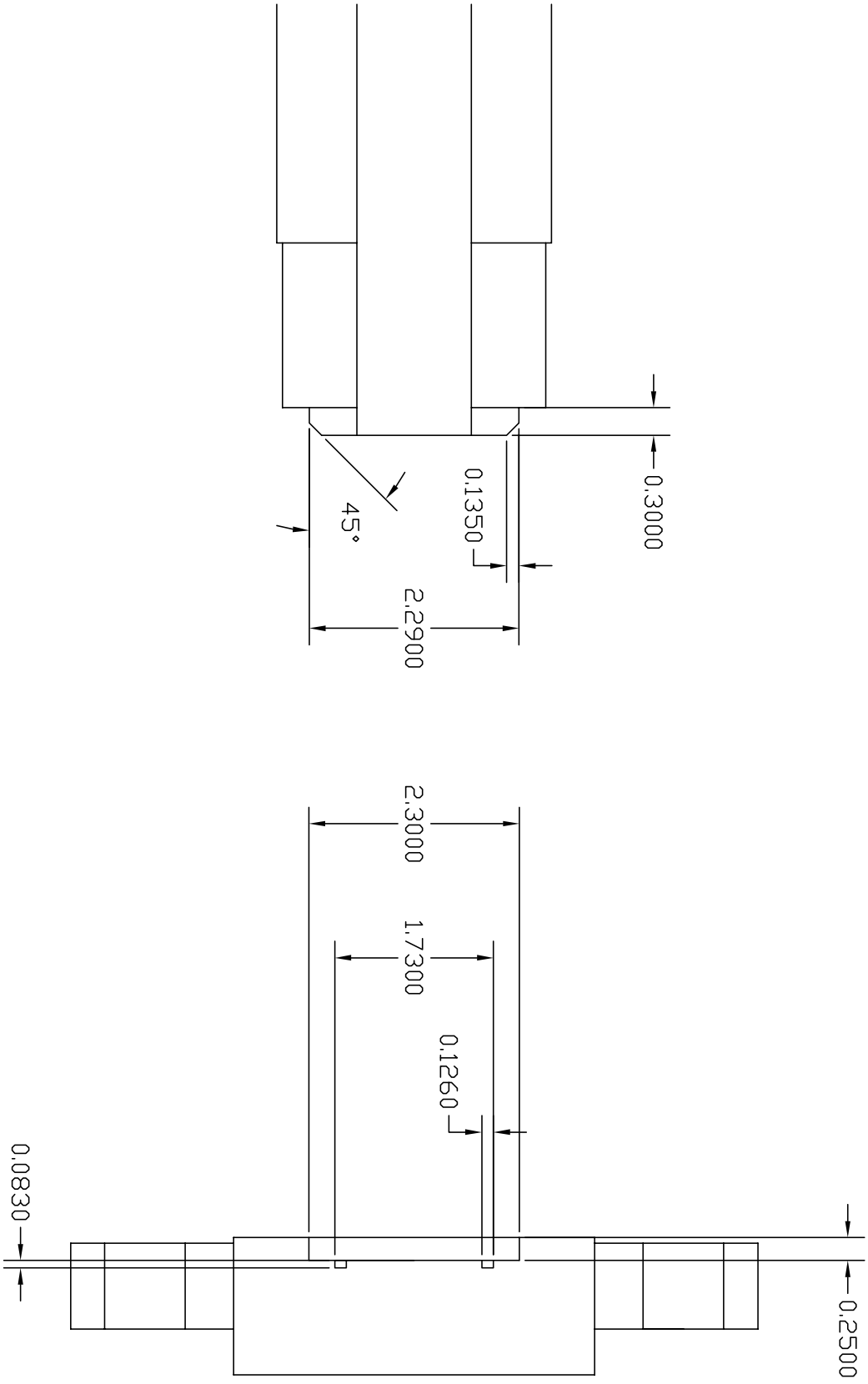


Figure E–8: Driver: Fill End Dimensions (inches)

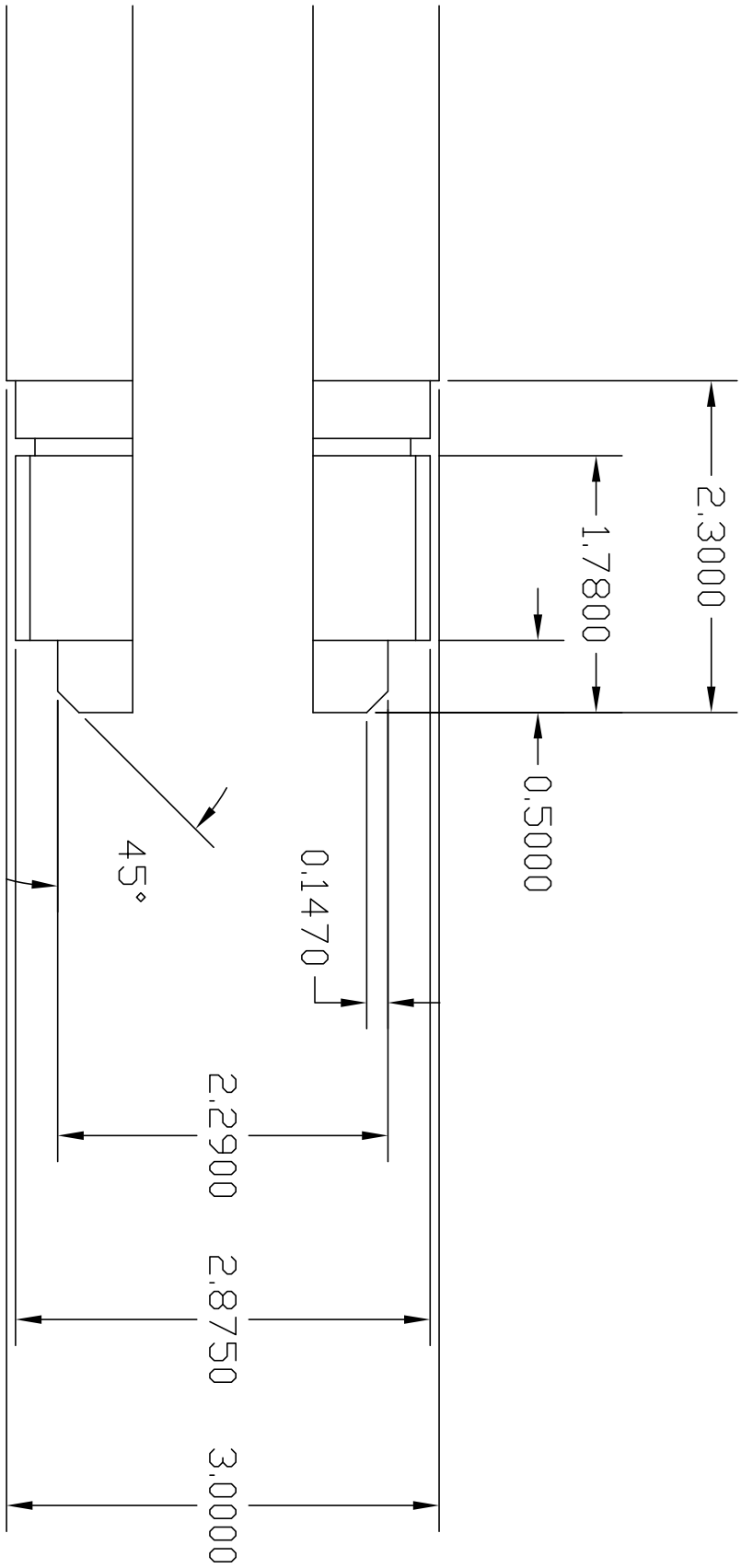


Figure E–9: Driver: Breech End Dimensions (inches)

# APPENDIX F
## Performance Predictions

### $x-t$ Diagrams for $2H_2+O_2$ driven gun system

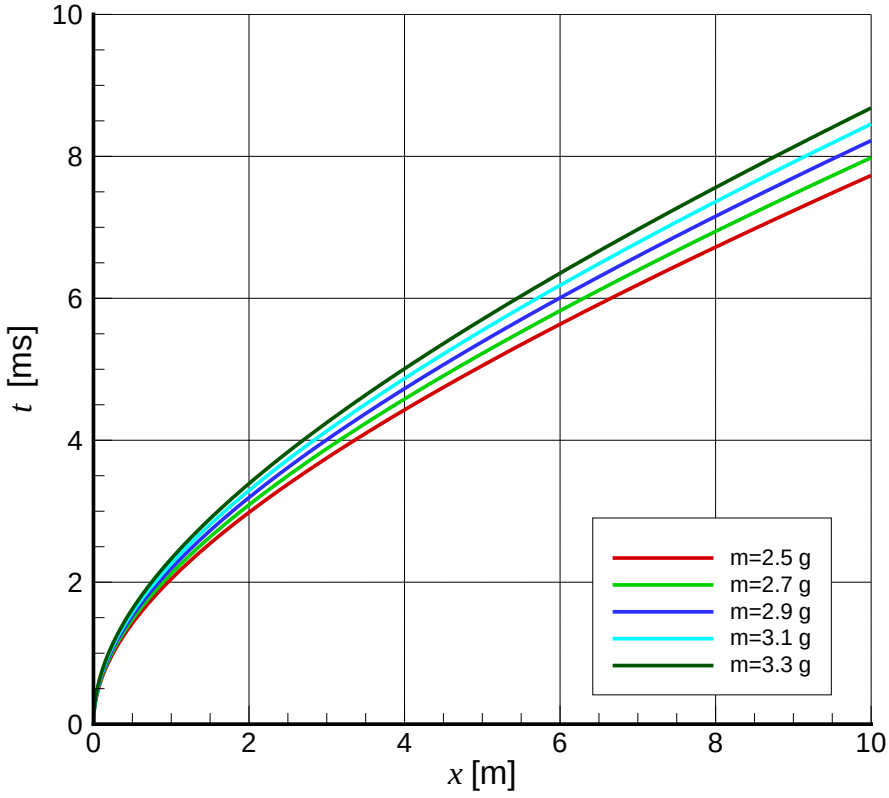


Figure F–1: $x-t$ diagram for various masses, predetonation pressure of 10 atm

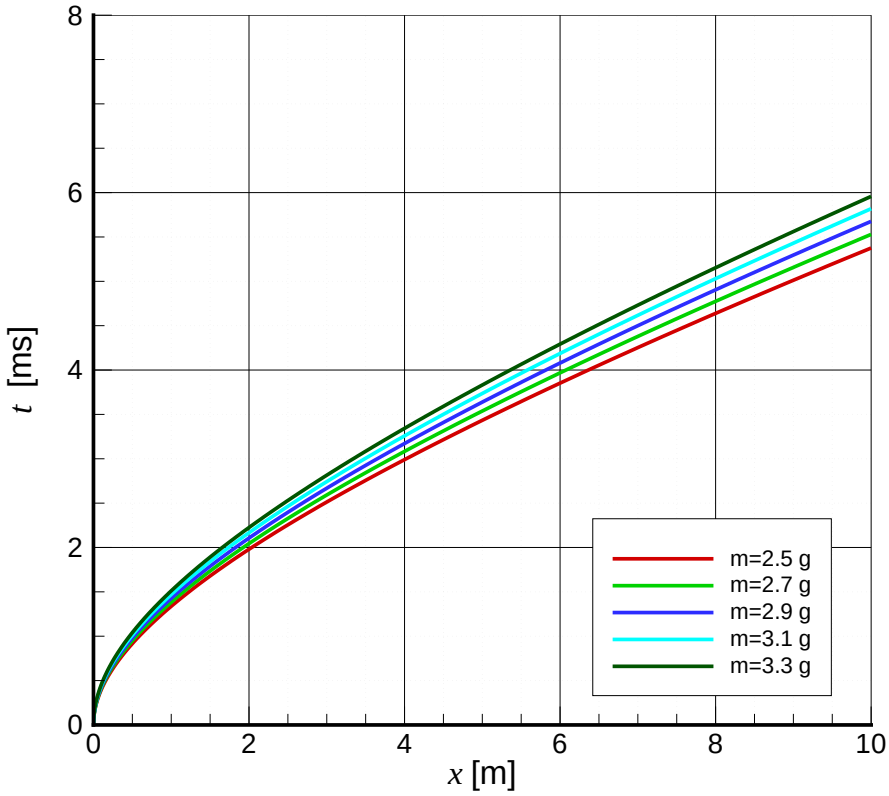


Figure F–2: $x - t$ diagram for various masses, predetonation pressure of 25 atm

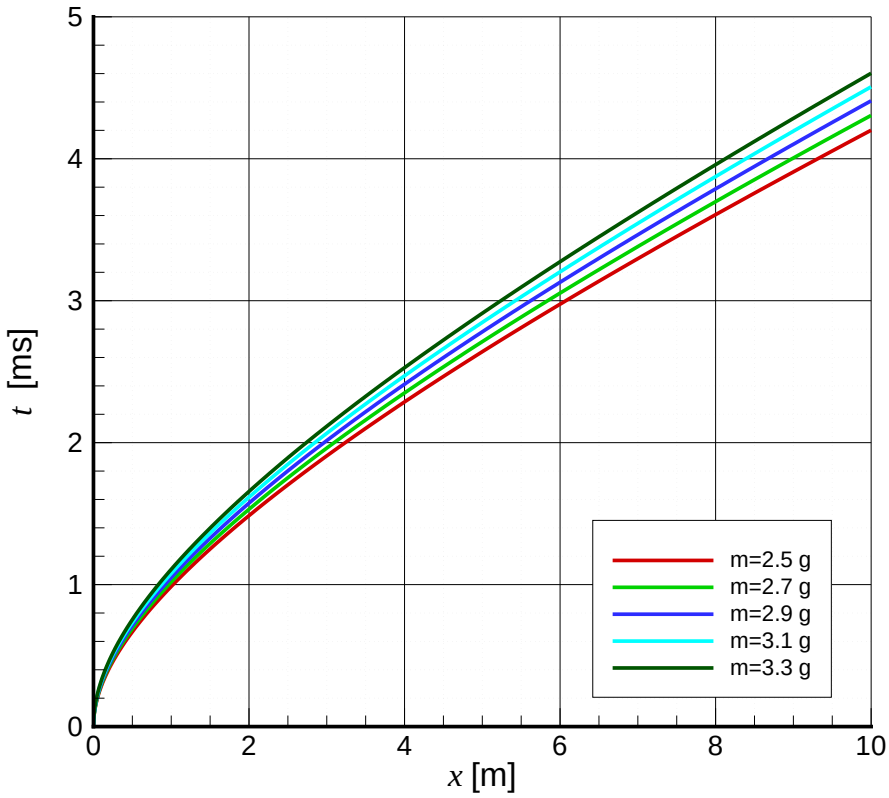


Figure F–3: $x - t$ diagram for various masses, predetonation pressure of 50 atm

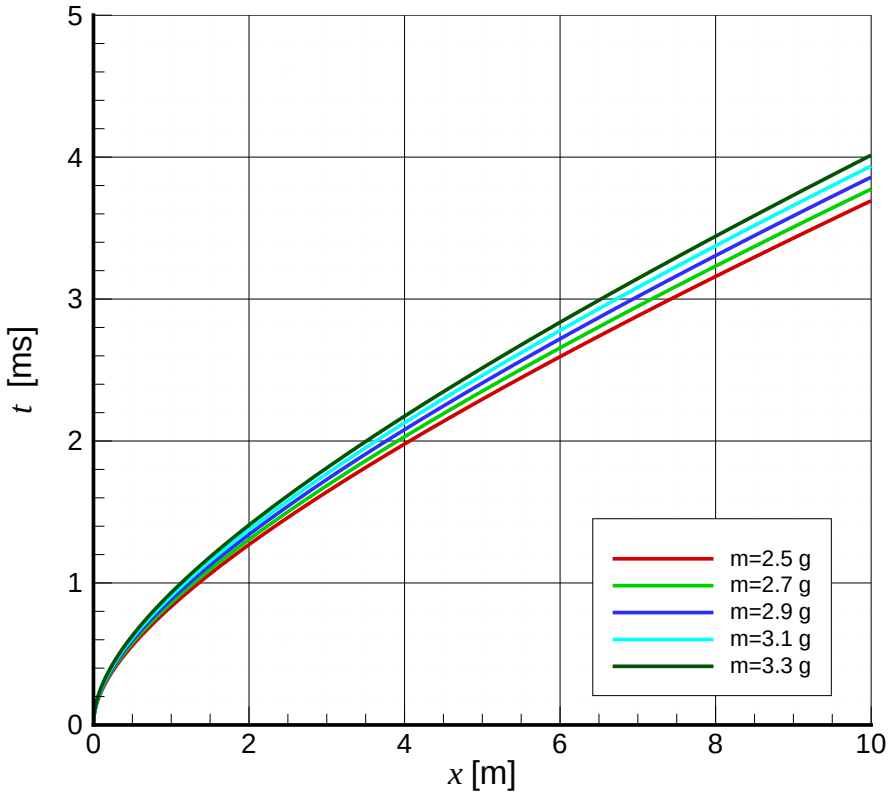


Figure F–4: $x - t$ diagram for various masses, predetonation pressure of 75 atm

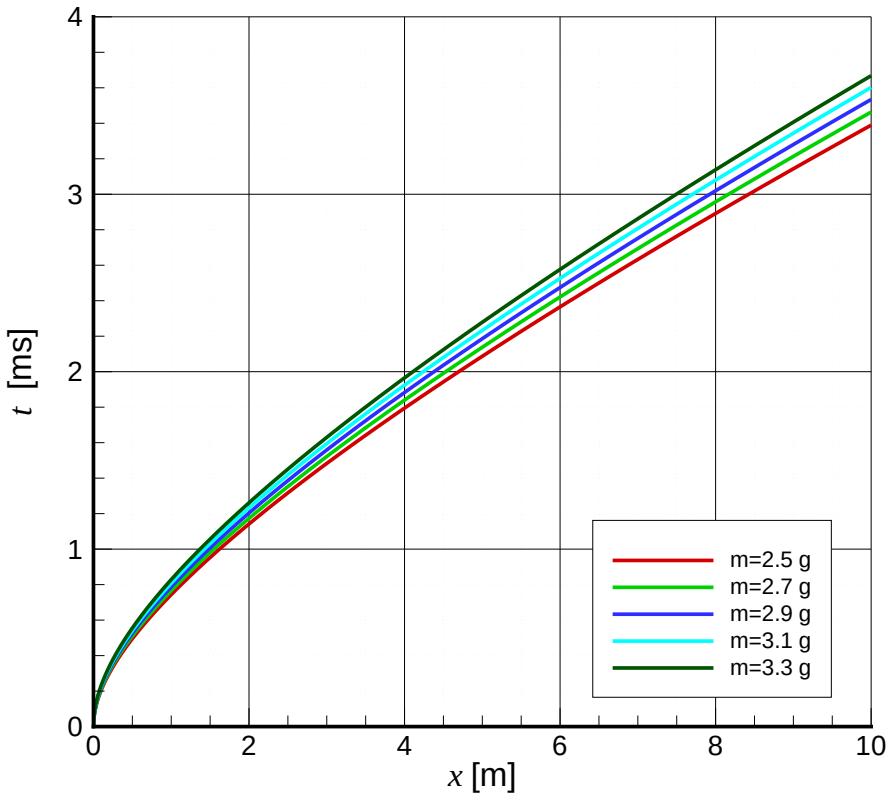


Figure F–5: $x - t$ diagram for various masses, predetonation pressure of 100 atm

## $x - u_p$ Diagrams for $2H_2+O_2$ driven gun system

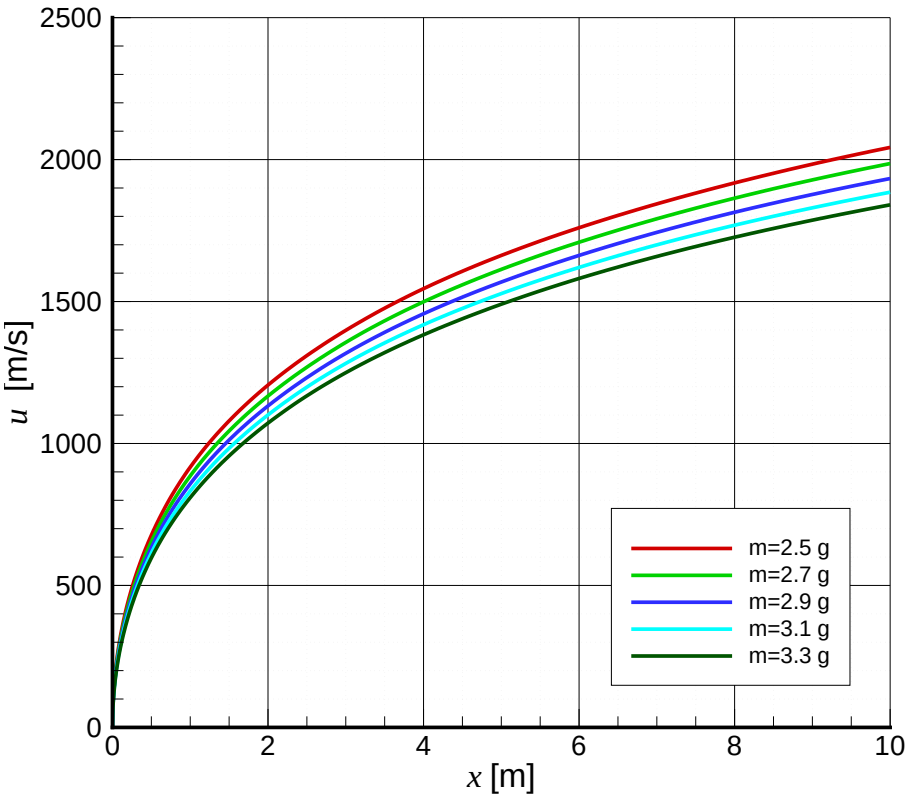


Figure F–6: $x - u_p$ diagram for various masses, predetonation pressure of 10 atm

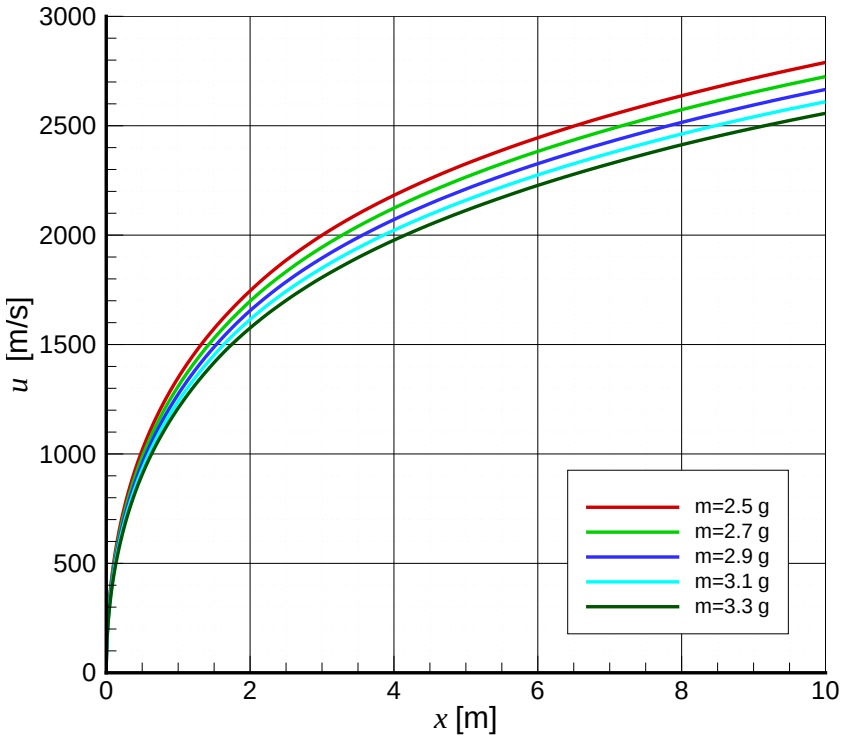


Figure F–7: $x - u_p$ diagram for various masses, predetonation pressure of 25 atm

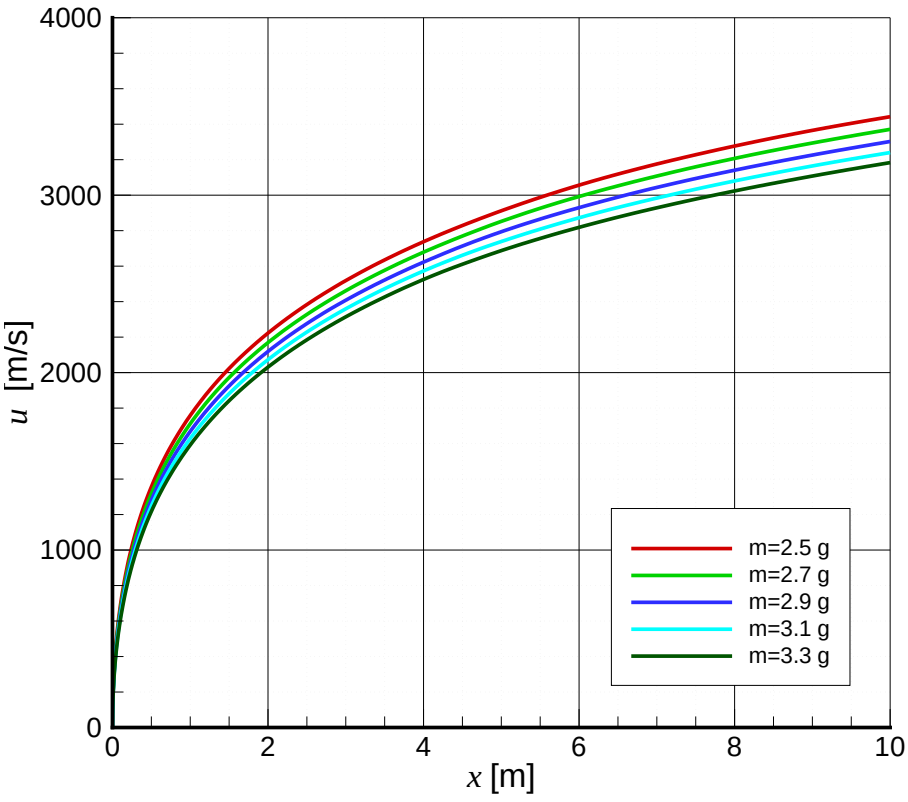


Figure F–8: $x - u_p$ diagram for various masses, predetonation pressure of 50 atm

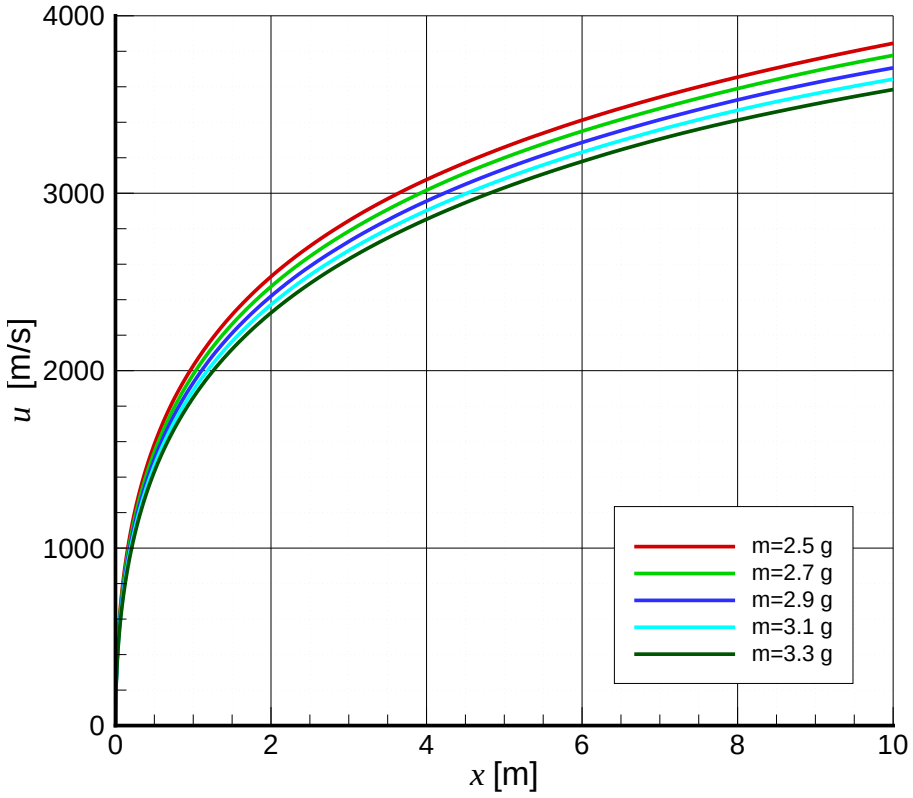


Figure F–9: $x - u_p$ diagram for various masses, predetonation pressure of 75 atm

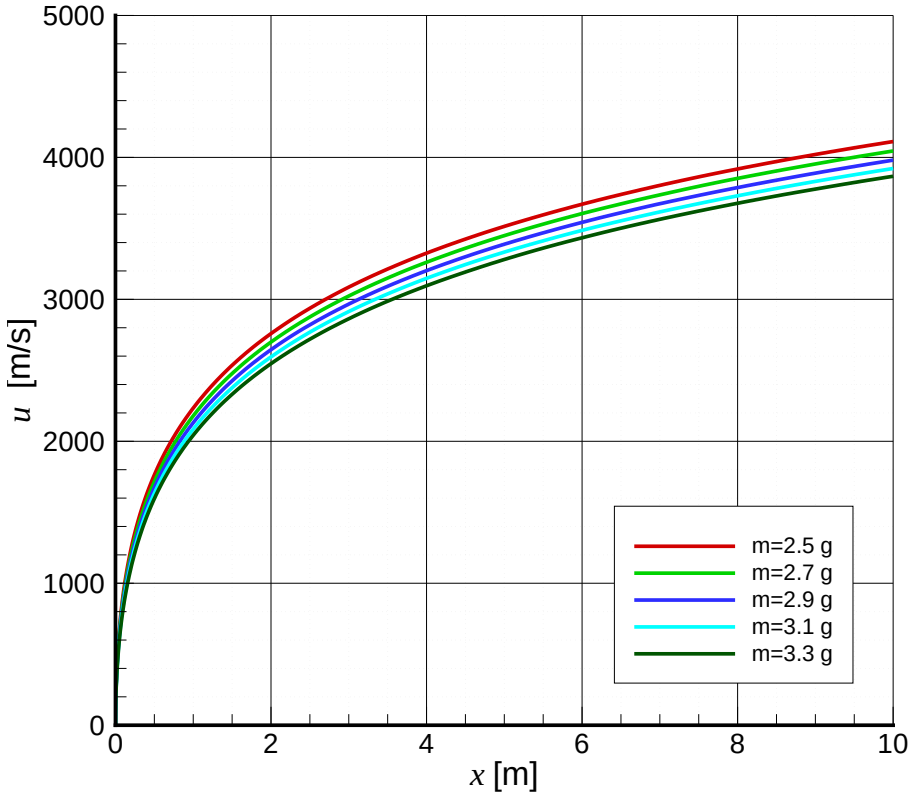


Figure F–10: $x - u_p$ diagram for various masses, predetonation pressure of 100 atm

# APPENDIX G
## Velocity Diagnostics Proof of Concept using Helium

Table G–1: Data for the helium shots fired into vacuum

| Shot # | $m_p$ [g] | $d_p$ [cm] | $l_p$ [cm] | $p_\circ$ [psi]* | $u_{1-2}$ [m/s] | $u_{2-3}$ [m/s] | $u_{ave}$ [m/s] |
|---|---|---|---|---|---|---|---|
| 1 | 2.58 | 1.262 | 1.938 | 427 | 474.1 | 472.6 | 473.4 |
| 2 | 2.58 | 1.262 | 1.938 | 770 | 614.8 | 612.2 | 613.5 |
| 3 | 2.286 | 1.224 | 1.844 | 1040 | 819.7 | 818.8 | 819.3 |
| 4 | 2.472 | 1.262 | 1.892 | 1540 | 928.6 | 929.3 | 929.0 |
| 5** | 2.273 | 1.247 | 1.905 | 1210 | 773.1 | 774.2 | 773.7 |
| 6 | 2.257 | 1.260 | 1.905 | 1840 | 994.7 | 993.4 | 995.6 |

* Gauge pressure

** Fired into air

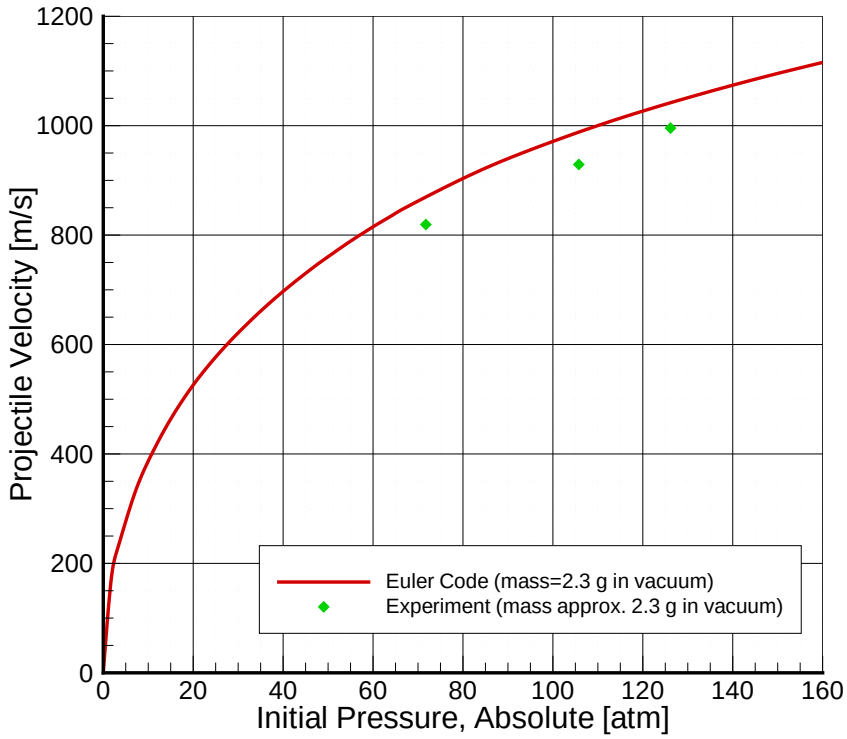


Figure G–1: Results for the helium gun calibration of the velocity coil gauge

## APPENDIX H
## Shot Data: Projectile

Table H–1: Projectile Data

| Shot # | Mat. | $m_p$ | $\theta$ | $d_p$ | $l_p$ | $l_s$ | $l_{BC}$ | $l_B$ | Type |
|---|---|---|---|---|---|---|---|---|---|
| 1 | PC | 1.580 | 90° | 0.499 | 0.565 | N/A | 0.125 | none | 1 |
| 2 | PC | 2.323 | 20° | 0.499 | 1.191 | 0.516 | 0.125 | none | 1 |
| 3 | PC | 2.319 | 20° | 0.499 | 1.190 | 0.508 | 0.125 | none | 1 |
| 4 | PC | 2.356 | 90° | 0.496 | 0.768 | N/A | 0.250 | none | 1 |
| 5 | PC | 1.913 | 90° | 0.496 | 0.648 | N/A | 0.250 | none | 1 |
| 6 | PC | 2.310 | 90° | 0.498 | 0.747 | N/A | 0.250 | none | 1 |
| 7 | PC | 3.371 | 90° | 0.497 | 1.015 | N/A | 0.225 | none | 2 |
| 8 | PC | 2.490 | 90° | 0.499 | 0.761 | N/A | 0.225 | none | 2 |
| 9 | PC | 2.560 | 90° | 0.497 | 0.771 | N/A | 0.225 | none | 2 |
| 10 | PC | 2.540 | 90° | 0.496 | 0.790 | N/A | 0.225 | none | 2 |
| 11 | PC | 2.270 | 90° | 0.501 | 0.751 | N/A | 0.250 | none | 4 |
| 12 | PC | 2.282 | 90° | 0.496 | 0.750 | N/A | 0.250 | none | 4 |
| 13 | PC | 2.246 | 20° | 0.496 | 0.750 | N/A | 0.250 | none | 4 |
| 14 | PC | 2.335 | 90° | 0.502 | 0.750 | N/A | 0.250 | none | 4 |
| 15 | Al+PC | 2.380 | 90° | 0.497 | 0.168* | 0.318* | 0.250 | none | 3 |
| 16 | Al+PC | 2.430 | 90° | 0.497 | 0.168* | 0.318* | 0.250 | none | 3 |
| 17 | PC | 2.293 | 90° | 0.499 | 0.751 | N/A | 0.250 | none | 4 |
| 18 | PC | 2.300 | 90° | 0.497 | 0.751 | N/A | 0.250 | none | 4 |
| 19 | Al | 3.040 | (90+45)° | 0.500 | 0.655 | 0.530 | 0.250 | yes | 4 |
| 20 | Al | 3.110 | (90+45)° | 0.500 | 0.656 | 0.531 | 0.250 | yes | 4 |
| 21 | Al | 2.990 | (90+45)° | 0.500 | 0.651 | 0.526 | 0.250 | yes | 4 |
| 22 | Al | 3.170 | (90+45)° | 0.500 | 0.648 | 0.523 | 0.250 | yes | 4 |
| 23 | Al | 3.050 | (90+45)° | 0.501 | 0.642 | 0.518 | 0.250 | yes | 4 |
| 24 | Al | 2.710 | 30° | 0.500 | 0.847 | 0.414 | 0.250 | yes | 5 |
| 25 | Al | 2.540 | 30° | 0.500 | 0.845 | 0.412 | 0.250 | yes | 5 |
| 26 | Al 7075 | 3.237 | (90+55)° | 0.500 | 0.467 | 0.238 | none | none | 4 |
| 27 | Al 7075 | 3.271 | (90+55)° | 0.500 | 0.469 | 0.252 | none | none | 4 |
| 28 | Al 7075 | 3.305 | (90+55)° | 0.499 | 0.457 | 0.247 | none | none | 4 |
| 29 | Al 7075 | 3.236 | (90+55)° | 0.500 | 0.450 | 0.244 | none | none | 4 |
| 30 | Al 7075 | 3.431 | (90+55)° | 0.504 | 0.472 | 0.247 | none | none | 4 |
| 31 | Al 7075 | 3.288 | (90+55)° | 0.500 | 0.459 | 0.246 | none | none | 4 |
| 32 | Al 7075 | 3.277 | (90+55)° | 0.501 | 0.472 | 0.242 | none | none | 4 |
| 33 | Al 7075 | 3.220 | (90+55)° | 0.492 | 0.465 | 0.250 | none | none | 4 |
| 34 | Al 7075 | 3.310 | (90+55)° | 0.495 | 0.643 | 0.350 | 0.190 | none | 4 |
| 35 | Al 7075 | 3.311 | (90+55)° | 0.500 | 0.472 | 0.242 | none | none | 4 |

| Shot # | Mat. | $m_p$ | $\theta$ | $d_p$ | $l_p$ | $l_s$ | $l_{BC}$ | $l_B$ | Type |
|---|---|---|---|---|---|---|---|---|---|
| 36 | Al 7075 | 3.288 | (90+55)° | 0.495 | 0.593 | 0.412 | 0.243 | none | 4 |
| 37 | Al 7075 | 3.277 | (90+55)° | 0.497 | 0.470 | 0.255 | none | none | 4 |
| 38 | Al 7075 | 3.220 | (90+55)° | 0.501 | 0.474 | 0.240 | none | none | 4 |
| 39 | Al 7075 | 3.310 | (90+55)° | 0.494 | 0.630 | 0.411 | 0.246 | none | 4 |
| 40 | Al 7075 | 3.311 | (90+55)° | 0.494 | 0.474 | 0.256 | none | none | 4 |
| 41 | Al 7075 | 3.310 | 20° | 0.497 | 1.085 | 0.400 | 0.250 | 0.400 | 6 |
| 42 | Al 7075 | 3.280 | 30° | 0.496 | 0.830 | 0.400 | 0.250 | 0.300 | 6 |
| 43 | Al 7075 | 3.310 | 30° | 0.494 | 0.836 | 0.400 | 0.250 | 0.300 | 6 |
| 44 | Al 7075 | 3.130 | 30° | 0.497 | 0.838 | 0.400 | 0.250 | 0.300 | 6 |
| 45 | Al 7075 | 3.240 | 45° | 0.495 | 0.647 | 0.400 | 0.250 | none | 6 |
| 46 | Al 7075 | 2.751 | 20° | 0.492 | 1.090 | 0.400 | 0.250 | 0.400 | 6 |
| 47 | Al 7075 | 2.700 | 45° | 0.495 | 0.648 | 0.400 | 0.250 | none | 6 |
| 48 | Al 7075 | 2.640 | 45° | 0.499 | 0.648 | 0.400 | 0.250 | none | 6 |
| 49 | Al 7075 | 2.768 | 60° | 0.501 | 0.544 | 0.400 | 0.250 | none | 6 |
| 50 | Al 7075 | 2.630 | 60° | 0.500 | 0.546 | 0.400 | 0.250 | none | 6 |
| 51 | Al 7075 | 2.680 | 45° | 0.500 | 0.650 | 0.400 | 0.250 | none | 6 |
| 52 | Al 7075 | 2.678 | 30° | 0.502 | 0.830 | 0.400 | 0.250 | 0.300 | 6 |
| 53 | Al 7075 | 2.519 | 60° | 0.498 | 0.543 | 0.400 | 0.250 | none | 6 |
| 54 | Al 7075 | 3.394 | 20° | 0.497 | 1.085 | 0.400 | 0.250 | none | 5 |
| 55 | Al 7075 | 3.012 | 30° | 0.499 | 0.828 | 0.400 | 0.250 | none | 5 |
| 56 | Al 7075 | 3.096 | 30° | 0.500 | 0.837 | 0.400 | 0.250 | none | 5 |
| 57 | Al 7075 | 3.384 | 20° | 0.499 | 1.088 | 0.400 | 0.250 | none | 5 |
| 58 | Ti | 3.630 | 20° | | | | | | |
| 59 | Ti | 3.420 | 30° | | | | | | |
| 60 | Ti | 3.240 | 30° | | | | | | |
| 61 | Ti | 3.770 | 20° | | | | | | |
| 62 | Al 7075 | 2.767 | 20° | 0.500 | 1.089 | 0.400 | 0.250 | 0.400 | 6 |
| 63 | Al 7075 | 2.854 | 20° | 0.502 | 1.088 | 0.400 | 0.250 | 0.400 | 6 |
| 64 | Al 7075 | 2.519 | 60° | 0.493 | 0.547 | 0.400 | 0.250 | none | 6 |
| 65 | Al 7075 | 3.140 | (90+55)° | 0.501 | 0.469 | 0.256 | none | none | 4 |
| 66 | Al 7075 | 3.160 | (90+55)° | 0.500 | 0.457 | 0.227 | none | none | 4 |
| 67 | Al 7075 | 3.713 | 30° | 0.498 | 0.831 | 0.400 | 0.250** | none | 6 |
| 68 | Al 7075 | 3.657 | 30° | 0.499 | 0.840 | 0.400 | 0.250** | 0.300 | 6 |
| 69 | Al 7075 | 4.413 | 20° | 0.499 | 1.087 | 0.400 | 0.250** | none | 6 |
| 70 | Al 7075 | 4.440 | 20° | 0.498 | 1.082 | 0.400 | 0.250** | 0.300 | 6 |
| 71 | Al 7075 | 3.864 | 30° | 0.498 | 0.826 | 0.400 | 0.250** | none | 6 |
| 72 | Al 7075 | 3.671 | 30° | 0.499 | 0.838 | 0.400 | 0.250** | 0.300 | 6 |
| 73 | Al 7075 | 4.512 | 20° | 0.499 | 1.080 | 0.400 | 0.250** | 0.300 | 6 |
| 74 | Al 7075 | 4.414 | 20° | 0.498 | 1.070 | 0.400 | 0.250** | none | 6 |
| 75 | Al 7075 | 6.318 | 30° | 0.497 | 1.177 | 0.750 | 0.250** | 0.375 | 6 |
| 76 | Al 7075 | 5.909 | 30° | 0.496 | 1.133 | 0.750 | 0.250** | 0.375 | 6 |
| 77 | Al 7075 | 7.238 | 20° | 0.496 | 1.436 | 0.750 | 0.250** | 0.500 | 6 |
| 78 | Al 7075 | 3.805 | 30° | 0.496 | 0.833 | 0.400 | 0.250** | 0.300 | 6 |
| 79 | Al 7075 | 4.555 | 20° | 0.493 | 1.100 | 0.400 | 0.250** | 0.300 | 6 |
| 80 | Al 7075 | 3.583 | 20° | 0.497 | 0.811 | 0.400 | 0.250** | 0.300 | 6 |

| Shot # | Mat. | $m_p$ | $\theta$ | $d_p$ | $l_p$ | $l_s$ | $l_{BC}$ | $l_B$ | Type |
|---|---|---|---|---|---|---|---|---|---|
| 81 | Al 7075 | 4.370 | 20° | 0.495 | 1.063 | 0.400 | 0.250** | 0.300 | 6 |
| 82 | Al 7075 | 6.976 | 20° | 0.497 | 1.430 | 0.750 | 0.250** | 0.375 | 6 |
| 83 | Al 7075 | 5.534 | 30° | 0.497 | 1.170 | 0.750 | 0.250** | 0.500 | 6 |
| 84 | Al 7075 | 5.669 | 30° | 0.497 | 1.186 | 0.750 | 0.250** | 0.500 | 6 |
| 85 | Al 7075 | 5.706 | 30° | 0.498 | 1.183 | 0.750 | 0.250** | 0.500 | 6 |
| 86 | Al 7075 | 3.997 | 30° | 0.464 | 0.904 | 0.500 | 0.219** | none | 6 |
| 87 | Al 7075 | 4.078 | 30° | 0.466 | 0.904 | 0.500 | 0.219** | none | 6 |
| 88 | Al 7075 | 4.070 | 30° | 0.465 | 0.905 | 0.500 | 0.219** | none | 6 |
| 89 | Al 7075 | 2.790 | 45° | 0.466 | 0.633 | 0.400 | 0.219** | none | 5 |
| 90 | Al 7075 | 2.773 | 45° | 0.466 | 0.633 | 0.400 | 0.219** | none | 5 |
| 91 | Al 7075 | 2.818 | 45° | 0.466 | 0.633 | 0.400 | 0.219** | none | 5 |
| 92 | Al 7075 | 2.793 | 45° | 0.466 | 0.633 | 0.400 | 0.219** | none | 5 |
| 93 | Al 7075 | 3.955 | 30° | 0.466 | 0.895 | 0.500 | 0.219** | none | 6 |
| 94 | Al 7075 | 3.047 | 30° | 0.466 | 0.804 | 0.400 | 0.219** | 0.300 | 5 |
| 95 | Al 7075 | 2.923 | 30° | 0.466 | 0.804 | 0.400 | 0.219** | 0.300 | 5 |
| 96 | Al 7075 | 4.791 | 30° | 0.466 | 1.004 | 0.600 | 0.219** | none | 5 |
| 97 | Al 7075 | 3.235 | 45° | 0.496 | 0.645 | 0.400 | 0.219** | none | 5 |
| 98 | Al 7075 | 4.284 | 45° | 0.496 | 0.648 | 0.400 | none | none | 5 |
| 99 | Al 7075 | 3.280 | 45° | 0.496 | 0.648 | 0.400 | 0.219** | none | 5 |
| 100 | Al 7075 | 4.299 | 45° | 0.495 | 0.649 | 0.400 | none | none | 5 |
| 101 | PC | 3.392 | 45° | 0.495 | 0.997 | 0.750 | none | none | 5 |
| 102 | PC | 3.350 | 45° | 0.502 | 0.993 | 0.750 | none | none | 5 |

* Here $l_p$ corresponds to the aluminum disc at the front of the projectile and $l_s$ corresponds to the Lexan (PC) section making up the rear of the projectile

** Here the Bridgeman seal is machined using a 7/16 ” ball mill rather than the 1/2 ” ball mill

# APPENDIX I
## Shot Data: Gun

Table I–1: Gun Data

| Shot # | Mixture | Gauge Pressure [bar] | Ignition Location | Barrel Length |
|---|---|---|---|---|
| 1 | Phi=1.5 | 36.20 | Back Flange | 6 ft |
| 2 | N/A | N/A | Back Flange | 6 ft |
| 3 | N/A | N/A | Back Flange | 6 ft |
| 4 | N/A | 62.05 | Back Flange | 6 ft |
| 5 | Phi=1 | 82.74 | Back Flange | 6 ft |
| 6 | Phi=1 | 72.39 | Back Flange | 6 ft |
| 7 | Phi=1 | 72.39 | Back Flange | 6 ft |
| 8 | Phi=1 | 72.39 | Back Flange | 6 ft |
| 9 | Phi=1 | 76.88 | Back Flange | 6 ft |
| 10 | Phi=1 | 77.29 | Back Flange | 6 ft |
| 11 | Phi=1 | 25.79 | Back Flange | 6 ft |
| 12 | Phi=1 | 51.57 | Back Flange | 6 ft |
| 13 | Phi=1 | 61.98 | Back Flange | 6 ft |
| 14 | Phi=1 | 51.64 | Back Flange | 6 ft |
| 15 | Phi=1 | 61.98 | Back Flange | 6 ft |
| 16 | Phi=1 | 62.95 | Back Flange | 6 ft |
| 17 | Phi=1 | 52.40 | Back Flange | 6 ft |
| 18 | Phi=1 | 46.47 | Back Flange | 6 ft |
| 19 | Phi=1 | 62.12 | Back Flange | 6 ft |
| 20 | Phi=1 | 82.94 | Back Flange | 6 ft |
| 21 | Phi=1 | 102.53 | Back Flange | 6 ft |
| 22 | Phi=1.5 | 89.63 | Back Flange | 6 ft |
| 23 | Phi=1 | 81.15 | Back Flange | 6 ft |
| 24 | Phi=1 | 82.81 | Back Flange | 6 ft |
| 25 | Phi=1 | 62.60 | Back Flange | 6 ft |
| 26 | Phi=1 | 25.79 | Back Flange | 12 ft |
| 27 | Phi=1 | 41.30 | Back Flange | 12 ft |
| 28 | Phi=1 | 62.40 | Back Flange | 12 ft |
| 29 | Phi=1 | 82.60 | Back Flange | 12 ft |
| 30 | Phi=1 | 25.86 | Back Flange | 12 ft |
| 31 | Phi=1+2He | 41.37 | Back Flange | 12 ft |
| 32 | Phi=1 | 62.12 | Back Flange | 6 ft |
| 33 | Phi=1 | 62.33 | Back Flange | 6 ft |
| 34 | Phi=1 | 62.12 | Back Flange | 6 ft |
| 35 | Phi=1 | 61.98 | Back Flange | 6 ft |

| Shot # | Mixture | Gauge Pressure [bar] | Ignition Location | Barrel Length |
|---|---|---|---|---|
| 36 | Phi=1 | 62.12 | Back Flange | 6 ft |
| 37 | Phi=1+2He | 62.40 | Back Flange | 6 ft |
| 38 | Phi=2 | 62.19 | Back Flange | 6 ft |
| 39 | Phi=1 | 83.08 | Back Flange | 6 ft |
| 40 | Phi=1 | 62.05 | Back Flange | 12 ft |
| 41 | Phi=1 | 62.05 | Back Flange | 12 ft |
| 42 | Phi=1 | 62.05 | Back Flange | 12 ft |
| 43 | Phi=1 | 62.05 | Back Flange | 12 ft |
| 44 | Phi=1 | 51.71 | Back Flange | 12 ft |
| 45 | Phi=1 | 51.71 | Back Flange | 12 ft |
| 46 | Phi=1 | 51.71 | Back Flange | 12 ft |
| 47 | Phi=1 | 51.71 | Back Flange | 12 ft |
| 48 | Phi=1 | 51.71 | Back Flange | 12 ft |
| 49 | Phi=1 | 51.71 | Back Flange | 12 ft |
| 50 | Phi=1 | 62.05 | Back Flange | 12 ft |
| 51 | Phi=1 | 62.05 | Back Flange | 12 ft |
| 52 | Phi=1 | 87.56 | Breech End | 12 ft |
| 53 | Phi=1 | 62.74 | Back Flange | 12 ft |
| 54 | Phi=1 | 62.05 | Back Flange | 12 ft |
| 55 | Phi=1 | 51.71 | Back Flange | 12 ft |
| 56 | Phi=1 | 62.05 | Back Flange | 12 ft |
| 57 | Phi=1 | 51.37 | Back Flange | 12 ft |
| 58 | Phi=1 | 63.09 | Back Flange | 12 ft |
| 59 | Phi=1 | 62.05 | Back Flange | 12 ft |
| 60 | Phi=1 | 62.40 | Back Flange | 12 ft |
| 61 | Phi=1 | 41.37 | Back Flange | 12 ft |
| 62 | Phi=1 | 41.37 | Back Flange | 12 ft |
| 63 | Phi=1 | 31.03 | Back Flange | 12 ft |
| 64 | Phi=1 | 102.04 | Back Flange | 12 ft |
| 65 | Phi=1* | 67.98 | Back Flange | 12 ft |
| 66 | Phi=1* | 63.64 | Back Flange | 12 ft |
| 67 | Phi=1* | 65.36 | Back Flange | 12 ft |
| 68 | Phi=1* | 65.71 | Back Flange | 12 ft |
| 69 | Phi=1* | 65.91 | Back Flange | 12 ft |
| 70 | Phi=1* | 66.12 | Back Flange | 12 ft |
| 71 | Phi=1* | 56.67 | Back Flange | 12 ft |
| 72 | Phi=1* | 86.60 | Back Flange | 12 ft |
| 73 | Phi=1* | 66.74 | Back Flange | 12 ft |
| 74 | Phi=1* | 86.39 | Back Flange | 12 ft |
| 75 | Phi=1* | 86.32 | Back Flange | 12 ft |
| 76 | Phi=1* | 65.91 | Back Flange | 12 ft |
| 77 | Phi=1* | 85.98 | Back Flange | 12 ft |
| 78 | Phi=1* | 86.46 | Back Flange | 6 ft |
| 79 | Phi=1* | 86.87 | Back Flange | 6 ft |
| 80 | Phi=1* | 65.91 | Back Flange | 6 ft |

| Shot # | Mixture | Gauge Pressure [bar] | Ignition Location | Barrel Length |
|---|---|---|---|---|
| 81 | Phi=1* | 66.19 | Back Flange | 6 ft |
| 82 | Phi=1* | 76.32 | Back Flange | 6 ft |
| 83 | Phi=1* | 76.32 | Back Flange | 6 ft |
| 84 | Phi=1* | 75.98 | Back Flange | 6 ft |
| 85 | Phi=1* | 75.29 | Back Flange | 6 ft |
| 86 | Phi=1* | 68.60 | Back Flange | 12 ft |
| 87 | Phi=1* | 66.19 | Back Flange | 12 ft |
| 88 | Phi=1* | 84.74 | Back Flange | 12 ft |
| 89 | Phi=1* | 65.78 | Back Flange | 12 ft |
| 90 | Phi=1* | 81.84 | Back Flange | 6 ft |
| 91 | Phi=1* | 65.98 | Back Flange | 6 ft |
| 92 | Phi=1* | 65.98 | Back Flange | 6 ft |
| 93 | Phi=1.5* | 67.15 | Back Flange | 6 ft |
| 94 | Phi=1* | 65.71 | Back Flange | 6 ft |
| 95 | Phi=1* | 65.71 | Back Flange | 6 ft |
| 96 | Phi=1* | 86.60 | Back Flange | 12 ft |
| 97 | Phi=1* | 86.46 | Breech End | 12 ft |
| 98 | Phi=1* | 86.25 | Breech End | 12 ft |
| 99 | Phi=1* | 64.53 | Breech End | 12 ft |
| 100 | Phi=1* | 86.87 | Breech End | 12 ft |
| 101 | Phi=1* | 66.19 | Breech End | 12 ft |
| 102 | Phi=1* | 43.99 | Breech End | 12 ft |

* These mixtures have 50 psi of Helium injected at the rear of the driver in order to protect the valves from experiencing the pressures of a direct detonation

## APPENDIX J
## Shot Data: Results

Table J–1: Velcoity data in m/s

| Shot # | System | $u_{1-2}$ | $u_{2-3}$ | $u_{3-4}$ | $u_{ave}$ | Survival | $l_{CG}$ [cm] |
|---|---|---|---|---|---|---|---|
| 1 | Shock Pins | no data | no data | N/A | no data | unknown | N/A |
| 2 | Shock Pins | no data | no data | N/A | no data | unknown | N/A |
| 3 | Shock Pins | no data | no data | N/A | no data | unknown | N/A |
| 4 | Shock Pins | no data | no data | N/A | no data | unknown | N/A |
| 5 | Shock Pins | no data | no data | N/A | no data | unknown | N/A |
| 6 | Shock Pins | no data | no data | N/A | no data | unknown | N/A |
| 7 | Coil Gauge 1 | no data | no data | N/A | no data | unknown | 7.5 |
| 8 | Coil Gauge 1 | 1132.9 | 1129.5 | N/A | 1131 | no | 7.5 |
| 9 | Coil Gauge 1 | 1811.6 | 1445.1 | N/A | 1628 | no | 7.5 |
| 10 | Coil Gauge 1 | 1582.3 | 1662.8 | N/A | 1623 | no | 7.5 |
| 11 | Coil Gauge 1 | 1353.8 | 1356.2 | N/A | 1355 | yes | 7.5 |
| 12 | Coil Gauge 1 | 2043.6 | 2038.0 | N/A | 2041 | yes | 7.5 |
| 13 | Coil Gauge 1 | 1445.1 | no data | N/A | 1445 | no | 7.5 |
| 14 | Coil Gauge 1 | 1820.4 | 1820.4 | N/A | 1820 | yes | 7.5 |
| 15 | Coil Gauge 1 | 1168.2 | 957.8 | N/A | 1063 | no | 7.5 |
| 16 | Coil Gauge 1 | 1464.8 | 1311.2 | N/A | 1388 | no | 7.5 |
| 17 | Coil Gauge 1 | 997.3 | 1001.3 | N/A | 999 | no | 7.5 |
| 18 | Coil Gauge 1 | 1768.9 | 1752.3 | N/A | 1761 | yes | 7.5 |
| 19 | Coil Gauge 1 | 1992.6 | 1988.3 | N/A | 1990 | yes | 7.5 |
| 20 | Coil Gauge 1 | 2306.3 | 2312.0 | N/A | 2309 | yes | 7.5 |
| 21 | Coil Gauge 1 | 1813.3 | 1818.6 | N/A | 1816 | no | 7.5 |
| 22 | Coil Gauge 1 | 2226.8 | 2221.6 | N/A | 2224 | yes | 7.5 |
| 23 | Coil Gauge 1 | no data | 2275.4 | N/A | 2275 | yes | 7.5 |
| 24 | Coil Gauge 1 | 1573.0 | 1595.4 | N/A | 1584 | no | 7.5 |
| 25 | Coil Gauge 1 | 2218.9 | 2209.8 | N/A | 2210 | yes | 7.5 |
| 26 | Coil Gauge 2 | 1457.7 | 1533.7 | 1449.3 | 1480 | yes | 5.0 |
| 27 | Coil Gauge 2 | 1634.0 | 1677.9 | 1683.5 | 1665 | yes | 5.0 |
| 28 | Coil Gauge 2 | 1886.8 | 2074.7 | 1930.5 | 1964 | yes | 5.0 |
| 29 | Coil Gauge 2 | no data | no data | no data | 2268* | no | 5.0 |
| 30 | Coil Gauge 2 | 892.9 | 881.8 | 887.4 | 887 | yes | 5.0 |
| 31 | Coil Gauge 2 | no data | no data | no data | no data | unknown | 5.0 |
| 32 | Coil Gauge 1 | 1843.3 | 1812.8 | N/A | 1828 | yes | 7.65 |
| 33 | Coil Gauge 1 | 1839.0 | 1830.0 | N/A | 1835 | yes | 7.65 |
| 34 | Coil Gauge 1 | 1852.0 | no data | N/A | 1852 | yes | 7.65 |
| 35 | Coil Gauge 1 | 1856.8 | 1834.5 | N/A | 1846 | yes | 7.65 |

| Shot # | System | $u_{1-2}$ | $u_{2-3}$ | $u_{3-4}$ | $u_{ave}$ | Survival | $l_{CG}$ [cm] |
|---|---|---|---|---|---|---|---|
| 36 | Coil Gauge 1 | 1922.0 | 1898.1 | N/A | 1910 | yes | 7.65 |
| 37 | Coil Gauge 1 | 1751 | 1735 | N/A | 1743 | yes | 7.65 |
| 38 | Coil Gauge 1 | 1826 | 1804 | N/A | 1815 | yes | 7.65 |
| 39 | Coil Gauge 1 | 2137 | 2102 | N/A | 2120 | yes | 7.65 |
| 40 | Coil Gauge 1 | 1798 | 1790 | N/A | 1794 | yes | 7.65 |
| 41 | Coil Gauge 1 | no data | no data | N/A | no data | no | 7.65 |
| 42 | Coil Gauge 1 | 2050 | 2027 | N/A | 2039 | yes | 7.65 |
| 43 | Coil Gauge 1 | no data | 1938 | N/A | 1938 | no | 7.65 |
| 44 | Coil Gauge 1 | 1735 | 1723 | N/A | 1729 | yes | 7.65 |
| 45 | Coil Gauge 1 | 1979 | 1968 | N/A | 1974 | yes | 7.65 |
| 46 | Coil Gauge 1 | 1086 | 1108 | N/A | 1097 | no | 7.65 |
| 47 | Coil Gauge 1 | 1875 | 1865 | N/A | 1870 | yes | 7.65 |
| 48 | Coil Gauge 1 | 1995 | 1979 | N/A | 1987 | yes | 7.65 |
| 49 | Coil Gauge 1 | 2027 | 2022 | N/A | 2025 | yes | 7.65 |
| 50 | Coil Gauge 1 | 2207 | 2201 | N/A | 2204 | yes | 7.65 |
| 51 | Coil Gauge 1 | 2194 | 2201 | N/A | 2198 | yes | 7.65 |
| 52 | Coil Gauge 1 | 2125 | 2150 | N/A | 2138 | yes | 7.65 |
| 53 | Coil Gauge 1 | 2151 | 2144 | N/A | 2148 | yes | 7.65 |
| 54 | Coil Gauge 1 | 2010 | 2003 | N/A | 2006 | yes | 7.65 |
| 55 | Coil Gauge 1 | 1836 | 1828 | N/A | 1832 | yes | 7.65 |
| 56 | Coil Gauge 1 | 2013 | 2000 | N/A | 2007 | yes | 7.65 |
| 57 | Coil Gauge 1 | 1780 | 1768 | N/A | 1774 | yes | 7.65 |
| 58 | Coil Gauge 1 | no data | no data | N/A | no data | no | 7.65 |
| 59 | Coil Gauge 1 | 1802 | 1733 | N/A | 1798 | yes | 7.65 |
| 60 | Coil Gauge 1 | 1828 | 1815 | N/A | 1822 | yes | 7.65 |
| 61 | Coil Gauge 1 | 1448 | 1435 | N/A | 1442 | yes | 7.65 |
| 62 | Coil Gauge 1 | 999 | 991 | N/A | 995 | no | 7.65 |
| 63 | Coil Gauge 1 | 1457 | 1449 | N/A | 1453 | yes | 7.65 |
| 64 | Coil Gauge 1 | 2733 | 2693 | N/A | 2713 | yes | 7.65 |
| 65 | Coil Gauge 1 | 1912 | 1904 | N/A | 1908 | yes | 7.65 |
| 66 | Coil Gauge 1 | 1847 | 1835 | N/A | 1841 | yes | 7.65 |
| 67 | Coil Gauge 1 | no data | no data | N/A | no data | unknown | 7.65 |
| 68 | Coil Gauge 1 | 1916 | 1902 | N/A | 1909 | yes | 7.65 |
| 69 | Coil Gauge 1 | no data | no data | N/A | no data | no | 7.65 |
| 70 | Coil Gauge 1 | 1726 | 1722 | N/A | 1724 | yes | 7.65 |
| 71 | Coil Gauge 1 | 1817 | 1707 | N/A | 1762 | yes | 7.65 |
| 72 | Coil Gauge 1 | no data | no data | N/A | no data | yes | 7.65 |
| 73 | Coil Gauge 1 | 1745 | 1730 | N/A | 1738 | yes | 7.65 |
| 74 | Coil Gauge 1 | 1978 | 1963 | N/A | 1971 | yes | 7.65 |
| 75 | Coil Gauge 1 | 1759 | 1742 | N/A | 1751 | yes | 7.65 |
| 76 | Coil Gauge 1 | 1602 | 1597 | N/A | 1600 | yes | 7.65 |
| 77 | Coil Gauge 1 | 1562 | 1546 | N/A | 1554 | yes | 7.65 |
| 78 | Coil Gauge 1 | no data | no data | N/A | no data | yes | 7.65 |
| 79 | Coil Gauge 1 | 1953 | 1943 | N/A | 1948 | yes | 7.65 |
| 80 | Coil Gauge 1 | 1833 | 1820 | N/A | 1827 | yes | 7.65 |

| Shot # | System | $u_{1-2}$ | $u_{2-3}$ | $u_{3-4}$ | $u_{ave}$ | Survival | $l_{CG}$ [cm] |
|---|---|---|---|---|---|---|---|
| 81 | Coil Gauge 1 | no data | no data | N/A | 1643* | yes | 7.65 |
| 82 | Coil Gauge 1 | no data | no data | N/A | no data | yes | 7.65 |
| 83 | Coil Gauge 1 | 1654 | 1661 | N/A | 1658 | yes | 7.65 |
| 84 | Coil Gauge 1 | no data | no data | N/A | no data | no | 7.65 |
| 85 | Coil Gauge 1 | no data | no data | N/A | no data | unknown | 7.65 |
| 86 | Coil Gauge 1 | 1513 | 1507 | N/A | 1510 | yes | 7.65 |
| 87 | Coil Gauge 1 | 1591 | 1577 | N/A | 1584 | yes | 7.65 |
| 88 | Coil Gauge 1 | 1913 | 1918 | N/A | 1916 | yes | 7.65 |
| 89 | Coil Gauge 1 | 1938 | 1933 | N/A | 1936 | yes | 7.65 |
| 90 | Coil Gauge 1 | 2240 | 2254 | N/A | 2247 | yes | 7.65 |
| 91 | Coil Gauge 1 | 1968 | 1953 | N/A | 1961 | yes | 7.65 |
| 92 | Coil Gauge 1 | 1884 | 1879 | N/A | 1882 | yes | 7.65 |
| 93 | Coil Gauge 1 | 1400 | 1309 | N/A | 1355 | yes | 7.65 |
| 94 | Coil Gauge 1 | 1995 | 1874 | N/A | 1935 | yes | 7.65 |
| 95 | Coil Gauge 1 | no data | no data | N/A | 1864* | yes | 7.65 |
| 96 | Coil Gauge 1 | no data | no data | N/A | 1655* | yes | 7.65 |
| 97 | Coil Gauge 1 | 2038 | 1913 | N/A | 1976 | yes | 7.65 |
| 98 | Coil Gauge 1 | no data | no data | N/A | no data | unknown | 7.65 |
| 99 | Coil Gauge 1 | 1584 | 1483 | N/A | 1534 | yes | 7.65 |
| 100 | Coil Gauge 1 | 1541 | 1446 | N/A | 1494 | yes | 7.65 |
| 101 | Coil Gauge 1 | 1256 | 1189 | N/A | 1223 | yes | 7.65 |
| 102 | Coil Gauge 1 | 1188 | 1117 | N/A | 1153 | yes | 7.65 |

* Indicates velocities measured between two non-consecutive probes, for example $u_{1-3}$

## APPENDIX K
## Mixture Data: Fixed CJ Detonation Pressure of 2400 bar

Table K–1: Pre-detonation pressure, in bar, for various mixtures corresponding to a CJ detonation pressure of 2400 bar

| $\chi$ | $2H_2+O_2$ $+\chi H_2$ | $H_2+O_2$ $+\chi He$ | $CH_4+2O_2$ $+1.5\chi He$ | $C_2H_4+3O_2$ $+2\chi He$ | $2C_2H_6+7O_2$ $+5\chi He$ |
|---|---|---|---|---|---|
| 0 | 110.31 | 110.31 | 71.693 | 62.222 | 61.900 |
| 1 | 113.46 | 109.68 | 80.863 | 71.525 | 72.816 |
| 2 | 121.58 | 111.47 | 87.883 | 78.444 | 80.749 |
| 3 | 131.59 | 114.38 | 93.907 | 84.165 | 87.272 |
| 4 | 142.47 | 117.99 | 99.416 | 89.212 | 93.033 |
| 5 | 153.48 | 122.12 | 104.66 | 93.851 | 98.362 |
| 6 | 164.68 | 126.68 | 109.78 | 98.239 | 103.45 |
| 7 | 175.83 | 131.62 | 114.88 | 102.48 | 108.41 |
| 8 | 186.89 | 136.91 | 120.02 | 106.63 | 113.33 |
| 9 | 197.81 | 142.51 | 125.24 | 110.76 | 118.27 |
| 10 | 208.60 | 148.37 | 130.58 | 114.89 | 123.26 |

Table K–2: CV explosion pressure, in bar, for various mixtures corresponding to a CJ detonation pressure of 2400 bar

| $\chi$ | $2H_2+O_2$ $+\chi H_2$ | $H_2+O_2$ $+\chi He$ | $CH_4+2O_2$ $+1.5\chi He$ | $C_2H_4+3O_2$ $+2\chi He$ | $2C_2H_6+7O_2$ $+5\chi He$ |
|---|---|---|---|---|---|
| 0 | 1222.60 | 1222.60 | 1212.99 | 1210.21 | 1210.44 |
| 1 | 1223.74 | 1222.17 | 1215.23 | 1212.56 | 1213.15 |
| 2 | 1225.98 | 1222.28 | 1216.92 | 1214.49 | 1215.19 |
| 3 | 1228.32 | 1222.43 | 1218.28 | 1216.09 | 1216.68 |
| 4 | 1230.86 | 1222.48 | 1219.21 | 1217.27 | 1217.86 |
| 5 | 1233.39 | 1222.40 | 1219.84 | 1218.23 | 1218.70 |
| 6 | 1235.93 | 1222.31 | 1220.20 | 1218.91 | 1219.20 |
| 7 | 1238.47 | 1222.29 | 1220.34 | 1219.41 | 1219.47 |
| 8 | 1241.04 | 1222.48 | 1220.36 | 1219.73 | 1219.63 |
| 9 | 1243.52 | 1223.00 | 1220.41 | 1219.70 | 1219.58 |
| 10 | 1245.97 | 1223.85 | 1220.43 | 1219.73 | 1219.63 |

Table K–3: Reflected CJ detonation pressure, in bar, for various mixtures corresponding to a CJ detonation pressure of 2400 bar

| $\chi$ | $2H_2+O_2$ $+\chi H_2$ | $H_2+O_2$ $+\chi$He | $CH_4+2O_2$ $+1.5\chi$He | $C_2H_4+3O_2$ $+2\chi$He | $2C_2H_6+7O_2$ $+5\chi$He |
|---|---|---|---|---|---|
| 0 | 5927.66 | 5927.66 | 6012.62 | 6027.44 | 6033.29 |
| 1 | 5914.10 | 5914.10 | 5978.14 | 5995.20 | 5995.32 |
| 2 | 5885.60 | 5898.05 | 5951.97 | 5970.03 | 5967.15 |
| 3 | 5854.40 | 5879.66 | 5928.82 | 5949.62 | 5943.60 |
| 4 | 5821.91 | 5861.01 | 5906.89 | 5931.27 | 5922.12 |
| 5 | 5791.80 | 5841.48 | 5887.09 | 5914.14 | 5902.39 |
| 6 | 5762.83 | 5821.00 | 5866.96 | 5898.10 | 5883.13 |
| 7 | 5735.39 | 5800.10 | 5847.36 | 5882.40 | 5864.84 |
| 8 | 5707.84 | 5779.68 | 5828.28 | 5866.77 | 5846.65 |
| 9 | 5681.67 | 5758.67 | 5809.48 | 5851.74 | 5828.47 |
| 10 | 5656.40 | 5737.93 | 5789.71 | 5836.74 | 5810.16 |

Table K–4: CV explosion temperature, in Kelvin, for various mixtures corresponding to CJ detonation pressure of 2400 bar

| $\chi$ | $2H_2+O_2$ $+\chi H_2$ | $H_2+O_2$ $+\chi$He | $CH_4+2O_2$ $+1.5\chi$He | $C_2H_4+3O_2$ $+2\chi$He | $2C_2H_6+7O_2$ $+5\chi$He |
|---|---|---|---|---|---|
| 0 | 4371.93 | 4371.93 | 4310.27 | 4619.84 | 4392.53 |
| 1 | 4124.03 | 4123.42 | 4080.34 | 4387.22 | 4163.78 |
| 2 | 3702.36 | 3909.36 | 3885.03 | 4192.38 | 3970.42 |
| 3 | 3319.78 | 3715.93 | 3711.34 | 4021.69 | 3799.30 |
| 4 | 2999.17 | 3536.66 | 3552.62 | 3867.90 | 3643.64 |
| 5 | 2734.44 | 3368.29 | 3405.03 | 3726.69 | 3499.40 |
| 6 | 2515.20 | 3209.23 | 3266.16 | 3595.18 | 3364.03 |
| 7 | 2331.84 | 3058.84 | 3134.53 | 3471.44 | 3235.86 |
| 8 | 2176.60 | 2917.00 | 3009.23 | 3354.06 | 3113.80 |
| 9 | 2043.57 | 2783.75 | 2889.77 | 3242.04 | 2997.16 |
| 10 | 1928.28 | 2659.13 | 2775.97 | 3134.73 | 2885.60 |

Table K–5: CV explosion sound speed, in m/s, for various mixtures corresponding to CJ detonation pressure of 2400 bar

| $\chi$ | $2H_2+O_2$ $+\chi H_2$ | $H_2+O_2$ $+\chi He$ | $CH_4+2O_2$ $+1.5\chi He$ | $C_2H_4+3O_2$ $+2\chi He$ | $2C_2H_6+7O_2$ $+5\chi He$ |
|---|---|---|---|---|---|
| 0 | 1618.5 | 1618.5 | 1340.8 | 1338.4 | 1326.3 |
| 1 | 1808.4 | 1797.5 | 1507.4 | 1495.2 | 1489.3 |
| 2 | 1921.0 | 1920.8 | 1629.5 | 1613.2 | 1610.2 |
| 3 | 1994.1 | 2010.1 | 1723.2 | 1705.5 | 1703.6 |
| 4 | 2041.0 | 2076.6 | 1797.1 | 1779.6 | 1777.9 |
| 5 | 2070.4 | 2126.5 | 1856.4 | 1840.3 | 1838.1 |
| 6 | 2088.2 | 2163.8 | 1904.6 | 1890.7 | 1887.5 |
| 7 | 2098.3 | 2190.7 | 1944.0 | 1932.8 | 1928.3 |
| 8 | 2103.0 | 2208.9 | 1976.0 | 1968.4 | 1962.2 |
| 9 | 2102.2 | 2219.5 | 2001.6 | 1998.6 | 1990.0 |
| 10 | 1928.28 | 2223.8 | 2021.4 | 2024.0 | 2012.5 |

Table K–6: CV explosion specific heat ratio, $\gamma$, for various mixtures corresponding to CJ detonation pressure of 2400 bar

| $\chi$ | $2H_2+O_2$ $+\chi H_2$ | $H_2+O_2$ $+\chi He$ | $CH_4+2O_2$ $+1.5\chi He$ | $C_2H_4+3O_2$ $+2\chi He$ | $2C_2H_6+7O_2$ $+5\chi He$ |
|---|---|---|---|---|---|
| 0 | 1.1455 | 1.1455 | 1.1442 | 1.1527 | 1.1461 |
| 1 | 1.1603 | 1.1713 | 1.1668 | 1.1715 | 1.1673 |
| 2 | 1.1835 | 1.1960 | 1.1873 | 1.1877 | 1.1863 |
| 3 | 1.2057 | 1.2217 | 1.2078 | 1.2031 | 1.2048 |
| 4 | 1.2250 | 1.2488 | 1.2288 | 1.2184 | 1.2238 |
| 5 | 1.2409 | 1.2773 | 1.2509 | 1.2342 | 1.2436 |
| 6 | 1.2540 | 1.3066 | 1.2741 | 1.2506 | 1.2644 |
| 7 | 1.2650 | 1.3359 | 1.2983 | 1.2678 | 1.2863 |
| 8 | 1.2745 | 1.3644 | 1.3232 | 1.2858 | 1.3090 |
| 9 | 1.2830 | 1.3911 | 1.3484 | 1.3047 | 1.3324 |
| 10 | 1.2907 | 1.4156 | 1.3732 | 1.3244 | 1.3560 |

## APPENDIX L
## Mixture Data: Fixed Reflected CJ Detonation Pressure of 5720 bar

Table L–1: Pre-detonation pressure, in bar, for various mixtures corresponding to a Reflected CJ detonation pressure of 5720 bar

| $\chi$ | $2H_2+O_2$ $+\chi H_2$ | $H_2+O_2$ $+\chi He$ | $CH_4+2O_2$ $+1.5\chi He$ | $C_2H_4+3O_2$ $+2\chi He$ | $2C_2H_6+7O_2$ $+5\chi He$ |
|---|---|---|---|---|---|
| 0 | 106.44 | 106.44 | 68.204 | 59.049 | 58.685 |
| 1 | 109.64 | 106.08 | 77.371 | 68.242 | 69.472 |
| 2 | 118.16 | 108.10 | 84.458 | 75.159 | 77.405 |
| 3 | 128.56 | 111.27 | 90.599 | 80.917 | 83.988 |
| 4 | 139.88 | 115.15 | 96.270 | 86.034 | 89.857 |
| 5 | 151.58 | 119.58 | 101.69 | 90.771 | 95.322 |
| 6 | 163.45 | 124.48 | 107.03 | 95.273 | 100.58 |
| 7 | 175.36 | 129.80 | 112.38 | 99.647 | 105.73 |
| 8 | 187.29 | 135.50 | 117.79 | 103.96 | 110.88 |
| 9 | 199.15 | 141.55 | 123.31 | 108.26 | 116.07 |
| 10 | 210.94 | 147.90 | 129.01 | 112.59 | 121.35 |

Table L–2: CV explosion pressure, in bar, for various mixtures corresponding to a Reflected CJ detonation pressure of 5720 bar

| $\chi$ | $2H_2+O_2$ $+\chi H_2$ | $H_2+O_2$ $+\chi He$ | $CH_4+2O_2$ $+1.5\chi He$ | $C_2H_4+3O_2$ $+2\chi He$ | $2C_2H_6+7O_2$ $+5\chi He$ |
|---|---|---|---|---|---|
| 0 | 1178.75 | 1178.75 | 1152.42 | 1146.67 | 1145.88 |
| 1 | 1182.81 | 1180.98 | 1161.31 | 1155.15 | 1155.86 |
| 2 | 1191.09 | 1184.49 | 1168.26 | 1162.08 | 1163.46 |
| 3 | 1199.95 | 1188.54 | 1174.28 | 1167.72 | 1169.74 |
| 4 | 1209.23 | 1192.51 | 1179.75 | 1172.67 | 1175.30 |
| 5 | 1218.03 | 1196.58 | 1184.53 | 1177.18 | 1180.20 |
| 6 | 1226.74 | 1200.83 | 1189.10 | 1181.22 | 1184.76 |
| 7 | 1235.13 | 1205.24 | 1193.37 | 1184.97 | 1188.89 |
| 8 | 1243.67 | 1209.76 | 1197.42 | 1188.55 | 1192.81 |
| 9 | 1251.91 | 1214.74 | 1201.38 | 1191.83 | 1196.63 |
| 10 | 1259.98 | 1219.99 | 1203.30 | 1194.98 | 1200.47 |

Table L–3: CJ detonation pressure, in bar, for various mixtures corresponding to a Reflected CJ detonation pressure of 5720 bar

| $\chi$ | $2H_2+O_2$ $+\chi H_2$ | $H_2+O_2$ $+\chi$He | $CH_4+2O_2$ $+1.5\chi$He | $C_2H_4+3O_2$ $+2\chi$He | $2C_2H_6+7O_2$ $+5\chi$He |
|---|---|---|---|---|---|
| 0 | 2313.79 | 2313.79 | 2280.14 | 2273.95 | 2271.97 |
| 1 | 2319.70 | 2319.15 | 2293.52 | 2286.33 | 2286.74 |
| 2 | 2331.71 | 2325.75 | 2303.98 | 2296.35 | 2297.82 |
| 3 | 2344.56 | 2333.40 | 2313.38 | 2304.59 | 2307.32 |
| 4 | 2357.86 | 2341.17 | 2322.36 | 2312.09 | 2316.08 |
| 5 | 2370.18 | 2349.30 | 2330.53 | 2319.17 | 2324.21 |
| 6 | 2382.16 | 2357.83 | 2338.84 | 2325.80 | 2332.14 |
| 7 | 2393.55 | 2366.52 | 2346.95 | 2332.28 | 2339.71 |
| 8 | 2405.12 | 2375.03 | 2354.87 | 2338.77 | 2347.24 |
| 9 | 2416.19 | 2383.80 | 2362.66 | 2345.03 | 2354.78 |
| 10 | 2426.99 | 2392.47 | 2370.87 | 2351.26 | 2362.37 |

Table L–4: CV explosion temperature, in Kelvin, for various mixtures corresponding to Reflected CJ detonation pressure of 5720 bar

| $\chi$ | $2H_2+O_2$ $+\chi H_2$ | $H_2+O_2$ $+\chi$He | $CH_4+2O_2$ $+1.5\chi$He | $C_2H_4+3O_2$ $+2\chi$He | $2C_2H_6+7O_2$ $+5\chi$He |
|---|---|---|---|---|---|
| 0 | 4365.12 | 4365.12 | 4300.82 | 4607.57 | 4381.75 |
| 1 | 4119.77 | 4118.18 | 4073.25 | 4377.68 | 4155.66 |
| 2 | 3700.58 | 3905.44 | 3879.62 | 4184.82 | 3964.15 |
| 3 | 3319.10 | 3713.10 | 3707.21 | 4015.59 | 3794.44 |
| 4 | 2998.94 | 3534.69 | 3549.52 | 3862.99 | 3639.89 |
| 5 | 2734.37 | 3366.97 | 3402.72 | 3722.75 | 3496.53 |
| 6 | 2515.18 | 3208.40 | 3264.50 | 3592.05 | 3361.88 |
| 7 | 2331.83 | 3058.36 | 3133.36 | 3468.96 | 3234.27 |
| 8 | 2176.60 | 2916.74 | 3008.44 | 3352.15 | 3112.66 |
| 9 | 2043.57 | 2783.62 | 2889.27 | 3240.59 | 2996.38 |
| 10 | 1928.28 | 2659.09 | 2775.62 | 3133.64 | 2885.09 |

Table L–5: CV explosion sound speed, in m/s, for various mixtures corresponding to Reflected CJ detonation pressure of 5720 bar

| $\chi$ | $2H_2+O_2$ $+\chi H_2$ | $H_2+O_2$ $+\chi He$ | $CH_4+2O_2$ $+1.5\chi He$ | $C_2H_4+3O_2$ $+2\chi He$ | $2C_2H_6+7O_2$ $+5\chi He$ |
|---|---|---|---|---|---|
| 0 | 1617.6 | 1617.6 | 1339.9 | 1337.2 | 1325.2 |
| 1 | 1805.6 | 1796.5 | 1506.3 | 1493.9 | 1488.1 |
| 2 | 1920.5 | 1919.9 | 1628.4 | 1611.9 | 1609.0 |
| 3 | 1993.9 | 2009.2 | 1722.2 | 1704.2 | 1702.5 |
| 4 | 2040.9 | 2075.8 | 1796.1 | 1778.4 | 1776.9 |
| 5 | 2070.4 | 2125.9 | 1855.6 | 1839.2 | 1837.2 |
| 6 | 2088.2 | 2163.3 | 1903.9 | 1889.6 | 1886.7 |
| 7 | 2098.3 | 2190.4 | 1943.4 | 1931.9 | 1927.6 |
| 8 | 2103.0 | 2208.7 | 1975.5 | 1967.6 | 1961.6 |
| 9 | 2104.0 | 2219.4 | 2001.2 | 1997.9 | 1989.5 |
| 10 | 2102.2 | 2223.7 | 2021.2 | 2023.4 | 2012.2 |

Table L–6: CV explosion specific heat ratio, $\gamma$, for various mixtures corresponding to Reflected CJ detonation pressure of 5720 bar

| $\chi$ | $2H_2+O_2$ $+\chi H_2$ | $H_2+O_2$ $+\chi He$ | $CH_4+2O_2$ $+1.5\chi He$ | $C_2H_4+3O_2$ $+2\chi He$ | $2C_2H_6+7O_2$ $+5\chi He$ |
|---|---|---|---|---|---|
| 0 | 1.1454 | 1.1454 | 1.1441 | 1.1525 | 1.1460 |
| 1 | 1.1602 | 1.1710 | 1.1665 | 1.1712 | 1.1670 |
| 2 | 1.1833 | 1.1957 | 1.1870 | 1.1873 | 1.1859 |
| 3 | 1.2056 | 1.2213 | 1.2074 | 1.2027 | 1.2045 |
| 4 | 1.2256 | 1.2485 | 1.2284 | 1.2180 | 1.2234 |
| 5 | 1.2409 | 1.2770 | 1.2505 | 1.2338 | 1.2432 |
| 6 | 1.2540 | 1.3063 | 1.2737 | 1.2501 | 1.2640 |
| 7 | 1.2650 | 1.3357 | 1.2979 | 1.2673 | 1.2859 |
| 8 | 1.2745 | 1.3642 | 1.3229 | 1.2854 | 1.3087 |
| 9 | 1.2830 | 1.3910 | 1.3481 | 1.3043 | 1.3321 |
| 10 | 1.2907 | 1.4155 | 1.3729 | 1.3240 | 1.3558 |

## APPENDIX M
## Mixture Data: Fixed Pre-Detonation Pressure of 106.44 bar

Table M–1: CV explosion pressure, in bar, for various mixtures corresponding to a pre-detonation pressure of 106.44 bar

| $\chi$ | $2H_2+O_2$ $+\chi H_2$ | $H_2+O_2$ $+\chi He$ | $CH_4+2O_2$ $+1.5\chi He$ | $C_2H_4+3O_2$ $+2\chi He$ | $2C_2H_6+7O_2$ $+5\chi He$ |
|---|---|---|---|---|---|
| 0 | 1178.75 | 1178.75 | 1819.64 | 2103.50 | 2112.15 |
| 1 | 1147.65 | 1185.11 | 1611.78 | 1827.40 | 1792.93 |
| 2 | 1071.58 | 1165.85 | 1481.43 | 1663.86 | 1614.28 |
| 3 | 992.20 | 1135.79 | 1385.12 | 1548.77 | 1491.76 |
| 4 | 919.29 | 1100.67 | 1307.33 | 1459.69 | 1397.95 |
| 5 | 854.82 | 1063.16 | 1241.00 | 1386.18 | 1321.07 |
| 6 | 798.56 | 1024.71 | 1182.41 | 1323.21 | 1255.20 |
| 7 | 749.54 | 986.31 | 1129.40 | 1267.61 | 1197.00 |
| 8 | 706.75 | 948.55 | 1080.68 | 1217.42 | 1144.43 |
| 9 | 669.09 | 911.90 | 1035.45 | 1171.44 | 1096.23 |
| 10 | 635.75 | 876.71 | 993.19 | 1128.73 | 1051.57 |

Table M–2: CJ detonation pressure, in bar, for various mixtures corresponding to a pre-Detonation pressure of 106.44 bar

| $\chi$ | $2H_2+O_2$ $+\chi H_2$ | $H_2+O_2$ $+\chi He$ | $CH_4+2O_2$ $+1.5\chi He$ | $C_2H_4+3O_2$ $+2\chi He$ | $2C_2H_6+7O_2$ $+5\chi He$ |
|---|---|---|---|---|---|
| 0 | 2313.79 | 2313.79 | 3600.31 | 4171.57 | 4188.10 |
| 1 | 2250.76 | 2327.23 | 3183.38 | 3617.25 | 3547.16 |
| 2 | 2097.77 | 2289.16 | 2921.79 | 3288.18 | 3188.47 |
| 3 | 1938.73 | 2229.82 | 2728.87 | 3056.88 | 2942.71 |
| 4 | 1792.67 | 2160.78 | 2573.58 | 2877.95 | 2755.00 |
| 5 | 1663.50 | 2087.27 | 2441.70 | 2731.05 | 2601.71 |
| 6 | 1550.83 | 2012.04 | 2325.68 | 2605.45 | 2470.87 |
| 7 | 1452.62 | 1936.72 | 2221.11 | 2494.96 | 2355.68 |
| 8 | 1366.82 | 1862.39 | 2125.25 | 2395.62 | 2251.99 |
| 9 | 1291.40 | 1789.88 | 2036.31 | 2304.86 | 2157.13 |
| 10 | 1224.65 | 1719.83 | 1953.11 | 2220.89 | 2069.31 |

Table M–3: Reflected CJ detonation pressure, in bar, for various mixtures corresponding to a pre-detonation pressure of 106.44 bar

| $\chi$ | $2H_2+O_2$ $+\chi H_2$ | $H_2+O_2$ $+\chi$He | $CH_4+2O_2$ $+1.5\chi$He | $C_2H_4+3O_2$ $+2\chi$He | $2C_2H_6+7O_2$ $+5\chi$He |
|---|---|---|---|---|---|
| 0 | 5714.86 | 5714.88 | 9020.60 | 10480.2 | 10529.6 |
| 1 | 5546.30 | 5735.05 | 7930.13 | 9037.06 | 8861.12 |
| 2 | 5144.50 | 5625.39 | 7245.76 | 8179.84 | 7927.78 |
| 3 | 4729.49 | 5462.92 | 6741.19 | 7578.10 | 7287.27 |
| 4 | 4349.66 | 5318.93 | 6334.90 | 7112.28 | 6798.04 |
| 5 | 4015.08 | 5080.76 | 5989.47 | 6730.30 | 6398.08 |
| 6 | 3724.33 | 4880.43 | 5685.93 | 6402.65 | 6056.73 |
| 7 | 3471.15 | 4681.39 | 5412.12 | 6115.17 | 5756.88 |
| 8 | 3250.66 | 4486.01 | 5161.38 | 5856.61 | 5486.10 |
| 9 | 3057.24 | 4295.67 | 4929.67 | 5620.27 | 5238.99 |
| 10 | 2886.28 | 4112.96 | 4712.50 | 5401.36 | 5010.36 |

Table M–4: CV explosion temperature, in Kelvin, for various mixtures corresponding to pre-detonation pressure of 106.44 bar

| $\chi$ | $2H_2+O_2$ $+\chi H_2$ | $H_2+O_2$ $+\chi$He | $CH_4+2O_2$ $+1.5\chi$He | $C_2H_4+3O_2$ $+2\chi$He | $2C_2H_6+7O_2$ $+5\chi$He |
|---|---|---|---|---|---|
| 0 | 4365.12 | 4365.12 | 4385.08 | 4746.40 | 4502.16 |
| 1 | 4115.98 | 4118.71 | 4124.34 | 4468.09 | 4229.25 |
| 2 | 3693.83 | 3903.45 | 3911.00 | 4246.38 | 4011.19 |
| 3 | 3313.39 | 3708.52 | 3725.68 | 4057.93 | 3824.38 |
| 4 | 2995.21 | 3528.26 | 3559.18 | 3891.69 | 3658.14 |
| 5 | 2732.23 | 3359.59 | 3406.37 | 3741.47 | 3506.60 |
| 6 | 2514.03 | 3200.87 | 3264.13 | 3603.36 | 3366.22 |
| 7 | 2331.23 | 3051.27 | 3130.48 | 3474.78 | 3234.70 |
| 8 | 2176.29 | 2910.47 | 3004.15 | 3353.92 | 3110.53 |
| 9 | 2043.42 | 2778.34 | 2884.40 | 3239.50 | 2992.74 |
| 10 | 1928.20 | 2654.81 | 2770.79 | 3130.60 | 2880.71 |

Table M–5: CV explosion sound speed, in m/s, for various mixtures corresponding to pre-detonation pressure of 106.44 bar

| $\chi$ | $2H_2+O_2$ $+\chi H_2$ | $H_2+O_2$ $+\chi He$ | $CH_4+2O_2$ $+1.5\chi He$ | $C_2H_4+3O_2$ $+2\chi He$ | $2C_2H_6+7O_2$ $+5\chi He$ |
|---|---|---|---|---|---|
| 0 | 1617.6 | 1617.6 | 1348.4 | 1349.9 | 1336.9 |
| 1 | 1805.0 | 4796.6 | 1514.1 | 1506.2 | 1498.9 |
| 2 | 1918.7 | 1919.4 | 1634.8 | 1622.6 | 1617.9 |
| 3 | 1991.7 | 2007.8 | 1726.8 | 1713.1 | 1709.5 |
| 4 | 2038.9 | 2073.3 | 1799.0 | 1785.5 | 1781.9 |
| 5 | 2068.9 | 2122.4 | 1856.9 | 1844.5 | 1840.5 |
| 6 | 2087.2 | 2159.0 | 1903.8 | 1893.3 | 1888.3 |
| 7 | 2097.6 | 2185.6 | 1942.0 | 1934.1 | 1927.8 |
| 8 | 2102.6 | 2203.6 | 1973.0 | 1968.4 | 1960.5 |
| 9 | 2103.7 | 2214.5 | 1997.9 | 1997.3 | 1987.3 |
| 10 | 2102.1 | 2219.1 | 2017.3 | 2021.8 | 2009.1 |

Table M–6: CV explosion specific heat ratio, $\gamma$, for various mixtures corresponding to pre-detonation pressure of 106.44 bar

| $\chi$ | $2H_2+O_2$ $+\chi H_2$ | $H_2+O_2$ $+\chi He$ | $CH_4+2O_2$ $+1.5\chi He$ | $C_2H_4+3O_2$ $+2\chi He$ | $2C_2H_6+7O_2$ $+5\chi He$ |
|---|---|---|---|---|---|
| 0 | 1.1454 | 1.1454 | 1.1453 | 1.1542 | 1.1476 |
| 1 | 1.1599 | 1.1711 | 1.1684 | 1.1738 | 1.1695 |
| 2 | 1.1825 | 1.1955 | 1.1889 | 1.1901 | 1.1885 |
| 3 | 1.2044 | 1.2208 | 1.2090 | 1.2053 | 1.2068 |
| 4 | 1.2237 | 1.2473 | 1.2296 | 1.2204 | 1.2254 |
| 5 | 1.2398 | 1.2752 | 1.2511 | 1.2357 | 1.2447 |
| 6 | 1.2532 | 1.3038 | 1.2736 | 1.2517 | 1.2648 |
| 7 | 1.2645 | 1.3325 | 1.2971 | 1.2683 | 1.2860 |
| 8 | 1.2742 | 1.3606 | 1.3212 | 1.2858 | 1.3080 |
| 9 | 1.2828 | 1.3872 | 1.3457 | 1.3040 | 1.3306 |
| 10 | 1.2906 | 1.4117 | 1.3699 | 1.3230 | 1.3535 |

## APPENDIX N
## Mixture Data: CV Explosion Pressure of 2400 bar

Table N–1: Pre-detonation pressure pressure, in bar, for various mixtures corresponding to a CV explosion pressure of 2400 bar

| $\chi$ | $2H_2+O_2$ $+\chi H_2$ | $H_2+O_2$ $+\chi$He | $CH_4+2O_2$ $+1.5\chi$He | $C_2H_4+3O_2$ $+2\chi$He | $2C_2H_6+7O_2$ $+5\chi$He |
|---|---|---|---|---|---|
| 0 | 213.06 | 213.06 | 139.45 | 121.00 | 120.55 |
| 1 | 219.65 | 211.80 | 156.86 | 138.65 | 141.35 |
| 2 | 236.36 | 215.46 | 170.36 | 151.87 | 156.59 |
| 3 | 256.14 | 221.46 | 182.08 | 162.90 | 169.22 |
| 4 | 277.09 | 228.90 | 192.91 | 172.71 | 180.48 |
| 5 | 298.38 | 237.41 | 203.32 | 181.80 | 190.99 |
| 6 | 319.64 | 246.77 | 213.57 | 190.46 | 201.10 |
| 7 | 340.67 | 256.85 | 223.83 | 198.89 | 211.04 |
| 8 | 361.38 | 267.52 | 234.21 | 207.22 | 220.95 |
| 9 | 381.76 | 278.67 | 244.75 | 215.52 | 230.92 |
| 10 | 401.79 | 290.20 | 255.49 | 223.88 | 241.01 |

Table N–2: CJ detonation pressure, in bar, for various mixtures corresponding to a CV explosion pressure of 2400 bar

| $\chi$ | $2H_2+O_2$ $+\chi H_2$ | $H_2+O_2$ $+\chi$He | $CH_4+2O_2$ $+1.5\chi$He | $C_2H_4+3O_2$ $+2\chi$He | $2C_2H_6+7O_2$ $+5\chi$He |
|---|---|---|---|---|---|
| 0 | 4711.85 | 4711.85 | 4749.09 | 4759.58 | 4758.69 |
| 1 | 4706.91 | 4713.91 | 4740.60 | 4750.79 | 4748.37 |
| 2 | 4698.09 | 4713.34 | 4734.06 | 4743.44 | 4740.92 |
| 3 | 4688.73 | 4712.68 | 4729.11 | 4737.66 | 4734.92 |
| 4 | 4679.07 | 4712.24 | 4725.41 | 4733.05 | 4730.47 |
| 5 | 4669.38 | 4712.16 | 4723.03 | 4729.46 | 4727.37 |
| 6 | 4659.91 | 4712.13 | 4721.54 | 4726.68 | 4725.26 |
| 7 | 4650.56 | 4711.62 | 4720.74 | 4724.90 | 4724.13 |
| 8 | 4640.93 | 4710.13 | 4720.41 | 4723.99 | 4723.60 |
| 9 | 4631.79 | 4707.43 | 4719.77 | 4723.32 | 4723.26 |
| 10 | 4622.72 | 4703.50 | 4718.73 | 4723.27 | 4722.87 |

Table N–3: Reflected CJ detonation pressure, in bar, for various mixtures corresponding to a CV explosion pressure of 2400 bar

| $\chi$ | $2H_2+O_2$ $+\chi H_2$ | $H_2+O_2$ $+\chi He$ | $CH_4+2O_2$ $+1.5\chi He$ | $C_2H_4+3O_2$ $+2\chi He$ | $2C_2H_6+7O_2$ $+5\chi He$ |
|---|---|---|---|---|---|
| 0 | 11637.6 | 11637.6 | 11897.7 | 11953.4 | 11962.7 |
| 1 | 11598.8 | 11616.1 | 11808.3 | 11867.5 | 11861.7 |
| 2 | 11521.3 | 11583.1 | 11740.4 | 11799.4 | 11787.4 |
| 3 | 11437.4 | 11545.4 | 11682.5 | 11744.7 | 11726.0 |
| 4 | 11350.5 | 11507.7 | 11630.2 | 11697.1 | 11672.7 |
| 5 | 11268.6 | 11469.4 | 11585.4 | 11654.5 | 11626.2 |
| 6 | 11189.3 | 11428.9 | 11542.1 | 11616.0 | 11583.1 |
| 7 | 11037.4 | 11386.6 | 11501.6 | 11580.7 | 11544.3 |
| 8 | 10965.1 | 11342.9 | 11463.3 | 11547.7 | 11507.2 |
| 9 | 10895.0 | 11295.2 | 11424.7 | 11516.5 | 11470.6 |
| 10 | 2886.28 | 11245.1 | 11383.4 | 11486.9 | 11433.6 |

Table N–4: CV explosion temperature, in Kelvin, for various mixtures corresponding to CV explosion pressure of 2400 bar

| $\chi$ | $2H_2+O_2$ $+\chi H_2$ | $H_2+O_2$ $+\chi He$ | $CH_4+2O_2$ $+1.5\chi He$ | $C_2H_4+3O_2$ $+2\chi He$ | $2C_2H_6+7O_2$ $+5\chi He$ |
|---|---|---|---|---|---|
| 0 | 4496.21 | 4496.21 | 4436.03 | 4776.76 | 4527.33 |
| 1 | 4203.92 | 4224.87 | 4185.97 | 4521.97 | 4277.98 |
| 2 | 3740.50 | 3991.49 | 3974.01 | 4309.15 | 4067.71 |
| 3 | 3336.86 | 3781.49 | 3786.10 | 4123.25 | 3882.18 |
| 4 | 3006.56 | 3588.05 | 3615.01 | 3956.30 | 3713.96 |
| 5 | 2737.60 | 3407.72 | 3456.56 | 3803.47 | 3558.65 |
| 6 | 2516.57 | 3238.81 | 3308.17 | 3661.60 | 3413.46 |
| 7 | 2332.43 | 3080.53 | 3168.22 | 3528.53 | 3276.59 |
| 8 | 2176.87 | 2932.56 | 3035.77 | 3402.74 | 3146.86 |
| 9 | 2043.69 | 2794.70 | 2910.27 | 3283.16 | 3023.58 |
| 10 | 1928.33 | 2666.72 | 2791.49 | 3167.07 | 2906.34 |

Table N–5: CV explosion sound speed, in m/s, for various mixtures corresponding to CV explosion pressure of 2400 bar

| $\chi$ | $2H_2+O_2$ $+\chi H_2$ | $H_2+O_2$ $+\chi He$ | $CH_4+2O_2$ $+1.5\chi He$ | $C_2H_4+3O_2$ $+2\chi He$ | $2C_2H_6+7O_2$ $+5\chi He$ |
|---|---|---|---|---|---|
| 0 | 1633.0 | 1633.0 | 1353.4 | 1352.6 | 1339.2 |
| 1 | 1820.3 | 1816.0 | 1523.4 | 1513.3 | 1505.9 |
| 2 | 1931.2 | 1941.1 | 1647.3 | 1633.3 | 1628.5 |
| 3 | 2000.9 | 2030.7 | 1741.8 | 1726.7 | 1722.9 |
| 4 | 2045.0 | 2096.7 | 1815.8 | 1801.4 | 1797.5 |
| 5 | 2072.7 | 2145.4 | 1874.9 | 1862.1 | 1857.6 |
| 6 | 2089.2 | 2180.9 | 1922.5 | 1912.3 | 1906.6 |
| 7 | 2098.9 | 2205.7 | 1961.0 | 1954.1 | 1946.7 |
| 8 | 2103.3 | 2221.8 | 1991.7 | 1989.1 | 1979.6 |
| 9 | 2104.1 | 2229.9 | 2015.8 | 2018.4 | 2006.2 |
| 10 | 2102.3 | 2232.1 | 2034.0 | 2042.9 | 2027.2 |

Table N–6: CV explosion specific heat ratio, $\gamma$, for various mixtures corresponding to CV explosion pressure of 2400 bar

| $\chi$ | $2H_2+O_2$ $+\chi H_2$ | $H_2+O_2$ $+\chi He$ | $CH_4+2O_2$ $+1.5\chi He$ | $C_2H_4+3O_2$ $+2\chi He$ | $2C_2H_6+7O_2$ $+5\chi He$ |
|---|---|---|---|---|---|
| 0 | 1.1475 | 1.1475 | 1.1460 | 1.1598 | 1.1479 |
| 1 | 1.1641 | 1.1756 | 1.1705 | 1.1831 | 1.1710 |
| 2 | 1.1877 | 1.2023 | 1.1927 | 1.2019 | 1.1915 |
| 3 | 1.2093 | 1.2296 | 1.2144 | 1.2184 | 1.2113 |
| 4 | 1.2275 | 1.2581 | 1.2367 | 1.2339 | 1.2315 |
| 5 | 1.2424 | 1.2874 | 1.2599 | 1.2488 | 1.2524 |
| 6 | 1.2549 | 1.3169 | 1.2839 | 1.2636 | 1.2741 |
| 7 | 1.2655 | 1.3460 | 1.3088 | 1.2779 | 1.2967 |
| 8 | 1.2748 | 1.3736 | 1.3340 | 1.2926 | 1.3200 |
| 9 | 1.2832 | 1.3992 | 1.3590 | 1.3074 | 1.3436 |
| 10 | 1.2908 | 1.4225 | 1.3833 | 1.3224 | 1.3671 |